DESIGN AND DEVELOPMENT OF CARBON ALLOTROPE BASED SOFT MATERIALS FOR BIOSENSING AND BIOIMAGING

Thesis Submitted for the Degree of

Doctor of Philosophy (Science)

to

Jadavpur University

August 2023

by

Monalisa Chowdhury
School of Biological Sciences
Indian Association for the Cultivation of Science
Jadavpur, Kolkata 700032
India

इंडियन एसोसियेशन फर दि कल्टिवेशन आफ साइंस
ইণ্ডিয়ান এ্যাসোসিয়েশন ফর দি কালটিভেশন অব সায়েন্স
Indian Association for the Cultivation of Science
2A & B Raja S. C. Mullick Road, Jadavpur,
Kolkata - 700032, India

Dr. Prasanta Kumar Das
Senior Professor
School of Biological Sciences

Phone : +91-33-2473-4971
Fax : +91-33-2473-2805
Email : bcpkd@iacs.res.in

To Whom It May Concern

This is to certify that the thesis entitled "**DESIGN AND DEVELOPMENT OF CARBON ALLOTROPE BASED SOFT MATERIALS FOR BIOSENSING AND BIOIMAGING**" submitted by Miss Monalisa Chowdhury who got her name registered on 10.09.2018 for the award of Ph.D. (Science) degree of Jadavpur University, is absolutely based upon her own work under the supervision of Prof. Prasanta Kumar Das and that neither this thesis nor any part of it has been submitted for either any degree/diploma or any other academic award anywhere before.

Prasanta Kr. Das 07/08/2023
(PRASANTA KUMAR DAS)

Signature of the supervisor
and date with official seal

Dr. Prasanta K. Das
Senior Professor
Chair-School of Biological Sciences
Indian Association for the Cultivation of Science
Jadavpur, Kolkata - 700032

Dedicated to Madhab,

Baba, Maa, Vai and Fasha

DECLARATION

The research work embodied in this thesis entitled "**DESIGN AND DEVELOPMENT OF CARBON ALLOTROPE BASED SOFT MATERIALS FOR BIOSENSING AND BIOIMAGING**" being submitted to Jadavpur University, Kolkata has been carried out at Indian Association for the Cultivation of Science, Jadavpur, under the supervision of Prof. Prasanta Kumar Das, Senior Professor, School of Biological Sciences, Indian Association for the Cultivation of Science. This work is original and has not been submitted in part or in full, for any degree or diploma to this or any other university.

Monalisa Chowdhury
07/08/2023

MONALISA CHOWDHURY

August 2023

CONTENTS

PREFACE

The research work integrated in the present thesis entitled as "**DESIGN AND DEVELOPMENT OF CARBON ALLOTROPE BASED SOFT MATERIALS FOR BIOSENSING AND BIOIMAGING**" deals with the exploration mostly on the advancement of carbon-based nanomaterial and study their diversified applications in the domain of biomedicine, especially in cancer disease, bioimaging and biosensing. The work also depicts the synthesis of metal doped soft carbon nanomaterials having superior physicochemical properties and cytocompatibility in biological milieu. The as synthesized carbon-based nanomaterial systems were also used as biomolecule sensors. Furthermore, these observations can potentially contribute to various applications in interdisciplinary sciences.

The present investigations have been carried out by the author in the School of Biological Sciences, Indian Association for the Cultivation of Science, Jadavpur, Kolkata 700032, India during the period 2017-2023 under the supervision of Prof. Prasanta Kumar Das.

The thesis contains four chapters in addition to general introduction.

The **Introduction** mainly highlights the scientific significance of nanomaterials especially carbon nanomaterial including carbon dots. It delivers a brief outline of how nature motivates the scientists to construct bio-inspired soft-nanomaterials and replicate their utility. It also provides a concise demonstration of amalgamation of biology with technology with the help of nanomaterials. These nano-dimension materials can also act in cellular environment mimicking the cellular functions. Carbon nanomaterials especially carbon dots get lot of attention due to their cytocompatibility, easy synthesis, tunable intrinsic fluorescence property, low toxicity etc in this domain. Drug delivery, theranostic property of carbon dots and its use in alternative therapies for cancer treatments is also emphasized in the introductory part.

Chapter 1 describes the development of riboflavin (photosensitizer) tailored surface functionalized carbon dot (RCD1s). RCD1s was designed to utilized in visible light induced targeted cancer therapy. Phenylboronic acid appended

PREFACE

biotinylated blue emitting carbon dot (CD1s) was covalently linked with riboflavin having "diol" moiety by using complementary boronate-diol linkage and fabricated water-soluble, green emitting RCD1s. Interestingly, this RCD1s has the ability to produce reactive oxygen species (ROS) such as hydroxyl and superoxide radicals under exposure of visible light (wavelength:460–490 nm). These ROS also can destroy the structure of DNA by oxidative pathway. We observed ~5-fold higher efficacy of killing cancer cells (B16F10 and HeLa) than non-cancer cell (NIH3T3) through ROS induced oxidative DNA damage. The presence of biotin on the surface of the riboflavin tethered carbon dot ensured the selective killing of cancer cells over normal cells.

Chapter 2 delineates the design and preparation of covalently tailored biotinylated Fe^{2+}-doped carbon dots (FCD_b). This blue emitting FCD_b was successfully used as a pro-drug activator, diagnostic probe, and target-specific delivery vehicle for anticancer drug paclitaxel in pro-drug–free drug combination therapy of cancer treatment. FCD_b can effectively sense H_2O_2 by fluorescence quenching as well as activate H_2O_2 (pro-drug), which oxidatively damage the DNA through the generation of reactive oxygen species (ROS). FCD_b was utilized as selective cellular markers for cancer cell B16F10 owing to their high H_2O_2 content, which was more distinct due to the overexpression of biotin receptor in cancer cell. Anticancer drug paclitaxel (PTX)-loaded FCD_b (FCD_b - PTX) was employed for the selective killing of B16F10 cancer cells. This pro-drug–free drug formulation (FCD_b - PTX) exhibited ~2.7- to 3.5-fold higher killing of B16F10 cells mostly via early as well as late apoptotic path in comparison to non-cancer NIH3T3 cells through the synergistic action of ROS (generated from H_2O_2 in the presence of FCD_b) and anticancer effect of PTX.

Chapter 3 illustrates alternative strategies using biochemical features of cancer cells to promote apoptosis. One such intrinsic important biochemical feature of malignant cells is hypoxia (scarcity of O_2 in tissue), alteration of which can lead to cell death. Hypoxia inducible factor 1α (HIF-1α) has the key role in hypoxia generation. Cobalt Chloride ($CoCl_2$) is a well known hypoxia mimicking agent, which is used for creating hypoxic environment in cellular level. Thus, we

synthesized biotinylated Co^{2+}-integrated carbon dot ($CoCD_b$) that specifically diagnose and selectively killed cancer cells with 3-3.1- fold higher efficiency over non-cancer cells by hypoxia induced apoptosis in absence of traditional therapeutic intervention. Immunoblotting assay in $CoCD_b$ treated MDA-MB-231 cells confirmed the increased expression of HIF-1α that was responsible for efficient killing of cancer cells. In 2D cells and 3D tumor spheroid, $CoCD_b$ treated cancer cells showed significant apoptosis via early apoptotic pathway.

Chapter 4 demonstrates the development of Copper (Cu^{+2}) doped carbon dot (CuCD) using hydrothermal method for the sensing of Guanine. Guanine is crucial part of DNA and any alteration in the concentration of this nucleobase can cause mutations, tumorigenesis and cell death. So, precise detection of this component in biological sample is essential for to know the early signals of various diseases and monitoring cellular environment. Literature supports the fact that Cu^{2+} can form a stronger binding in presence of guanine that can lead to DNA denaturation which is similar to acid denaturation. Considering this fact, we prepared Cu^{2+} doped carbon dot (CuCD) having blue emission under UV light irradiation. Cu^{2+} acted as an integral part of the system and thus used as a sensor for guanine. The fluorescence property of CuCD got quenched in presence of guanine having LOD - 1.57 μM. Importantly, guanine was sensed by CuCD with high selectivity and sensitivity against other nucleobases of DNA (adenine, cytosine, thymine) as well as with respect to many other monovalent, divalent ions, amino acids and biomolecule. We further exploited this nature of CuCD in the bioimaging of guanine treated cell lines.

Each chapter (**Chapter 1** to **4**) begins with a short Introduction followed by Results and Discussion, Conclusion, Experimental section, Characterization Data of the synthesized carbon nanomaterials and finally the References.

ACKNOWLEDGEMENT

ACKNOWLEDGEMENT

In the verge of accomplishment of one of my treasured dream, my doctoral research, I wanted to express my gratitude, sincere gratification, immense respect and love for everyone who stood beside me, accompanied me or supported me in the terrain of my journey. Research is collective work encompassing zillion forms of experiences. Through this long six years journey I experienced the ups and downs of this path specially the one and half years of covid-19 pandemic. This journey would not have been complete without the sincere and honest efforts & help from my supervisor, co-workers, friends, my family and well wishers who have been an integral part of this saga for all these years. My cordial thanks to all the people mentioned here and others whose names I might have omitted unwittingly.

Fast and foremost I sincerely express my heartfelt respect, gratitude and thanks to my supervisor Prof. Prasanta Kumar Das for his inspiring support and guidance, scientific or otherwise, remarkable patience and constant encouragement throughout the different stages of my doctoral investigations. It would have been impossible to achieve this dream without his enduring care and motivation in so many different but unique ways even when he has lot on his plate.

I take the pleasure of acknowledging my institute Indian Association for the Cultivation of Science (IACS) for providing me this beautiful platform to do my research work and also University Grant Commission (UGC) and IACS for my doctoral fellowship.

I also gratefully recognize the support of the faculty members of our department, Prof. Arindam Banerjee, Dr. Rupa Mukhopadhyay, Dr. Siddhartha Shankar Jana, Dr. Deepak Kumar Sinha, Dr. Prosenjit Sen and Dr. Benubrata Das. I thank Prof. Pradyut Ghosh of our institute for his sincere help.

It gives me immense pleasure to offer my sincere thanks to CSS facility , all other sections and all other staffs of the department namely Gour da, chanchal da, Shovon da, Prasenjit da, Ashok da. I thank Banik da, Supriyo da, Sumon da, Goutam da, Bhola da, Champa di and Gopal da, who have all helped during several experimental works. I am very grateful to the workers of the canteen for their untiring services at all times.

ACKNOWLEDGEMENT

I gratefully acknowledge all my departmental colleagues Sudipta, Priyanka, Arpana, Srijita Di, Arijit Da for their support during the course of my PhD work.

It will be incomplete if I don't mention my Research Scholar Association (RSA) colleagues Debdutta Di, Manjistha, Arnab and Student Affair Commision (SAC) members for the fun and happiness during the rehearsals of fest and fresher's welcome functions that breathe the fresh air during my long PhD schedule.

I am always indebted to my school, my college (both in U.G and P.G) for giving me the environment and guidance for proper growing. and all my teachers who planted the seeds of my interest in chemistry during these days specially Archana Di, Meenakhi Di, S.P.G Sir, Ashish Sir, B.N.D Sir, Baren Sir, S.K Sir, A.D Sir, A.R Sir, S.K.M Sir, U.A Sir, A.K.P Sir and many more.

Finally talking about my lab, it was my second home and the time I spent in here was full with love, life and happiness. I was always in debt to GOD for giving me such a wonderful group to work with and gave me opportunity to know this beautiful people with whom I can just be myself. Thank you is not enough for you people. You all mean more to me than just my labmates. The love, affection and guidance for my work from all my senior labmates Krishnendu da, Saheli di, Soumik da, Pritam da, Debayan were immense. I am indebted for my life to all of them. Also, thanks to my senior lab members with whom I have not shared lab yet they encourage me by their works and thinking. I owe heartful thanks to all my junior labmates Sudeshna, Aftab, Kathakoli, Afreen, Debolina, Rajarshee, Ambalika whose company always boosted me up and a special thanks to Aparajita Di whose cheerful and wise words always guide me through my journey. I have special words of thanks for Debolina with whom most of my lab hours were spent and who always stood by me irrespective of my good or bad times. Last but not least, I must mention name of the other co-passenger of the same ship, Anup whose constant support, cooperation and goofiness make the work entertaining and I do not want to shorten you with only thanks. The tight bonding and understanding with him provided me a blissful period during this journey. I will cherish all of them for showering me with some wonderful memories and colourful days in IACS both inside and outside the lab.

ACKNOWLEDGEMENT

I owe my heartful thanks to my friends namely Swarup, Bapi, Aruntima, Piya, Saheli, Nupur, Saswati, Sayantika, Kalyan, Ayan, Snehashis, Suvankar , Arcko who blessed me with a life of joy in the hours when lab lights were off. My special thanks to my childhood and most precious friend of my life Eashu, whose ceaseless love, affection, support and guidance was, always the guiding light of my life through this journey.

I also pay my gratitude and express my deepest appreciation to all my family members. I am thankful to my late thakuma, jethu, brorma, borokaka, borokaki, chotokaka, chotokaki, boropisi, boropisemosai, chotopisi, chotopisemosai, mama, mami, masi, late dida, Dadamini, boudi, Choton da, boudi, Saheb Da, Piku, Kuheli, Piu, Subho, my little nephews Soujanya, Deep and little niece Arnika for their throughout unconditional love and care for me.

Finally, I must say that all this is because of my Ma and Baba. They have given me everything which let me stand on that platform. Words are not enough to thank them because it is my parents who make me what I am today and without them I would not have been so lucky as I am today. I have no words to acknowledge the sacrifices you made to bring me up at this stage. A special Thanks for my younger brother Chotu for trusting me, standing beside me in all my hard times and unconditionally loving and caring for me. Irrespective of your young age your practical mind, taught me how to deal certain situations in life. I am absolutely blessed and I am very grateful for where I am today and all this is because of you three.

Now the most important acknowledgement of all above is the acknowledgement of the Divine Power. Without the mercy of this power nothing can ever happened in universe. I am grateful to Madhab, Whose constant presence felt by me throughout my journey. His blessings, patience, divine guidance and protection from my own darkness make me capable to successfully endure this journey.

Monalisa Chowdhury

August

LIST OF ABBREVIATION

ABBREVIATIONS

AFM	:	Atomic force microscopy
Boc	:	*tert*-Butoxycarbonyl
CD	:	Circulardichroism
CDs	:	Carbon Dots
$CoCl_2,7H_2O$	:	Cobalt chloride heptahydrate
$CuCl_2,2H_2O$	:	Copper chloride dihydrate
0D	:	Zero dimensional
1D	:	One-dimensional
2D	:	Two-dimensional
3D	:	Three-dimensional
DCC	:	*N*, *N*′-dicyclohexylcarbodiimide
DCF	:	2′,7′-Dichlorofluorescein
DCM	:	Dichloromethane
DCFH-DA	:	Dichlorofluorescein diacetate
DFO	:	Desferrioxamine
DMAP	:	4-*N*, *N*-(dimethylamino)pyridine
DMEM	:	Dulbecco'smodifiedeagle's medium
DMF	:	*N*, *N*-Dimethylformamide
DNA	:	Dioxyribonucleic acid
DPBF	:	1,3-diphenylisobenzophuran

LIST OF ABBREVIATION

EDC	:	1-ethyl-3-(3-(dimethylamino)propyl)-carbodiimide
EDTA	:	Ethylenediaminetetraacetic acid
EPR	:	Electron Paramagnetic Resonance
EthD-1	:	Ethidium homodimer-1
EtOAc	:	Ethyl acetate
FBS	:	Fetal bovine serum
FEG-TEM	:	Field-emission gun transmission electronmicroscopy
$FeSO_4,7H_2O$	:	Ferrous sulfate heptahydrated
FITC	:	Fluorescein isothiocyanate
FTIR	:	Fourier transform infrared
GNP	:	Gold Nanoparticle
GO	:	Graphene oxide
H_2SO_4	:	Sulphuric acid
HIF-1α	:	hypoxia inducible factor 1α
HOBt	:	Hydroxybenzotriazole
HRMS	:	High resolution mass spectrometry
KBr	:	Potassium bromide
MeOH	:	Methanol
MTT	:	(3-(4,5-Dimethylthiazol-2-yl)-2,5-diphenyltetrazolium bromide
NHS	:	N-hydroxy succinimide
NMR	:	Nuclear magnetic resonance

LIST OF ABBREVIATION

PBS	:	Phosphate-buffered saline
PHDs	:	Prolylhydroxylases domain-containing protein
PI	:	Propidium Iodide
PL	:	Photo Luminescence
PTX	:	Paclitaxel
PVDF	:	Polyvinylidene difluoride
ROS	:	Reactive Oxygen Species
SSI	:	Suspension Stability Index
SDS-PAGE	:	Sodium Dodecyl Sulphate-Polyacrylamide Gel Electrophoresis
TBST	:	Tris buffer saline containing Tween-20
TFA	:	Trifluoroacetic acid
TRIS	:	Tris(hydroxymethyl)aminoethane
UV	:	Ultra-violet
XRD	:	X-ray diffraction
XPS	:	X-ray Photoelectron Spectroscopy

SYNOPSIS

Mother Nature beautifully and intricately designed everything even from a smallest particle of atom to the dimension of universe. In this voyage of unknown with science as a companion, human always intrigued by the question that how the "life" is formed? Nature has meticulously constructed the building block of life i.e. "cell" from non-living components. Formation of DNA (the functional unit of life) by purine, pyrimidine base pair using H-bonding, synthesis of a particular protein from codon (a sequence of three consecutive nucleotides in a DNA or RNA molecule that codes for a specific amino acid) and so on. Each and every function that cell has to sustain requires different forces as well as different dimensions of self-assembled structures. Nature always exploited nanometer scale components to fabricate the collage of life. In today's world scientists are trying to understand this nano-dimensional area of materials, which have unique properties and functions that may guide us to decode the principles of nature. Materials having nanometer scale dimensions (10^{-9} meter scale) are called nanomaterial. In the field of science and technology, carbon-based nanomaterials (CNMs) especially carbon dots (CDs) are becoming attractive and emerging nanomaterials. The most interesting and inherent property of CDs are their stable photoluminescence property, biocompatibility and low toxicity. These remarkable characteristics mixed with their tunable surface emission property through the variation of diverse surface functionalities, fluorescence, CDs possess strong ability to bind with other organic and inorganic molecules. Subsequently, it makes them a potent candidate for photocatalysis, biochemical, and chemical sensing, in live cell bioimaging for real-time study of dynamic cellular processes, drug carrier and also a theranostic agent itself. Overall, in this thesis, I explored carbon dots as drug delivery agent, bioimaging probe, as a pro drug agent as well as a theranostic agent in different alternative therapies for cancer diagnosis and treatment.

Chapter 1 describes synthesis of phenylboronic acid appended biotinylated blue emitting carbon dot (**CD1s**). A well-known photosensitizer riboflavin having 'diol' moiety, was covalently linked with this **CD1s** to prepare riboflavin tailored green emitting carbon dot (**RCD1s**). The Lewis acid-base complementary boronic

acid-diol interaction was exploited to make the covalent linkage between the surface functionalizing agent of **CD1s** and riboflavin to develop **RCD1s**.TEM and AFM images confirmed the size of **RCD1s**was between 3-5 nm (Figure 1).

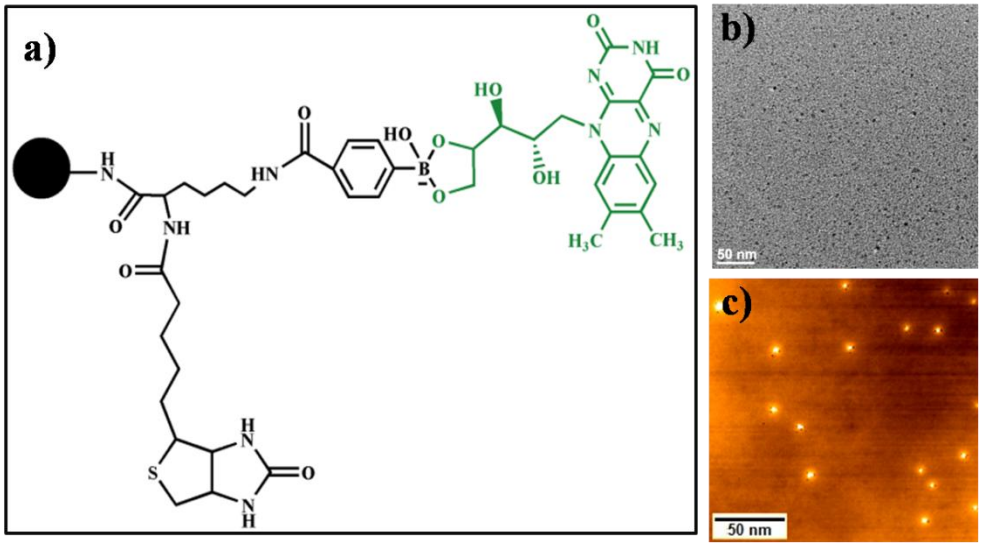

Figure1. (a) Structure, (b) TEM image, (c) AFM image of **RCD1s**.

This synthesized **RCD1s** has the ability to produce reactive oxygen species (ROS) such as hydroxyl and superoxide radicals under the exposure of visible light (wavelength: 460-490 nm). These reactive oxygen species also can destroy the structure of DNA by oxidative pathway. **RCD1s** successfully labeled HeLa, B16F10 melanoma cells over non-cancerous cell NIH3T3 by exploiting its fluorescence and cancer cell targeting moiety, biotin as biotin receptors are overexpressed in cancer cells than normal cells. Thus, as a result ~5-fold higher killing of cancer cells was noted in comparison to non-cancer cells possibly due to the oxidative damage of DNA by visible light (wavelength: 460-490 nm)triggered generation of ROS in presence of target specifically internalized **RCD1s** within cancer cells (Figure 2).Hence, the newly developed **RCD1s** will have notable prospects in theranostic applications in cancer treatment.

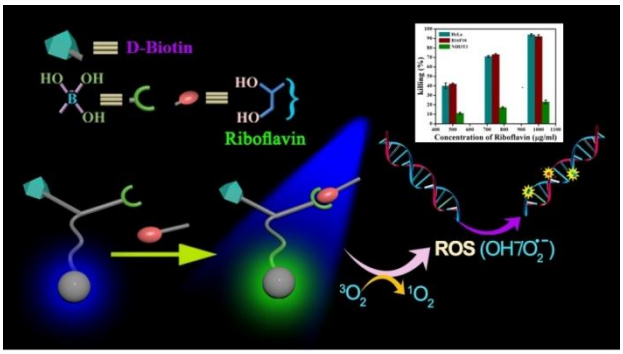

Figure 2. Schematic representation of visible light induced targeted cancer therapy by **RCD1s** through oxidative DNA damage.

Chapter 2 delineates the design and preparation of covalently tailored biotinylated Fe^{2+}-doped blue emitting carbon dots (FCD_b).TEM and AFM images confirmed that the size of FCD_b was around 3–5 nm (Figure 3).The XPS analysis of FCD_b showed peak at 710 eV confirmed the presence of iron in the divalent (Fe^{2+}) state in FCD_b. Fe^{2+} in FCD_b acted as pro drug in presence of H_2O_2 and generated reactive oxygen species (ROS) which led to cancer cell death as H_2O_2 is over expressed in cancer cells.

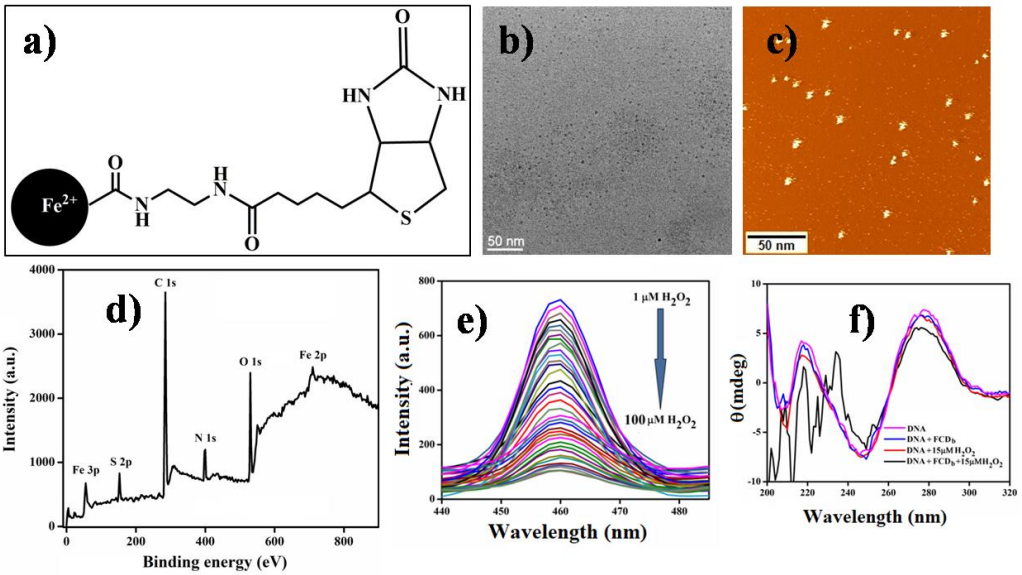

Figure 3. (a) Structure, (b) TEM image, (c) AFM image, (d) XPS of **FCD_b**, (e) fluorescence quenching in presence of H_2O_2 and **FCD_b** and (f) CD spectra CT DNA in presence of H_2O_2 and **FCD_b**.

SYNOPSIS

FCD_b was used as a pro-drug activator as well as a target-specific delivery vehicle for anticancer drug paclitaxel in pro-drug–free drug combination therapy of cancer treatment. After successfully generated ROS from H_2O_2, we loaded anticancer drug paclitaxel in FCD_b and FCD_b-PTX conjugate was formulated. This newly formulated FCD_b-PTX exhibited ~2.7- to 3.5-fold higher killing ofB16F10 malignant cells than NIH3T3 normal cells through early and late apoptotic pathways (Figure 4).FCD_b-PTX formulation successfully exhibited synergistic action toward efficient killing compared to that of only PTX and/or FCD_b as a result of combination therapy, and at the same time, it was selective to cancer cells.

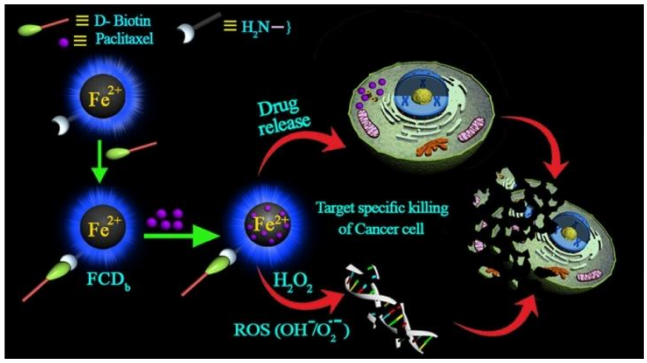

Figure 4. Schematic representation of paclitaxel-loaded biotinylated Fe^{2+}-doped carbon dot (**FCD_b-PTX**) in prodrug-free drug combination therapy where **FCD_b** act as pro drug and paclitaxel (PTX) as free drug.

Chapter 3 deals with the synthesis and development of biotinylated Co^{2+}-integrated carbon dot (**$CoCD_b$**) for activating HIF-1α protein, which can specifically and effectively kill cancer cells by hypoxia induced apoptosis. This Co^{2+}-doped carbon dot (**$CoCD_b$**) was blue-emitting in nature (Figure 5). The evaluation of hypoxia is primarily determined from the expression of endogenous hypoxia-related protein hypoxia-inducible factor (HIF-1α).The molecules that are used to stabilize HIF-1α are usually known as hypoxia-mimetic agents. Some of the familiar hypoxia-mimetic agents are desferrioxamine (DFO) and cobalt chloride ($CoCl_2$). $CoCl_2$ is known to imitate the hypoxia both in vivo and in vitro through inhibition of prolylhydroxylases (PHDs) activity. Co^{2+} substitutes Fe^{2+} in PHDs, the main enzyme that cause the degradation of HIF-1α under normoxic conditions.Co^{2+}- as a doping agent in carbon dot was utilized to activate the pro-drug HIF-1αprotein that can

induce apoptosis via hypoxia. Beside the Co^{2+}-doping, we also surface functionalized the carbon dots with biotin moiety which specifically targeted the cancer cells (MDA-MB-231, HeLa) over the normal cells (NIH3T3, HEK-293) as biotin receptors are overexpressed in cancer cells.

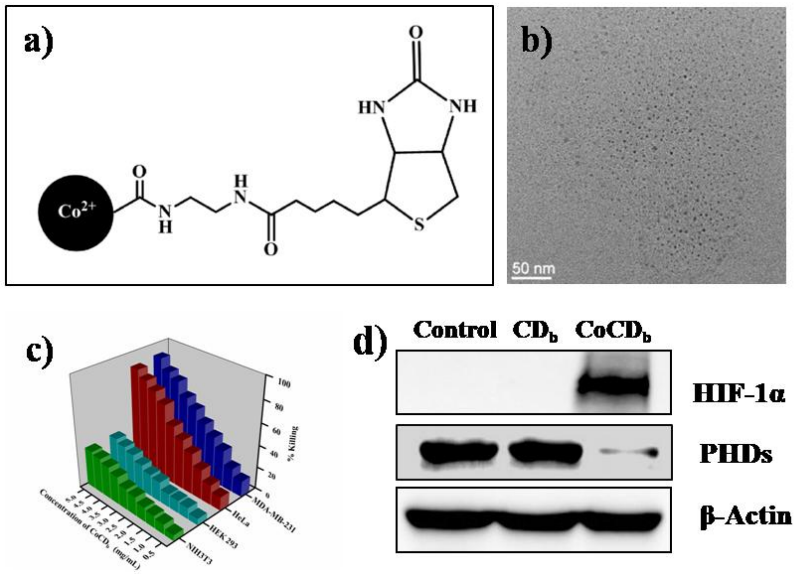

Figure 5. (a) Structure, (b) TEM image of **CoCD$_b$**, (c) 2D MTT assay and (d) Western blotting of HIF-1α and PHDs in presence of **CoCD$_b$**.

Various physical characterization and cytocompatible analysis were conducted before screening the anticancer efficacy of **CoCD$_b$** in 2D and 3D cell culture systems. In immunoblotting assay, the expression of HIF-1αand PHDs was also checkedin presence of **CoCD$_b$**. This biotinylated Co^{2+}-doped carbon dot (**CoCD$_b$**) selectively sensed and killed malignant cells over normal cells via hypoxia induced apoptosis using Co^{2+} as pro-drug activator and HIF-1α as pro-drug (Figure 5). Both 2D and 3D cell studies exhibited ~ 3-3.1 fold higher killing of cancer cells over the normal cells and ~ 65% killing of tumor spheroid in a span of 72 h (Figure 6).

SYNOPSIS

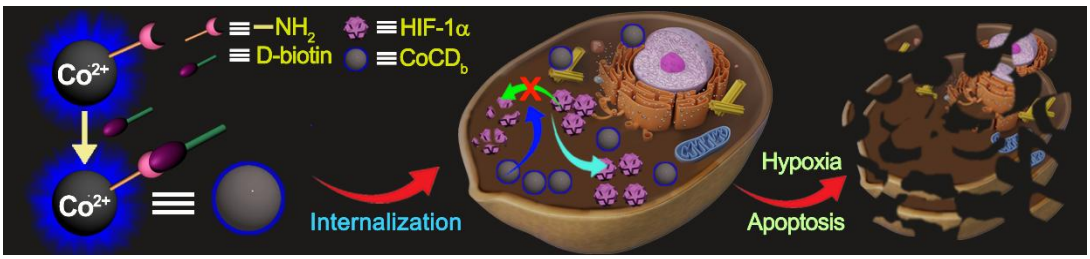

Figure 6. Schematic representation of Target Specific Killing of Cancer Cells by Co^{2+} Doped Biotinylated Carbon Dot (**$CoCD_b$**) where Co^{2+} elevated HIF-1α protein and caused Hypoxia Induced Apoptosis.

Chapter 4 of this present thesis is focused on development of copper (Cu^{2+}) doped carbon dot for sensing of guanine nucleobase.Guanine, one of the two important purine bases existing in DNA, involved in processes such as energy transduction, cell signaling is of great importance to cellular studies. Any alteration of variation in guanine concentration can cause deficiency and mutation in causing various diseases including AIDS, cancer. So sensing of guanine is very crucial for human health monitoring. Copper (Cu^{2+}) doped carbon dot (**CuCD**) was synthesized via hydrothermal method and exhibited blue emitting excitation dependent emission fluorescence at 428 nm when excited at 340 nm.

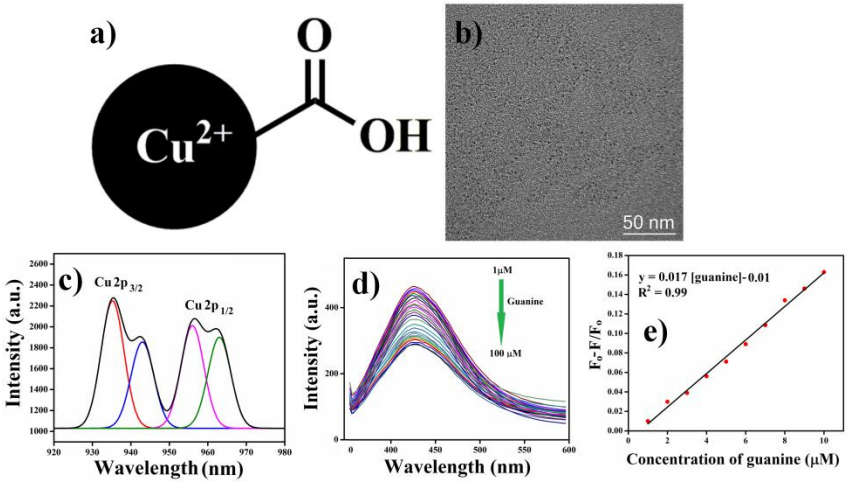

Figure 7. (a) Structure, (b) TEM image, (c) deconvulated XPS spectra, (d fluorescence quenching of **CuCD** in presence of guanine and (e) LOD of guanine in presence of **CuCD**

The microscopic characterization that is TEM and AFM concluded its size ~ 5 nm. The deconvulated XPS spectra proved the presence of Cu^{2+} in **CuCD**. The

fluorescence intensity of **CuCD** get quenched significantly when the concentration of guanine increased from 1μM to 100 μM (Figure 7). The limit of detection was around 1.57 μM. We investigated the selectivity of guanine against other nucleobases adenine, cytosine, and thymine. Interestingly, very less significant changes in the fluorescence intensity of **CuCD** was noted in presence of other nucleobases in comparison to the presence of guanine (100 μM). Importantly, guanine was sensed by **CuCD** with high selectivity and sensitivity against other nucleobases of DNA (adenine, cytosine, and thymine) as well as with respect to many other monovalent, divalent ions, amino acids and biomolecule. Guanine has also significant role in cellular functions which is why we wanted to explore the capability of **CuCD** in guanine treated cell lines with respect to their control ones. In cellular studies, this **CuCD** can efficiently quenched guanine treated cell line (B16F10 and NIH3T3) with respect to the control untreated ones. So, therefore a highly sensitive and selective ratiometric fluorescence probe **CuCD** for guanine detection was synthesized which was utilized for cellular studies as potential biomarker.

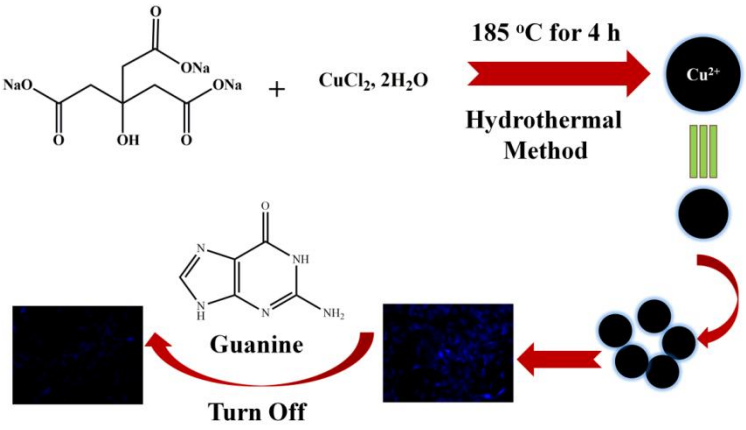

Figure 8. Schematic representation of synthesis of Cu^{2+} Doped Carbon Dot (**CuCD**) for sensitive and selective guanine sensing.

INTRODUCTION

Learning is the only thing, the mind never exhausts, never fears and never regrets.

—Leonardo Da Vinchi

INTRODUCTION

"Simplicity is the ultimate sophistication"

– Leonardo Da Vinci

Sophistication is the ultimate inherent characteristics of *Mother Nature*. Nature imparts wisdom and subtlety in every action, creation and destruction created by her. From the early stages of genesis, human unlike any other living creatures astonished by natures simple yet sophisticated patterns to maintain balance between every living and non-living existence. Although in respect to the galactic scale, humans have inhabited the Earth for only a tiny sliver of time but thanks to accidentally acquired imagination, and ability to analyze, humans can dare to chase the mysteries of Mother Nature. From the smallest particle of atom to the dimension of universe discovered till date, everything is beautifully and intricately tailored and attempted by the greatest scientist of all. How the forces inside a small atom can create an energy that can cause destruction hitherto undreamt of? How a tiny seed can grow to a full grown tree? Why fishes in the ocean swim in a definite direction? She is the great inventor of all the puzzles which we merely comprehend. That is why maybe we "re-search" the knowledge, the wisdom, which is already existed in our environment and called ourselves "re-searcher". It is true that our ability to question "why" and "how" in the domain of unknown lead to some answers but the majority of the domain are yet to be explored. The primary weapon of humankind to explore these mysteries is "Science". Science involves the pursuit of knowledge covering general truth or the operations of fundamental laws, the logical interpretation of collective thoughts about the world and how it behaves. From the very fast use of fire to explore the galaxies, science proved itself a reliable companion towards us in the voyage of uncertainty of nature's conundrum (Figure 1).[1]

INTRODUCTION

Figure 1. *The science of Nature (taken from references 1).*

NATURE: THE ULTIMATE SCIENTIST

In the ab initio origin of earth, nature was hostile and adverse to the growth of any life form. Like a scientist who is doing every experiment in her lab to get a desired result. Now from one of those experiments, nature gives earth the gift of "Life" but how, that's the tricky part. Amazingly when life grows from one cell to multiple cells and that manifested to plant, animals, human beings and many more, nature also evolved into a mother who can nourish us in every way possible but tamed us with her wild nature. Like a teacher, who teaches us where to see but did not tell us what to see and last but not the least a scientist who created magic with her every experiment. Till today we used the science as the key and curiosity as a fuel to unlock some of her tricks. Like designing air-plane and sub-marine by observing the mechanism of flying of birds and mechanism of smooth sailing of deep sea fish or using natural forces to create electricity for civilization are some examples of the discoveries made by human using science as key (Figure 2).[2,3] Nature has meticulously constructed the building block of life i.e. "cell" from non-living components. Formation of DNA (the functional unit of life) by purine, pyrimidine base pair using H-bonding, synthesis of a particular protein from codon (a sequence of three consecutive nucleotides in a DNA or RNA molecule that codes for a specific amino acid) and so on (Figure 2).[4-7] Each and every function that cell has to sustain requires different forces as well as different dimensions of self-

assembled structures. Nature always exploited nanometer scale components to fabricate the collage of life. In today's world, scientists are trying to understand this nano-dimensional area of materials, which have unique properties and functions that may guide us to decode the principles of nature.

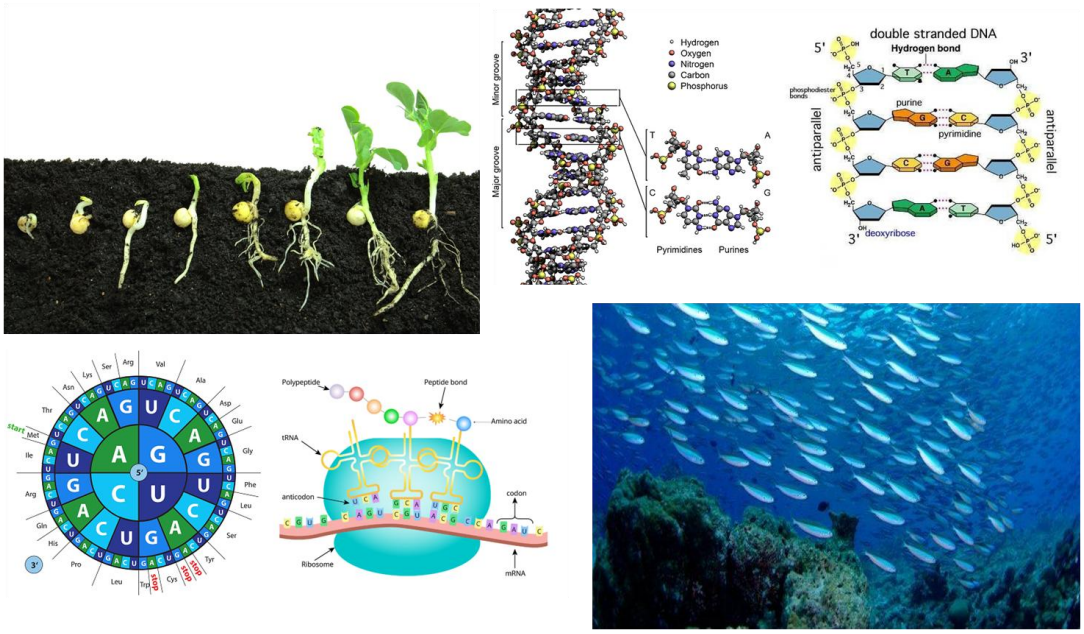

Figure 2. *The mysteries of Nature (taken from references 2-7).*

NANOMATERIALS

Cell is nothing but beautifully woven interrelated functions and properties of nano dimensional components such as protein, enzyme, nucleotide etc. Nano dimension is defined as one billionth of the unit of length i.e. nanometer (10^{-9} meter) range. "Nano" means "dwarf" in Greek which in other words represents something small. A more general description of nanomaterial is matter with at least one dimension sized from 1-100 nm (Figure 3).[8-11]

INTRODUCTION

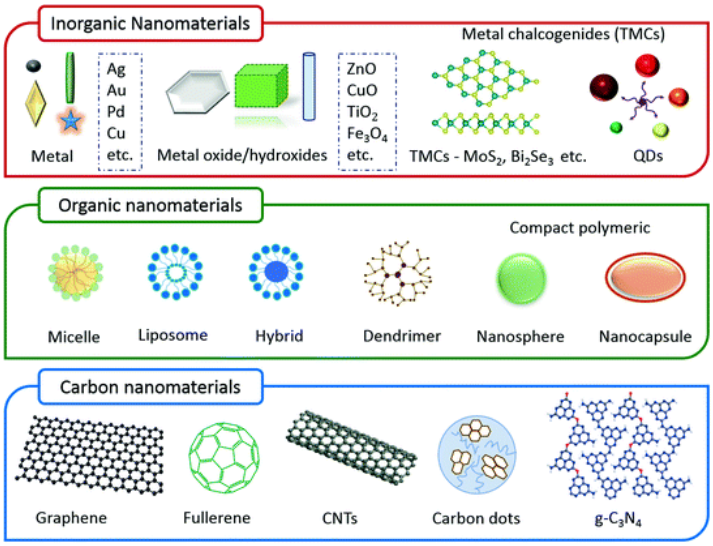

Figure 3. *Nanomaterials (taken from references 11).*

For many decades following nature's footsteps, scientists continuously explored the natural nanostructures in diverse area of research. Moth-eye nanostructures-pseudo-regular arrays of nanopillars first described on corneal surfaces of the nocturnal moth *Spodoptera eridania* served as a prototype for bio-inspired anti-reflective coating with broad technological applications, from solar cells to art paintings. Nanostructures covering the corneas of the eyes of small fruit flies can be helpful to produce safe biodegradable nano-coating with antimicrobial, anti-reflective, and self-cleaning properties in a cost-effective and eco-friendly way.[12-13] These nanomaterials have unique physicochemical properties which provide versatile scaffolds in sensing, catalysis, therapeutics, opto-electronics etc. The process where nanomaterials are fabricated for different purposes is called nanotechnology.

NANOTECHNOLOGY

Nanotechnology is the engineering of functional systems at the 10^{-9} meter scale. In its actual sense, nanotechnology refers to the projected ability to construct advanced systems from nanomaterials, using recent techniques and tools to generate high performance products.[14] At present, nanotechnology has significant impact on almost all areas of science, society and industry.[15-23] It offers the most

promising opportunity to get a grip on the desired purpose of utilizing functional nanomaterials in different domain across the discipline from surface science, organic chemistry, semiconductor physics to molecular biology, biocatalysis, nano-medicine, drug delivery etc (Figure 4).[24-26]

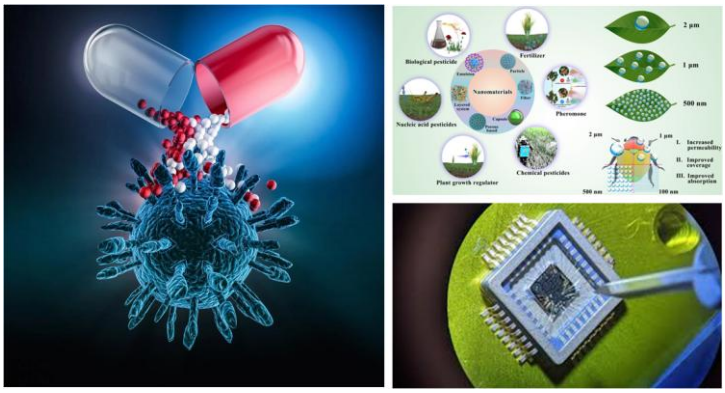

Figure 4. *Nanotechnology in various fields (taken from references 24-26).*

This inter-disciplinary branch of sciences has started to offer better, safer, and smarter products for the home to medicine to agriculture and in many others.[18-23] The nanomaterials research domain includes the study of materials having unique physicochemical properties arising from their nanoscale dimensions. Carbon nanomaterials (such as carbon nanotube, graphene, fullerenes), various metal nanoparticles (gold nanoparticle, silver nanoparticle etc.), nanorods, quantum dots (Figure 3) are the integral components of nanotechnology.[8, 27-30]

NANOBIOTECHNOLOGY

Nanobiotechnology is an extensively studied branch where amalgamation of biology and nanotechnology took place with purpose and objectives. This area primarily defined materials involved in monitoring and controlling of biological processes. Biomolecules in cellular environment execute their functions in marvelous complexity. To understand this nano dimensional network of functions, nanomaterials mimicking biomolecules open a new gateway of research for scientist.

INTRODUCTION

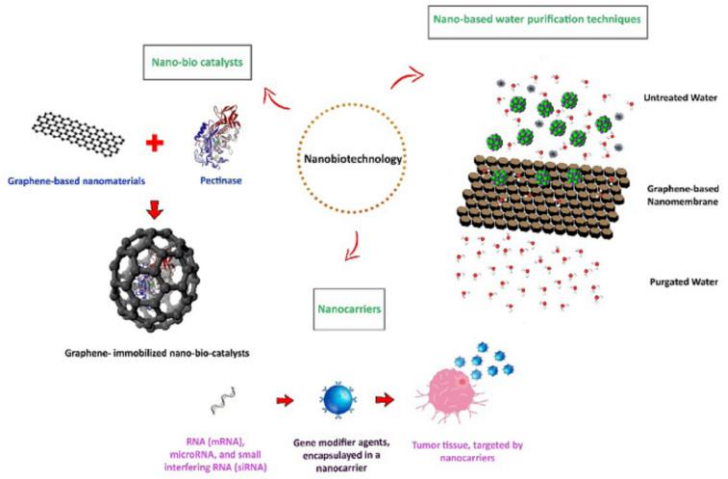

Figure 5. *Nanobiotechnology in biology (taken from references 33).*

Modifying enzyme behaviour via nanoparticle-protein conjugation technique,[31] fabricating nanoparticle surface for the purpose of sensing or modulating nanomaterials for used as nano medicine, tissue engineering are some of the recent applications in this field (Figure 5).[32,33] This is the genesis of different nanodevices that allow scientists to imagine and construct systems not only to understand but also to recreate biological mechanism.

NANOTECHNOLOGY IN BIOCATALYSIS

Biocatalysis refers to the use of biological systems or their parts to catalyze chemical reactions by enzyme, a protein molecule having catalytic ability, controls the activity of a living system. Enzymes consist of globular proteins with linear chain assembly of amino acids that fold to produce a 3D structure. Enzyme catalyzed all the biochemical reactions that are absolutely essential for the continuation of life. Hundreds of thousands of enzymes, each having specific functions different from the other create a large inter-connected system throughout the body of every living being. In human body, even the slightest movement of our muscles is governed by enzyme myosin which hydrolyses ATP to generate muscle contraction. The paramount importance of enzymes within the living world instigates us to use them in synthetic and technological advancement of science, such as high catalytic rate of the enzymes was exploited by the researchers in

different industrial purpose ranging from bio-bleaching of the paper to the most efficient recovery of oil or gas. Nanotechnology offered a new pathway for regulating enzyme behaviour through surface interactions, tuning or inhibiting enzyme behaviour, nanoparticle-protein conjugation technique and so on (Figure 6).[34-38]

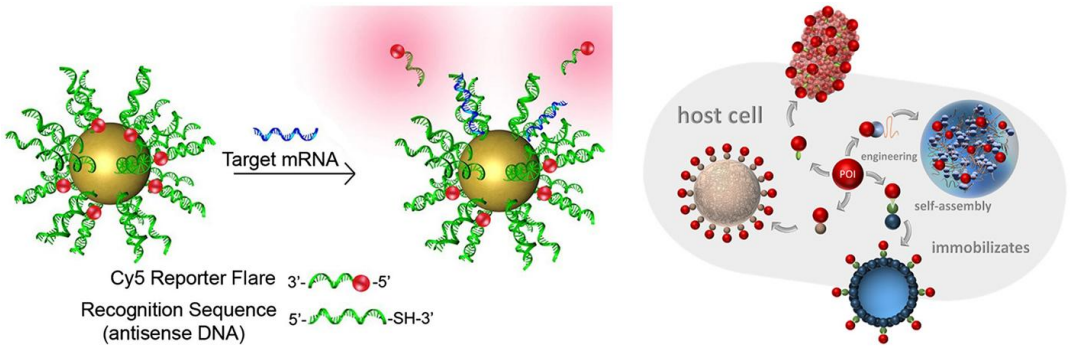

Figure 6. *Nanotechnology in biocatalysis (taken from references 37,38).*

NANOTECHNOLOGY IN BIOMEDICINE

In recent years, as new type of diseases, viruses are emerged to disrupt human life everyday, so is the urgency to create new generation drug among scientist also leveled up. Such as a new generation drug delivery system, which can simultaneously improve the bioavailability and reduce the cytotoxic effect of a drug, a therapeutic agent which itself act as a drug in presence of some specific cellular conditions etc. In this context, the possibility of using nanomaterials is showing huge promise and consequently conventional drug design systems are being rejuvenated with the option to include nanomaterials. Research for the development of nanomaterials, in the area of bioimaging, on the delivery of a particular drug or as a drug are ongoing (Figure 7).[39,40] Nanomaterials designed for the purpose of these things should possess the following characteristics, biocompatibility towards all cells and tissues, capability of penetrating into cells, target specificity and last but not the least removal of nanomaterial from the biological system easily. In general, nanoparticles used in the field of biotechnology range in particle size between 10 and 500 nm, seldom exceeding 700 nm. The nano-size of these particles allows various communications with biomolecules on the cell surfaces and within the cells in way that can be decoded and designated to

various biochemical and physiochemical properties of these cells. Similarly, it's potential application in drug delivery system and noninvasive imaging offered various advantages over conventional pharmaceutical agents.[41-43]

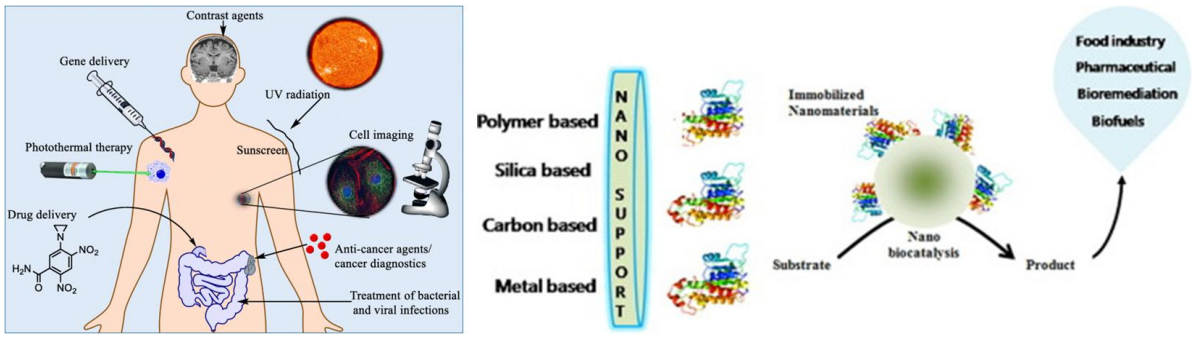

Figure 7. *Nanotechnology in biomedicine (taken from references 39,40).*

METALLIC NANOPARTICLES

In 1908 Faraday first discovered the existence of metallic nanoparticles in solution and Mie gave the quantitative explanation of their colour. In medieval era, metallic nanoparticles were actually used to decorate cathedral windows. Owing to the unique characteristics of metal nanoparticles, it has made a special place in the domain of nanotechnology (Figure 8).[44-46] The most important feature of nanoparticles is their surface area to volume ratio, where it easily allows them to interact with other particles, which make diffusion faster and is feasible at lower temperatures. These nanoparticles also have interesting characteristics such as surface Plasmon resonance and optical properties. [47,48]

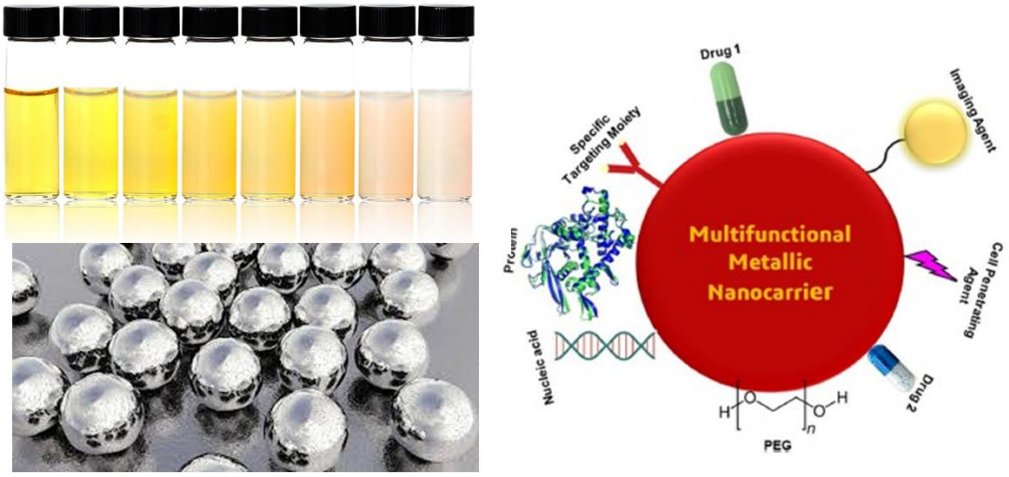

Figure 8. *Metallic Nanoparticles (taken from references 44-46).*

Silver nanoparticle (AgNP) and gold nanoparticle (GNP) are one of the most exploited metallic nanoparticles in recent era. Egyptians and Chinese have used solution of gold in different purposes, be it metaphysical or healing of wounds. Bulk gold is considered as an inert material and extensively used in jewelry, coins, dentistry, and electronic devices. However, when its size gets decreased to nanodimension, gold loses its inertness and exhibits a striking reactive behavior. As with all metals, GNP contains loosely bound surface electrons due to which it shows good electrical and thermal conductivity. The color in the bulk state is yellow and in nano-dimension it exhibits ruby red color.[49,50] There is also an effort to incorporate silver nanoparticles into a wide range of medical devices, including bone cement, surgical instruments, surgical masks, etc. Moreover, it has also been shown that ionic silver, in the right quantities, is suitable in treating wounds. In fact, silver nanoparticles are now replacing silver sulfadiazine as an effective agent in the treatment of wounds.[51,52] Due to the ultrafine size, magnetic properties, and biocompatibility of superparamagnetic iron oxide nanoparticles (SPION), it has a promising future for various biomedical applications, such as enhanced resolution contrast agents for MRI, targeted drug delivery, imaging, cancer, diabetes, and atherosclerosis.[53] However, these nanoparticles often suffer from cytotoxicity, particles instability, impurity, difficulty in synthesis that restrict their application specially in biological arena.

INTRODUCTION

CARBON NANOMATERIALS

Carbon nanomaterials are a class of low-dimensional materials that have aroused a great deal of interest in the past 30 years since the spectacular debut of fullerene in 1985. In the field of science and technology, carbon-based nanomaterials (CNMs) are becoming attractive and emerging nanomaterials. Due to the existence of diverse allotropes of carbon, from renowned allotropic phases such as amorphous carbon, graphite and diamonds to newly discovered carbon nanotubes (CNTs), graphene oxide (GO), graphene quantum dots (GQDs), fullerene and carbon dots(CDs), carbon-based materials have recently become prized across the research domain (Figure 9).[54-60]

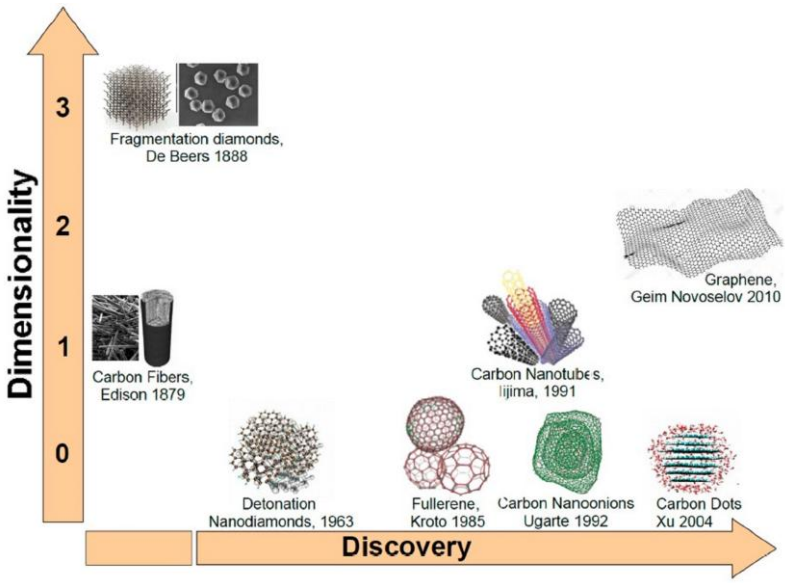

Figure 9. *Carbon nanomaterials (taken from references 54).*

Each member of the carbon family exhibits inimitable features. Nanomaterials are attractive for a number of different applications, including energy production, biomedical applications, environmental protection, information technology, food, agriculture and many others (Figure 10).[55,61-65]

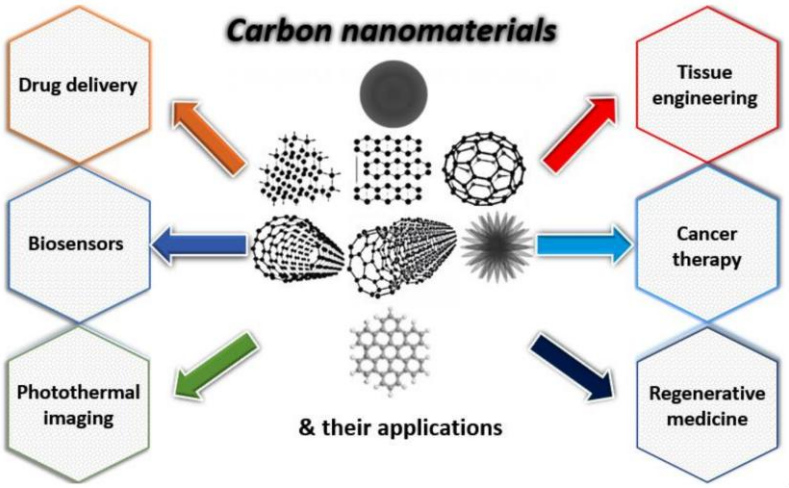

Figure 10. *Applications of carbon nanomaterials (taken from references 65).*

Natural carbon-based nanoparticles exist only in negligible quantities. Therfore, the overwhelming majority are engineered, or artificially synthesized so that significant efforts have been recently devoted for both the mass production of structurally homogeneous nanomaterials with well controlled surfaces and interfaces and their assembly into device architectures. In this scenario, the carbon-based nanomaterials have become one of the dominating materials in several sensor applications. A literature survey reveals that more than 2200 publications are related to nanomaterial and sensing and roughly about 50% of them are based on carbon nanomaterials. Among several carbon nanomaterial allotropes graphene, single walled nanotube (SWNT), carbon dots are most explored candidates in this area of research. While graphene, SWNT carbon nanomaterials are mainly comprised of sp^2 carbon atoms forming a seamless network of conjugated π-electrons, carbon dots have with mixed sp^2 and sp^3 carbon atoms plus defects and heteroatoms in their backbone. The past decade has witnessed a burst in biomedical research using carbon nanomaterials, which are advantageous primarily owing to small size, unique optical properties, and large surface area. The elegant marriage between nanoscience and biology originates from the similar dimensions between nanomaterials and many fundamental biomolecules that are crucial to maintain the basic functions of life. These carbon nanomaterials can be used as a sensor, a drug delivery vehicle, a therapeutic agent and so on.

INTRODUCTION

GRAPHENE: 2D CARBON NANOMATERIAL

Along with diverse nanomaterials, nanotechnology research has been dominated by the emerging class of materials called graphene due to its unique physicochemical properties. Graphene is a single layer of carbon atoms organized in a 2D structure with a trigonal planar lattice. Tight packing of carbon atoms into 2D honeycomb lattice structure plays key role for several intrinsic features of graphene. Besides these exotic physical properties of graphene that lead to the development of novel graphene-based nanoelectronics and nanophotonics, the large surface area, high mechanical flexibility, and capability of chemical functionalization of graphene and graphene derivatives have opened up a new horizon in biomedical research. As for the other carbon nanostructures, chemical functionalization of graphene is one of the crucial steps of material preparation that determines the final properties and the kind of applications namely electronics, filler in nanocomposite synthesis, biomaterials/biomedicine, sensing, energy, environment and etc.[66-68] Functionalization transforms the zero-gap graphene in a semiconductor suitable for electronic applications. In case of biomaterials, an appropriate surface chemistry renders water soluble graphene a suitable nanoplatform for drug delivery, such as tissue engineering and other applications. There have been an increasing number of studies on the use of graphene and graphene oxide (GO) for various biological and medical applications including biosensing, imaging, and therapy (Figure 11).[69,70]

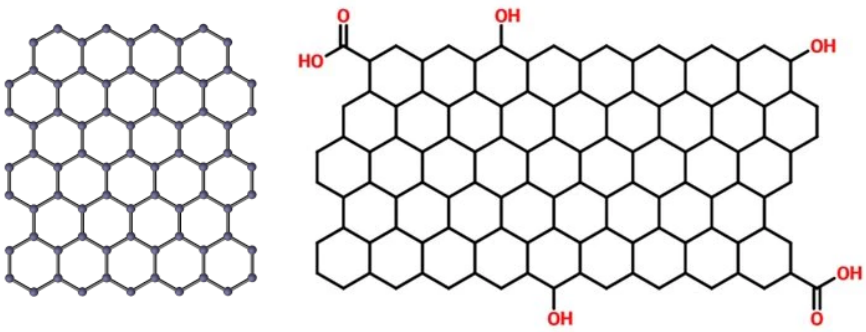

Figure 11. *2D allotrope graphene and graphene oxide (taken from references 69,70).*

INTRODUCTION

SINGLE WALLED CARBON NANOTUBE (SWCNT): 1D CARBON NANOMATERIAL

Among other carbon-based nanomaterials, carbon nanotubes (CNTs) are one of the carbon allotropes with exceptional properties suitable to be used from materials science to biotechnology. They were discovered in 1991 by the Japanese researcher S. Iijima. CNTs are one-dimensional form of carbon possessing a perfect hollow cylindrical shape and comprise of sp^2 carbon atom which form single or multiple coaxial tubes of graphitic sheets called single-walled carbon nanotubes (SWCNTs) and multiple-walled carbon nanotubes (MWCNTs). CNTs have stimulated a significant amount of interest from many different fields owing to their unique mechanical, chemical, electrical, and optical properties.[71-73] Arc discharge, laser ablation and chemical vapor deposition (CVD) are basic methods for the synthesis of CNTs (Figure 12).[74] Currently, one of the most investigated and commonly used techniques for CNT production is CVD. Their high aspect ratio, high conductivity, high chemical stability and sensitivity and fast electron-transfer rate make them exceedingly fit for biosensing applications. The basic element of CNT-based biosensors is the immobilization of biomolecules on its surface, therefore enhancing recognition and the signal transduction process. On the basis of their target recognition and sensitivity they are used in drug delivery and in cancer therapy. The huge surface area of the nanotubes having aromatic backbone helps in the adsorption of a wide range of cargo like DNA, proteins, drugs and so forth through hydrophobic adsorption. Additionally, covalent attachment is also another way for hooking up the desired cargo on the CNT surface.

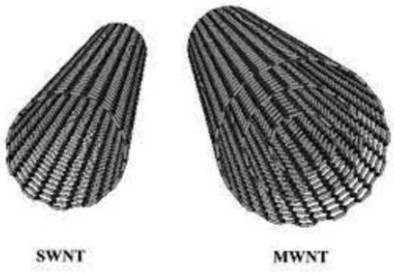

Figure 12. *1D allotrope carbon nanotube (CNT) (taken from references 74).*

INTRODUCTION

CARBON DOT: ZERO D CARBON NANOMATERIAL

Among many kinds of nanoparticles, metal nanoparticles usually comprising of heavy metals are toxic in nature and thus have limited applications in the field of biomedicine. In case of carbon nanotube (CNT), the length of CNT has a great impact on the toxicity of CNT due to the failure of their cellular internalization. Moreover, prolonged use of CNT led to severe inflammation, which caused progressive fibrosis. In case of graphene, several parameters including concentration, lateral dimension, surface property and functional groups, greatly influence its toxicity in biological systems. In a nutshell for both in vitro and in vivo uses, the known toxicity and potential environmental hazard associated with many of these materials may represent serious limitations.[61] Therefore, the search for benign nanomaterials of similar optical properties continues. Carbon dot, also known as the carbon nanodot, carbon quantum dot, represents another class of carbonaceous nanomaterial besides 2D carbon allotrope carbon nanotube and 1D carbon allotrope graphene. With the gradual development of science in nanotechnology, ample research provided knowledge about the existence of different nano-allotropes of carbon, and in 2004, avant-garde carbon nanomaterials named carbon dots (CDs) were discovered. However, the actual era of the CDs chemistry started in 2006 with a revolutionary study by Sun et al. Since then, a tremendous amount of experimentation has been performed in the field of CDs chemistry. The newly developed 'zero-dimensional' and intrinsically fluorescent CDs are the 'green' addition of mysterious dimension of nano. CDs have dimensions smaller than 10 nm (Figure 13).[75] CDs possess a carbon-based skeleton and a large number of oxygen-containing groups on the surface making them easily dispersible in water. CDs composed mainly of sp^2 hybrid conjugated carbon as the core and a shell of organic functional groups (e.g., N–H, C=O, -OH, -COOH, C–N, C-O) or polymer aggregates (Figure 13).[75-80] Due to presence of abundant surface groups, fluorescent CDs possess rather strong ability to bind with other organic and inorganic molecules. Scientists have progressively exploited this property of CDs and used them in diverse domain of sciences. So far, CDs can be synthesized mainly via two routes and the structures of the resulting CDs are also very

different. One is top-down approach and other is bottom-up approach. Top-down approach refers to breaking down larger carbon structures via chemical oxidation, discharge, and ultrasonic methods. Bottom up method refers to the conversion of smaller carbon structure into CDs of the desired size via hydrothermal treatment, ultrasonic treatment, pyrolysis, microwave synthesis and solvothermal method etc.[77,78] The most interesting and inherent property of CDs are their stable photoluminescence property, biocompatibility and low toxicity. These remarkable characteristics mixed with their tunable surface emission property[81-83] makes them a potent candidate for photocatalysis, biochemical, and chemical sensing, in live cell bioimaging for real-time study of dynamic cellular processes, drug carrier and also a theranostic agent itself.[84-87]

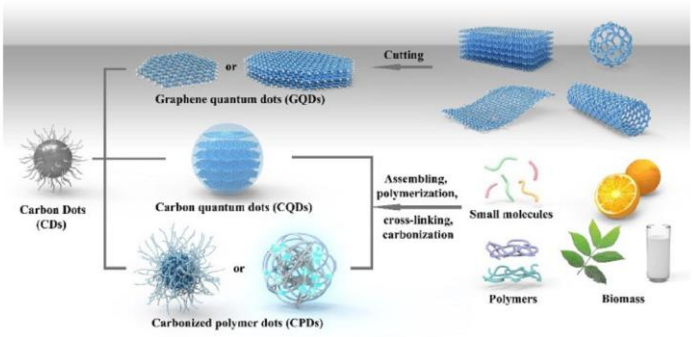

Figure 13. *Zero D allotrope carbon dot (CD) (taken from references 75).*

SYNTHETIC PROCEDURES

Traditionally, among many methods, the synthesis of CDs can be categorized into two main types which classified into “top-down” and “bottom-up” approaches. Compare to top down approach, bottom up approach is more environment friendly, easy to conduct and the precursors are mostly biomolecules. In “bottom-up” approaches, small organic precursors can be polymerized and carbonized into CDs by means of hydrothermal/ solvothermal synthesis, pyrolysis, microwave-assisted polymerization, and so on.[77,80] The precursor for making carbon dots can be graphite, fullerene, single-walled or multiwalled carbon nanotubes, graphene, carbon fibers, candle soot, glycerol, glucose, citrate, aromatic organic compounds,

and many other bioorganic precursors including silk, orange juice, banana juice, honey and even food waste.

(a) Pyrolysis Method

Pyrolysis is an irreversible thermal decomposition reaction in which decomposition of organic materials take place in an inert atmosphere. It involves physical as well as chemical changes in organic materials resulting in solid residue containing carbon (Figure 14).[88] Generally, pyrolysis is conducted at oxygen-less environment in low oxygenor. CDs fragments were purified via post treatments like filtration, dialysis, centrifugation. Bourlinos et al. synthesized Gd(III)-doped CDs having diameter ~ 3.2 nm with dual fluorescence via pyrolysis method.[89] Feng et al. synthesized CDs from citric acid via thermal pyrolysis method having diameter ranging from 5 to 8 nm.[90]

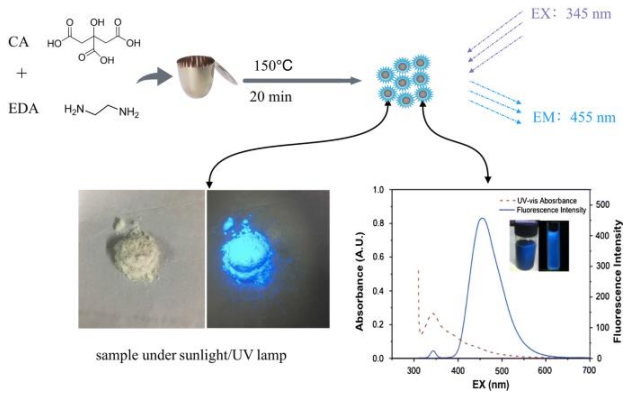

Figure 14. *Pyrolysis method (taken from references 88).*

(b) Hydrothermal Method

In 2007, Liu and coworkers first prepared CDs by hydrothermal /solvothermal methods. These methods are economical, eco-friendly, easy to handle, and impregnable route to synthesize CDs from saccharides, amines, organic acids and their derivatives. The hydrothermal method is used to prepare carbon dots by mixing carbon source and solvent and heating in autoclave. In this method, the influence of impurities in the air is avoided because the reaction is carried out in a closed reactor. The prepared carbon dots are relatively uniform,

and most of the carbon dots synthesized by the hydrothermal method have good water solubility (Figure 15).[91] Zboril et al. prepared full-color CDs via a hydrothermal method from citric acid and urea in *N*,*N*-dimethylformamide with well controlled fluorescence at blue, green, yellow, or red wavelengths.[92] Zhang et al. synthesized fluorescent CDs for the first time from small organic compound, l-ascorbic acid via hydrothermal method. The as-prepared CDs had a diameter of 2 nm.[93]

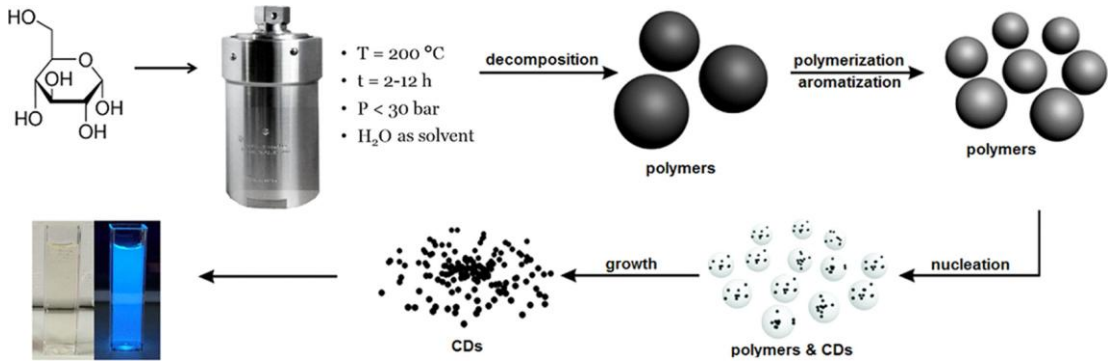

Figure 15. *Hydrothermal method (taken from references 91).*

(c) Microwave assisted pyrolysis Method

The microwave-assisted method is an augmentation to the solvothermal/ hydrothermal technique where microwave is utilized instead of heat. Microwave heating is a method that uses a microwave to raise the temperature rapidly in a short time to polymerize and carbonize the reactant precursor molecules to form carbon dots (Figure 16).[94] In this method, the particle size and the quantum yields of fluorescent CDs depend on the reaction time. The advantages are that it is convenient and fast, the preparation conditions are simple, raw materials are easily available, etc.[95] Zhu et al. synthesized fluorescent CDs having size ~ 3.7 nm using microwave irradiation using aqueous solution of saccharides and polyethylene glycol in a domestic microwave oven (500 W) for nearly 3 min.[96]

INTRODUCTION

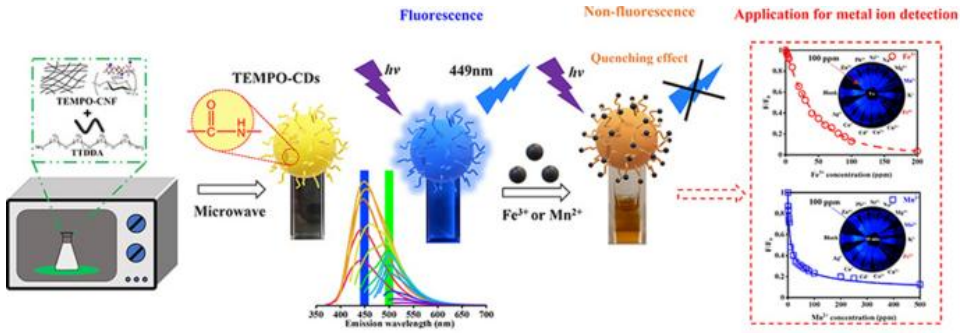

Figure 16. *Microwave assisted pyrolysis Method (taken from references 94).*

PHOTOLUMINESCENCE PROPERTY OF CDs

CDs have strong absorption in the ultraviolet region, which can also get extended to visible region. The luminescence properties of CDs are mainly the photoluminescence and electrochemical luminescence, in which photoluminescence is the most prominent performance. This optical property can be easily tuned by merely changing the surface property of CDs. CDs have high fluorescence stability, tunable excitation, and emission wavelengths. Although the emitting mechanisms of CDs are still not clear, some researchers speculated that the emitting mechanisms of CDs involve quantum confinement effect, stabilizing surface trap, or exciton recombination radiation.[97-100]

(a) UV-Absorption Property of CDs

Generally, CDs exhibit absorption in the UV−visible region. The peaks are usually generated from π-π* transitions of conjugated C=C system and n-π* transitions of C-O, C-N, or C-S groups. Typically, one or more absorption peaks can be clearly observed in the UV region ranged from 260 nm to 320 nm and, a tail can extend to the overall visible region. The absorption band could be modulated via various surface passivation/functionalization techniques.[101,102]

(b) Fluorescence Property of CDs

Fluorescence is one of the most appealing properties of CDs from both fundamental and applied perspectives especially in biological domain. In most cases, the CDs display excitation-dependent fluorescence characteristics; however,

the excitation-independent emission is also reported which may be attributed to their uniform size and surface chemistry.[103,104] Compared with other fluorescent materials such as traditional quantum dots (QDs) containing cadmium/lead, rare-earth nanomaterials, and organic dyes, CDs have advantages of better light stability, greater cytocompatibility and so on (Figure 17).[105]

Tunable Emission Property of CDs

The surface state mechanism of CDs has been widely studied by researchers. The surface state, including the degree of surface oxidation and surface functional groups, is directly correlated to the intrinsic fluorescence property of CDs. The intriguing fact about the optical property is that it can be easily tuned by just changing the surface chemistry of CDs using surface passivating agents, changing reaction condition and also by doping elements in the core of carbon dots.[106-108] Tuning of emission property of CDs, make them an interesting candidate to exploit in the area of bioimaging, sensing, drug delivery and as theranostic agent.

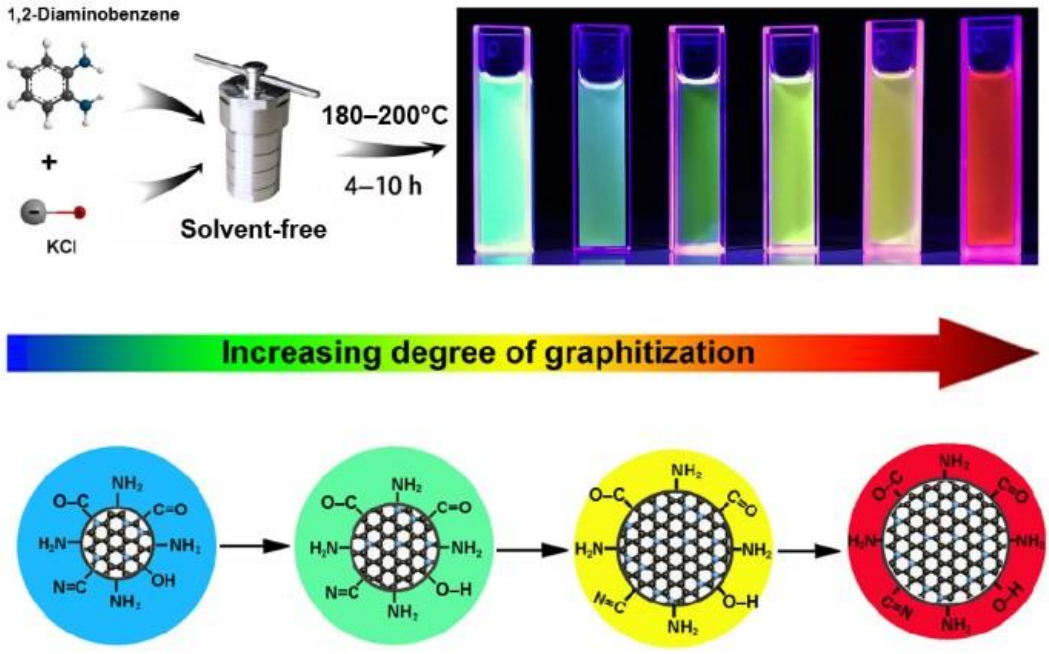

Figure 17. *Optical property of carbon dots (taken from references 105).*

INTRODUCTION

Application of CDs

(a) Sensors

A biosensor is a device that measures biological or chemical molecules by generating signals proportional to the concentration of an analyte in the reaction. In recent times nanotechnology provides the opportunity to fabricate binding affinities of nanomaterials with various biomolecules (proteins, nucleic acids and microbial pathogens) through changing the chemistry of surface. Nanomaterial like carbon dots are used as sensor for more than decade because of their excellent optical property, flexibility in surface modification, excitation-dependent multicolor emission, considerable biocompatibility and high photostability. The CDs-based biosensors can be used for visual monitoring of glucose, cellular copper, phosphate, iron, potassium, H_2O_2, pH, nucleic acid and inherent biochemical changes in cancer cells.[109,110] Changes in pH and temperature in and around a cell can be the result of the natural ebb and flow of cell homeostasis, when the changes are minimal. However, a more drastic rise or fall in these factors usually signals that a disruption to cell metabolism and viability has ensued such as the presence of a tumor (Figure 18a).[78]

(b) Bioimaging probe

Bioimaging is a technique that can directly visualize biological events in real-time and non-invasive ways via probes and detectors. Fluorescence imaging is one of the imaging modalities which has become a powerful approach for disease diagnosis due to its convenience, low cost, high sensitivity, non-invasiveness, and long-term observation techniques. CDs are considered as a potential candidate for bioimaging application due to its unique fluorescent nature, high photobleaching resistivity, less cytotoxicity, and better aqueous solubility in comparison to the traditional semiconductor quantum dots which are considered to be toxic to human to some extent. CDs show great potential for fluorescent bioimaging and multimodal bioimaging of cells and tissues. Various CDs have been used

extensively for imaging cells, microorganisms, and plant tissue.[111,112] Generally, CDs can quickly enter into cells through various cellular mechanisms owing to their dimension and are distributed into different organelles such as mitochondria, lysosome etc and/or nucleolus based on the different nanostructures of CDs and types of cells. Imaging organelles, biomolecules, chemical reaction pattern is profitable to understand and study different cellular level diseases such as cancer, Alzheimer's disease, Parkinson's disease, diabetes, and so on (Figure 18b).[78]

(c) Drug delivery/ Therapeutic agent

Drug delivery, the safe and effective treatment, refers to carry the drug to a specific location in the body and releasing it in a sustained manner. Thus, the controlled drug release and efficient selectivity in drug delivery systems are crucial for increasing local therapeutic effects and minimizing side effects of that drug on non-infectious and/or non-cancerous tissue. Traditional drug carrier does not have the observability and traceability. Therefore, it is an attractive prospect to combine medical therapy and bioimaging diagnostics for visual drug distribution and monitoring of their effects. In this context, CDs have the potential to be utilized as multifunctional vehicle for drug delivery owing to intrinsic fluorescence property, low toxicity, chemical inertness and excellent biocompatibility.[113,114] CDs have advantages in visualizing drug accumulation and activities at the therapeutic sites via their fluorescent properties, which are vital for estimating therapeutic efficacies of medicines. Besides being carriers, CDs themselves behave with therapeutic performances such as antibacterial activity, anticancer activity, antiviral activity, and antioxidant activity.[115] In recent times, CDs are also used to manipulate the intrinsic factors of cellular functions that can lead to desired result for specific diseases and thereby can act as a diagnostic as well as therapeutic agent (Figure 18c).[78]

INTRODUCTION

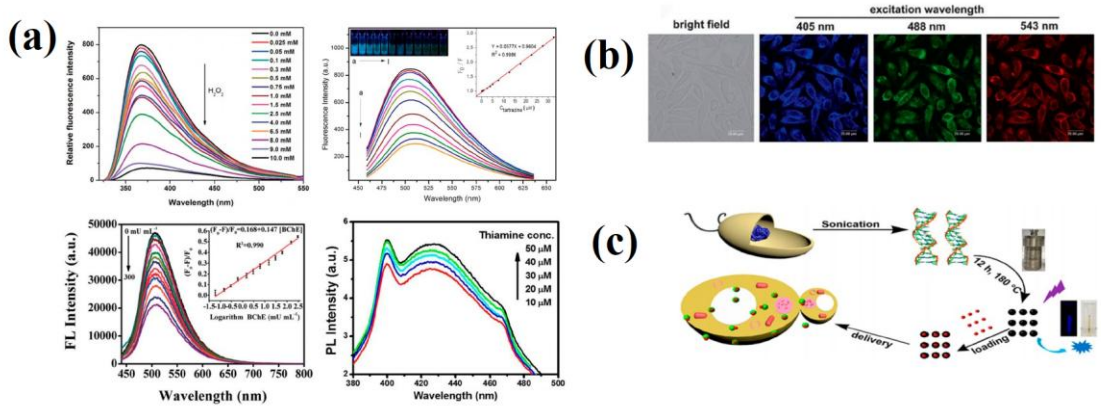

Figure 18. *Carbon Dot as (a) sensor, (b) bioimaging and (c) drug delivery agent (taken from references 78).*

CANCER

Cancer, a multifaceted challenge, having intricate complexity, diverse gene mutations and potential to invade tissue lineages concern the scientists globally for a long time. Cancer actually is a group of diseases involving abnormal cell proliferation with the potential to spread to other parts of the body. It's complexity is one of the leading causes of human death. Due to the societal and economical implications of this pathology, tremendous efforts have been made by researchers over the past several decades to improve the available therapeutic options.[116-119] For many decades, traditional treatment like surgery, chemotherapy, radiotherapy etc. are the most promising pathways of battling against cancer. Unfortunately, most anticancer agents display a narrow therapeutic window due to their lack of bioavailability, rapid blood/renal clearance, nonspecific selectivity, low accumulation in tumors, severe multidrug resistance and adverse side effects for healthy tissues.[120-123] Despite having a large number of potent chemotherapeutic anticancer agents, there have been very few significant progresses in cancer treatment. With the aim to increase traditional treatment efficacy and decrease the limitations of systematic side effects researchers are now wanted to develop alternate methods for cancer treatment.

INTRODUCTION

Looking for new alternative methods for cancer treatment is a continuous process with a focus on the balance between the advantage and drawback of systematic therapies. In this context, using inherent characteristics (biochemical, functional and genetic) of cancer cells that distinguish them from normal cells are the important biomarkers for creating alternative therapies.

PRESENT THESIS

Photosensitizer Tailored Surface Functionalized Carbon Dots for Visible Light Induced Targeted Cancer Therapy.

Over the decades researchers across the world have focused in the development of novel cancer therapeutic strategies. There are many traditional therapies such as chemotherapy, radiotherapy etc are the front line warriors in the field of cancer treatment. However, their capabilities to fight against cancer are restricted by their limitations. Therefore, researchers are in search for alternative novel cancer therapeutic strategies in modern times. In this context, reactive oxygen species (ROS) that are responsible for killing of cancer cells have been exploited recently in cancer therapeutics. ROS generation is induced inside the cells by using different methods such as using fenton reagent, photosensitizer in presence of a specific wavelength etc. A photosensitizer is a molecule which upon exposure to light of suitable wavelength (visible or near-infrared), produces ROS such as singlet oxygen, results in the killing of cancer cells through oxidative DNA damage. Considering the above facts, we developed a photosensitizer tethered tumor targeting delivery agent using carbon dot (CDs), which specifically deliver the photosensitizer inside the cancer cell without affecting its photochemical behavior. CDs have the potential to be utilized as vehicle for drug delivery systems owing to low toxicity, chemical inertness and excellent biocompatibility.

In this context, in chapter 1, I synthesized a photosensitizer (riboflavin) tailored surface functionalized carbon dot (RCD1s) to utilize it in visible light induced targeted cancer therapy. At first, phenylboronic acid appended biotinylated blue emitting carbon dot (CD1s) was synthesized. Riboflavin having “diol” moiety

was covalently linked with this CD1s to prepare green emitting RCD1s by using complementary boronate-diol linkage. Microscopic and spectroscopic techniques were used to characterize RCD1s. Interestingly, this newly synthesized RCD1s has the ability to produce reactive oxygen species (ROS) under exposure of visible light (wavelength: 460-490 nm) and can destroy the structure of DNA by oxidative damage. RCD1s was also exploited to selectively recognize HeLa and B16F10 cells over noncancerous cell NIH3T3 using its fluorescence property as well as through biomarker biotin present in the surface of RCD1s. RCD1s was found to kill HeLa and B16F10 melanoma cells over noncancer cell NIH3T3 by ~5-fold higher efficacy through ROS induced oxidative DNA damage (Figure 19).

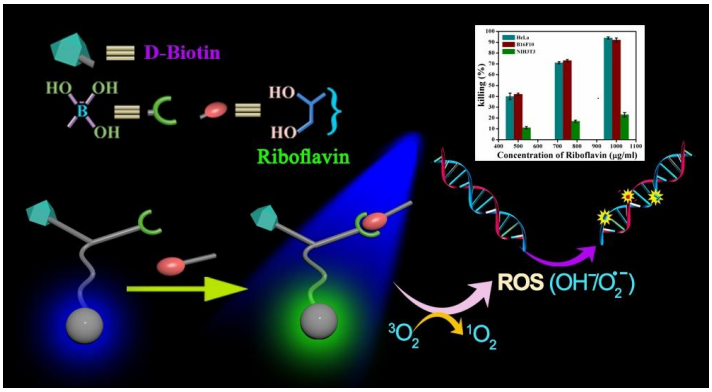

Figure 19. ***Schematic representation of the synthesis of riboflavin tailored carbon dot (RCD1s) generating light induced reactive oxygen species (ROS) led to the selective cancer cell apoptosis.***

Paclitaxel-Loaded Biotinylated Fe^{2+}-Doped Carbon Dot: Combination Therapy in Cancer Treatment.

Combination chemotherapy is preferred over treatment with single agents to combat most cancers as it targets multiple cell-survival pathways at the same time and delays the onset of resistance. Generally, combining several types of therapy such as radiotherapy and chemotherapy or co-administration of multiple therapeutic agents (pro-drug–free drug, free drug– free drug, etc.) with different mechanisms of function for achieving synergistic action is referred as combination therapy.[124,125] Cancer, a multidimensional challenge, where multitudinous approaches like surgery, immunotherapy, chemotherapy, etc. are being used in the

past few decades, yet limitations of these conventional treatments make them less potent to completely curbing this disease. Therefore, as a new alternative method, combination therapy can achieve long-term tumor remission and increases median survival.

Considering the above fact, in chapter 2, I wanted to use pro drug-free drug combination therapy using carbon dots as a prodrug activator as well as delivery vehicle for free drug. Keeping that in our mind, I plan to use H_2O_2 which is over expressed in cancer cells as a prodrug and Fe^{2+} doped carbon dot as a pro-drug activator as one of the components in combination therapy. For the next component, we plan to use anticancer drug paclitaxel as a free drug. Herein, I prepared covalently tailored biotinylated Fe^{2+}-doped carbon dots (FCD_b). Microscopic and spectroscopic methods were used to characterize aqueous soluble FCD_b. FCD_b can effectively sense H_2O_2 by fluorescence quenching as well as activate H_2O_2 (pro-drug), which led to cell death due to the generation of reactive oxygen species (ROS). FCD_b was also utilized as selective cellular markers for cancer cell B16F10 owing to their high H_2O_2 content, which was more distinct due to the overexpression of biotin receptor in cancer cell. Anticancer drug paclitaxel (PTX)also loaded in FCD_b (FCD_b -PTX) was employed for the selective killing of B16F10 cancer cells. This pro-drug–free drug formulation (FCD_b -PTX) exhibited ~2.7- to 3.5-fold higher killing of B16F10 cells mostly via early as well as late apoptotic path in comparison to non-cancer NIH3T3 cells (Figure 20).

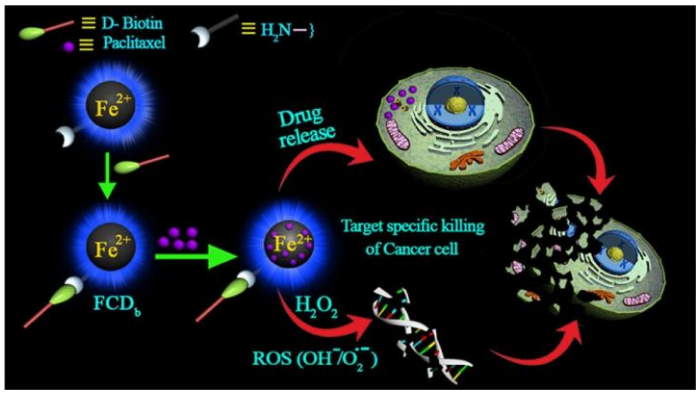

Figure 20. ***Schematic representation of paclitaxel loaded biotinylated Fe^{2+} doped carbon dot (FCD_b) as a theranostic agent in pro-drug-free drug combination therapy where Fe^{2+} act as a pro drug activator and paclitaxel used as a free drug in selective killing of cancer cell.***

INTRODUCTION

Co^{2+} Doped Biotinylated Carbon Dot: A Theranostic Agent for Target Specific Killing of Cancer Cells via Hypoxia Induced Apoptosis.

Conventional cancer treatments have systematic side effects that stand against its desirable therapeutic efficacy. Alternative strategies using biochemical features of cancer cells to promote apoptosis are finding notable significance. One such important biochemical features of malignant cells is hypoxia, alteration of which can lead to apoptosis. Hypoxia is one of the important biochemical features of malignant cells that differ from normal cells. Physiological oxygen concentration in tissues (normoxia) gets reduced during abnormal rate of cell division in cancer progression. This lack of balance in the oxygen level makes the cancer cells hypoxic in nature. Under hypoxic condition adaptive cellular responses are regulated by the stabilization/degradation ratio of α-subunit of the transcription factor HIF-1. Increase and stabilization of HIF-1α induce several factors that led to cell damage and apoptosis. $CoCl_2$ is known to imitate the hypoxia both in vivo and in vitro through inhibition of prolylhydroxylases domain-containing protein (PHDs) activity. Co^{2+} substitutes Fe^{2+} in PHDs, the main enzyme that cause the degradation of HIF-1α under normoxic conditions. Co^{2+} acted as pro-drug activator, which can activate HIF-1α and induce apoptotic cell death. In this context, doping of carbon dot with various materials without affecting its intrinsic property and using them in therapeutic systems is an interesting research domain. Herein, we aim to include Co^{2+} as an integral element of carbon dot that needs to be delivered inside cancer cells. We synthesized biotinylated Co^{2+}-integrated carbon dot ($CoCD_b$) that specifically diagnose and selectively killed cancer cells with ~3-3.1- fold higher efficiency over non-cancer cells by hypoxia induced apoptosis in absence of traditional therapeutic intervention. Immunoblotting assay in $CoCD_b$ treated MDA-MB-231 cells confirmed the increased expression of HIF-1α that was responsible for efficient killing of cancer cells. Both 2D and 3D cell studies exhibited ~3-3.1-fold higher killing of cancer cells over normal cells and ~65% killing of tumor spheroid in a span of 72 h (Figure 21).

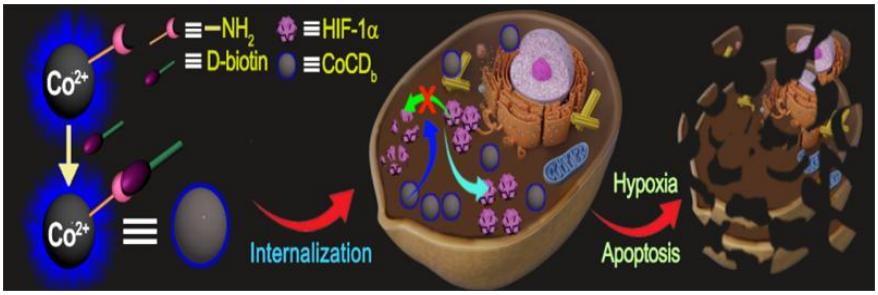

Figure 21. ***Schematic representation of Biotinylated Co^{2+}-integrated carbon dot ($CoCD_b$) by hypoxia induced apoptosis. Co^{2+} altered the concentration of HIF-1α, the key factor of hypoxia and thus selectively killed cancer cells.***

Cu^{2+} Integrated Carbon Dot as Efficient Bioprobe for Guanine Nucleobase.

Deoxyribonucleic acid (DNA) is a genetic molecule, made up of bases and nucleotides which plays significant role in biological heritage storage in all living cells. Among all the four nucleotide bases of DNA (guanine (G), adenine (A), thymine (T), and cytosine (C)) guanine is one of the important bases involved in different biological processes which are crucial for cell survival. Among all the nucleotide base guanine is the most vulnerable to oxidize. The principal oxidation product of guanine is 8-oxo-Gua, was considered as a useful biomarker of DNA damage by oxidative stress. Due to this reason the change in guanine concentration can cause deficiency and mutation in the immunity system and it leads to some diseases including cancer. Thus, to find an appropriate way to determine the concentration of guanine is very significant for cellular environment. Considering the above facts, herein I report development of copper (Cu^{2+}) doped carbon dot via hydrothermal method having blue emitting fluorescence (λ_{max}= 428 nm). I explored a fluorescent turn-off method using the prepared CuCD as fluorescent probes to realize a simple, sensitive and selective detection of guanine. The fluorescence intensity of CuCD got quenched significantly in presence of guanine due to the formation of a stable interaction between Cu^{2+} ions and guanine. Accordingly, the CuCD was used as fluorescence probes for application in the detecting guanine having the LOD = 1.57 μM. Importantly, guanine was sensed by CuCD with high selectivity and sensitivity against other nucleobases of DNA

(adenine, cytosine, thymine) as well as with respect to many other monovalent, divalent ions, amino acids and biomolecule. In cellular studies, this CuCD can efficiently quenched guanine treated cell line (B16F10 and NIH3T3) with respect to the control untreated ones. So, therefore a highly sensitive and selective ratiometric fluorescence probe CuCD for guanine detection was synthesized which was also utilized for cellular studies as potential biomarker (Figure 22).

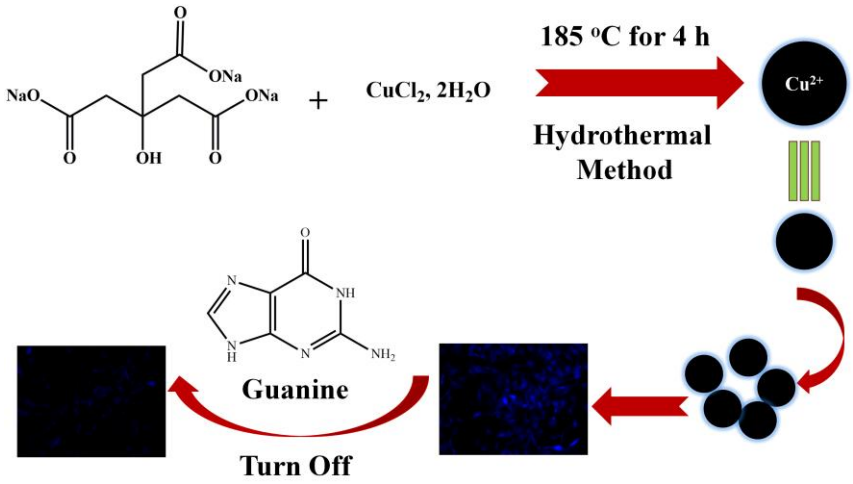

Figure 22. ***Schematic representation of synthesis of blue emitting Cu^{2+} integrated carbon dot (CuCD). The inherent fluorescence property of CuCD got quenched in presence of guanine which was utilized to investigate the bioimaging of guanine treated cell lines.***

REFFERENCES

1. https://biologydictionary.net/natural-science/
2. https://www.scienceabc.com/nature/seed-grow-tree.html
3. https://www.cleanerseas.com/climate-change-fish-migration/
4. https://www.quora.com/What-evidence-do-we-have-that-in-the-helical-form-of-the DNA-molecule-the-base-pairs-are-composed-of-one-purine-and-one-pyrimidine
5. https://en.wikipedia.org/wiki/DNA
6. https://www.blueheronbio.com/codon-optimization/
7. https://www.vedantu.com/biology/start-codons-in-dna-and-rna
8. Rao, C. N. R.; Kulkarni, G. U. P.; Thomasa, J., Edwards, P. P. Metal Nanoparticles and their Assemblies.*Chem. Soc. Rev.* **2000**, *29*, 27.
9. Thelakkat, M.; Schmitz,C.; Schmidt, H.W. Fully Vapor-Deposited Thin-Layer Titanium Dioxide Solar Cells. *Adv. Mater.***2002**, *14*, 577.
10. West, L.; Halas, N. Applications of Nanotechnology to Biotechnology Commentary. *Curr. Opin. Biotech.* **2000**, *11*, 215.
11. https://edgeofspace.in/nanomaterials-revolutionizing-the-aerospace-industry/
12. Kryuchkov, M.; Lehmann, J.; Schaab, J.; Cherepanov, V.; Blagodatski, A.; Fiebig, M.; Katanaev, V. L. Alternative Moth-Eye Nanostructures: Antireflective Properties and Composition of Dimpled Corneal Nanocoatings in Silk-Moth Ancestors. *J Nanobiotechnol* **2017**, *15*, 61.
13. Kryuchkov, M.; Bilousov, O.; Lehmann, J.; Fiebig, M.; Katanaev, V. L. Reverse and Forward Engineering of Drosophila Corneal Nanocoatings. *Nature* **2020**, *585*, 383.

14. Murray, C. B.; Kagan C. R.; Bawendi, M. G. Synthesis and Characterization of Monodisperse Nanocrystals and Close-Packed Nanocrystal Assemblies. *Annu. Rev. Mater. Sci.* **2000**, *30*, 545.

15. Mnyusiwalla, A.; Daas, A. S.; Singer, P. A. 'Mind The Gap': Science and Ethics in Nanotechnology. *Nanotechnology* **2003**, *14*, R9.

16. Hughes, M. P. AC Electrokinetics: Applications for Nanotechnology. *Nanotechnology* **2000**, *11*, 124.

17. Ferrari, M. Cancer Nanotechnology: Opportunities and Challenges. *Nat. Rev. Cancer* **2005**, *5*, 161.

18. Whitesides, G. M. Nanoscience, Nanotechnology, and Chemistry. *Small* **2005**, *1*, 172.

19. Seeman, N. C. At the Crossroads of Chemistry, Biology, and Materials: Structural DNA Nanotechnology. *Chem. Biol.* **2003**, *10*, 1151.

20. Rao, C. N. R.; Muller, A.; Cheetham, A. K. *The Chemistry of Nanomaterials* (Volume 1), **2004**.

21. Zhu, S. D.; Chu,Y.; Qiu, S. The Homotopy Perturbation Method for Discontinued Problems Arising in Nanotechnology. *Comput. Math. Appl.* **2009**, *58*, 2398.

22. Srilatha, B. Nanotechnology in Agriculture. *J. Nanomed. Nanotechnol.* **2011**, *2*, 123.

23. Freitas Jr. R. A.; *Nanomedicine* (Volume 1: Basic Capabilities) **1999**.

24. https://ieeenano.org/nano-blog

25. https://www.azonano.com/news.aspx?newsID=38484

26. An, C.; Sun, C.; Li, N.; Huang, B.; Jiang, J.; Shen, Y.; Wang, C.; Zhao, X.; Cui, B.; Wang, C.; Li, X.; Zhan, S.; Gao, F.; Zeng, Z.; Cui, H.; Wang. Y. Nanomaterials and Nanotechnology for the Delivery of Agrochemicals: Strategies towards Sustainable Agriculture. *Journal of Nanobiotechnology* **2022**, *20*, 11.

27. Pal, A.; Chhikara, B. S.; Govindaraj, A.; Bhattacharya, S.; Rao, C. N. R. Synthesis and Properties of Novel Nanocomposites Made of Single-Walled Carbon Nanotubes and Low Molecular Mass Organogels and their Thermo-Responsive Behavior Triggered by Near IR Radiation. *J. Mater.Chem.* **2008**,*18*, 2593.

28. Corma, A. H.; Garcia, P. M. N.; Primo, A.; Calvino, J. J.; Trasobares, S. Gold Nanoparticles in Organic Capsules: A Supramolecular Assembly of Gold Nanoparticles and Cucurbituril. *Chem. Eur. J.* **2007**, *13*, 6359.

29. Thelakkat, M.; Schmitz, C.; Schmidt, H.W. Fully Vapor-Deposited Thin-Layer Titanium Dioxide Solar Cells. *Adv. Mater.* **2002**, *14*, 577.

30. Josephson, L.; Kircher, M. F.; Mahmood, U.; Tang, Y.; Weissleder, R. Near-Infrared Fluorescent Nanoparticles as Combined MR/Optical Imaging Probes. *Bioconjugate Chem.* **2002**, *13*, 554.

31. Pengo, P.; Baltzer, L.; Pasquato, L.; Scrimin, P. Substrate Modulation of the Activity of an Artificial Nanoesterase Made of Peptide-Functionalized Gold Nanoparticles. *Angew. Chem. Int. Ed.* **2007,** *46*, 400.

32. Cheon, J.; Lee, J. H. Synergistically Integrated Nanoparticles as Multimodal Probes for Nanobiotechnology. *Acc. Chem. Res.* **2008**, *41*, 1630.

33. Shahcheraghi, N.; Golchin, H.; Sadri, Z.; Tabari, Y.; Borhanifar, F.; Makani, S. Nano-Biotechnology, an Applicable Approach for Sustainable Future. *3 Biotech* **2022**, *12*, 65.

34. Williams, R. J.; Mart, R. J.; Ulijn, R. V. Exploiting Biocatalysis in Peptide Self-Assembly. *Peptide Science* **2010**, *94*, 107.

35. Kim, B.C.; Nair, S.; Kim, J.; Kwak, J.H.; Grate, J.W.; Kim, S.H.; Gu, M.B. Preparation of Biocatalytic Nanofibres with High Activity and Stability via Enzyme Aggregate Coating On Polymer Nanofibres. *Nanotechnology* **2005**, *16*, S382.

36. K. T.; sriwong, Matsuda, T. Recent Advances in Enzyme Immobilization utilizing Nanotechnology for Biocatalysis. *Org. Process Res. Dev.* **2022**, *26*, 1857.

37. Reshmy, R.; Philip, E.; Sirohi, R.; Tarafdar , A.; Arun, K.B.; Madhavan, A.; Binod, P.; Awasthi, M.K.; Varjani, S.; Szakacs, G.; Sindhu, R. Nanobiocatalysts: Advancements and Applications in Enzyme Technology. *Bioresour. Technol.* **2021**, *337*, 125491.

38. O¨lçu¨cu, G.; Klaus, O.; Jaeger, K. E.; Drepper, T.; Krauss, U. Emerging Solutions for in Vivo Biocatalyst Immobilization: TailorMade Catalysts for Industrial Biocatalysis. *ACS Sustainable Chem. Eng.* **2021**, *9*, 8919.

39. Heath, J. R. Nanotechnologies for Biomedical Science and Translational Medicine. *PNAS* **2015**, *112*, 14436.

40. Anderson, S.D.; Gwenin, V. V.; Gwenin, C. D. Magnetic Functionalized Nanoparticles for Biomedical, Drug Delivery and Imaging Applications. *Nanoscale Res. Lett.* **2019**, *14*, 188.

41. Fortina, P.; Kricka, L. J.; Surrey S.; Grodzinsky, P. Nanobiotechnology: The Promise and Reality of New Approaches to Molecular Recognition. *Trends Biotechnol.* **2005**, *23*, 168.

42. Lowe, C. R. Nanobiotechnology: The Fabrication and Applications of Chemical and Biological Nanostructures. *Curr. Opinion Struct. Biol.* **2000**, *10*, 428.

43. Niemeyer, C. M. Self-Assembled Nanostructures Based on DNA: Towards the Development of Nanobiotechnology. *Curr. Opinion Chem. Biol.* **2000**, *4*, 609.

44. https://www.fortislife.com/silver-nanoparticles-silver-nanopowders

45. https://www.sbcgold.com/blog/silver-nanoparticles-new-technology-impact-silver-demand/

46. Chandrakala, V.; Aruna, V.; Angajala, G. Review on Metal Nanoparticles as Nanocarriers: Current Challenges and Perspectives in Drug Delivery Systems. *Emergent Materials* **2022**, *5*, 1593.

47. Yang, X.; Yang, M.; Pang, B.; Vara, M.; Xia, Y.; Gold Nanomaterials at Work in Biomedicine. *Chem. Rev.* **2015**, *115*, 10410.

48. Mulvaney, P. *The beauty and elegance of Nanocrystals : How invisibly small particles will colour and shape our future*, University of Melbourne, **2004**.

49. Leuvering, J. H. W.; Coverde, B. C.; Thal, P. J. H. M.; Schuurs, A. H. W. M. A Homogeneous Sol Particle Immunoassay for Human Chorionic Gonadotrophin Using Monoclonal Antibodies. *J. Immunol. Methods* **1983**, *60*, 9.

50. Deelder, A. M.; Dozy, M. H. Applicability of Sol Particle Immunoassay (SPIA) for Detection of Schistosoma Mansoni Circulating Antigens. *Acta Leiden.* **1982**, *48*, 17.

51. Sondi, I., Salopek-Sondi, B. Silver Nanoparticles as Antimicrobial Agent: A Case Study on E. Coli as a Model for Gram-Negative Bacteria. *J. Colloid Interface Sci.* **2004**, *275*, 177.

52. Esteban-Tejeda, L.; Malpartida, F.; Esteban-Cubillo, A.; Pecharroman, C.; Moya, J. S. The Antibacterial and Antifungal Activity of a Soda-Lime Glass Containing Silver Nanoparticles. *Nanotechnology* **2009**, *20*, 085103.

53. Estelrich, J.; Escribano, E.; Queralt, J.; Busquets, M. A. Iron Oxide Nanoparticles for Magnetically-Guided and Magnetically-Responsive Drug Delivery. *Int J Mol Sci.* **2015**, *16*, 8070.

54. Speranza, G. Carbon Nanomaterials: Synthesis, Functionalization and Sensing Applications. *Nanomaterials* **2021**, *11*, 967.

55. Hong, G.; Diao, S.; Antaris, A. L.; Dai, H. Carbon Nanomaterials for Biological Imaging and Nanomedicinal Therapy. *Chem. Rev.* **2015**, *115*, 10816.

56. Diederich, F.; Thilgen, C. Covalent Fullerene Chemistry. *Science* **1996**, *271*, 317.

57. Iijima, S.; Ichihashi, T. Single-Shell Carbon Nanotubes of 1-nm Diameter. *Nature* **1993**, *363*, 603.

58. Shang, J. Z.; Ma, L.; Li, J. W.; Ai, W.; Yu, T.; Gurzadyan, G. G. The Origin of Fluorescence from Graphene Oxide. *Sci. Rep.* **2012**, *2*, 792.

59. Sun, Y. P.; Zhou, B.; Lin, Y.; Wang, W.; Fernando, K. A. S.; Pathak, P.; Meziani, M. J.; Harruff, B. A.; Wang, X.; Wang, H. F.; Luo, P. J. G.;Yang, H.; Kose, M. E.; Chen, B. L.; Veca, L. M.; Xie, S. Y. Quantum-Sized Carbon Dots

for Bright and Colorful Photoluminescence. *J. Am. Chem. Soc.* **2006**, *128*, 7756.

60. Bacon, M.; Bradley, S. J.; Nann. T. Graphene Quantum Dots. *Part. Part. Syst. Charact.* **2014**, *31*, 415.

61. Maiti, D.; Tong, X.; Mou, X.; Yang. K. Carbon-Based Nanomaterials for Biomedical Applications: A Recent Study. *Front. Pharmacol.* **2019**, *9*, 1401.

62. Jariwala, D.; Sangwan, V. K.; Lauhon, L. J.; Marksab T. J.; Hersam, M. C. Carbon Nanomaterials for Electronics, Optoelectronics, Photovoltaics, and Sensing. *Chem. Soc. Rev.* **2013**, *42*, 2824.

63. Verma, S. K.; Das A. K.; Gantait, S.; Kumar, V.; Gurel, E. Applications of Carbon Nanomaterials in the Plant System: A Perspective View on the Pros and Cons. *Sci. Total Environ.* **2019**, *667*, 485.

64. Loh, K. P.; Ho, D.; Chiu, G. N. C.; Leong, D. T.; Pastorin, G.; Chow. E. K. H. Clinical Applications of Carbon Nanomaterials in Diagnostics and Therapy. *Adv. Mater.* **2018**, *30*, 1802368.

65. Mahor, A.; Singh, P. P.; Bharadwaj, P.; Sharma, N.; Yadav, S.; Rosenholm, J. M.; Bansal, K. K. Carbon-Based Nanomaterials for Delivery of Biologicals and Therapeutics: A Cutting-Edge Technology. *C* **2021**, *7*, 19.

66. Li, C.; Adamcik, J.; Mezzenga, R. Biodegradable Nanocomposites 0f Amyloid Fibrils and Graphene with Shape-Memory and Enzyme-Sensing Properties. *Nat. Nanotechnol.* **2012**, *7*, 421.

67. Muszynski, R.; Seger, B.; Kamat, P. V. Decorating Graphene Sheets with Gold Nanoparticles. *J. Phys. Chem. C* **2008**, *112*, 5263.

68. Aliyev, E. M.; Khan, M. M.; Nabiyev, A. M.; Alosmanov, R. M.; Zadeh, I. A. B.; Shishatskiy, S.; Filiz, V. Covalently Modified Graphene Oxide and Polymer of Intrinsic Microporosity (PIM-1) In Mixed Matrix Thin-Film Composite Membranes. *Nanoscale Res. Lett.* **2018**, *13*, 359.

69. https://www.ossila.com/en-in/products/reduced-graphene-oxide-powders

70. https://www.acsmaterial.com/blog-detail/industrial-scale-graphene-nanoplatelets-dispersions.html

71. Shao, L.; Tobias, G.; Salzmann, C. G.; Ballesteros, B.; Hong, S. Y.; Crossley, A.; Davis, B. G.; Green, M. L. H. Removal of Amorphous Carbon for the Efficient Sidewall Functionalization of Single-Walled Carbon Nanotubes. *Chem. Commun.* **2007**, 5090.

72. Goodwin, A. P.; Tabakman, S. M.; Welsher, K.; Sherlock, S. P.; Prencipe, G.; Dai, H. Phospholipid− Dextran with a Single Coupling Point: A Useful Amphiphile for Functionalization of Nanomaterials. *J. Am. Chem. Soc.* **2009**, *131*, 289.

73. Prato, M.; Kostarelos, K.; Bianco, A. Functionalized Carbon Nanotubes in Drug Design and Discovery. *Acc. Chem. Res.* **2008**, *41*, 60.

74. Reddy, B. P. N.; Gupta, B.; Gacche, R. N. An Arsenal for 21st Century Noxious Diseases: Carbon Nanomaterials. *IJNA.* **2009**, *3*, 61.

75. Liu, J.; Li, R.; Yang, B. Carbon Dots: A New Type of Carbon-Based Nanomaterial with Wide Applications. *ACS Cent. Sci.* **2020**, *6*, 2179.

76. Zhu, S.; Meng, Q.; Wang, L.; Zhang, J.; Song, Y.; Jin, H.; Zhang, K.; Sun, H.; Wang, H.; Yang, B. Highly Photoluminescent Carbon Dots for Multicolor Patterning, Sensors, and Bioimaging. *Angew. Chem., Int. Ed.* **2013**, *52*, 3953.

77. Sharma, A.; Das, J. Small Molecules Derived Carbon Dots: Synthesis and Applications in Sensing, Catalysis, Imaging, and Biomedicine. *J Nanobiotechnol* **2019**, *17*, 92.

78. Cui, L.; Ren, X.; Sun, M.; Liu, H.; Xia, L. Carbon Dots: Synthesis, Properties and Applications. *Nanomaterials* **2021**, *11*, 3419.

79. Jorns, M.; Pappas, D. A Review of Fluorescent Carbon Dots, their Synthesis, Physical and Chemical Characteristics, and Applications. *Nanomaterials* **2021**, *11*, 1448.

80. Anwar, S.; Ding, H.; Xu, M.; Hu, X.; Li, Z.; Wang, J.; Liu, L.; Jiang, L.; Wang, D.; Dong, C.; Yan, M.; Wang, Q.; Bi, H. A Mini Review on Carbon Quantum

Dots: Preparation, Properties, and Electrocatalytic Application. *ACS Appl. Bio Mater.* **2019**, *2*, 2317.

81. Liu, M. L.; Chen, B. B.; Li, C. M.; Huang, C. Z. Carbon Dots: Synthesis, Formation Mechanism, Fluorescence Origin and Sensing Applications. *Green Chem.* **2019**, *21*, 449.

82. Bao, L.; Liu, C.; Zhang Z. L.; Pang, D. W. Photoluminescence-Tunable Carbon Nanodots: Surface-State Energy-Gap Tuning. *Adv. Mater.* **2015**, *27*, 1663.

83. Ding, H.; Yu, S. B.; Wei J. S.; Xiong, H. M. Full-Color Light-Emitting Carbon Dots with a Surface-State-Controlled Luminescence Mechanism. *ACS Nano* **2016**, *10*, 484.

84. Zhu, S.; Meng, Q.; Wang, L.; Zhang, J.; Song, Y.; Jin, H.; Zhang, K.; Sun, H.; Wang, H.; Yang, B.Highly Photoluminescent Carbon Dots for Multicolor Patterning, Sensors, and Bioimaging. *Angew. Chem., Int. Ed.* **2013**, *52*, 3953.

85. Huang, H.; Li, C.; Zhu, S.; Wang, H.; Chen, C.; Wang, Z.; Bai, T.; Shi, Z.; Feng, S. Histidine-Derived Nontoxic Nitrogen-Doped Carbon Dots for Sensing and Bioimaging Applications. *Langmuir* **2014**, *30*, 13542.

86. Ahmed, G. H. G.; La´ıno, R. B.; Calzon, J. A. G.; Garc´ıa, M. E. D. Fluorescent Carbon Nanodots for Sensitive and Selective Detection of Tannic Acid in Wines. *Talanta* **2015**, *132*, 252.

87. Yang, S. T.; Cao, L.; Luo, P. G.; Lu, F.; Wang, X.; Wang, H.; Meziani, M. J.; Liu, Y.; Qi, G.; Sun, Y. P. Carbon Dots for Optical Imaging in Vivo. *J. Am. Chem. Soc.* **2009**, *131*, 11308.

88. Ma, C.; Yin, C.; Fan, Y.; Yang X.; Zhou, X. Highly Efficient Synthesis Of N-Doped Carbon Dots With Excellent Stability Through Pyrolysis Method. *J. Mater. Sci.* **2019**, *54*, 9372.

89. Bourlinos, A.B.; Trivizas G.; Karakassides M.A.; Baikousi, M.; Kouloumpis, A.; Gournis, D.; Bakandritsos, A.; Hola, K.; Kozak, O.; Zboril, R.; Papagiannouli, I.; Aloukos, P.; Couris, S. Green and Simple Route toward

Boron Doped Carbon Dots with Significantly Enhanced Non-Linear Optical Properties**.** *Carbon*. **2015**, *83*, 173.

90. Feng, T.; Ai, X.; An, G.; Yang, P.; Zhao, Y. Charge-Convertible Carbon Dots for Imaging-Guided Drug Delivery with Enhanced *in Vivo* Cancer Therapeutic Efficiency. *ACS Nano* **2016**, *10*, 4410.

91. Papaioannou, N.; Titirici, M. M.; Sapelkin, A. Investigating the Effect of Reaction Time on Carbon Dot Formation, Structure, and Optical Properties. *ACS Omega* **2019**, *4*, 21658.

92. Hola, K.; Sudolska, M.; Kalytchuk, S.; Nachtigallova, D.; Rogach, A. L.; Otyepka, M.; Zboril, R. Graphitic Nitrogen Triggers Red Fluorescence in Carbon Dots. *ACS Nano* **2017**, *11*, 12402.

93. Zhang, B.; Liu, C.; Liu, Y. A Novel One-Step Approach to Synthesize Fluorescent Carbon Nanoparticle. *Eur J Inorg Chem.* **2010**, *28*, 4411.

94. Hu, D.; Lin, K. H.; Xu, Y.; Kajiyama, M.; Neves, M. A.; Ogawa, K.; Enomae, T. Microwave-Assisted Synthesis of Fluorescent Carbon Dots From Nanocellulose for Dual-Metal Ion-Sensor Probe: Fe (III) And Mn (II). *Cellulose* **2021**, *28*, 9705.

95. Zhu, H.; Wang, X.; Li, Y.; Wang, Z.; Yang, F.; Yang, X. Microwave Synthesis of Fluorescent Carbon Nanoparticles with Electrochemiluminescence Properties. *Chem. Commun.* **2009**, 5118.

96. Liu, Y.; Xiao, N.; Gong, N.; Wang, H.; Shi, X.; Gu, W.; Ye, L. Microwave-Assisted Polyol Synthesis of Gadolinium-Doped Green Luminescent Carbon Dots as a Bimodal Nanoprobe. *Carbon*. **2014**, *30*, 10933.

97. Zhu, S.; Meng, Q.; Wang, L.; Zhang, J.; Song, Y.; Jin, H.; Zhang, K.; Sun, H.; Wang, H.; Yang, B. Highly Photoluminescent Carbon Dots for Multicolor Patterning, Sensors, and Bioimaging. *Angew. Chem., Int. Ed.* **2013**, *52*, 3953.

98. Bao, L.; Liu, C.; Zhang Z. L.; Pang, D. W. Photoluminescence-Tunable Carbon Nanodots: Surface-State Energy-Gap Tuning. *Adv. Mater.* **2015**, *27*, 1663.

99. Essner, J. B.; Kist, J. A.; Polo-Parada, L.; Baker, G. A. Artifacts and Errors Associated with the Ubiquitous Presence of Fluorescent Impurities in Carbon Nanodots. *Chem. Mater.* **2018**, *30*, 1878.

100. Kim, S.; Hwang, S. W.; Kim, M. K.; Dong, Y. S.; Dong, H. S.; Chang, O. K.; Yang, S. B. ; Park, J. H.; Hwang, E.; Choi, S. H.; Ko, G.; Sim, S.; Sone, C.; Choi, H. J.; Bae, S.; Hong, B. H. Anomalous Behaviors of Visible Luminescence from Graphene Quantum Dots: Interplay between Size and Shape. *ACS Nano* **2012**, *6*, 8203.

101. Jiang, F.; Chen, D.; Li, R.; Wang, Y.; Zhang, G.; Li, S.; Zheng, J.; Huang, N.; Gu, Y.; Wang, C.; Shu, C. Eco-Friendly Synthesis of Size-Controllable Amine-Functionalized Graphene Quantum Dots with Antimycoplasma Properties. *Nanoscale* **2013**, *5*, 1137.

102. Liu, J. H.; Li, R. S.; Yuan, B.; Wang, J.; Li, Y. F.; Huang, C. Z. Mitochondria-Targeting Single-Layered Graphene Quantum Dots with Dual Recognition Sites for ATP Imaging in Living Cells. *Nanoscale* **2018**, *10*, 17402.

103. Xu, J.; Wang, C.; Li, H.; Zhao, W. Synthesis of Green-Emitting Carbon Quantum Dots with Double Carbon Sources and their Application as a Fluorescent Probe for Selective Detection of Cu^{2+} Ions. *RSC Adv.* **2020**, *10*, 2536.

104. Ganguly, S.D.P.; Banerjee, S.; Das, N.C. Advancement in Science and Technology of Carbon Dot-Polymer Hybrid Composites. *Funct. Compos. Struct.* **2019**, *1*, 022001.

105. Ding, H.; Zhou, X. X.; Zhang, Z. H.; Zhao, Y. P.; Wei, J. S.; Xiong H. M. Large Scale Synthesis of Full-Color Emissive Carbon Dots from a Single Carbon Source by a Solvent-Free Method. *Nano Research* **2022**, *15*, 3548.

106. Li, H.T.; He, X.D.; Kang, Z.H.; Huang, H.; Liu, Y.; Liu, J.L.; Lian, S.Y.; Tsang, C.H.; Yang, X.B.; Lee, S.T. Water-Soluble Fluorescent Carbon Quantum Dots and Photocatalyst Design. *Angew. Chem.* **2010**, *122*, 4532.

107. Wang, L.; Zhu, S. J.; Wang, H. Y.; Qu, S. N.; Zhang, Y. L.; Zhang, J. H.; Chen, Q. D.; Xu, H. L.; Han, W.; Yang B.; Sun, H. B. Common Origin of Green

Luminescence in Carbon Nanodots and Graphene Quantum Dots. *ACS Nano* **2014**, *8*, 2541.

108. Zhang, Y. J.; Yuan, R. R.; He, M. L.; Hu, G. C.; Jiang, J. T.; Xu, T.; Zhou, L.; Chen, W.; Xiang, W. D.; Liang, X. J. Multicolour Nitrogen-Doped Carbon Dots: Tunable Photoluminescence and Sandwich Fluorescent Glass-Based Light-Emitting Diodes. *Nanoscale* **2017**, *9*, 17849.

109. Jiang, Y.; Wang, B.; Meng, F.; Cheng, Y.; Zhu, C. Microwave-Assisted Preparation of N-Doped Carbon Dots as a Biosensor for Electrochemical Dopamine Detection. *J. Colloid Interface Sci.* **2015**, 452, 199.

110. Song, Y.; Yan, X.; Li, Z.H.; Qu, L.B.; Zhu, C.Z.; Ye, R.Y.; Li, S.Q.; Du, D.; Lin, Y.H. Highly Photoluminescent Carbon Dots Derived from Linseed and their Applications in Cellular Imaging and Sensing. *J. Mater. Chem. B* **2018**, *6*, 3181.

111. Dias, C.; Vasimalai, N.; PSárria, M.; Pinheiro, I.; Vilas-Boas, V.; Peixoto, J.; Espiña, B. Biocompatibility and Bioimaging Potential of Fruit-Based Carbon Dots. *Nanomaterials* **2019**, *9*, 199.

112. Wang, Y.; Anilkumar, P.; Cao, L.; Liu, J.; Luo, P.; Tackett, K.; Sahu, S.; Wang, P.; Wang, X.; Sun, Y. Carbon Dots of Different Composition and Surface Functionalization: Cytotoxicity Issues Relevant to Fluorescence Cell Imaging. *Exp. Biol. Med.* **2011**, *236*, 1231.

113. Ding, H.; Du, F.; Liu, P.; Chen, Z.; Shen, J. DNA-Carbon Dots Function as Fluorescent Vehicles for Drug Delivery. *ACS Appl. Mater. Interfaces* **2015**, *7*, 6889.

114. Ding, H.; Zhang, F.; Zhao, C.; Lv, Y.; Ma, G.; Wei, W.; Tian, Z. Beyond a Carrier: Graphene Quantum Dots as a Probe for Programmatically Monitoring Anti-Cancer Drug Delivery, Release, and Response. *ACS Appl. Mater. Interfaces* **2017**, *9*, 27396.

115. Liu, J.; Li, R.; Yang, B. Carbon Dots: A New Type of Carbon-Based Nanomaterial with Wide Applications. *ACS Cent Sci.* **2020**, *6*, 2179.

116. Fisher, R.; Pusztai, L.; Swanton, C. Cancer Heterogeneity: Implications for Targeted Therapeutics. *Br J Cancer.* **2013**, *108*, 479.

117. Siegel, R.L.; Miller, K.D.; Jemal, A. Cancer Statistics, 2016. *CA Cancer J Clin.* **2016**, *66*, 7.

118. Schottenfeld, D.; Fraumeni Jr, J.F. Cancer Epidemiology and Prevention. Oxford University Press; 2006.

119. Yoo, K.Y.; Shin, H.R. Cancer Epidemiology and Prevention. *Korean J Epidemiol.* **2003**, *25*, 1.

120. Maverakis, E.; Cornelius, L. A.; Bowen, G. M.; Phan, T.; Patel, F. B.; Fitzmaurice, S.; He, Y.; Burrall, B.; Duong, C.; Kloxin, A. M.; Sultani, H.; Wilken, R.; Martinez, S. R.; Patel, F. Metastatic Melanoma – A Review of Current and Future Treatment Options. *Acta Derm.- Venereol.* **2015**, *95*, 516.

121. Delaney, G.; Barton, M.; Jacob, S. Estimation of an optimal radiotherapy utilization ratefor melanoma. *Cancer* **2004**, *100*, 1293.

122. Cumberlin, R.; DeMoss, E.; Lassus, M.; Friedman, M. Isolation perfusion for malignant melanoma of the extremity: a review. *J. Clin. Oncol.* **1985**, *3*, 1022.

123. Win-Piazza, H.; Schneebergera, V.; Chena, L.; Pernazzac, D.; Lawrencec, H. R.; Sebtib, S. M.; Lawrencec, N. J.; Wu, J. Enhanced anti-melanoma efficacy of interferon alfa-2b via inhibition of Shp2. *Cancer Lett.* **2012**, *320*, 81.

124. Desale, S. S.; Soni, K. S.; Romanova, S.; Cohenb, S. M.; Bronich, T. K. Targeted Delivery of Platinum-Taxane Combination Therapy in Ovarian Cancer. *J. Control. Release* **2015**, *220*, 651.

125. Ge, Y.; Ma, Y.; Li, L. The Application of Prodrug-Based Nano-Drug Delivery Strategy in Cancer Combination Therapy. *Colloids Surf. B: Biointerfaces* **2016**, *146*, 482.

CHAPTER 1

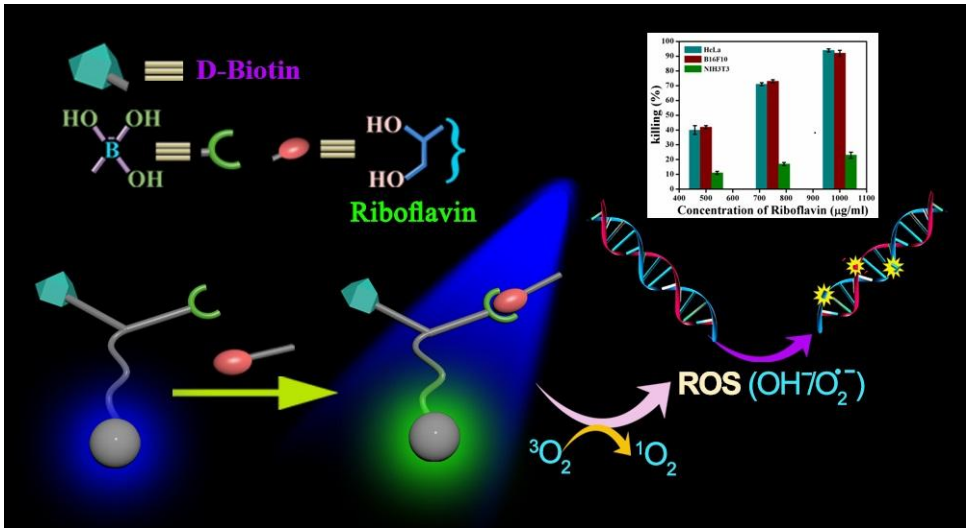

Photosensitizer Tailored Surface Functionalized Carbon Dots for Visible Light Induced Targeted Cancer Therapy

CHAPTER 1

Photosensitizer Tailored Surface Functionalized Carbon Dots…

1.INTRODUCTION

Cancer is a high priority health concern globally. Most commonly used methods for treating this deadly disease include surgery, chemotherapy, immunotherapy, radiation therapy, etc., and each method has its advantages as well as limitations.[1-4] Looking for new alternative methods for cancer treatment is a continuous process with a focus on the balance between the advantage and drawback of treatment. In this context, reactive oxygen species (ROS) (superoxide ($O_2^{\bullet-}$), hydroxyl radical ($^{\bullet}OH$), etc.) that are responsible for killing of cancer cells have been exploited recently in cancer therapeutics with the aim of limited side effects.[5–9] ROS generation is induced inside the cells by using transition metal, enzymes, and photo responsive materials to offer minimally invasive treatment against cancers that include prostate cancer, skin cancer, epithelial precancerous lesions, and others.[5,10-15] Utilization of photo responsive materials such as photosensitizers explicitly for the killing of malignant or premalignant tissues to fight against skin cancer or actinic keratosis is acquiring extensive importance due to the precision of the method achieved with modern instruments.[16-18]

A photosensitizer is a molecule that produces a chemical change in another molecule through a photochemical process.[19]Upon exposure to light of suitable wavelength (visible or near-infrared), the photosensitizer can transfer energy to molecular oxygen and produces ROS such as singlet oxygen, hydrogen peroxide, superoxide, and hydroxyl radicals. [20-24] Thus, irradiation with a particular light (specific wavelength) on the targeted tissue of tumor cells results in the killing of cancer cells by ROS through oxidative DNA damage in the presence of an appropriate photosensitizer.[25,26] To date, photosensitizer-induced cancer treatment has been developed using different photosensitizers such as photofrin, chlorine e6, phthalocyanine, purlytin, padoporfin, lutrin, etc.[27] However, the mentioned photosensitizers suffer from major limitations such as poor chemical purity, poor water solubility, less target specificity, and intense accumulation in skin.[20,28-30]

Considering the above facts, we planned to develop a photosensitizer tethered tumor targeting bioprobe that can specifically deliver the photosensitizer

inside the cancer cell without affecting its photochemical behavior. In this context, intrinsically fluorescent carbon dot, a zero-dimensional green nanomaterial, has been gaining extensive attention in the field of biomedicine, theranostic due to its ease of surface passivation, superior cytocompatibility, and high water solubility.[31-35] However, light induced target specific cancer therapy using carbon dots is still at its nascent stage.

Herein, we report the synthesis of phenylboronic acid appended biotinylated blue emitting carbon dot (CD1s). A well-known photosensitizer riboflavin having "diol" moiety was covalently linked with this CD1s to prepare riboflavin tailored carbon dot (RCD1s). The Lewis acid–base complementary boronic acid–diol interaction was exploited to make the covalent linkage between the surface functionalizing agent of CD1s and riboflavin to develop RCD1s. Microscopic and spectroscopic techniques were used to characterize both CD1s and RCD1s. Interestingly, the newly synthesized RCD1s was found to produce ROS under the exposure of visible light (wavelength: 460–490 nm). RCD1s was found to be sufficiently stable in biological milieu as well as highly cytocompatible toward mammalian cells. More importantly, RCD1s successfully labeled HeLa and B16F10 melanoma cells over noncancerous cell NIH3T3 by exploiting its fluorescence and cancer cell targeting moiety, biotin. Notably, under irradiation of visible light (wavelength: 460–490 nm), RCD1s was found to kill HeLa and B16F10 melanoma cells over noncancer cell NIH3T3 by ~5-fold higher efficacy through ROS induced oxidative DNA damage.

2.RESULTS AND DISCUSSION

In cancer therapy, many procedures were developed to fight with this deadly decease such as chemotherapy where anticancer drugs were used for killing of cancer cells. However, chemotherapy has several harmful side effects including anemia, nausea, and many others. Recently, metallic and nonmetallic nanoparticles were exploited in different areas like nanocatalysis, biomedicine, etc.[36-38] Many nanoparticles based target specific delivery vehicles were developed

from transition elements for transporting anticancer drugs. In light induced cancer therapy, the near-infrared region (NIR) light was used for in vivo as well as in vitro cancer therapy. Moreover, in some cases, lanthanides (Yb^{3+}, Er^{3+}) for upconversion of nanoparticles (Table 1), [12,39-45] doped transition metals (Ti^{4+}) were also used for light induced cancer therapy.[10,12] However, these nanoparticles may accumulate in the body accounting for the severe adverse effect in human health. Considering all the above facts, we wanted to develop a metal free, highly cytocompatible system that can kill cancer cell without the assistance of any anticancer drug. With this intention, we wanted to use photosensitizers, which can generate reactive oxygen species (ROS) under exposure of light of specific wavelength.[20-24] Target specific delivery of photosensitizers within cancer cells and successive irradiation with light will have the potential to kill those cancer cells through in situ generated ROS induced oxidative DNA damage.[25,26] In this context, judicious design and development of delivery vehicle are essential to selectively transport the photosensitizer within the cancer cells over noncancer cells. It would be advantageous if the photosensitizer itself is an integral part of the delivery vehicle so that it is not required to encapsulate or additionally connected to delivery vehicle. Moreover, the photosensitizer should be linked to the targeted delivery vehicle in such a way that its' photochemical property remains unaffected. Considering the above-mentioned requirements, we planned to prepare phenylboronic acid (PBA) appended biotinylated carbon dot as delivery vehicles, which can be linked with diol containing photosensitizer, riboflavin through complementary boronate-diol interaction (Scheme 1).

Table 1. Previous Reports on Green and Photo-induced Diverse Theranostic Applications.

Journal	Title/summary	Comment
Biomaterials **2013**, *34*, 7715	Graphene oxide covalently grafted upconversion nanoparticles for combined NIR mediated imaging and photothermal/photodynamic cancer therapy.[39]	Lanthanides (Yb^{3+}, Er^{3+}) have been used to synthesize the upconversion nanoparticle. However, carbon based nanoparticles are more bio-friendly rather than metallic one.
Environ. Chem. Lett. **2016**, *14*, 195	Efficient oxidation and epoxidation using a chromium(VI)-based magnetic nanocomposite.[40]	Chromium based nano composite was used for oxidation and epoxidation.
ACS Nano, **2016**, *10*, 4410	Charge-convertible carbon dots for imaging-guided drug delivery with enhanced in vivo cancer therapeutic efficiency.[41]	pH controlled study. No target specific delivery to cancer cells.
ACS Appl. Mater. Interfaces **2016**, *8*, 11288	Glucose, 1,2-ethylenediamine and phosphoric acid derived hollow carbon dot as a nanocarrier for doxorubicin delivery and biological imaging.[42]	No target specific delivery to cancer cells.
ACS Appl. Mater. Interfaces **2016**, *8*, 23533	One-Pot To Synthesize Multifunctional Carbon Dots with cyanine dye and poly(ethylene glycol) for Near Infrared Fluorescence Imaging and Photothermal Cancer Therapy.[43]	Cyanine dye has been used. However, commercial dyes often suffer from photobleaching property.
ACS Appl. Mater. Interfaces **2017***, 9, 18639*	Biocompatible Chitosan−Carbon Dot Hybrid Nanogels for NIR Imaging-Guided Synergistic Photothermal-Chemo Therapy.[44]	pH controlled study. No target specific delivery to cancer cells. Anti cancer drug was used which has systemic side effects
Catal. Let. **2018**, *148*, 2929	Novel Leaking-Free, Green, Double Core/Shell, Palladium-Loaded Magnetic Heterogeneous Nanocatalyst for Selective Aerobic Oxidation.[45]	Palladium containing nanocomposite was used for selective aerobic oxidation.
ACS Appl. Mater. Interfaces **2018**, *10*, 1976	Nitrogen and Fluorine Codoped, Colloidal TiO_2 Nanoparticle: Tunable Doping, Large Red-Shifted Band Edge, Visible Light Induced Photocatalysis, and Cell Death.[12]	Presence of Transition metal which have adverse effects on human health.

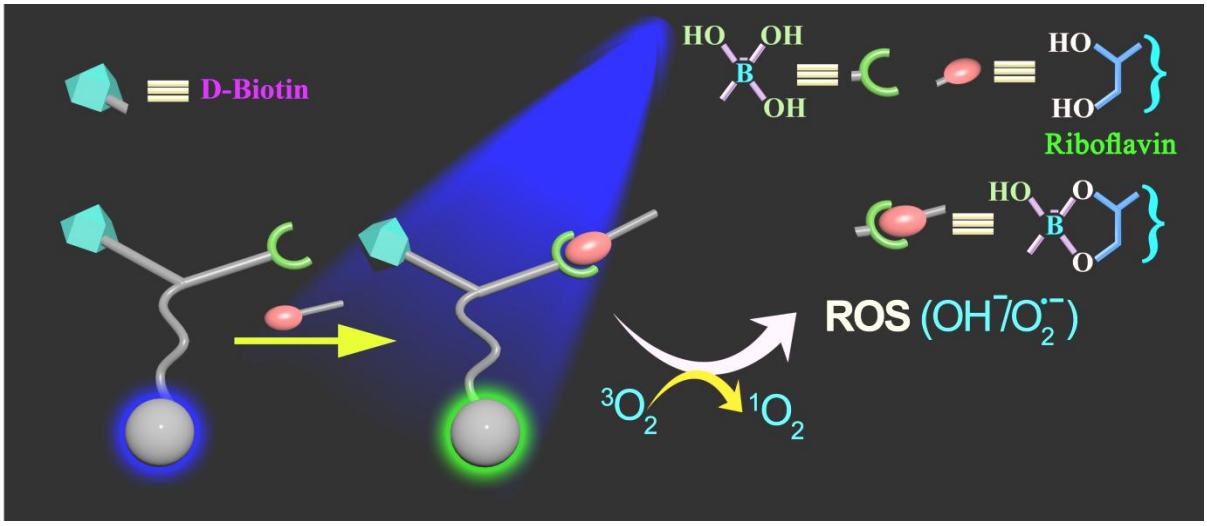

Scheme 1. Pictorial representation on the synthesis of riboflavin tailored carbon dot (**RCD1s**) and light induced generation of reactive oxygen species (ROS) by **RCD1s**.

2.1 Synthesis and Characterization of Surface Modified Carbon Dots (CD1s and CD2s).

To prepare the PBA appended biotinylated carbon dot, at first a surface functionalizing agent (F1) was synthesized by coupling phenylboronic acid and target specific motif biotin through lysine spacer (Scheme 2, Experimental Section). Biotin (Vitamin B7) receptor is one of the prominent one as target-specific motif among the many that are reported tumor-target-specific moieties such as hyaluronic acid, folic acid, RGD, monoclonal antibodies, 17-β- estradiol, etc.[46-48] Biotin is important for all growing cells; however, it is necessary in significant amount for malignant cells and tissues like cancer.[48-54] Consequently, we used biotin in surface functionalizing agent (F1) so that it can specifically detect cancer cells over normal cells. This PBA appended biotinylated surface functionalizing agent (F1) was coupled with a native carbon dot, which has a carbon core of citric acid and glycine for surface passivation to produce CD1 (Scheme 2, Experimental Section). CD1 is insoluble in water, and hence, it was converted to its sodium salt (**CD1s**, Figure 1a) using NaOH. The synthesized **CD1s** is highly soluble in water, and it will be utilized for marking of cancer cells target specifically as well as the carrier/linker for photosensitizer, riboflavin. In **RCD1s**, the presence of biotin moiety makes it potent to differentiate between cancer cells over normal cells. To

further establish this point, we synthesized a new molecule **RCD2s**, which is devoid of biotin moiety. To prepare **RCD2s**, boc appended surface functionalizing agent (F2) was synthesized by coupling phenylboronic acid through lysine spacer (Scheme 3, Experimental Section). This boc appended surface functionalizing agent (F2) was coupled with a native carbon dot, which has a carbon core of citric acid and glycine for surface passivation to produce CD2 (Scheme 3, Experimental Section). CD2 is insoluble in water and hence it was converted to its sodium salt (**CD2s**, Scheme 3, Experimental Section) using NaOH. The synthesized **CD2s** is highly soluble in water and it will be utilized to link with photosensitizer, riboflavin.

The zeta potential value of **CD1s** solution was -24.8 mV, which indicates the considerable stability of carbon dot in aqueous media. Microscopic characterization of newly produced carbon dot was carried out by TEM and AFM. TEM images revealed that the size of **CD1s** was 3-5 nm (Figure 1b). The data obtained from 2D and 3D AFM images are also in concurrence to that of TEM image (Figure 1c, 5a). The basic elemental study for **CD1s** was carried out by XPS. XPS analysis of **CD1s** showed characteristic peaks of C 1s, N 1s, and O 1s orbitals at 285, 418, and 532 eV, respectively (Figure 2a). Along with these peaks, two more peaks were observed at 190 and 160 eV corresponding to B 1s and S 2p orbitals, respectively (Figure 2a). This investigation proves that both B and S are present in the synthesized carbon dot as the surface functionalization of **CD1s** comprise of phenylboronic acid and biotin. The deconvoluted spectra of B 1s orbital exhibited peaks corresponding to B-C bond and B-OH bond at 191.6 and 193.3 eV (Figure 2b). The **CD1s** was also investigated through TGA. It was noteworthy that the TGA plot of **CD1s** showed a decrease in weight between 100 and 150 °C, which corresponded to the decomposition surface functionality of **CD1s** (Figure 2c). After the decomposition, approximately 14% of residues remained, which indicated the amount of native carbon dot present in the sample. Hence, around 86% of overall **CD1s** consists of surface functionalized moiety that was attached to the native carbon dot. Fluorescence spectra of **CD1s** showed excitation dependent blue emission with emission maxima at 420 nm upon excitation 340 nm (Figure 2d). Under UV light (365 nm), **CD1s** solution showed bright blue fluorescence (inset, Figure 2d), which is consistent with the emission behavior of **CD1s**.

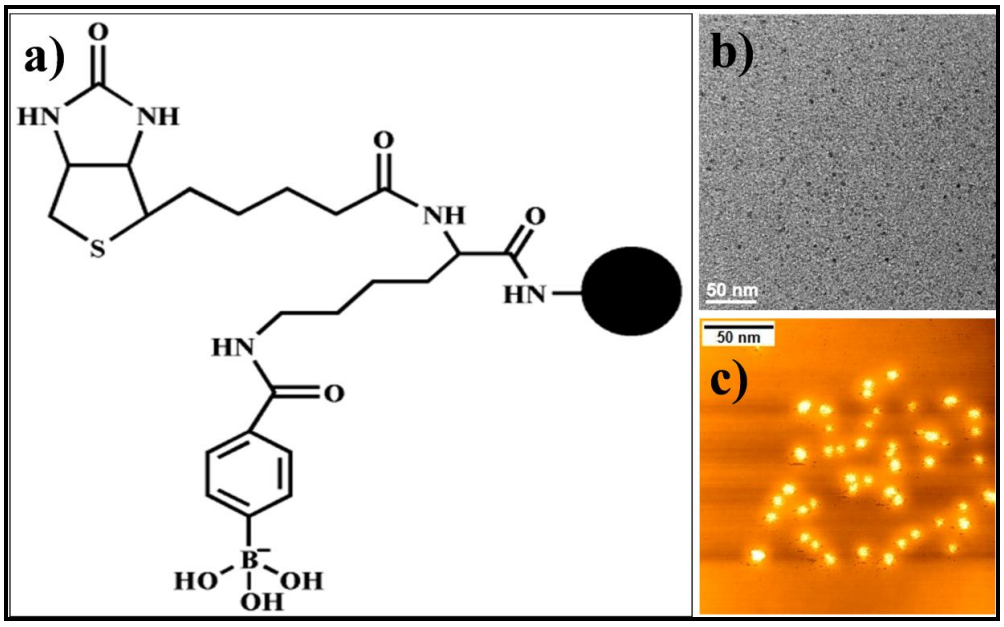

Figure 1. a) Chemical structure of **CD1s**, b) TEM, c)AFM images of **CD1s**.

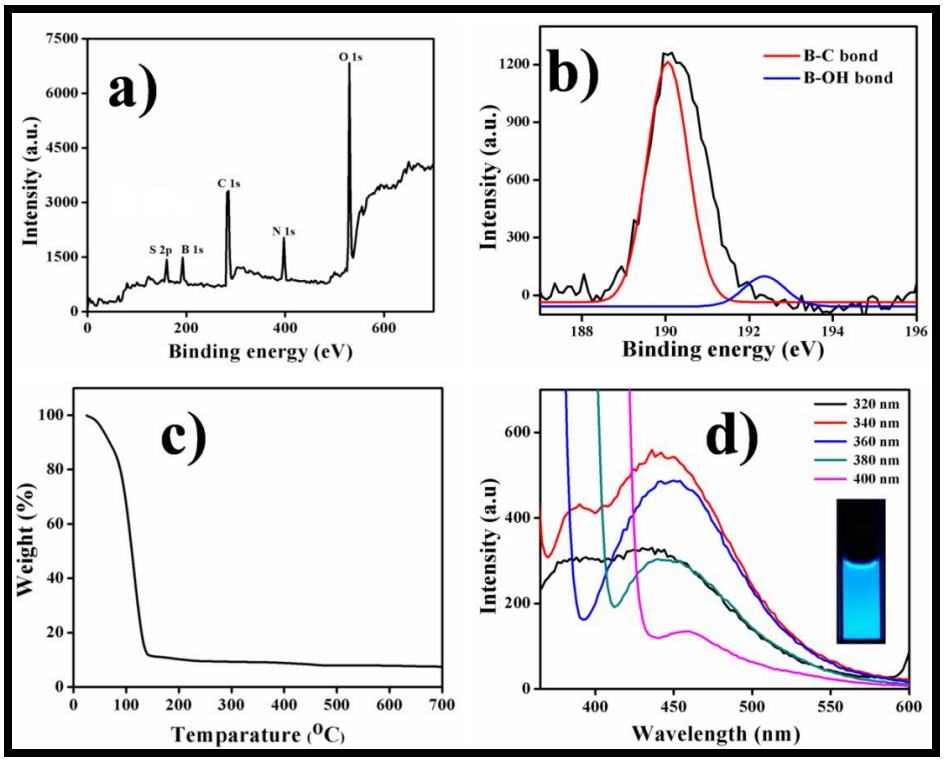

Figure 2. a) XPS spectra of **CD1s**, b) deconvoluted B 1s orbital of **CD1s**, c) TGA plots of **CD1s** and d) Fluorescence spectra of **CD1s** and corresponding blue fluorescence of **CD1s** in water under UV irradiation (365 nm) (inset).

Photosensitizer Tailored Surface Functionalized Carbon Dots…

2.2 Synthesis and Characterization of Riboflavin Tethered CD1s (RCD1s) and CD2s (RCD2s).

Riboflavin is a wellknown photosensitizer having 1,2-diol moiety, which would be appropriate for linking with the boronic acid moiety by a boronate-diol covalent interaction.[55,56] Thus, it has been chosen to couple with **CD1s** having PBA moieties in its surface functionality through boronate-diol interaction to synthesize **RCD1s** (Figure 4a, Scheme 2, Experimental Section). The formation riboflavin adduct (**RCD1s**) from **CD1s** in the presence of riboflavin was investigated by UV-visible spectroscopy. Different weight ratios (w/w) of riboflavin and **CD1s** were mixed (5:1, 1:1, 1:2, 1:3, 1:4, 1:5, 1:6), and the UV-visible spectra of these different solutions of varying weight ratios were recorded (Figure 3). The absorbance spectra of **CD1s** showed λ_{max} at 274 nm, which remained unchanged for the mixtures of **CD1s** and riboflavin at high (5:1, w/w) and equivalent (1:1, w/w) content of riboflavin. Notably, the λ_{max} **CD1s** was red-shifted up to 295 nm with increasing concentration of **CD1s** in the mixture of riboflavin and **CD1s** (from 1:2 to 1:5, w/w) indicating the change in surface property of **CD1s**. Covalent surface modification of the **CD1s** with riboflavin was reflected by the red shifting of λ_{max} in UV-vis spectra possibly due to the formation of **RCD1s** adduct having new λ_{max} (Figure 3). The absorption maxima did not change further upon increasing the concentration of **CD1s** in the mixture of **CD1s** and riboflavin mixtures at 1:6, w/w, which possibly indicates the saturation of **CD1s** surface by riboflavin through boronate-diol bond formation. Thus, for all further experiments and investigations, we prepared **RCD1s** using 1:5 w/w riboflavin and **CD1s**.

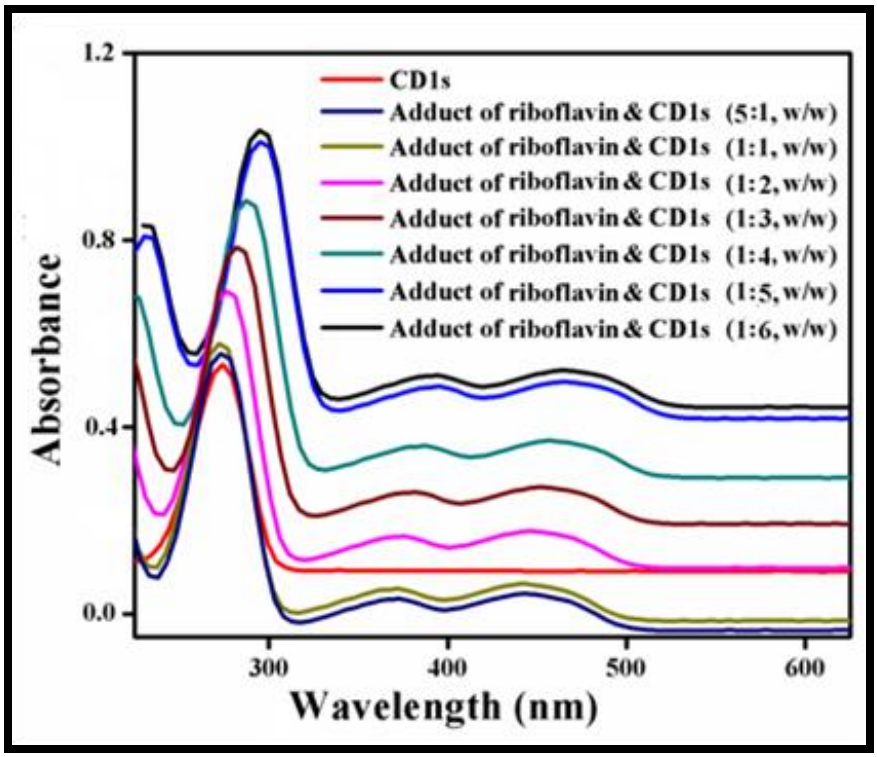

Figure 3. UV-visible spectra of **CD1s** and riboflavin adducts at different weight ratio.

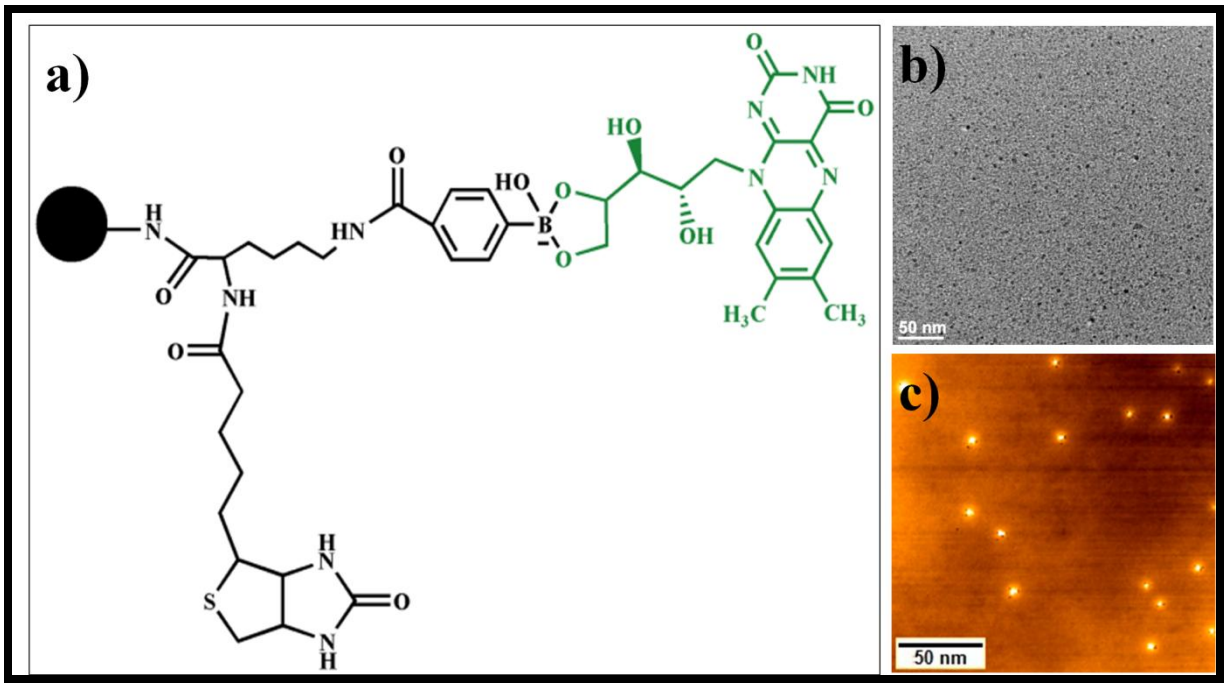

Figure 4. a) Chemical structure of **RCD1s**, b) TEM and c) AFM images of **RCD1s**.

Photosensitizer Tailored Surface Functionalized Carbon Dots...

From TEM and AFM (2D and 3D) images, it was observed that the size of the riboflavin tethered carbon dots (**RCD1s**) was 3-5 nm (Figures 4b,c and 5b). The zeta potential value of **RCD1s** was -27.5 mV, indicating its high aqueous stability. Elemental analysis also confirmed that **RCD1s** also contains B and S along with three main elements C, N, and O (Figure 6a). However, deconvoluted spectra of the B 1s orbital of **RCD1s** are quite different from that of corresponding **CD1s**. The deconvoluted spectra of B 1s orbital exhibited peaks corresponding to B-C bond and B-OH bond at 190.0 and 192.4 eV similar to that of **CD1s** (Figure 6b).[57] Along with these, a new peak at 190.8 eV was observed corresponding to the B-O linkage due to formation of boronate-diol adduct (Figure 6b).[57] The TGA plot of **RCD1s** showed decomposition of surface functionality of **RCD1s** between 300 and 400 °C, which is different compared to that of **CD1s** (Figure 6c). This result indicates different surface functionality of **RCD1s** compared to that of **CD1s**. Emission behavior of **RCD1s** is predominantly controlled by the riboflavin moiety. The fluorescence spectra of **RCD1s** showed emission maxima at 526 nm upon excitation at 450 nm, which indicated green emission of **RCD1s**, but it showed no emission maxima upon excitation at 340 nm (Figure 6d). **RCD2s** was synthesized following the same procedure as **RCD1s** (Figure 7a, Scheme 3, Experimental Section). **RCD2s** was also characterized by TEM, XPS, and fluorescence microscopy. The size of **RCD2s** was also found to be between 3 and 5 nm according to the TEM image (Figure 7b). XPS analysis of **RCD2s** showed characteristic peaks of C 1s, N 1s, O 1s, and B 1s orbitals at 285 eV, 418 eV, 529 eV, and 193 eV, respectively (Figure 7c). The fluorescence spectra of **RCD2s** also showed emission maxima at 524 nm upon excitation at 450 nm, indicating green emission of **RCD2s** (Figure 7d). Under the blue light (460-490 nm), both the aqueous solution of **RCD1s** and **RCD2s** showed bright green fluorescence (inset, Figure 6d, 7d), which is consistent with their emission behavior.

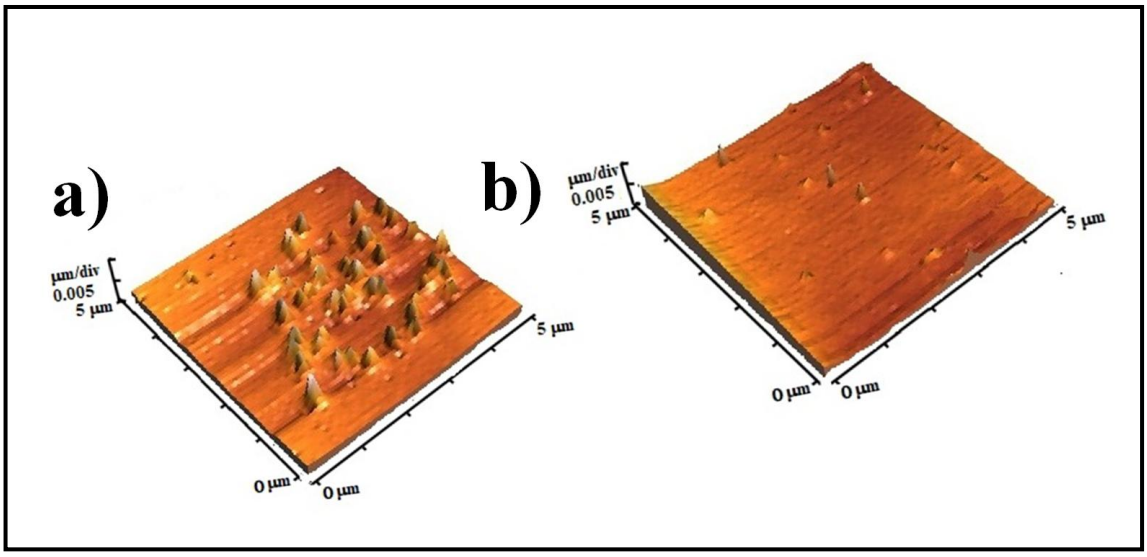

Figure 5. 3D AFM images of a) **CD1s** and b) **RCD1s**.

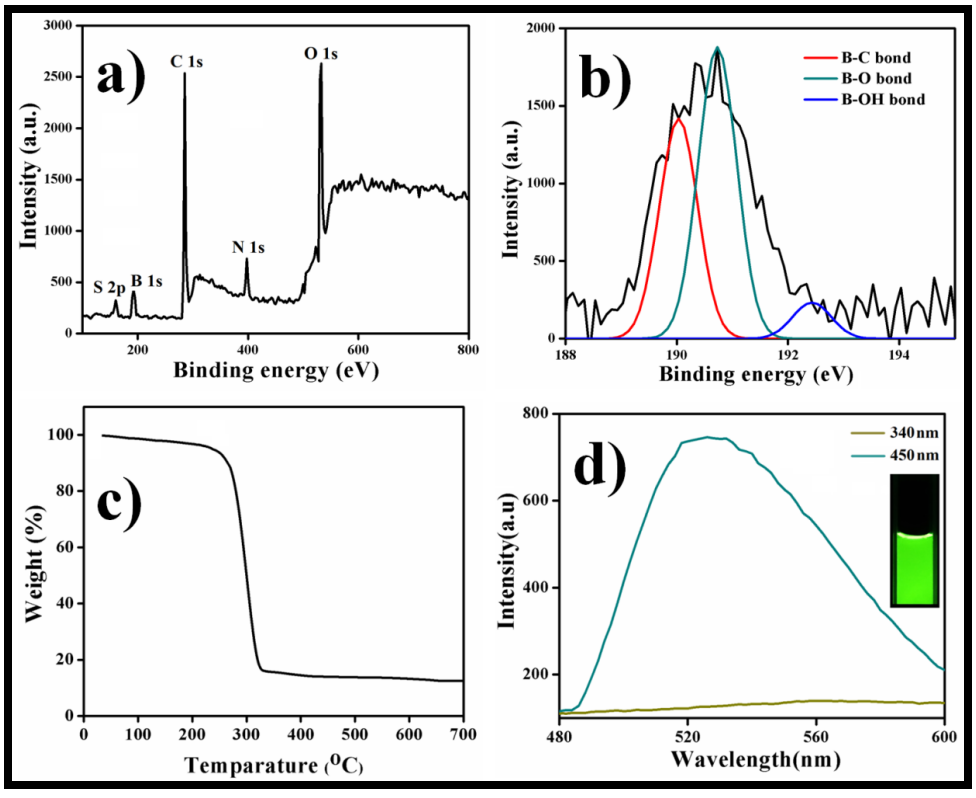

Figure 6. a) XPS spectra of **RCD1s**, b) deconvoluted B 1s orbital of **RCD1s**, c) TGA plots of **RCD1s**, d) Fluorescence spectra of **RCD1s** where [riboflavin] = 5 µg/mL, [**CD1s**] = 25 µg/mL under UV irradiation and under blue light irradiation and corresponding green fluorescence of **RCD1s** in water under blue light irradiation (460-490 nm, inset).

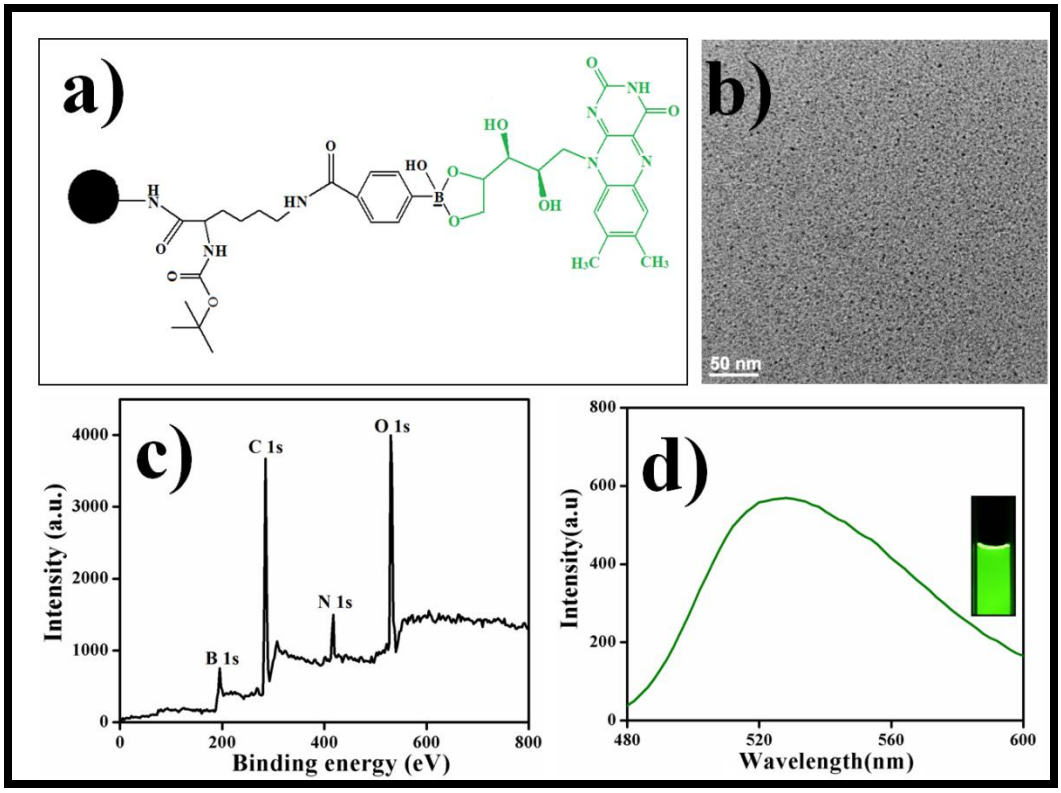

Figure 7. a) Chemical structure of **RCD2s**, b) TEM, c) XPS spectra of **RCD2s**, d) fluorescence spectra of **RCD2s** where [riboflavin] = 5 μg/mL, [**CD2s**] = 25 μg/mL and corresponding green fluorescence of **RCD2s** in water under visible blue light irradiation (460-490 nm, inset).

2.3 Generation of ROS from RCD1s upon Exposure of Visible Light.

Riboflavin is a well-known photosensitizer that produces ROS under exposure of light. In previous instances, riboflavin has been used to produce ROS under UV irradiation. However, exposure of UV light is mostly undesirable for biological systems in particular for mammalian cells. Therefore, we intended to exploit the photosensitivity of riboflavin in such a way that it can produce ROS under visible light irradiation (wavelength: 460–490 nm). Considering the emission behavior of **RCD1s**, we investigated the effect of visible light on riboflavin tethered carbon dots. With this aim, **RCD1s** solution (adduct of 5 μg/mL riboflavin and 25 μg/mL **CD1s**) was irradiated with visible light (460-490 nm) at different time spans (1-10 min) in presence 1,3-diphenylisobenzofuran (DPBF = 20 μg/mL). DPBF is an UV-active molecule that possesses a highly specific reactivity toward ROS.[10] In the presence

of ROS, DPBF forms an endoperoxide, which finally decomposes to produce 1,2-dibenzoylbenzene (Scheme 4).[10]

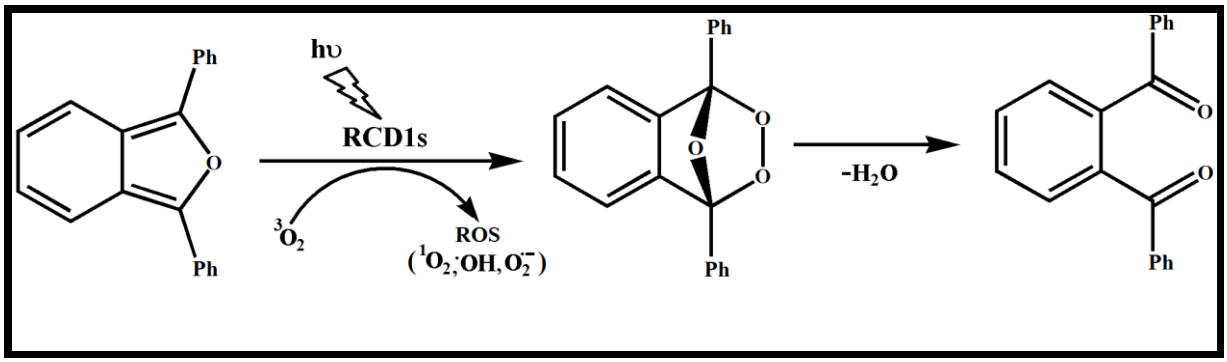

Scheme 4. Scheme of decomposition of DPBF in presence of **RCD1s** under visible light exposure.

This ROS mediated decomposition of DPBF was followed by measuring the change in the absorption at λ_{max} (436 nm) in the UV-vis spectra of DPBF. The absorption maxima of DPBF and its intensity did not change in the presence of only **RCD1s** (Figure 8a). However, the absorbance of DPBF at λ_{max} (436 nm) was found to be gradually reduced with increase in the time of light irradiation in the presence of **RCD1s**. This indicates the production of a higher amount of ROS from riboflavin containing carbon dots with increasing exposure time of light that led to the decomposition of DPBF. To further verify the visible light induced generation of ROS from **RCD1s**, we have carried out the UV-vis experiment for DPBF and **RCD1s** mixture in the presence of radical scavenger, thiourea with 10 min irradiation of light. Upon the addition of thiourea to the mixture of **RCD1s** solution (adduct of 5 μg/mL riboflavin and 25 μg/mL **CD1s**) and DPBF (20 μg/mL), it was found that the DPBF regained its absorbance intensity at λ_{max} (436 nm) (Figure 8b). Steady increase in the absorbance of DPBF at λ_{max} (436 nm) was noted as the concentration of thiourea increased from 1 to 4 μM (Figure 8b). This was possibly due to the prevention in the ROS mediated decomposition of DPBF. Scavenging of light induced generation of ROS (hydroxyl and superoxide radicals) from **RCD1s** by thiourea resulted in minimization of decrease in absorbance of DPBF at λ_{max} (436

nm). Hence, it confirms the generation of ROS from **RCD1s** under the exposure of visible light (Scheme 4).

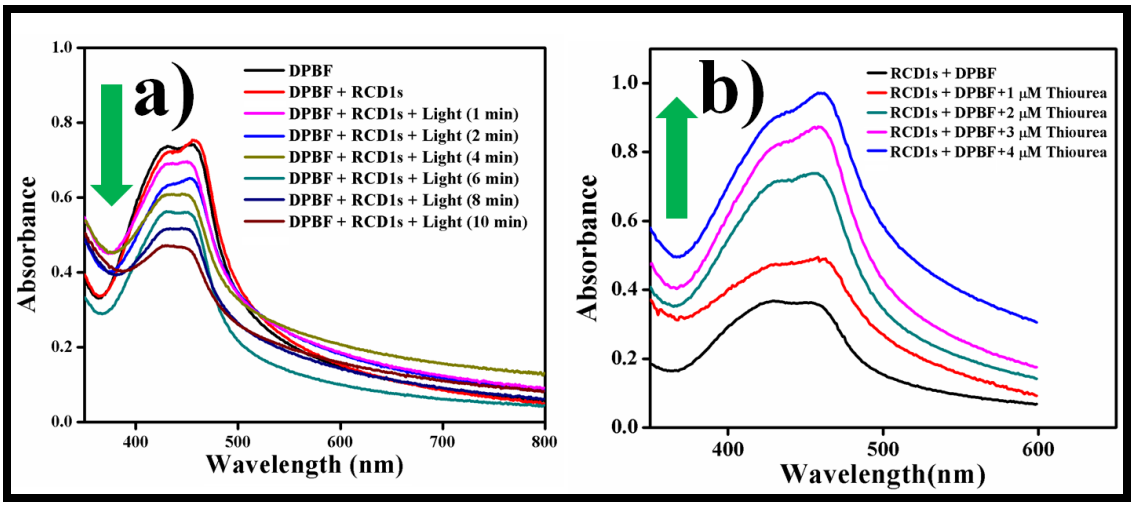

Figure 8. a) Detection of visible light (460-490 nm) induced ROS generation from **RCD1s** in presence of DPBF (absorption at 436 nm) and b) absorption of DPBF in presence of **RCD1s** where [riboflavin] = 5 μg/mL, [**CD1s**] = 25 μg/mL and thiourea under visible light irradiation (10 min). [DPBF] = 20 μg/mL.

The light induced production of ROS from riboflavin present in **RCD1s** was further investigated by EPR spectroscopy. There was no signal in the EPR spectrum of only **RCD1s** in the absence of light. However, a strong EPR signal was seen upon irradiation of light to **RCD1s** solution (Figure 9). This finding is concurrent with the previous report that showed the generation of EPR signal due to the formation of superoxide radical.[7] In the present study, the strong EPR signal can be attributed to the formation of free radicals (hydroxyl and superoxide radicals) due to the light triggered formation of ROS from **RCD1s** (Figure 9).

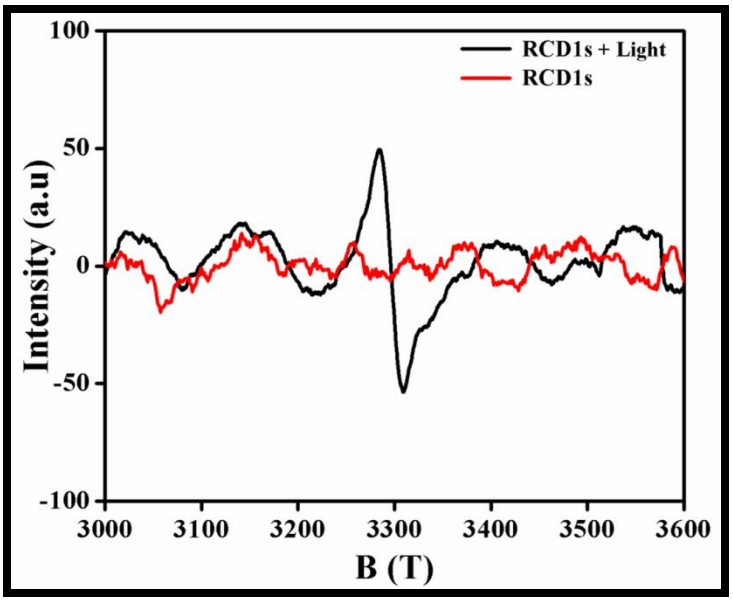

Figure 9. EPR spectra of **RCD1s** in presence and absence of visible light (wavelength: 460-490 nm). The red spectrum represents the only **RCD1s** where [riboflavin] = 5 μg/mL, [**CD1s**] = 25 μg/mL and black spectra represents **RCD1s** where [riboflavin] = 5 μg/mL, [**CD1s**] = 25 μg/mL in presence of visible light for 10 min.

2.4 Oxidative DNA Damage in the Presence of Light.

Next, we investigated the ability of the in situ generated ROS (from riboflavin containing carbon dot upon irradiation of light) in damaging the DNA structure via oxidative pathway. We initially investigated the oxidative damage of DNA from UV–vis spectroscopy in the presence of **RCD1s** and visible light. In the presence of only **RCD1s** (40 μg/mL riboflavin and 200 μg/mL **CD1s**), the spectral pattern of calf thymus DNA (CT-DNA) at absorption maxima (260 nm) did not change in UV–vis spectra (Figure 10a). However, with increasing exposure time of visible light (460-490 nm) in a mixture of CT-DNA (25 μg/mL) and **RCD1s**, the absorbance maxima steadily disappeared and flattened (Figure 10a). This indicated the loss in the structural integrity of CT-DNA presumably due to the oxidative damage by ROS generated from **RCD1s** upon exposure of light. This oxidative damage of DNA in the presence of **RCD1s** and visible light was further investigated by DNA-gel electrophoresis. In agarose gel (1 wt %, ethidium bromide (EB) was used as staining reagent), electrophoresis was performed using calf thymus DNA, **RCD1s**–CT-DNA

mixture, and visible light pretreated **RCD1s**-CT-DNA mixture ([RCD1s] = adduct of 40 μg/mL riboflavin and 200 μg/mL **CD1s**; [CT-DNA] = 25 μg/mL). After migration of both CT-DNA and **RCD1s**-CT-DNA mixture, almost comparable intensities of band were observed in case of UV irradiated agarose gel (lane 1 and 2, Figure 10b) stained by EB. In contrast, the smeared band was observed for visible light pretreated **RCD1s**-CT-DNA mixture (lane 3, Figure 10b). Thus, the CT-DNA in the visible light pretreated **RCD1s**-CT-DNA column expectedly was sheared randomly through oxidation by ROS.[58] This smearing of DNA clearly indicates degradation of DNA due to ROS generation through **RCD1s** upon exposure of light.

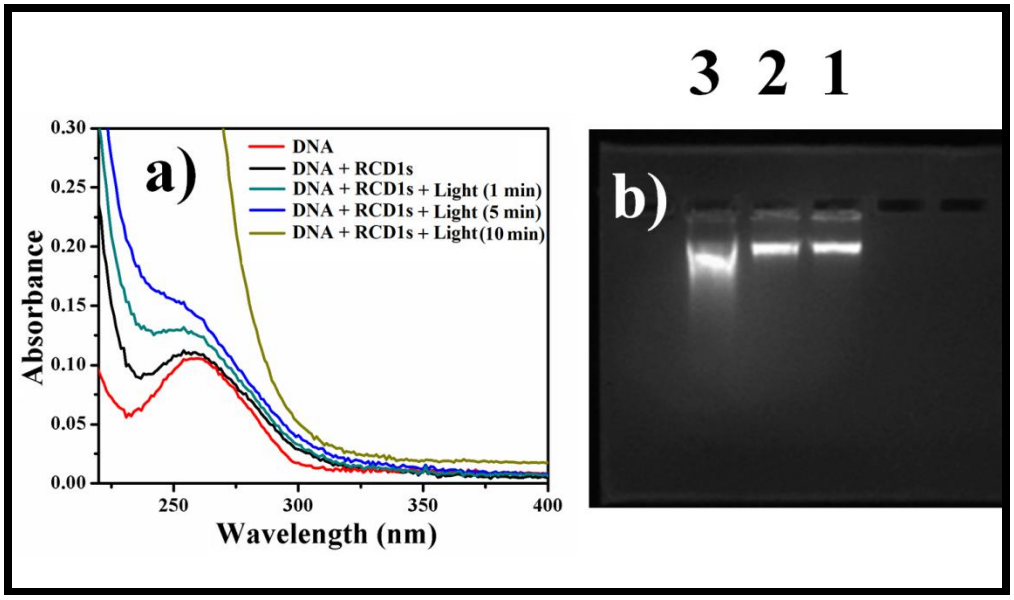

Figure 10. a) UV-visible spectra of free CT DNA, CT DNA-**RCD1s** and visible light irradiated CT DNA-**RCD1s** and visible light exposure time was varied from 1-10 min. b) Photograph of UV irradiated agarose gel after migration of free CT DNA, CT DNA-**RCD1s** and visible light irradiated CT DNA-**RCD1s.** In case of **RCD1s**, [riboflavin] = 40 μg/mL, [**CD1s**] = 200 μg/mL, and [CT DNA] = 25 μg/mL. Visible light (wavelength = 460-490 nm); exposure time = 10 min.

2.5 Media Stability and Cell Viability of RCD1s.

Prior to utilizing this light sensitive riboflavin tethered carbon dot for biorelated applications, we investigated its stability in biological milieu for a course of time as well as the cytocompatibility against mammalian cells. The stability of **RCD1s** was investigated in DMEM media where the concentration of FBS was increased up to

75%. **RCD1s** ([riboflavin] = 1000 µg/mL and [**CD1s**] = 5 mg/mL) was added to FBS-DMEM media where the amount of FBS has been varied and kept for 48 h. The long-time stability of **RCD1s** was also investigated by the addition of **RCD1s** ([riboflavin] = 500-1000 µg/mL and [**CD1s**] = 2.5-5.0 mg/mL) to FBS (10%)-DMEM media and maintained it for 10 days. It was found visually that **RCD1s** was stable in biological media at different concentration of FBS up to 75% (Figure 11a). SSI of **RCD1s** in media was also found more than 90% for varying concentrations of FBS (0-75%) as well as up to 10 days (Figure 11b). The stability of **RCD1s** in the presence of light was investigated where the aqueous solution of **RCD1s** was exposed to UV light (wavelength and power are 365 nm and 12 W, respectively). It was observed that **RCD1s** solution did not show any photobleaching property, and emission property of **RCD1s** remained unchanged even after 200 min of UV irradiation (Figure 11c).

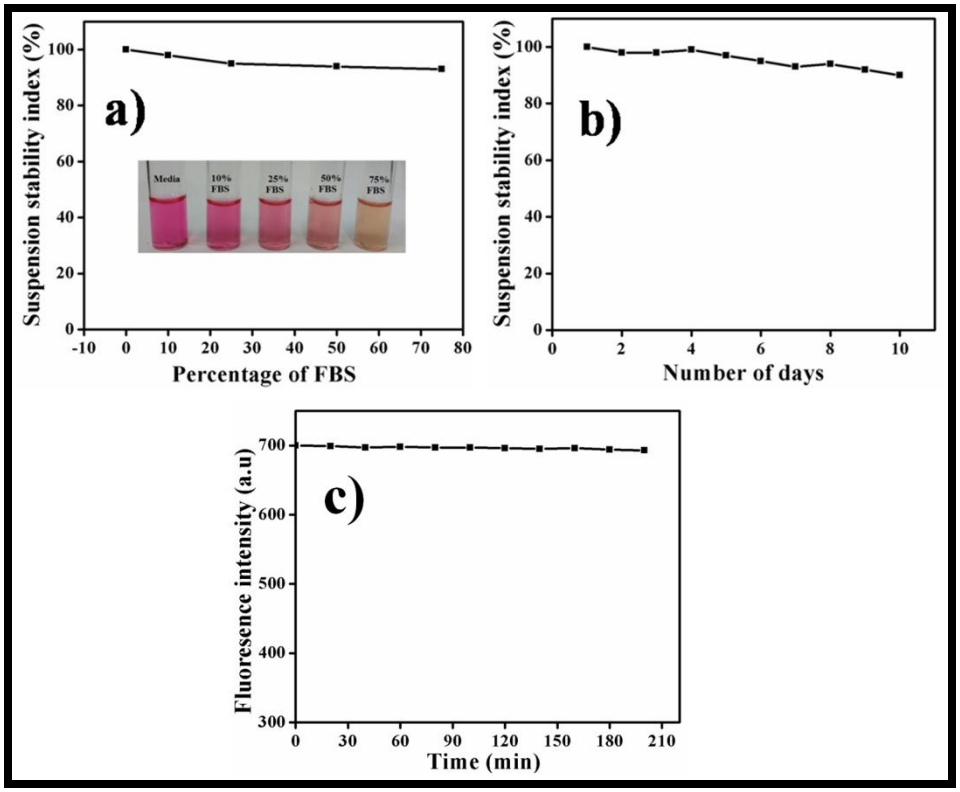

Figure 11. Suspension stability index of **RCD1s** solution where [riboflavin] = 500-1000 µg/mL, [**CD1s**] = 2.5-5.0 mg/mL and with respect to a) FBS concentration (0-75%) in DMEM media, b) number of days in 10% FBS in DMEM media and c) Photostability of **RCD1s** solution under UV (wavelength 365 nm, power 12 W) light irradiation up to 200 min. **RCD1s** solution was excited at 450 nm.

Photosensitizer Tailored Surface Functionalized Carbon Dots…

Next, we investigated the cytocompatibility of **RCD1s** and **RCD2s** against HeLa, B16F10, and NIH3T3 cells by MTT assay. Different concentrations of **RCD1s** and **RCD2s** ([**CD1s** or **CD2s**] = 2.5-5.0 mg/mL and [riboflavin] = 500-1000 µg/ mL) were added to HeLa, B16F10 melanoma cells, and noncancerous NIH3T3 cells. Interestingly, it was found that the cell viabilities of **RCD1s** and **RCD2s** were 90-95% toward HeLa and B16F10 melanoma cells as well as noncancerous NIH3T3 cells after 24 h incubation (Figure 12).

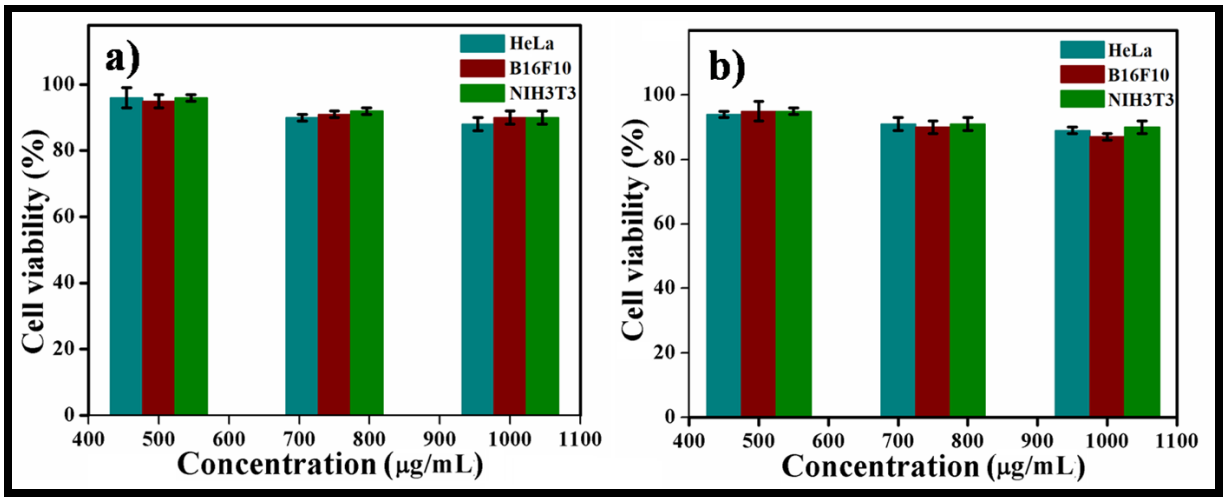

Figure 12. Percentage cell viability of HeLa, B16F10 and NIH3T3 cells with varying concentrations of a) **RCD1s** where [riboflavin] = 500-1000 µg/mL, [**CD1s**] = 2.5-5.0 mg/mL and concentrations of b) **RCD2s** where [riboflavin] = 500-1000 µg /mL, [**CD2s**] = 2.5-5.0 mg/mL after 24 h incubation. The standard deviation and experimental errors were in the range of 1-3% and 3-5% respectively, in triplicate experiments.

2.6 Target Specific Imaging of Cancer Cells.

The possible utilization of RCD1s as bioimaging probe depends on the factors such as it should have high cell viability and intrinsic fluorescence character. Moreover, successful modification of surface with biotin moiety makes these carbon dots potentially target selective toward cancer cells. The cancer cell surface is overexpressed with specific receptors that can be recognized by biotin cellular transporters provided with tumor-targeting modules and subsequently may facilitate its internalization or deliver the uploaded cargo target specifically within tumor cells. To this end, **RCD1s** ([riboflavin] = 200 µg/mL and [**CD1s**] = 1000

μg/mL) were incubated with HeLa, B16F10 melanoma cells, and noncancerous NIH3T3 cells, separately, for 6 h, followed by observed under fluorescence microscope. Interestingly, HeLa and B16F10 cells showed bright green fluorescence, whereas there was no significant fluorescence observed for NIH3T3 cells under similar experimental conditions (Figure 13). **RCD1s** inclusive of biotin moiety could easily get internalized into cancer cells having biotin over-expressed receptors and fluoresce the cells with its green emission. In contrast, no notable fluorescence was observed for non-cancer cells as it could not uptake the **RCD1s** efficiently in absence of over-expressed biotin receptor.

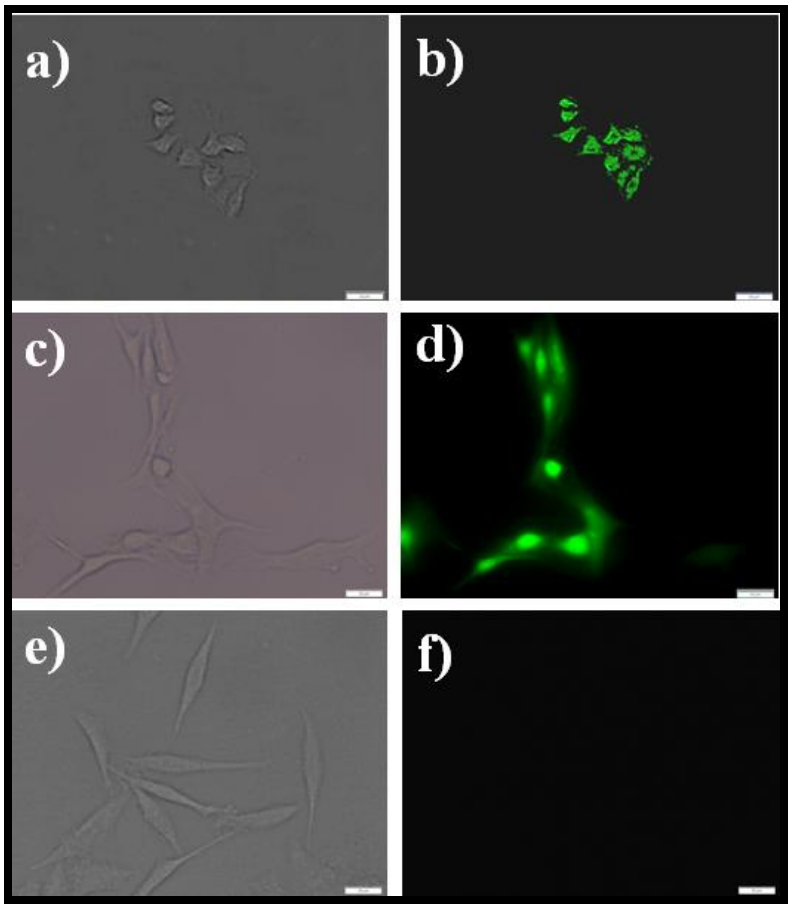

Figure 13. Bright field and fluorescence microscopic images of cells after 6 h incubation with **RCD1s** where [riboflavin] = 200 μg/mL, [**CD1s**] = 1000 μg/mL, (a,b) HeLa (c,d) B16F10 (e,f) NIH3T3 cells. Scale bars correspond to 20 μm.

In the control experiment, we used **RCD2s**, devoid of any biotin moiety. In this regard, **RCD2s** ([riboflavin] = 200 μg/ mL and [**CD2s**] = 1000 μg/mL) was

incubated with HeLa, B16F10 cells, and noncancerous NIH3T3 cells, separately, for 6 h, followed by observed under fluorescence microscope. In case of **RCD2s**, both cancerous cells (HeLa and B16F10) and normal cells NIH3T3 showed bright green fluorescence (Figure 14). **RCD2s**, devoid of biotin moiety, could not make any difference between noncancerous cells and biotin receptor overexpressed cancer cells. Hence, **RCD2s** was internalized in HeLa, B16F10, and NIH3T3 cells with equal efficiency resulting in green fluorescence for both cancer and noncancer cells. Hence, the presence of biotin on the surface of functionalized carbon dot is a key factor for selective imaging of cancer cells over noncancerous cells.

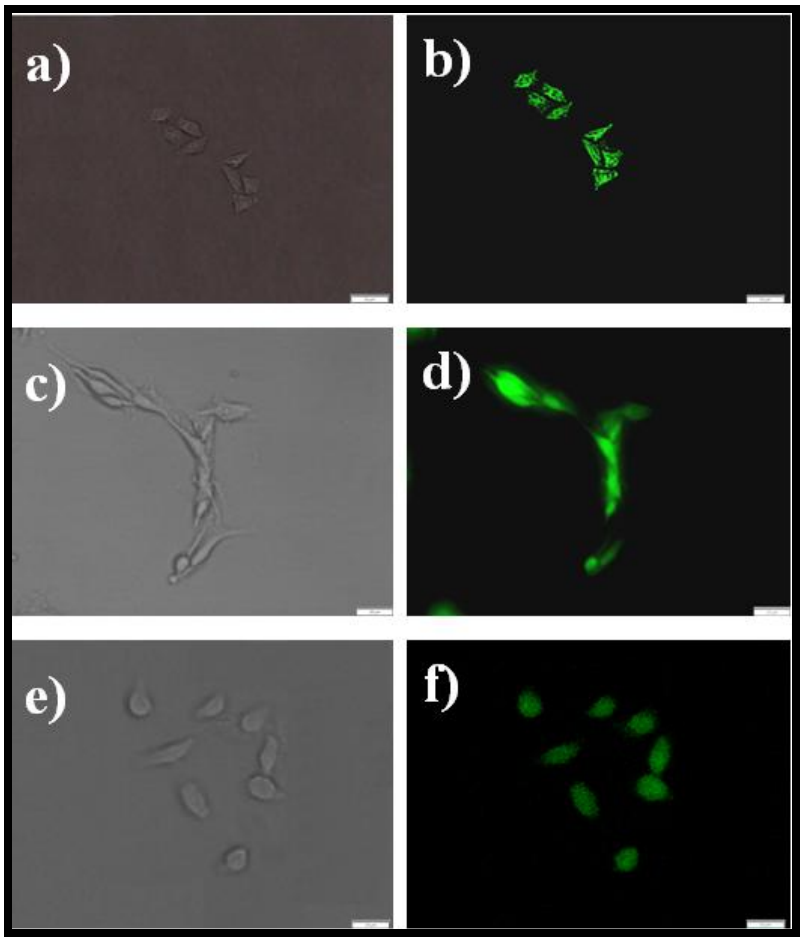

Figure 14. Bright field and fluorescence microscopic images of cells after 6 h incubation with **RCD2s** where [riboflavin] = 200 μg/mL, [**CD2s**] = 1000 μg/mL, (a,b) HeLa (c,d) B16F10 (e,f) NIH3T3 cells. Scale bars correspond to 20 μm.

2.7 Visible Light Induced Killing of Cancer Cells by RCD1s.

In the preceding sections, we observed the oxidative DNA damaging ability by the in situ generated ROS from **RCD1s** in the presence of visible light as well as its biotin receptor mediated target specific internalization within tumor cells. These two intrinsic characteristics of riboflavin tethered carbon dot prompted us to examine the selective killing ability of cancer cell by **RCD1s** upon irradiation of light. At this point, we investigated the killing of HeLa, B16F10, and noncancer NIH3T3 cells by MTT assay. HeLa, B16F10, and NIH3T3 cells were incubated with varying concentrations of **RCD1s** ([riboflavin] = 500-1000 μg/mL and [**CD1s**] = 2.5-5.0 mg/ mL) for 12 h. The cells were then exposed to visible light (wavelength: 460-490 nm) for 10 min followed by incubation for another 6 and 12 h, respectively. In case of 6 h incubation, the % killing of HeLa cells increased from 11 ± 2% to 51 ± 2% with increasing concentration of **RCD1s** from 500 to 1000 μg/ mL (Figure 15a). The % killing of B16F10 cells also increased from 13 ± 1% to 55 ± 2% with increasing concentration of **RCD1s** from 500 to 1000 μg/mL (Figure 15a). However, for 12 h incubation, the % killing of HeLa cells steadily increased from 40 ± 3% to 94 ± 1%, and that for B16F10 cells also increased from 42 ± 1% to 92 ± 4% where **RCD1s** concentration was varied from 500 to 1000 μg/mL (Figure 15a). In contrast, under similar experimental conditions and concentration range of **RCD1s** ([riboflavin] = 500-1000 μg/mL and [**CD1s**] = 2.5-5 mg/mL), only 4 ± 1% to 9 ± 2% of the NIH3T3 cells were found to be dead for 6 h incubation (Figure 15a). In case of 12 h incubation, 23 ± 2% of the NIH3T3 cells were killed at the highest concentration of **RCD1s** ([riboflavin] = 1000 μg/mL and [**CD1s**] = 5 mg/mL) (Figure 15b). Thus, ~5-fold higher killing of cancer cells was noted in comparison to non-cancer cells possibly due to the oxidative damage of DNA by light triggered generation of ROS in the presence of target specifically internalized **RCD1s** within cancer cells.

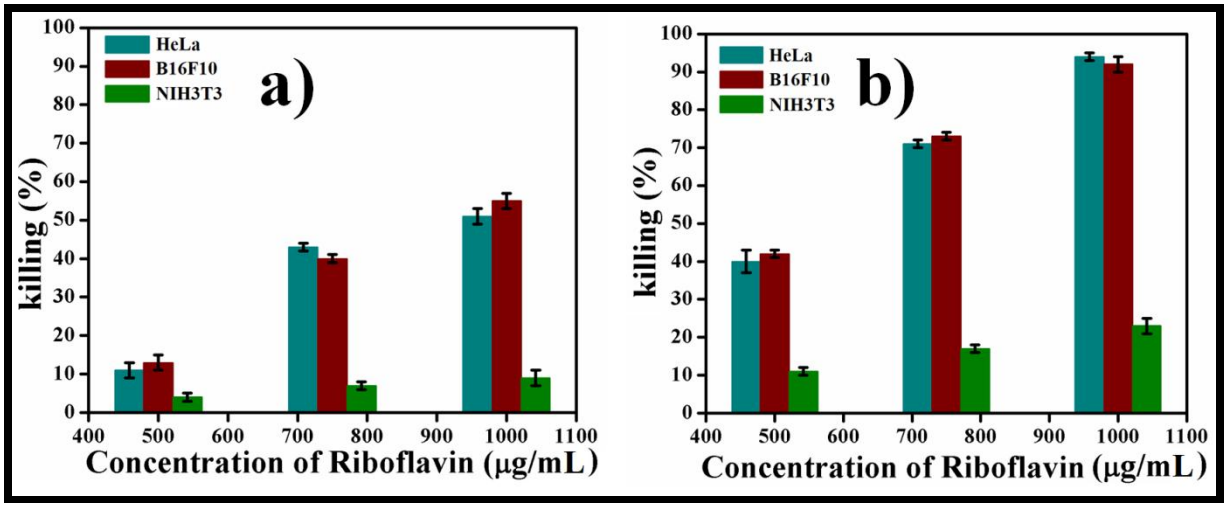

Figure 15. % Killing of HeLa, B16F10 and NIH3T3 cells incubated with varying concentrations of **RCD1s** where [riboflavin] = 500-1000 μg/mL and [**CD1s**] = 2.5-5.0 mg/mL for a) 6 h and b) 12 h. visible light exposure time = 10 min and wavelength of light = 460-490 nm. The standard deviation and experimental errors were in the range of 1-3% and 3-5% respectively in triplicate experiments.

MTT assay was also carried out in the presence of **RCD2s** and visible light to investigate the killing of both cancer cells and normal cells. HeLa, B16F10, and NIH3T3 cells were incubated with varying concentrations of **RCD2s** ([riboflavin] = 500-1000 μg/mL and [**CD2s**] = 2.5-5.0 mg/mL) for 12 h. The cells were then exposed to visible light (wavelength: 460-490 nm) for 10 min followed by incubation for another 12 h. The % killing of HeLa cells increased from 60 ± 2% to 92 ± 1% and that for B16F10 cells increased from 60 ± 1% to 93 ± 2% with increasing concentration of **RCD2s** from 500 to 1000 μg/mL (Figure 16). In contrast to the observation for **RCD1s**, the % killing of NIH3T3 cells by **RCD2s** was found to be significant, which increased from 58 ± 1% to 89 ± 2% with increasing concentration of **RCD2s** from 500 to 1000 μg/mL (Figure 16).

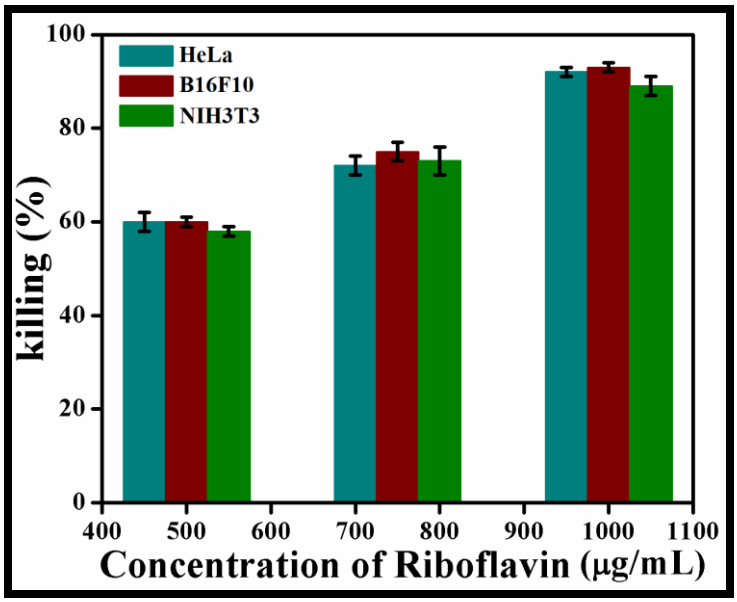

Figure 16. % Killing of HeLa, B16F10 and NIH3T3 cells incubated with varying concentrations of **RCD2s** where [riboflavin] = 500-1000 μg/mL and [**CD2s**] = 2.5-5.0 mg/mL for 12 h. Visible light exposure time = 10 min and wavelength of light = 460-490 nm. The standard deviation and experimental errors were in the range of 1-2% and 3-5%, respectively in triplicate experiments.

RCD2s killed both cancer cells and normal cells in the presence of mentioned visible light with similar efficiency due to the absence of biotin moiety on its surface (Figure 16). Consequently, there was no selectivity for **RCD2s** to be internalized only in cancer cells resulting in killing of both cancer and noncancerous cells. This observation further concludes that the presence of biotin is essential for distinguishing cancer cells over normal cells.

Furthermore, exposure time of light is an important parameter in the **RCD1s** mediated target specific killing of cancer cells. To investigate it, we again carried out MTT assay against HeLa, B16F10 melanoma cells, and noncancer NIH3T3 cells in different time exposures of light (1 min, 5 and 10 min) with a varying concentration range of **RCD1s** ([riboflavin] = 500-1000 μg/mL and [**CD1s**] = 2.5-5 mg/ mL) keeping all other experimental conditions identical. Irradiation of **RCD1s** included cells with visible light (460-490 nm) for 1 min led to 12 to 26% killing of HeLa cells and 5 to 28% killing of B16F10 cells upon increasing concentration of **RCD1s** from 500 to 1000 μg/mL. Similarly, killing of HeLa and B16F10 cells

increased from 31 to 82%, 34 to 81%, and 47 to 90%, 42 to 92% upon irradiation for 5 and 10 min, respectively (Figure 17a,b). In contrast, enhancement in the irradiation time from 1 to 10 min marginally increased the % killing from 3 to 15% to 11 to 23% with increasing concentration of **RCD1s** from 500 to 1000 µg/mL for NIH3T3 cell (Figure 17c). This clearly depicts that with increase in exposure time of light, the ROS mediated killing of cancer cells markedly improves by **RCD1s**.

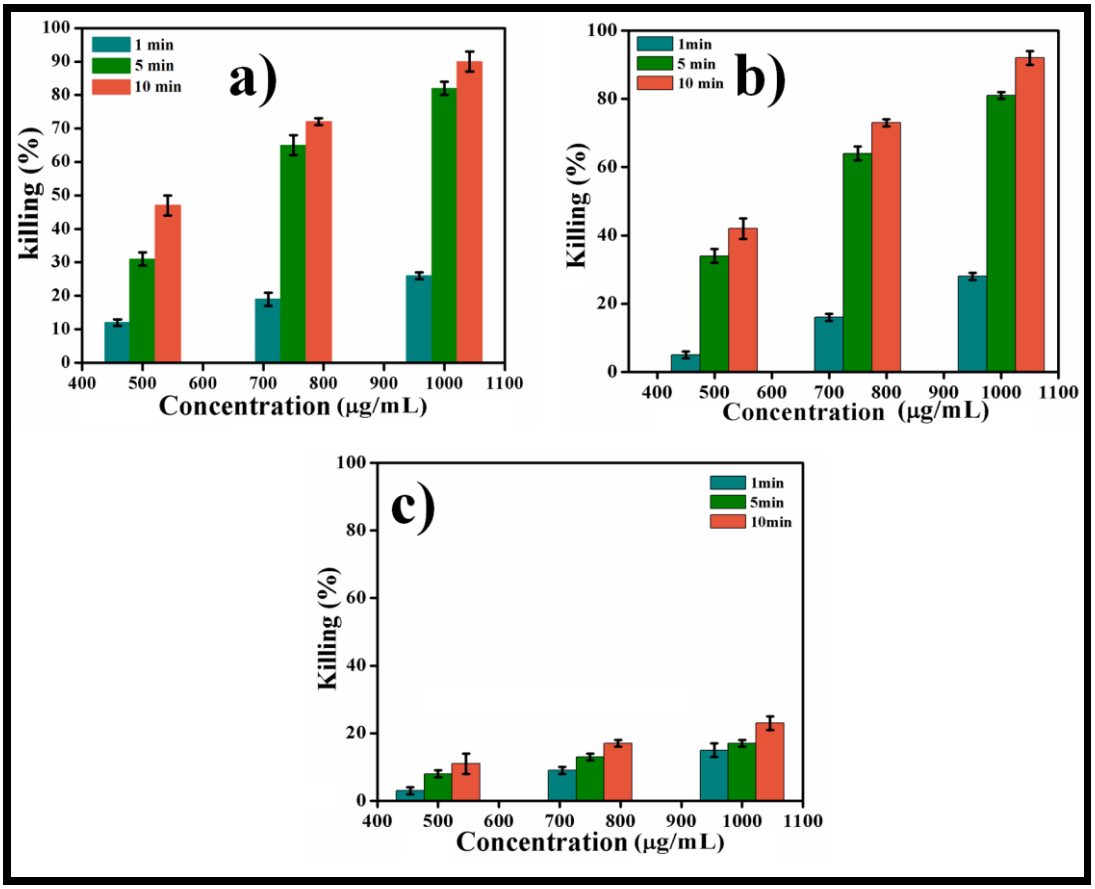

Figure 17. Percentage killing of a) HeLa b) B16F10 and c) NIH3T3 cells with varying concentrations of **RCD1s** where [riboflavin] = 500-1000 µg/mL, and [**CD1s**] = 2.5-5.0 mg/mL as well as varying exposure time of visible light. Wavelength of light = 460-490 nm. The standard deviation and experimental errors were in the range of 1-4% and 3-5%, respectively in triplicate experiments.

Along with this, in case of free riboflavin, only -10% killing of Hela, B16F10 and NIH3T3 was observed at 1000 µg/mL of riboflavin after 12 h treatment and 10 min exposure of visible light under similar experimental conditions (Figure 18).

This confirms the important role of biotinylated **CD1s** in selective and efficient killing of cancer cells.

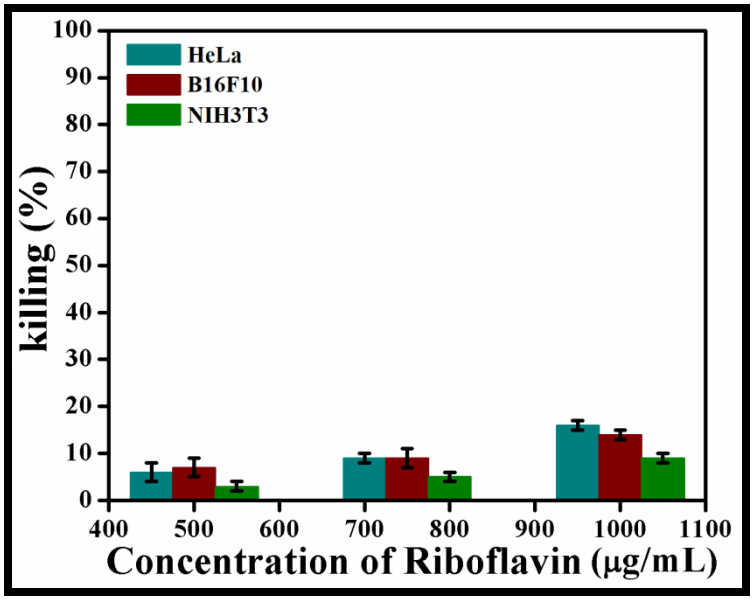

Figure 18. % Killing of HeLa, B16F10 and NIH3T3 cells incubated with varying concentrations of riboflavin where [riboflavin] = 500-1000 µg/mL for 12 h. Visible light exposure time = 10 min and wavelength of light = 460-490 nm. The standard deviation and experimental errors were in the range of 2-4% and 3-5%, respectively in triplicate experiments.

We also performed cancer cell killing experiment where the biotin-mediated specific transportation of **RCD1s** within HeLa and B16F10 cells was examined by pre-treating the cells with biotin. The biotin receptor positive cells (HeLa, B16F10) were pre-incubated with biotin solution (2 mM) for 1 h, and these treated cells were incubated with the **RCD1s** ([riboflavin] = 500-1000 µg/mL and [CD1s] = 2.5-5.0 mg/mL) for another 12 h. The cells were then exposed to visible light (wavelength: 460-490 nm) for 10 min followed by incubation for another 12 h. The % killing of HeLa cells observed from 15 ± 2% to 19 ± 2% and that for B16F10 cells from 14 ± 1% to 20 ± 3% where **RCD1s** concentration was varied from 500 to 1000 µg/ mL (Figure 19a,b). These experimental results showed that the extent of killing of biotin receptor positive cells (HeLa, B16F10) was significantly less as compared to that observed for the biotin-untreated HeLa and B16F10 cells (Figure 15). The pretreatment with the biotin probably led to the blocking of the overexpressed

biotin receptors in the biotin receptor positive cells (HeLa, B16F10) so that **RCD1s** could not be internalized in biotin-treated cancerous cells (HeLa, B16F10) significantly as compared to that biotin-untreated cancerous cells. These data suggest the biotin receptor-mediated internalization of **RCD1s**.

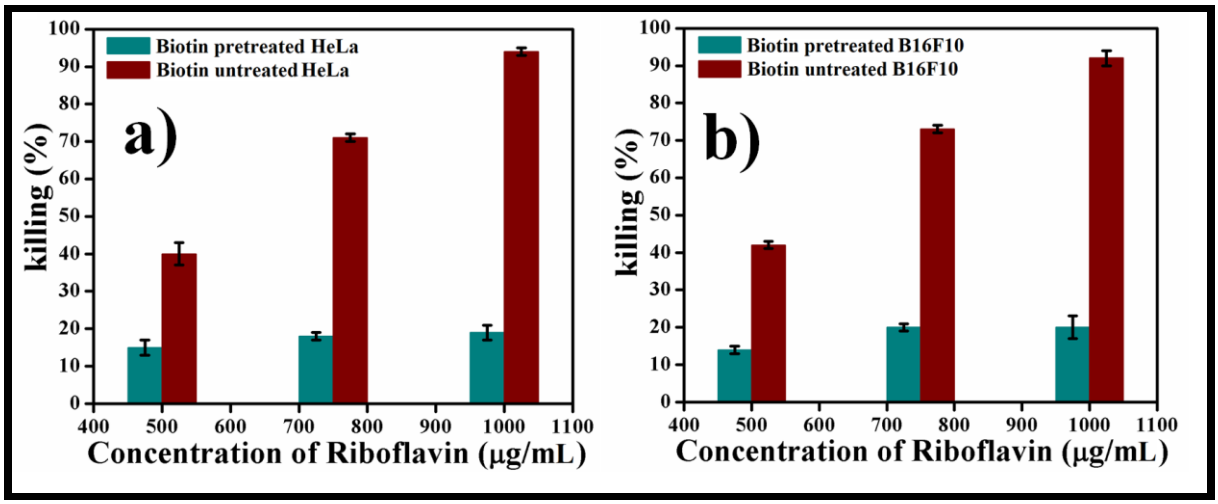

Figure 19. Percentage killing of biotin pre-treated and biotin untreated a) HeLa and b) B16F10 cells with varying concentrations of **RCD1s** where [riboflavin] = 500-1000 μg/mL, and [**CD1s**] = 2.5-5.0 mg/mL as well as varying exposure time of visible light. Concentration of free biotin solution was 2 mM. Wavelength of light = 460-490 nm. The standard deviation and experimental errors were in the range of 1-3% and 2-4%, respectively in triplicate experiments.

Next, HeLa, B16F10, and NIH3T3 cells pretreated (for 12 h) with ([riboflavin] = 500 μg/mL and [**CD1s**] = 2.5 mg/mL) were exposed to visible light for 10 min followed by another incubation of 12 h. Finally, the cells were treated with LIVE/ DEAD viability kit, and consequently, fluorescence images were recorded (Figure 20). Predominant presence of both green cells and red cells for cancerous HeLa and B16F10 cells indicates maximum presence of dead cells (Figure 20a-d). On the other hand, for the noncancer cell NIH3T3, maximum presence of only green cells and minimum presence of red cells indicate an abundance of alive cells (Figure 20e,f). Hence, the LIVE/DEAD assay further confirms the visible light triggered **RCD1s** mediated selective and efficient killing of cancer cells presumably through ROS mediated oxidative DNA damage in contrast to that of normal cells that are considerably viable toward light irradiated **RCD1s**.

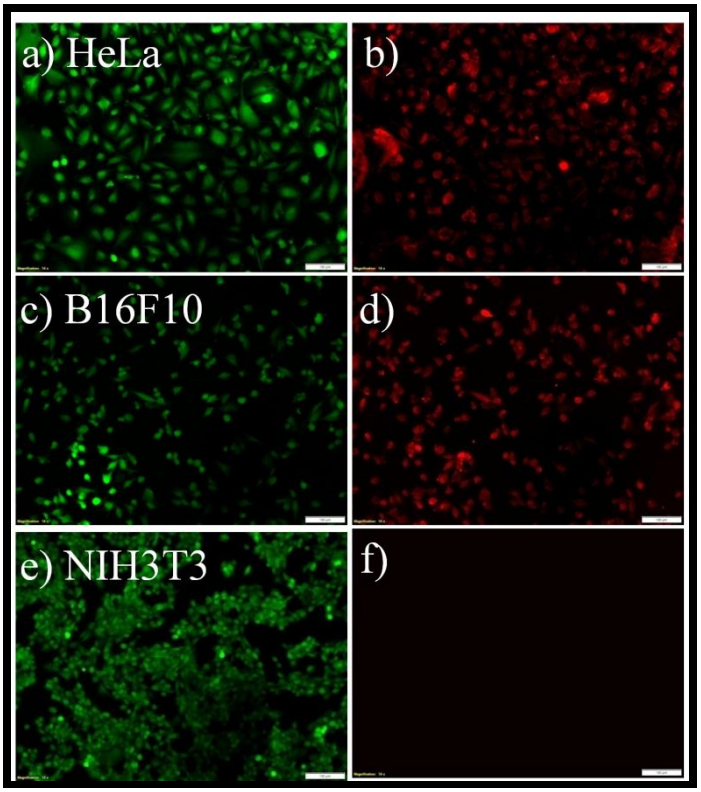

Figure 20. LIVE/DEAD fluorescence microscopic images of the cells incubated for 12 h with **RCD1s** where [riboflavin] = 500 μg/mL and [**CD1s**] = 2.5 μg/mL (a and b) HeLa cells, (c and d) B16F10 cells, (e and f) NIH3T3 cells. Scale bars correspond to 20 μm.

2.8 UV Light Induced Killing of Cancer Cells by RCD1s.

In the preceding sections, we observed the killing of cancer cells and normal cells in the presence of **RCD1s** and visible light (460-490 nm). Next, we were curious to know whether photoinduced generation of ROS and consequent killing of cancer cells is specific to visible light (460-490 nm). Consequently, we performed killing experiments via MTT assay for **RCD1s** triggered by UV light (340-420 nm) and also in the presence of only UV light for three cell lines, that is, HeLa, B16F10, and NIH3T3 normal cells. In the presence of both **RCD1s** ([riboflavin] = 1000 μg/mL and [**CD1s**] = 5 mg/mL) and UV light as well as in the presence of only UV light (340-420 nm), the % of killing varied from 8 to 21% irrespective of the nature of cells upon varying exposure time of light from 1 to 10 min (Figure 21). Hence, the

observed selective killing of cancer cells by biotinylated riboflavin tethered carbon dot, **RCD1s**, is specifically triggered by visible light (460-490 nm).

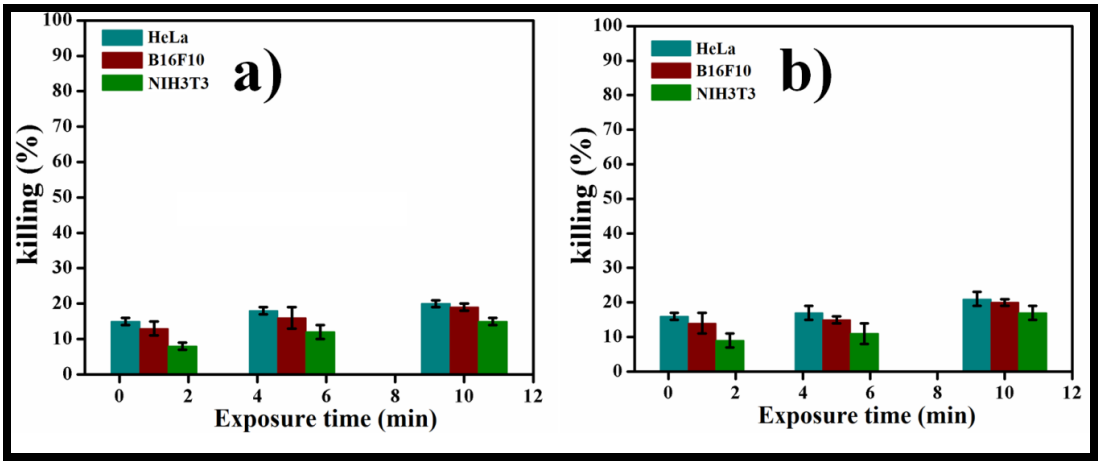

Figure 21. a) % Killing of HeLa, B16F10 and NIH3T3 cells incubated with **RCD1s** where [riboflavin] = 1000 μg/mL, and [**CD1s**] = 5.0 mg/mL for 12 h irradiated with UV light; b) HeLa, B16F10 and NIH3T3 cells irradiated with only UV light in absence of **RCD1s**. UV light exposure time = 1-10 min and wavelength of UV light = 390-420 nm. The standard deviation and experimental errors were in the range of 1-4% and 3-5% respectively, in triplicate experiments.

3.CONCLUSION

In summary, I have developed green emitting riboflavin tailored surface functionalized carbon dots (**RCD1s**) that selectively stain the cancer cell as well as target specifically killing the cancer cell in the presence of visible light. **RCD1s** has excellent stability in biological media and has remarkable cytocompatibility toward the mammalian cells. This newly designed **RCD1s** has a biotin moiety that facilitates its selective internalization within cancer cells, and the phenylboronic acid moiety helps to link the photosensitizer, riboflavin, via boronic acid-diol covalent linkage. In the presence of visible light (wavelength: 460-490 nm), **RCD1s** generates ROS (hydroxyl, superoxide radicals), which has the potential to damage the DNA structure via oxidative pathway. The presence of biotin on the surface of the riboflavin tethered carbon dot as well as the photoinduced generation of ROS by visible light (wavelength: 460-490 nm) was essential for the selective killing of cancer cells over normal cells. Thus, in the presence of visible light, **RCD1s** selectively killed the cancer cells specifically over normal cells. Hence, the newly developed **RCD1s** will have notable prospects in theranostic applications.

4.EXPERIMENTAL SECTION

4.1 Materials

Silica gel (60-120 mesh and 100-200 mesh), dicyclohexylcarbodiimide (DCC), 4-(N,N-dimethylamino) pyridine (DMAP), N-hydroxysuccinimide (NHS), trifluoroacetic acid, 4-carboxyphenylboronic acid, 1-ethyl-3-(3-(dimethylamino)propyl)-carbodiimide (EDC), pyridine, palladium 10% on activated charcoal, dimethylformamide (DMF), agarose for gel electrophoresis, ethidium bromide, Calf Thymus DNA, Celite545, citric acid, ethylenediamine, NaOH, Na2CO3, and rest of the reagents were purchased from SRL, India. All the studies were done using Milli-Q water. D-Biotin, Nα- Boc-Nε-Cbz-L-lysine, 1,3-diphenylisobenzophuran (DPBF), riboflavin, bromophenol blue, MTT (3-(4,5-dimethylthiazol-2-yl)-2,5-diphenyltetrazolium bromide), and other deuteriated solvents for NMR were purchased from Sigma-Aldrich. Dialysis tubing was procured from Thermo Scientific SnakeSkin (3.5K MWCO). Live- dead kit for eukaryotic cells was procured Genetix, India. Dulbecco's modified Eagle's medium (DMEM), heat inactivated fetal bovine serum (FBS), and trypsin from porcine pancreas were bought from Himedia. 1H NMR spectra were recorded in AVANCE 300 and Bruker spectrometers (500 MHz). Fluorescence spectra and UV- visible spectra were recorded in Varian Cary Eclipse luminescence spectrometer and PerkinElmer Lambda 25, respectively. Thermo Scientific Espresso was used for centrifugation. Zeta potential was measured in Nano-ZS of Malvern Instruments Limited. HeLa, NIH3T3, and B16F10 cells were procured from NCCS, Pune, India.

4.2 Synthesis of Native Carbon Dot (CD).

For the synthesis of native carbon dot (CD), 3.0 g of citric acid (14 mmol) and 0.84 g of ethylenediamine (14 mmol) were dissolved in 5 mL of Milli-Q water.[32]The solution was mixed and lyophilized to dry. The dried mass was heated for 2 h at 200 °C and then cooled to room temperature. The brownish-black mass was extracted with 1 N HCl, and the suspension was centrifuged for 30 min at 12 000

rpm to discard the residue. The supernatant was dried by lyophilization to obtain the CD with yield of ~65%.

4.3 Synthesis of Surface Modified Carbon Dots (CD1s, RCD1s, CD2s, and RCD2s).

In a typical experiment, Nα-Boc-Nε-Cbz-Lysine (1.0 equiv) (compound 1, Scheme 2) was taken. The C-terminal end of the amino acid was protected by esterification by stirring a methanolic mixture of the amino acid with dropwise addition of thionyl chloride ($SOCl_2$) (Scheme 2). This ester protected amino acid (compound 2) was then deprotected by trifluoroacetic acid (1.5 equiv) in dry DCM. After stirring for 4 h, the solvent was evaporated and dried. The dried mass was then dissolved in MeOH and treated with Na_2CO_3 (solid). The solution was then filtered and evaporated to get the free amine (compound 3). In a separate reaction, NHS linked biotin was synthesized by taking Dbiotin (1 equiv), DCC (1.1 equiv), and NHS (1.1 equiv) in 10 mL of dry DMF, and the mixture was stirred overnight under N_2 atmosphere. To this NHS-biotin mixture, free amine (compound 3) and pyridine were added followed by stirring of the solution overnight. The DMF was distilled out, and the residue mixture was purified using silica gel (100-200 mesh) and chloroform/methanol as eluent to get pure compound 4. Pd on activated charcoal was added to the methanolic solution of compound 4 under hydrogen (H_2) atmosphere, and the reaction mixture was stirred overnight at room temperature to remove benzyl protection. The whole mixture was filtered in a Celite-545 column where hot methanol was used as eluent. Solvent was evaporated on a rotary evaporator and dried under high vacuum. Finally, crystallization from methanol/diethyl ether afforded the pure amine (compound 5). In another reaction, NHS linked 4-carboxyphenylboronic was synthesized by utilizing 4-carboxyphenylboronic acid, DCC (1.5 equiv), and NHS (1.1 equiv) in dry DMF, and the mixture was stirred overnight under N_2 atmosphere. To this NHS linked 4-carboxyphenylboronic acid, compound 5 and dry pyridine (excess) were added followed by stirring of the mixture overnight. The DMF was distilled out, and the residue mixture was purified through column chromatography by using silica gel (100-200 mesh) and chloroform/methanol as eluent to obtain pure compound 6.

Compound 6 was dissolved in methanol and hydrolyzed by stirring with NaOH (1N) for 14-16 h. Acidification of the reaction mixture was done with HCl (1N), and then this mixture was extracted with ethyl acetate followed by washing with brine. EtOAc part was dried over anhydrous sodium sulfate and evaporated to obtain the solid residue. The solid residue was purified through column chromatography using silica gel (60-120 mesh) and chloroform/methanol used as eluent to get the pure acid (compound F1).

Next, we took the mixture of native carbon dot (CD) (1 equiv), EDC (10 equiv), DMAP (10 equiv), and compound F1 (10 equiv) in dry DMF and stirred for whole night. The DMF was dried out under vacuum, and the crude was taken in DCM and filtered. The DCMpart filtrate was evaporated in rotary evaporator to obtain surface modified carbon dot, CD1. The terminal boronic acid of CD1 was then converted to corresponding sodium salt (i.e., CD1s) by adding 0.1(N) NaOH (standardized) to the methanolic solution of CD1. After little stirring, the solvent was removed by lyophilization in Virtis4KBTXL-75 freeze drier to get the Na-salt of CD1, that is, **CD1s** (Scheme 2). **CD1s** was then coupled with riboflavin simply by mixing with the weight ratio of 1:5 w/w for riboflavin and **CD1s**. The mixture was shaken for 15 min followed by dialysis (MWCO - 3.5K) against PBS buffer (pH = 7.4). The solution remained in the dialysis bag was taken out and lyophilized to get the riboflavin tethered carbon dot (**RCD1s**) (Scheme 2).

CHAPTER 1

Photosensitizer Tailored Surface Functionalized Carbon Dots…

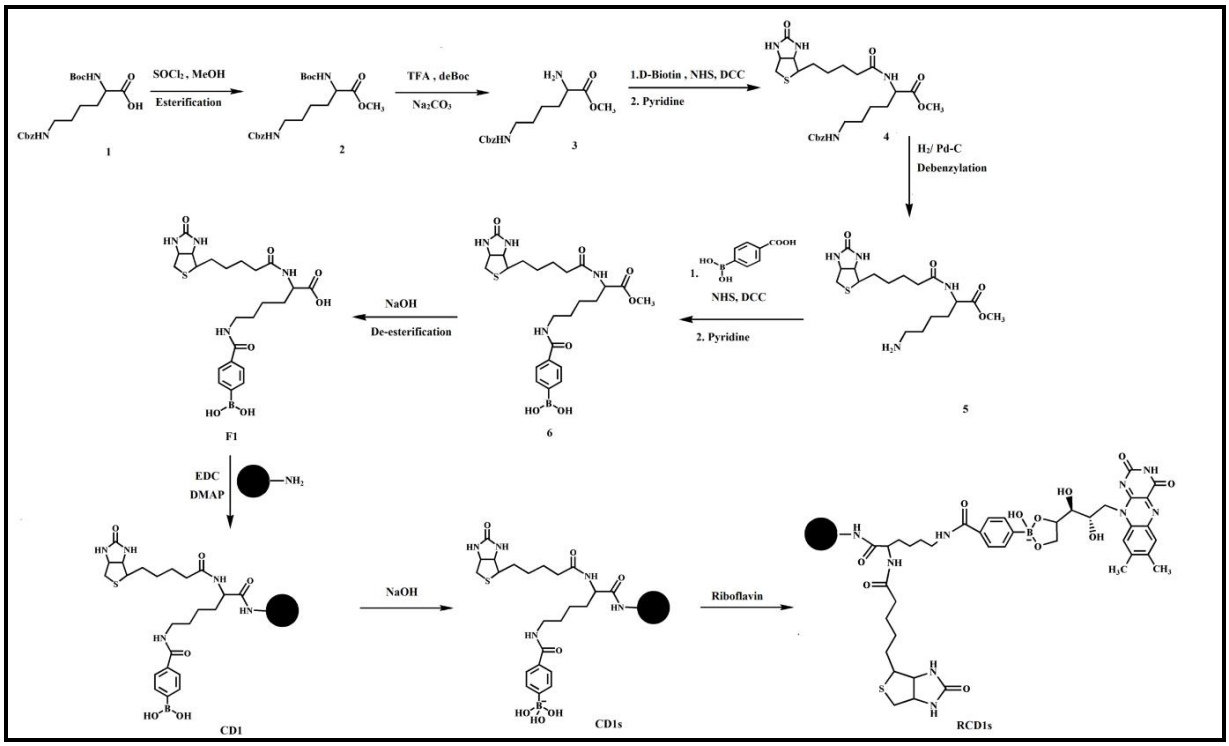

Scheme 2. Synthetic scheme of **CD1s** and **RCD1s**.

Now to synthesize **CD2s**, the ester protected amino acid (compound 2) was prepared in a similar way as mentioned in the preceding paragraph. Pd on activated charcoal was added to the methanolic solution of compound 2 under hydrogen (H_2) atmosphere, and the reaction mixture was stirred overnight at room temperature to remove the benzyl group (Scheme 3). The whole mixture was filtered in a Celite-545 column where hot methanol was used as eluent. Solvent was evaporated on a rotary evaporator and dried under high vacuum. Finally, crystallization from methanol/diethyl ether afforded the amine (compound 3a). In a similar way, NHS linked 4-carboxyphenylboronic acid was synthesized as mentioned above. To this NHS linked 4-carboxyphenylboronic acid, compound 3a and dry pyridine (excess) were added followed by stirring of the mixture overnight. The DMF was distilled out, and residue mixture was purified through column chromatography by using silica gel (100-200 mesh) and chloroform/methanol as eluent to obtain pure compound 4a. The obtained compound 4a was dissolved in methanol and hydrolyzed by stirring with NaOH (1N) for 14−16 h. Acidification of

the reaction mixture was done with HCl (1N), and then this mixture was extracted with EtOAc followed by washing with brine. EtOAc part was dried over anhydrous sodium sulfate and evaporated to obtain the solid residue. The solid residue was purified through column chromatography using silica gel (60−120 mesh) and chloroform/methanol used as eluent to get the pure acid (compound F2).**CD2s** was synthesized from compound F2 using similar method as **CD1s** (Scheme 3). **RCD2s** was also synthesized from CD2s using a similar experimental procedure using in the preparation of **RCD1s** (Scheme 3). Detailed characterization data of CD1s, RCD1s, and RCD2s have been provided in the characterization section with the corresponding NMR spectra.

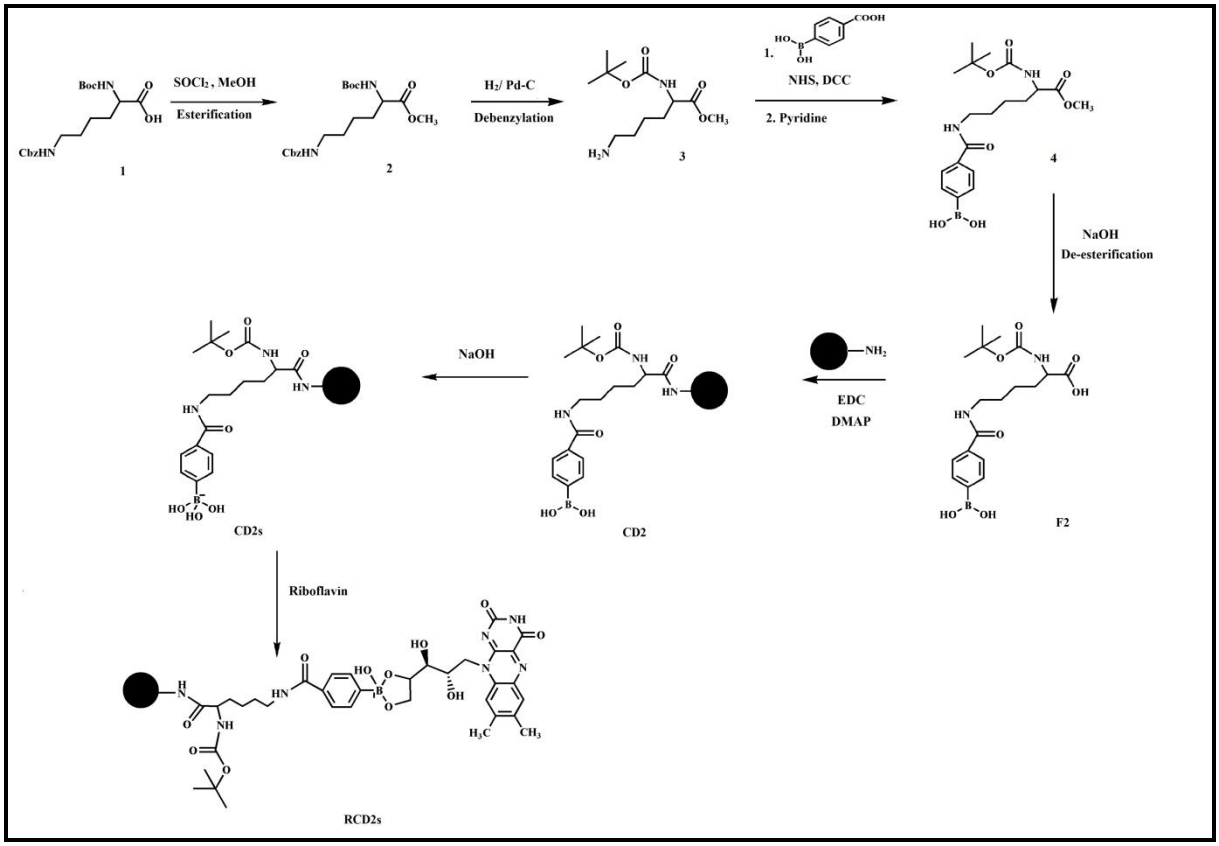

Scheme 3. Synthetic scheme of **CD2s** and **RCD2s**.

4.4 Characterization.

Sample preparation for TEM was performed by drop casting of **CD1s**, **RCD1s**, and RCD2s solutions on Cu-coated grids (300-mesh) and dried for 4 h before imaging in 2100F UHR microscope (JEOL JEM). For AFM, a drop of **CD1s** and **RCD1s** solution was put on fresh mica surfaces and air-dried overnight before taking images on Veeco, model AP0100 microscope (noncontact mode). For X-ray photoelectron spectroscopy (XPS), two drops of **CD1s**, **RCD1s**, and **RCD2s** solutions were cast on rectangular Cu plates and dried for 8 h before investigation in a X-ray photoelectron spectrometer (Omicron series 0571). X-ray diffraction (XRD) spectra of dried **CD1s** and **RCD1s** were obtained on a diffractometer (Bruker D8 Advance) having CuKα radiation (α = 0.15406 nm) as the source (voltage and current was 40 kV and 30 mA, respectively). Electron paramagnetic resonance (EPR) was done on a JEOL JES-FA 200 instrument.

4.5 UV–vis Spectroscopy.

Formation of **RCD1s** in different weight ratios of **CD1s** and riboflavin was followed by recording UV–vis spectra in a quartz cell (path length 10 mm). Sample temperature was fixed at 25 °C by a Peltier thermostat. For ROS generation, we recorded UV–vis spectra of 1,3-diphenylisobenzofuran (DPBF). Multiple sets of samples were used containing (i) only DPBF (20 μg/mL); (ii) **RCD1s** ([riboflavin] = 5 μg/mL and [**CD1s**] = 25 μg/ mL) with DPBF of same concentration; and (iii) the same concentration of RCD1s and DPBF irradiated with visible light (460-490 nm) of different exposure time (1-10 min). A similar experiment was also carried out using **RCD1s** and DPBF with 10 min exposure of visible light in the presence of thiourea (1-4 μM).

In case the **RCD1s** mediated ROS induced oxidative DNA damage experiments, we prepared four sets of conjugates by maintaining the same concentration of **RCD1s** as above and calf thymus CT-DNA (25 μg/mL) and a controlled set with only CT-DNA (25 μg/mL) in PBS buffer (pH = 7.4). We mixed the **RCD1s** and CT-DNA and shook the conjugates for 15 min. The light (460–490 nm) was then exposed on the conjugates with varying time from 1 to 10 min and another one remained

unexposed to light. In each case, the mixture was centrifuged to 12 000 rpm for 30 min. CT-DNA pellets were collected as residue and further dissolved in PBS buffer (pH = 7.4) solution. The UV spectra of these CT-DNA containing PBS buffer solutions were recorded.

4.6 Fluorescence Spectroscopy.

Excitation dependent emission spectra of **CD1s** (25 µg/mL) were recorded with varying λ_{ex} from 340 to 400 nm using excitation and emission slits at 10 nm. In case of **RCD1s** ([riboflavin] = 5 µg/mL and[**CD1s**] = 25 µg/mL), the fluorescence spectra were recorded at λ_{ex}, 340 nm and at λ_{ex}, 450 nm using similar excitation and emission slits as that of **CD1s**. In case of **RCD2s** ([riboflavin] = 5 µg/mL and [**CD2s**] = 25 µg/mL), the fluorescence spectra were recorded at λ_{ex}, 450 nm using similar excitation and emission slits as that of **CD1s**.

4.7 EPR Spectroscopy.

For EPR experiment, two sets of samples were prepared. The first set of **RCD1s** solution was prepared in Milli- Q water (1 mL) having [riboflavin] = 5 µg/mL and [**CD1s**] = 25 µg/ mL without exposure of light. The second set of RCD1s solution was prepared maintaining same experimental concentration followed by exposure of visible light for 10 min. Then 200 µL of two sets of solutions was taken separately in two EPR tubes, and EPR spectra of these solutions were measured at −80 °C temperature.

4.8 Gel Electrophoresis.

The 1% gel for the electrophoresis study was prepared by dissolution of agarose (900 mg) in 25 mL of 1x buffer (Tris-boric acid-EDTA). Ethidium bromide (2 µL, 1 mg/mL) was added in the agarose solution during the gel preparation. We prepared three solutions, (i) only CT-DNA (25 µg/mL) in PBS buffer (20 mM, pH = 7.4), (ii) mixture of CT-DNA (25 µg/mL) and **RCD1s** ([riboflavin] = 40 µg/mL and [**CD1s**] = 200 µg/mL) in PBS buffer (20 mM, pH = 7.4) with no light exposure, and (iii) mixture of CT-DNA and **RCD1s** having same concentration as above under exposure of light (10 min). Next, 5 µL of bromophenol blue (to track the CT-DNA) taken in 30% v/v glycerol was added to all sets of samples. Then 100 µL of each

solution was taken and separately loaded on to the agarose gel. The gel was run at E = 85 V cm−1 for 30 min, and an image of the gel was taken upon irradiation with UV light.

4.9 Media Stability of RCD1s.

Stability of **RCD1s** in biological media was investigated using [riboflavin] = 1000 µg/mL [**CD1s**] = 5 mg/mL. The solution was added to FBS containing DMEM media having a different concentration of FBS (0–75%), and it was kept for 2 days. The long time stability of **RCD1s** was investigated by addition of **RCD1s** solution ([riboflavin] = 1000 µg/mL [CD1s] = 5 mg/mL) to FBS containing DMEM media (10%), and the solutions were kept untouched for 10 days. In each case, the supernatant of the solution was taken at different time spans, and the absorbance of the supernatant was recorded at 295 nm to measure the suspension stability index (SSI).

SSI = $A_t/A_0 \times 100$ where A_t = absorbance of the solution after a specific time span at 295 nm, and A_0 = initial absorbance of the solution at 295 nm.

4.10 Cell Culture.

HeLa, B16F10, and NIH3T3 cells were cultured in FBS containing DMEM (10%) medium having antibiotic (100 mg/L streptomycin and 100 IU/mL penicillin). Cells were grown in cell culture flask and kept in a humidified condition (5% CO2 and 37 °C). Subculture was performed in every 2 days after 75% confluence of cultured cells. The adherent cells were detached from surface of culture flask by using trypsin. These cells were utilized for further cellular studies.

4.11 Bioimaging.

Cancer cells HeLa, B16F10, and noncancerous NIH3T3 cells were grown maintaining 104 cells per well in a chamber slide before the experiment. Cells were treated individually with **RCD1s** and **RCD2s** solution having [riboflavin] = 200 µg/mL and [**CD1s**] or [**CD2s**] = 1 mg/mL for 6 h. Treated cells were washed with PBS buffer and then fixed with paraformaldehyde (4%) for 30 min. Then glycerol solution (50%) was used to mount the cells on slide followed by covering the slide

with a coverslip and kept for 1 day. Images were taken in Olympus IX83 inverted microscope using an excitation filter of BP460-495 nm and a band absorbance filter covering wavelength below 505 nm at 40× magnification. Exposure time was <100 ms, and the microscopic object was 40 X UPIanFLN.

4.12 MTT Assay.

Cytocompatibility of **RCD1s** and **RCD2s** was examined by the microculture MTT reduction method. Herein, an insoluble colored formazan was produced from tetrazolium salt by mitochondrial dehydrogenase present in live cells. The amount of formazan produced was calculated spectrophotometrically, which is proportional to the number of alive cells. Prior to the assay, HeLa, B16F10, and NIH3T3 cells were separately cultured in a 96-well plate for a day with 15 000 cells per well. Cells were treated for 12 h at 37 °C under 5% CO_2 with varying concentrations of **RCD1s** where [riboflavin] = 500-1000 µg/mL and [**CD1s**] = 2.5-5 mg/mL and **RCD2s** where [riboflavin] = 500-1000 µg/mL and [**CD2s**] = 2.5-5 mg/mL. In case of cell viability assay using only riboflavin separately, the concentration of riboflavin was also varied from 500 to 1000 µg/ mL. The absorbance of produced formazan (dissolved in DMSO) was measured at 570 nm using BioTek Elisa Reader. The number of alive cells was expressed as following:

% viability = (A_{570} (treated cells)-background) /(A_{570}(untreated cells)-background) x 100 (1)

In case of killing experiment by **RCD1s** and **RCD2s**, MTT assay was performed as described above for the cells pretreated with **RCD1s** and **RCD2s** followed by exposure of visible light (460–490 nm) for 1–10 min in each well, and the cells were incubated for another 12 h. The number of surviving cells was analyzed following

eq 1.

Another controlled cell killing experiment was performed after pretreatment of excess biotin solution (2 mM) in HeLa and B16F10 cells. After that, the cells were again incubated with **RCD1s** for 12 h followed by exposure of visible light for 10 min in each well, and the wells were incubated for another 12 h. The number of surviving cells was analyzed following eq 1.

Cell killing experiment was also performed using **RCD1s** in the presence of UV light (340–420 nm) and under only UV light in absence **RCD1s** in HeLa, B16F10 cancer cells, and NIH3T3 normal cells. MTT assay was performed as described above for the cells pretreated with and without **RCD1s** followed by exposure of UV light for 1-10 min in each well, and the cells were incubated for another 12 h. The number of surviving cells expressed was analyzed following eq 1.

4.13 LIVE/DEAD Viability Assay.

Cytocompatibility of HeLa, B16F10, and NIH3T3 cells in the presence of **RCD1s** under exposure of visible light (10 min) was examined by LIVE/DEAD assay kit (for eukaryotic cells) as reported earlier. The LIVE/DEAD assay kit is composed of amixture of two nucleic acid binding stains, Calcein AM (acetomethoxy) (component A) and ethidium homodimer-1 (component B). The green fluorescence due to Calcein AM corresponds to live cells while red fluorescence due to ethidium homodimer-1 corresponds to dead cells. Just prior to assay, 4 µL of the supplied EthD-1 solution and 1 µL of the supplied calcein AM stock solution were mixed in 2 mL of PBS buffer, and the solution was vortexed. The resulting mixture was then added to **RCD1s** ([riboflavin] = 500 µg/mL and [**CD1s**] = 2.5 mg/mL), pretreated (for 12 h at 37 °C), and visible light (460-490 nm) irradiated (10 min) B16F10 and NIH3T3 cells and incubated for 30 min. Images of the cells were subsequently taken in Olympus IX83 microscope at 10× magnification. Excitation filter BP460-495 nm and a band absorbance filter covering wavelength below 505 nm were used for calcein intercalation. Excitation filter BP530-550 and a band absorbance filter covering wavelength below 570 nm were used for ethidium homodimer-1 intercalation.

5.CHARACTERIZATION DATA

5.1 Characterization of surface functionality of CD1s.

^{1}H NMR (500 MHz, TMS, D_2O, ppm): δ = 1.08- 1.12, 1.21- 1.31, 1.60- 1.73 (m, 10H, methelyne protons of D-biotin and L-lysine residue), 1.88 (s, 3H, B-$(OH)_3$), 2.22-2.23 (m, 2H, -CH_2-CH_2-CH-CO-NH- of L- lysine), 2.31-2.39 (m, 2H, -CH_2-CO- of D-

biotin), 3.07-3.14 (m, 2H, -C<u>H</u>$_2$-S- of D-biotin), 3.45-3.52 (m, 2H, -C<u>H</u>$_2$-NH-CO- of L- lysine), 3.65-3.69 (m,1H, -C<u>H</u>-S- of D-biotin), 4.73-4.83 (m, 1H, chiral proton of L-lysine moiety and 2H, -NH-C<u>H</u>-C<u>H</u>-NH- of D-biotin; peaks have overlapped with solvent peak), 6.62-6.63 and 8.04-8.05 (d, 4H aromatic proton of phenyl boronic acid unit).

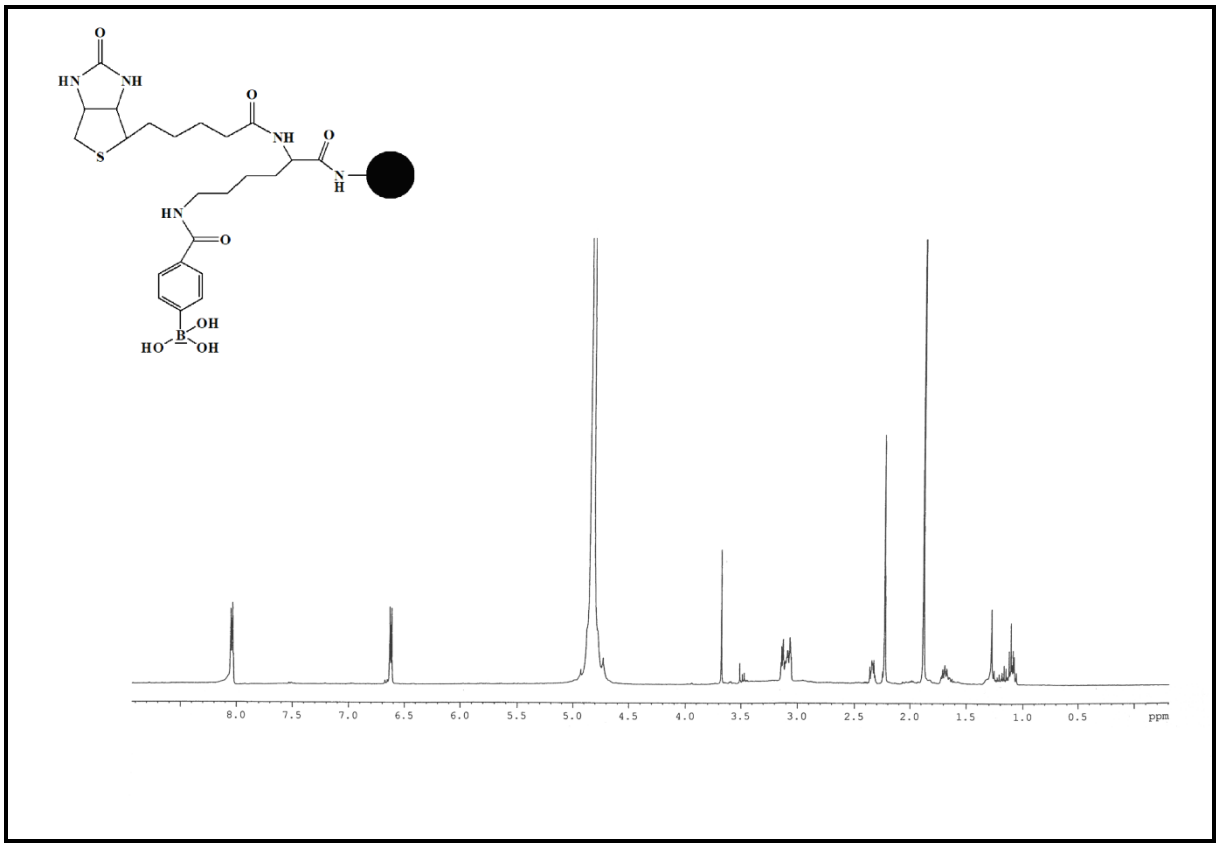

5.2 Characterization of surface functionality of RCD1s.

^{1}H NMR (500 MHz, TMS, D2O, ppm): δ = 1.08- 1.12, 1.21- 1.31, 1.60- 1.73 (m, 10H, methelyne protons of D-biotin and L-lysine residue), 1.88 (s, 3H, B-(OH)3), 2.22-2.23 (m, 2H, -CH2-C<u>H</u>2-CH-CO-NH- of L- lysine), 2.31-2.39 (m, 8H, -C<u>H</u>2-CO- of D-biotin and benzyl protons of riboflavin), 3.07-3.14 (m, 2H, -C<u>H</u>2-S- of D-biotin and 1H of -C<u>H</u>2-N- of riboflavin), 3.37-3.41 (m, 1H, -C<u>H</u>2-N- of riboflavin and 1H, -C<u>H</u>-CH-CH2-N- of riboflavin), 3.45-3.52 (m, 2H, -C<u>H</u>2-NH-CO- of L- lysine), 3.55-3.57 (m, 1H, -CH-C<u>H</u>-CH2-N- of riboflavin), 3.59-3.62 (m, 1H, -C<u>H</u>-O-B- of riboflavin), 3.65-3.69 (m, 1H, -C<u>H</u>-S- of D-biotin), 3.93-3.95 and 4.19-4.22 (m, 2H,

-CH2-O-B- of riboflavin) 4.73-4.83 (m, 1H, chiral proton of L-lysine moiety and 2H, -NH-CH-CH-NH- of D-biotin; peaks have overlapped with solvent peak), 5.92 (s, 1H, aromatic proton of benzene unit of riboflavin), 6.62-6.63 (d, 2H aromatic proton of phenyl boronic acid unit), 6.75 (s, 1H, aromatic proton of benzene unit of riboflavin), 8.04-8.05 (d, 2H aromatic proton of phenyl boronic acid unit.

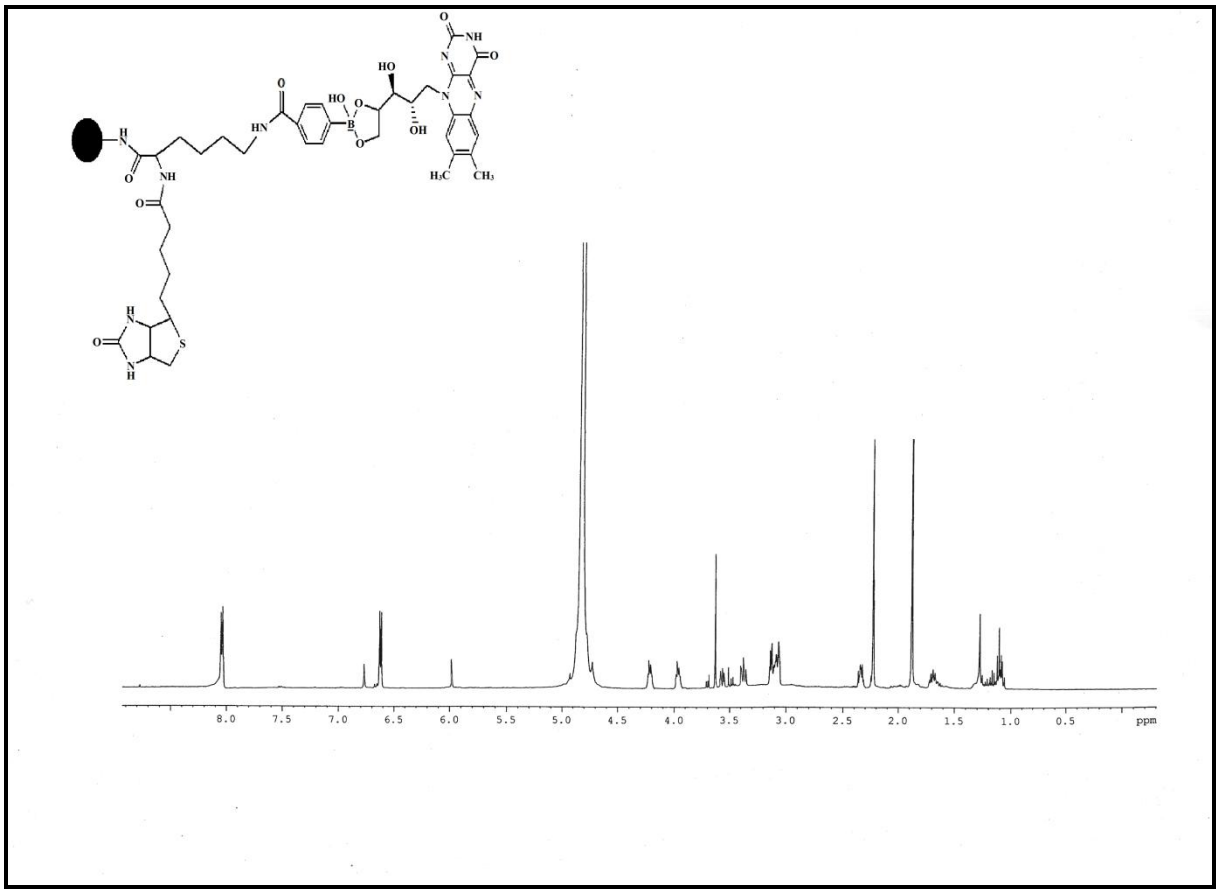

5.3 Characterization of surface functionality of RCD2s

^{1}H NMR (500 MHz, TMS, D_2O, ppm): δ = 1.21- 1.30, (m, 4H, methelyne protons L-lysine residue) 1.52 - 1.54 (s, 9H, methyl protons of boc.), 1.88 (s, 1H, B-$(OH)_3$), 2.22-2.23 (m, 2H, -CH_2-CH_2-CH-CO-NH- of L- lysine), 2.38 (s, 6H, benzyl protons of riboflavin), 3.14-3.22 (m, 2H, -CH_2-NH-CO- of L- lysine and 1H of -CH_2-N- of riboflavin), 3.38-3.40 (m, 1H, -CH_2-N- of riboflavin and 1H, -CH-CH_2-N- of riboflavin), 3.55-3.60 (m, 1H, -CH-CH-CH_2-N- of riboflavin and 1H, -CH-O-B- of riboflavin), 3.93-3.97 and 4.19-4.24 (m, 2H, -CH_2-O-B- of riboflavin) 4.7-4.73 (m,

1H, chiral proton of L-lysine moiety; peaks have overlapped with solvent peak), 5.94 (s, 1H, aromatic proton of benzene unit of riboflavin), 6.69-7.00 (d, 2H aromatic proton of phenyl boronic acid unit), 6.75 (s, 1H, aromatic proton of benzene unit of riboflavin), 7.7-7.8 (d, 2H aromatic proton of phenyl boronic acid unit).

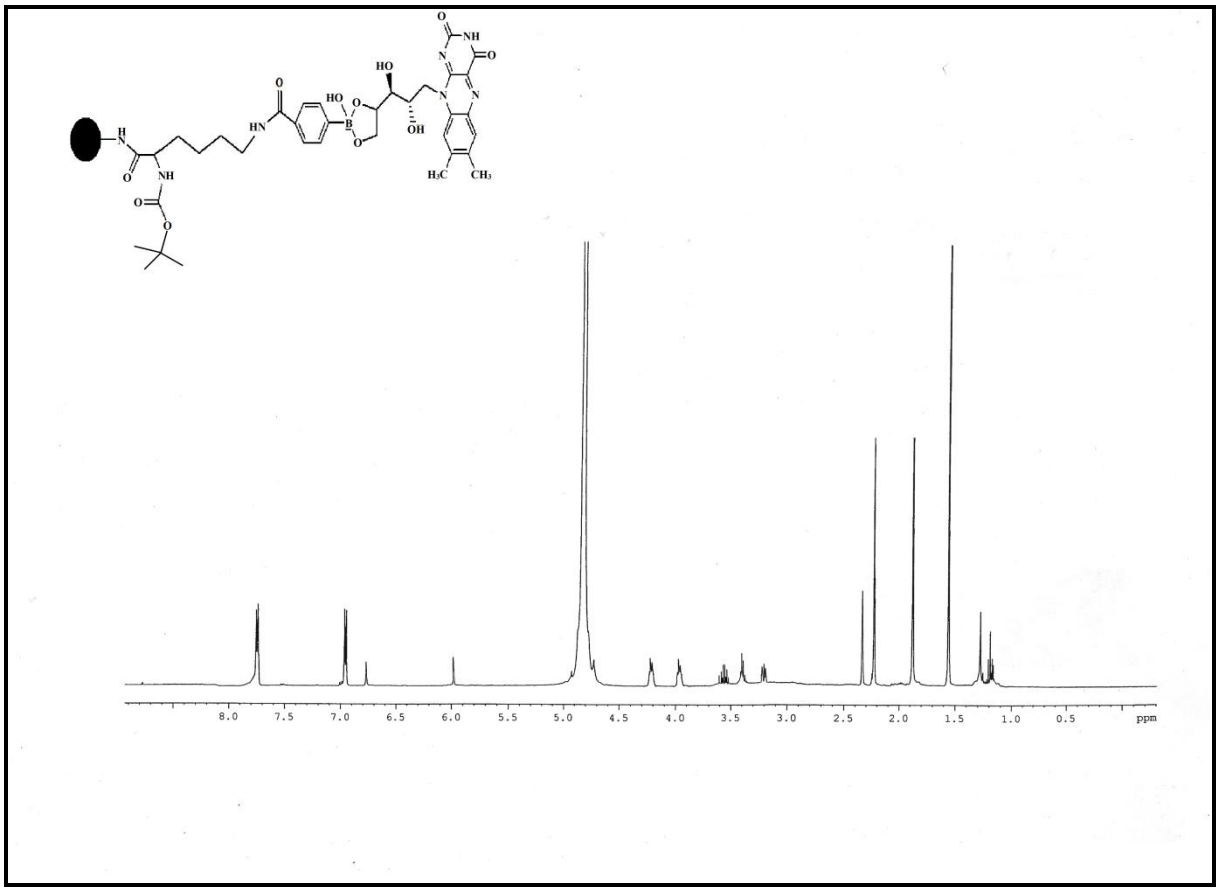

6.REFERENCES

1. Maverakis, E.; Cornelius, L. A.; Bowen, G. M.; Phan, T.; Patel, F. B.; Fitzmaurice, S.; He, Y.; Burrall, B.; Duong, C.; Kloxin, A. M.; Sultani, H.; Wilken, R.; Martinez, S. R.; Patel, F. Metastatic Melanoma–A Review of Current and Future Treatment Options. *Acta Derm Venereol* **2015**, *95*, 516-524.
2. Delaney, G.; Barton, M.; Jacob, S. Estimation of an Optimal Radiotherapy Utilization Rate for Melanoma. *Cancer* **2004**, *100*, 1293-1301.
3. Cumberlin, R.; DeMoss, E.; Lassus, M.; Friedman, M. Isolation Perfusion for Malignant Melanoma of The Extremity: A Review. *J. Clin. Oncol.* **1985**, *3*, 1022-1031.
4. Win-Piazzaa, H.; Schneebergera, V.; Chena, L.; Pernazzac, D.; Lawrencec, H. R.; Sebtib, S. M.; Lawrencec, N. J.; Wu, J. Enhanced Anti-Melanoma Efficacy of Interferon Alfa-2b via Inhibition of Shp2. *Cancer Lett.* **2012**, *320*, 81-85.
5. Wlassoff, W. A.; Albright, C. D.; Sivashinski, M. S.; Ivanova, A.; Appelbaum, J.G.; Salganik, R. I. Hydrogen Peroxide Overproduced in Breast Cancer Cells can Serve as an Anticancer Prodrug Generating Apoptosis-Stimulating Hydroxyl Radicals under the Effect of Tamoxifen-Ferrocene Conjugate. *J. Pharm. Pharmacol.* **2007**, *59*, 1549-1553.
6. Chakraborty, D.; Sarkar, S.; Das, P. K. Blood Dots: Hemoglobin-Derived Carbon Dots as Hydrogen Peroxide Sensors and Pro-Drug Activators. *ACS Sustainable Chem. Eng.* **2018**, *6*, 4661-4670.
7. Nagababu, E.; Rifkind, J. M. Reaction of Hydrogen Peroxide with Ferrylhemoglobin: Superoxide Production and Heme Degradation. *Biochemistry* **2000**, *39*, 12503-12511.
8. Luo, Y.; Henle, E. S.; Linn, S. Oxidative Damage to DNA Constituents by Iron-Mediated Fenton Reactions. *J. Biol. Chem.* **1996**, *271*, 21167-21176.
9. Salganik, R. I.; Albright, C. D.; Rodgers, J.; Kim, J.; Zeisel, S. H.; Sivashinskiy, M.; Van Dyke, T. A. Dietary Antioxidants Depletion: Enhancement of Tumor Apoptosis and Inhibition on Brain Tumor Growth in Transgenic Mice. *Carcinogenesis* **2000**, *21*, 909-914.

10. Wang, Y.; Wang, H.; Liu, D.; Song, S.; Wang, X.; Zhang, H. Graphene Oxide Covalently Grafted Upconversion Nanoparticles for Combined NIR Mediated Imaging and Photothermal/Photodynamic Cancer Therapy. *Biomaterials* **2013**, *34*, 7715-7724.

11. Oberley, T. D.; Oberley, L. W. Antitumor Enzyme Level in Cancer. *Histol. Histopathol.* **1997**, *12*, 525-535.

12. Biswas, A.; Chakraborty, A.; Jana, N. R. Nitrogen and Fluorine Codoped, Colloidal TiO_2 Nanoparticle: Tunable Doping, Large Red-Shifted Band Edge, Visible Light Induced Photocatalysis, and Cell Death. *ACS Appl. Mater. Interfaces* **2018**, *10*, 1976-1986.

13. Qian, H. S.; Guo, H. C.; Ho, P. C. L.; Mahendran, R.; Zhang, Y. Mesoporous-Silica-Coated Up-Conversion Fluorescent Nanoparticles for Photodynamic Therapy. *Small* **2009**, *5*, 2285-2290.

14. Wang, C.; Tao, H.; Liang, C.; Zhuang, L. Near-Infrared Light Induced in Vivo Photodynamic Therapy of Cancer Based on Upconversion Nanoparticles. *Biomaterials* **2011**, *32*, 6145-6154.

15. Agostinis, P.; Berg, K.; Cengel, K. A.; Foster, T. H.; Girotti, A. W.; Gollnick, S. O.; Hahn, S. M.; Hamblin, M. R.; Juzeniene, A.; Kessel, D.; Korbelik, M.; Moan, J.; Mroz, P.; Nowis, D.; Piette, J.; Wilson, B. C.; Golab, J. Photodynamic Therapy of Cancer: An Update. *CA Cancer J. Clin.* **2011**, *61*, 250-281.

16. Zhao, B.; He, Y.Y. Recent Advances in the Prevention and Treatment of Skin Cancer using Photodynamic Therapy. *Expert Rev. Anticancer Ther.* **2010**, *10*, 1797-1809.

17. Ware, M. A.; Daeninck, P.; Maida, V. A Review of Nabilone in the Treatment of Chemotherapy-Induced Nausea and Vomiting. *Ther Clin Risk Manag* **2008**, *4*, 1-9.

18. Brancaleon, L.; Moseley, H. Laser and Non-Laser Light Sources for Photodynamic Therapy. *Lasers Med Sci.* **2002**, *17*, 173-186.

19. McNaught, A. D.; Wilkinson, A. *Compendium of Chemical Terminology, 2nd ed.* Blackwell Scientific Publications: Oxford, U.K., 1997.

20. Zhanga, J.; Jianga, C.; Longo, J. P. F.; Azevedo, R. B.; Zhanga, H.; Muehlmann, L. A. An Updated Overview on the Development of New Photosensitizers for Anticancer Photodynamic Therapy. *Acta Pharm Sin B* **2018**, *8*, 137-146.

21. Hamblin, M. R. Fullerenes as Photosensitizers in Photodynamic Therapy: Pros and Cons. *Photochem. Photobiol. Sci.* **2018**, *17*, 1515-1533.

22. Diaz, M. G.; Huang, Y. Y.; Hamblin, M. R. Use of Fluorescent Probes for ROS to Tease Apart Type I and Type II Photochemical Pathways in Photodynamic Therapy. *Methods* **2016**, *109*, 158-166.

23. Buchalska, M.; Łabuz, P.; Bujak, Ł.; Szewczyk, G.; Sarna, T.; Maćkowski, S.; Macyk, W. New Insight into Singlet Oxygen Generation at Surface Modified Nanocrystalline TiO_2 – The Effect of Near-Infrared Irradiation. *Dalton Trans.* **2013**, *42*, 9468.

24. Zhou, Z.; Song, J.; Nie, L.; Chen, X. Reactive Oxygen Species Generating Systems Meeting Challenges of Photodynamic Cancer Therapy. *Chem. Soc. Rev.* **2016**, *45*, 6597-6626.

25. Hadjur, C.; Wagnieres, G.; Ihringer, F.; Monnier, P.; Bergh, H. V. D. Production of the Free Radicals $O_2^{\bullet-}$ and $^{\bullet}OH$ by Irradiation of the Photosensitizer Zinc (II) Phthalocyanine. *J. Photochem. Photobiol. B* **1997,** *38*, 196-202.

26. Pan, L.; Liu, J.; Shi, J. Intranuclear Photosensitizer Delivery and Photosensitization for Enhanced Photodynamic Therapy with Ultralow Irradiance. *Adv. Funct. Mater.* **2014**, *24*, 7318-7327.

27. Allison, R. R.; Sibata, C. H. Phd Oncologic Photodynamic Therapy Photosensitizers: A Clinical Review. *Photodiagnosis Photodyn Ther* **2010**, *7*, 61-75.

28. Li, X.; Lee, S.; Yoon, J. Supramolecular Photosensitizers Rejuvenate Photodynamic Therapy. *Chem. Soc. Rev.* **2018**, *47*, 1174-1188.

29. Sharman, W. M.; Allen, C. M.; Van Lier, J. E. Photodynamic Therapeutics: Basic Principles and Clinical Applications. *Drug Discov. Today*. **1999**, *4*, 507-17.

30. Triesscheijn, M.; Baas, P.; Schellens, J. H. M.; Stewarta, F. A. Photodynamic Therapy in Oncology. *The Oncologist* **2006**, *11*, 1034-1044.

31. Baker, S. N.; Baker, G. A. Luminescent Carbon Nanodots: Emergent Nanolights. *Angew. Chem., Int. Ed.* **2010**, *49*, 6726-6744.

32. Sarkar, S.; Das, K.; Das, P. K. Estradiol Hemisuccinate-Modified Surface-Engineered Carbon Dots: Target-Specific Theranostic Agent. *ACS Sustainable Chem. Eng.* **2017**, *5*, 8356-8369.

33. Datta, K. K. R.; Qi, G.; Zboril, R.; Giannelis, E. P. Yellow Emitting Carbon Dots with Superior Colloidal, Thermal, and Photochemical Stabilities. *J. Mater. Chem. C* **2016**, *4*, 9798-9803.

34. Cao, L.; Wang, X.; Meziani, M. J.; Lu, F. S.; Wang, H. F.; Luo, P. G.; Lin, Y.; Harruff, B. A.; Veca, L. M.; Murray, D.; Xie, S. Y.; Sun, Y. P. Carbon Dots for Multiphoton Bioimaging. *J. Am. Chem. Soc.* **2007**, *129*, 11318-11319.

35. Bourlinos, A. B.; Stassinopoulos, A.; Anglos, D.; Zboril, R.; Karakassides, M.; Giannelis, E. P. Surface Functionalized Carbogenic Quantum Dots. *Small* **2008**, *4*, 455-458.

36. Maleki, A. Fe_3O_4/SiO_2 Nanoparticles: An Efficient And Magnetically Recoverable Nanocatalyst for the One-Pot Multicomponent Synthesis of Diazepines. *Tetrahedron* **2012**, *68*, 7827-7833.

37. Maleki, A.; Movahed, H.; Ravaghi, P. Magnetic Cellulose/Ag as a Novel Eco-Friendly Nanobiocomposite to Catalyze Synthesis of Chromene-Linked Nicotinonitriles. *Carbohydrate Polymers* **2017**, *156*, 259-267.

38. Maleki, A. Green Oxidation Protocol: Selective Conversions of Alcohols and Alkenes to Aldehydes, Ketones and Epoxides by Using a New Multiwall Carbon Nanotube based Hybrid Nanocatalyst via Ultrasound Irradiation. *Ultrasonics – Sonochemistry* **2018**, *40*, 460-464.

39. Wang, Y.; Wang, H.; Liu, D.; Song, S.; Wang, X.; Zhang, H. Graphene Oxide Covalently Grafted Upconversion Nanoparticles for Combined NIR Mediated Imaging and Photothermal/Photodynamic Cancer Therapy. *Biomaterials* **2013**, *34*, 7715-7724.

40. Maleki, A.; Rahimi, R.; Maleki, S. Efficient Oxidation and Epoxidation Using a Chromium(VI)-Based Magnetic Nanocomposite. *Environ. Chem. Lett.* **2016**, *14*, 195-199.

41. Feng, T.; Ai, X.; An, G.; Yang, P.; Zhao, Y. Charge-Convertible Carbon Dots for Imaging-Guided Drug Delivery with Enhanced In Vivo Cancer Therapeutic Efficiency. *ACS Nano* **2016**, *10*, 4410-4420.

42. Gong, X.; Zhang, Q.; Gao, Y.; Shuang, S.; Choi, M. M. F.; Dong, C. Phosphorus and Nitrogen Dual-Doped Hollow Carbon Dot as a Nanocarrier for Doxorubicin Delivery and Biological Imaging. *ACS Appl. Mater. Interfaces* **2016**, *8*, 11288−11297.

43. Zheng, M.; Li, Y.; Liu, S.; Wang, W.; Xie, Z.; Jing, X. One-Pot to Synthesize Multifunctional Carbon Dots for Near Infrared Fluorescence Imaging and Photothermal Cancer Therapy. *ACS Appl. Mater. Interfaces* **2016**, *8*, 23533−23541.

44. Wang, H.; Mukherjee, S.; Yi, J.; Banerjee, P.; Chen, Q.; Zhou, S. Biocompatible Chitosan−Carbon Dot Hybrid Nanogels for NIR Imaging-Guided Synergistic Photothermal−Chemo Therapy. *ACS Appl. Mater. Interfaces* **2017**, *9*, 18639−18649.

45. Maleki, A.; Kari, T. Novel Leaking-Free, Green, Double Core/Shell, Palladium-Loaded Magnetic Heterogeneous Nanocatalyst for Selective Aerobic Oxidation. *Catal. Let.* **2018**,*148*, 2929–2934.

46. Garu, A.; Moku, G.; Gulla, S. K.; Chaudhuri, A. Genetic Immunization with In Vivo Dendritic Cell-Targeting Liposomal DNA Vaccine Carrier Induces Long-Lasting Antitumor Immune Response. *Mol. Ther*. **2016**, *24*, 385-397.

47. Reddy, B. S.; Banerjee, R. 17b-Estradiol-Associated Stealth-Liposomal Delivery of Anticancer Gene to Breast Cancer Cells. *Angew. Chem., Int. Ed.* **2005**, *44*, 6723-6727.

48. Brahmachari, S.; Ghosh, M.; Dutta S.; Das, P. K. Biotinylated Amphiphile-Single Walled Carbon Nanotube Conjugate for Target-Specific Delivery to Cancer Cells. *J. Mater. Chem. B* **2014**, *2*, 1160-1173.

49. Yang, W.; Cheng, Y.; Xu, T.; Wang, X.; Wen, L. Targeting Cancer Cells with Biotin-Dendrimer Conjugates. *Eur. J. Med.* **2009**, *44*, 862-868.

50. Dinda, S.; Sarkar, S.; Das, P. K. Glucose Oxidase Mediated Targeted Cancer Starving Therapy by Biotinylated Self-Assembled Vesicles. *Chem. Commun.* **2018**, *54*, 9929-9932.

51. Ahmeda, K. K.; Gearya, S. M.; Salema, A. K. Surface Engineering Tumor Cells with Adjuvant-Loaded Particles for Use as Cancer Vaccines. *J. Control. Release* **2017**, *248*, 1-9.

52. Ojima, I. Guided Molecular Missiles for Tumor-Targeting Chemotherapy-Case Studies using the Second-Generation Taxoids as Warheads. *Acc. Chem. Res.* **2008**, *41*, 108-119.

53. Zhong, Y.; Meng, F.; Deng, C.; Zhong, Z. Ligand-Directed Active Tumor-Targeting Polymeric Nanoparticles for Cancer Chemotherapy. *Biomacromolecules* **2014**, *15*, 1955-1969.

54. Yellepeddi, V. K.; Kumar, A.; Palakurthi, S. Biotinylated Poly(Amido)Amine (PAMAM) Dendrimers as Carriers for Drug Delivery to Ovarian Cancer Cells in Vitro. *Anticancer Research* **2009**, *29,* 2933-2944.

55. Brooks, W. L. A.; Sumerlin, B. S. Synthesis and Applications of Boronic Acid-Containing Polymers: From Materials to Medicine. *Chem. Rev.* **2016**, *116*, 1375-1397.

56. Kubo, Y.; Nishiyabu, R.; James, T. D. Hierarchical Supramolecules and Organization using Boronic Acids Building Blocks. *Chem. Commun.* **2015**, *51*, 2005-2020.

57. Wang, S.; Jing, X.; Wang, Y.; Si, J. High Char Yield of Aryl Boron-Containing Phenolic Resins: The Effect of Phenylboronic Acid on the Thermal Stability and Carbonization of Phenolic Resins. *Polym. Degrad. Stab.* **2014**, *99*, 1-11.

58. Matushek, M. G.; Bonten, M. J. M.; Hayden M. K. Rapid Preparation of Bacterial DNA for Pulsed-Field Gel Electrophoresis. *J. Clin. Microbiol.* **1996**, *34*, 2598-2600.

CHAPTER 2

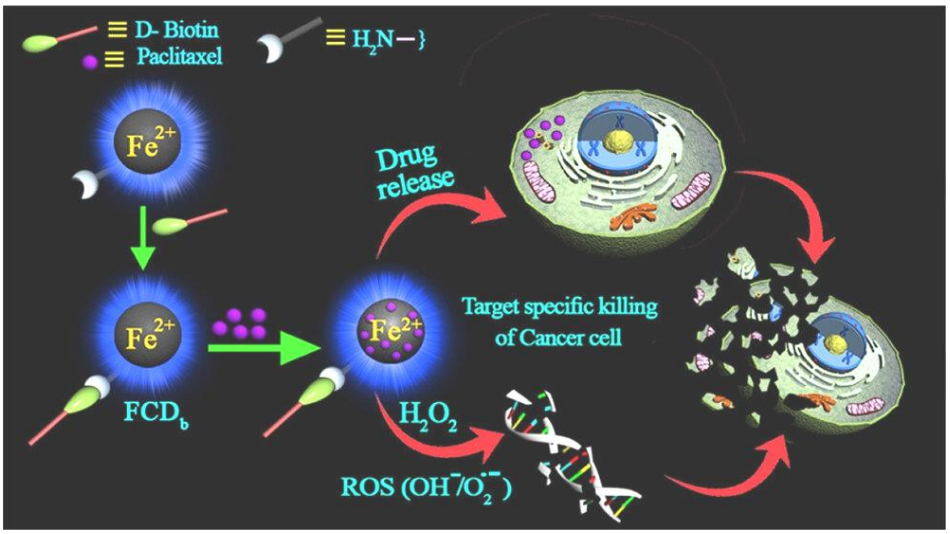

Paclitaxel-Loaded Biotinylated Fe^{2+}-Doped Carbon Dot: Combination Therapy in Cancer Treatment

CHAPTER 2

Paclitaxel-Loaded Biotinylated Fe^{2+}-Doped Carbon Dot…

1.INTRODUCTION

Cancer, a multidimensional challenge, has been spreading its clutches globally since many decades. Multitudinous approaches like surgery, immunotherapy, chemotherapy, etc. are being used in the past few decades, yet complete curbing of this deadly disease remains challenging.[1-4]The shortfall of selectivity against cancer cells, toxic side effects, and limited procedures for the clinical use of single drug are the major limitations in cancer therapy.[5,6] Any particular anticancer drug is reported to function through a distinct mechanism in chemotherapy, which in general can kill both cancer and normal cells. Therefore, new alternative methods are required to be adapted for enhancement in the treatment efficacy. In recent days, combination therapy is emerging with the hope of achieving minimal side effects and improved therapeutic efficiency. Generally, combining several types of therapy such as radiotherapy and chemotherapy or co-administration of multiple therapeutic agents (pro-drug–free drug, free drug–free drug, etc.) with different mechanisms of function for achieving synergistic action is referred to as combinationtherapy.[7-11]In this study, we are planning to explore “pro drug-free drug” combination as an emerging route in chemotherapy.

Pro-drugs are inert biomolecules that get activated in vivo by enzymatic or chemical reactions in the presence of anactivator.[5] Pro-drugs are often used to (i) improve solubility in water or lipid membrane, (ii) decrease side effects, and (iii)increase cellular uptake.[12-14] It is widely known that H_2O_2 is over expressed in cancer cells, and it produces reactive oxygen species (ROS) in the presence of transition metals (e.g.,Fe^{2+}).[15-20] These ROS (superoxide (O^{2}•–), hydroxyl radical(•OH), etc.) could become the cause of cell death through oxidative DNA damage.[21-24] So, we plan to use H_2O_2 as a pro drug and Fe^{2+} as a pro-drug activator as one of the components in combination therapy. Importantly, the chosen components(free drug or pro-drug) should act through different mechanisms so that multidrug resistance as well as anticancer drug-induced toxicity can be minimized.[7,25,26] In this regard, we plan to use anticancer drug paclitaxel as a free drug. Binding of paclitaxel to microtubules and subsequent chromosome breakage is known to kill malignant cells through inhibition of cell replication and migration.[27-31]

CHAPTER 2

Paclitaxel-Loaded Biotinylated Fe^{2+}-Doped Carbon Dot…

As we envisage pro-drug-free drug combination chemotherapy, we also need to choose target-specific cellular transporter for maximized therapeutic efficacy. Selective transportation of cargo inside cancer cells is always a great concern. Considering the overexpression of biotin receptors in cancer cells, we wanted to make use of biotin as targeting ligand in the drug delivery vehicle.[32-35] To this end, zero dimensional, water-soluble carbon-dot nanoparticle having intrinsic fluorescence could be a good choice as cellulartransporter.[36-40] Hence, we aim to develop a paclitaxel-loaded biotinylated carbon dot, which can act as a sensing probe forH_2O_2 (pro-drug) and activate H_2O_2 in cancer cells to generate ROS and also selectively deliver paclitaxel for killing of malignant cells. Carbon dot-based target-specific delivery vehicle in pro-drug–free drug combination therapy is rare, in particular where cellular transporter itself is an activator of pro-drug.

Herein, we report the development of paclitaxel-loaded biotinylated Fe^{2+}-doped blue-emitting carbon dot (FCD_b-PTX) for H_2O_2 sensing, which can selectively and effectively kill the cancer cells by pro-drug–free drug combination therapy. Microscopic, spectroscopic, and cytocompatible investigations were carried out before the use of (FCD_b-PTX) in cellular studies. Biotinylation of carbon dot facilitated the selective internalization of pro-drug activator Fe^{2+} and anticancer drug paclitaxel within cancer cells. ROS generated from H_2O_2 in the presence of Fe^{2+} caused oxidative DNA damage to cancer cells, and loaded paclitaxel boosted the killing of cancer cells through its specific mechanism of action. Consequently, FCD_b-PTX exhibited selective and -2.7 to 3.5-fold higher killing of B16F10 malignant cells of over normal cells, NIH3T3.

2.RESULTS AND DISCUSSION

Combination therapy is emerging as a cornerstone in cancer therapy. In this mode of treatment, co-administration of multiple therapeutic agents generally takes place to achieve synergistic anti-proliferative effect against cancer cells. The amalgamation of various types of therapy (e.g., chemotherapy, radiotherapy, immunotherapy, etc.) enhances efficacy compared to the single-therapy approach as it targets key pathways in an additive manner.[11]This approach has long been

adopted as the standard model for treating many cancer types. A proper combination of therapeutic processes or the administered drugs can achieve improved therapeutic benefits, target specificity, and reduced metastatic potential by arresting mitotically active cells. In this study, we are planning to investigate the efficacy of pro-drug–free drug combination in targeted cancer therapy. Killing of cancer cells by reactive oxygen species (ROS) in the presence of Fe^{2+} has recently attracted attention. A high content of hydrogen peroxide(H_2O_2) in cancer cells is known to facilitate the over production of ROS in the presence of Fe^{2+}, which thereby kills malignant cells through oxidative DNA damage.[21] Accordingly, we decided to use H_2O_2 as an essential pro-drug in the presence of Fe^{2+}-based bioprobe. To this end, judicious design and development of aFe^{2+}-doped carbon dot can act as a pro-drug activator, sensor, as well as target-specific cellular transporter for anticancer drug, paclitaxel. In view of this, we have developed aFe^{2+}-doped carbon dot surface-functionalized with biotin moiety (FCD_b) as a target-specific therapeutic and diagnostic agent in this pro-drug–free drug combination therapy (Scheme 1).

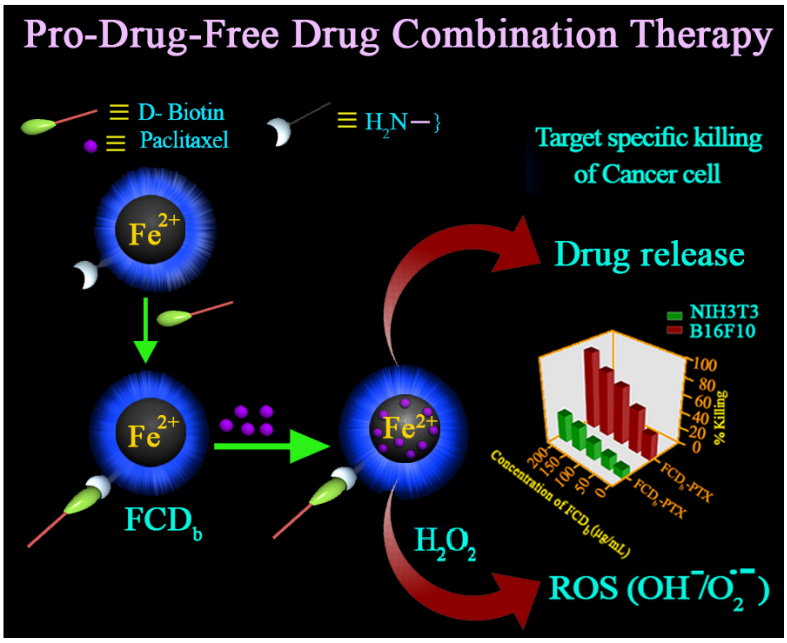

Scheme 1. Pictorial presentation of paclitaxel loaded biotinylated Fe^{2+} doped carbon dot (**FCD_b**) as a theranostic agent in pro-drug-free drug combination therapy.

CHAPTER 2

Paclitaxel-Loaded Biotinylated Fe^{2+}-Doped Carbon Dot…

2.1 Fe^{2+}-Doped CarbonDot (FCD) and Biotinylated Fe^{2+}-Doped CarbonDot (FCD_b).

Fe^{2+} doped carbon dot (**FCD**) was prepared via hydrothermal method using equivalent amount of citric acid, ethylenediamine, and Fe_2SO_4. Citric acid was used as source of carbon core, Fe^{2+} as doping element and ethylenediamine was utilized for surface functionalization (Figure 1a). Synthesized **FCD** was surface functionalized by biotin moiety via covalent amide bond (**FCD_b**, Scheme 2, (Experimental Section) Figure 2a) to enable the cargo delivery vehicle to be target specific by recognizing the over-expressed biotin receptors. Biotin (vitamin B7) is an essential requirement for all kinds of growing cells; however, its necessity is highly demanding for rapidly growing cells and tissues like cancer. Thereby, biotin receptors have become important target-specific motifs because of their over-expression in cancer cells.[32] These synthesized **FCD** and **FCD_b** were soluble in water and the corresponding zeta potential (ζ) values were -13.1 mV and -16.4 mV, respectively indicating its stability in aqueous medium. Microscopic characterization of Fe^{2+} doped carbon dot **FCD** and **FCD_b** was investigated by TEM and AFM. The data from TEM images confirmed the size of **FCD** and **FCD_b** was around 3-5 nm (Figure 1b, 2b). AFM images also supported the result obtained from TEM image (Figure 1d, 2d).

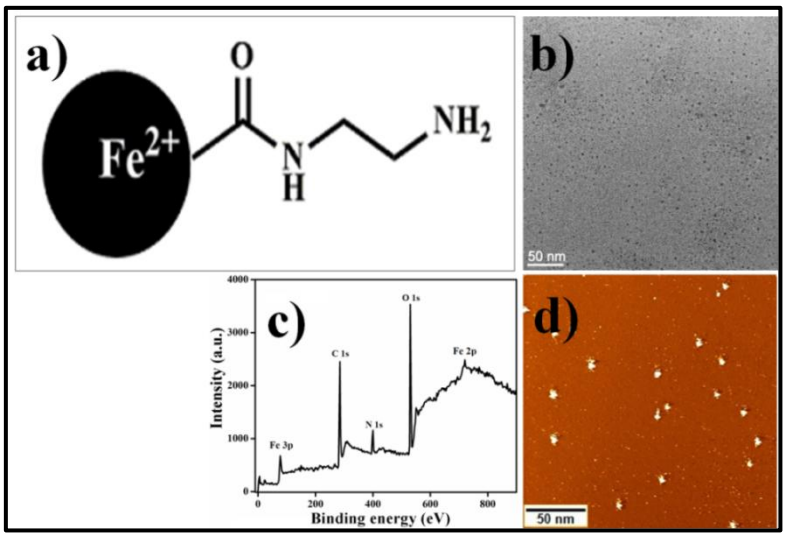

Figure 1. a) Chemical structure of **FCD**, b) TEM image, c) XPS spectrum and d) AFM image of **FCD**.

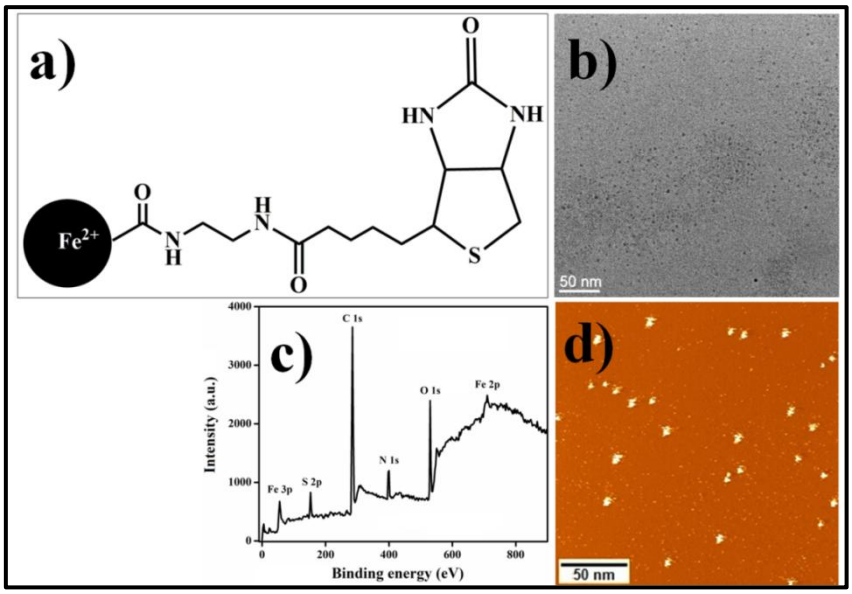

Figure 2. a) Chemical structure, b) TEM image, c) XPS spectrum and d) AFM image of **FCD_b**.

The XPS analysis of **FCD** showed peaks at 284, 406, and 529 eV, that correspond to C (1s), N (1s), and O (1s) orbitals, respectively (Figure 1c).[37] Two more peaks at 53 eV and 710 eV, corresponding to the orbital Fe 3p and Fe 2p, respectively were observed (Figure 1c).[41] In particular, the peak at 710 eV confirmed the presence of iron in the divalent (Fe^{2+}) state in **FCD**.[42] Elemental analysis (XPS) of **FCD_b** also confirmed the presence of iron along with main elements (C, N, and O) (Figure 2c). Along with these peaks, one more peak was observed at 160 eV corresponding to 2p orbitals of S (Figure 2c) confirming the presence of S (from biotin moiety) in **FCD_b**.[43] According to XPS, **FCD** contains C (60%), O (24%), N (10%), and Fe (6%) and **FCD_b** contains C (56%), O (22%), N (10%), S (6%) and Fe (6%). EDX analysis quantifies the elements contents in the synthesized **FCD** and **FCD_b**(Figure 3a,b). According to EDX data (Figure 3a),**FCD** contains O (22%), N (12%), and Fe (6%), which was similar with the data from XPS. Similar trend was observed in case of EDX of **FCD_b**(Figure 3b) in concurrence with the respective XPS data. Further characterization of **FCD** and **FCD_b** was carried out by XRD analysis. The peak ranges from 20-25°established the amorphous nature of prepared **FCD** and **FCD_b**(Figure 4a,b).[37]We observed excitation dependent blue emission with emission maxima for both **FCD** and **FCD_b** at 460 nm and 469 nm, respectively upon excited

at 230 nm (Figure 4c, d). Aqueous solution of both **FCD** and **FCD_b** displayed blue fluorescence (inset, Figure 4c,d), under UV light irradiation (254 nm), which is in concurrence with the emission behavior of the respective surface functionalized carbon dots.

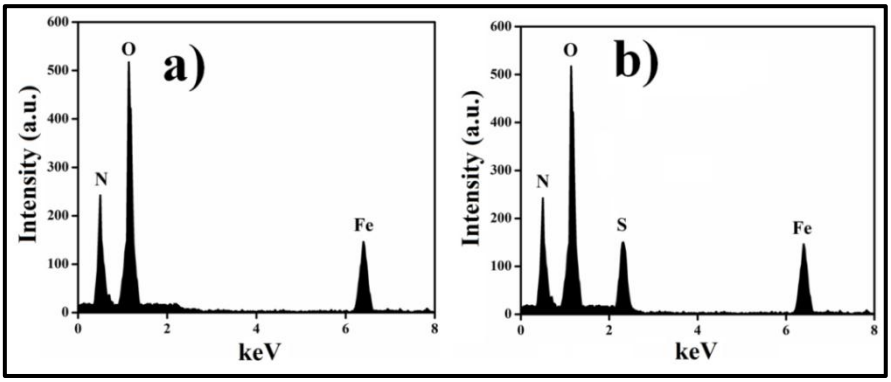

Figure 3. EDX analysis of a) **FCD** and b)**FCD_b**. Sample was crusted on carbon coated Cu grid for the experiment. Thus, C content was not included in EDX analysis.

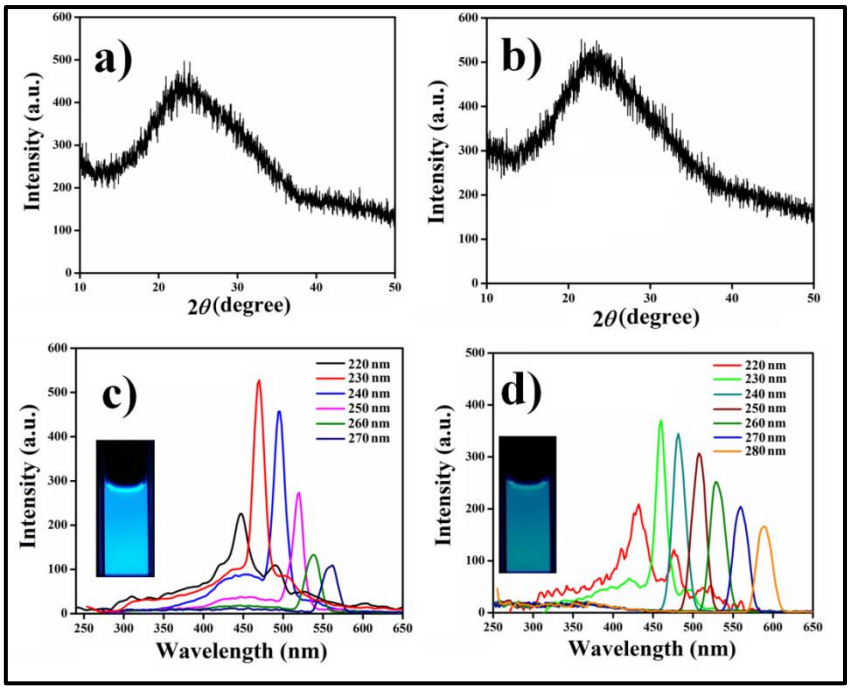

Figure 4. a) XRD spectrum of **FCD_b**, b) XRD spectrum of **FCD** and excitation-dependent emission spectra of c)**FCD_b** and d) **FCD** (inset in panel are photographs showing the blue fluorescence of **FCD_b** and **FCD** solution under UV irradiation, 254 nm)

2.2 Hydrogen Peroxide Sensing by FCD_b and FCD.

ROS (reactive oxygen species) has enormous significance in regular biochemical phenomena inside cells. Over-expressed H_2O_2 is one of the important biochemical characteristics of malignant cells due to higher amount of superoxide dismutase in mitochondria as well as less amount of catalase and glutathione peroxidase.[15,17,44-45] In presence of Fe^{2+}, H_2O_2 (pro-drug) can produce ROS and thus oxidatively damage the DNA.[21] Subsequently, we used newly synthesized **FCD_b** and **FCD** for sensing of H_2O_2 by utilizing its inherent fluorescence property as well as Fenton like reactivity of Fe^{2+}. For this purpose, the intensity of fluorescence spectra of the aqueous **FCD_b** and **FCD** solutions (25 µg/mL) were recorded in presence of various concentration of H_2O_2 from 1 to100 µM (Figure 5a, 6a). The emission intensities of **FCD_b** at 469 nm and **FCD** at 460 nm were found to be steadily quenched with increasing concentration of H_2O_2. In both cases, the quenching effect was maximum at around 100 µM of H_2O_2. The correlation curve between fluorescence intensity of **FCD_b/FCD** and H_2O_2 concentration (0-100 µM) was plotted (Figure 5b, 6b). The fluorescence response curve was plotted (defined as $(F_0 - F)/F$, where F_0 is the emission intensity of the native **FCD_b** and **FCD** and F is the emission intensity of **FCD_b** and **FCD** in presence of H_2O_2) against the concentration of H_2O_2 that demonstrated a linear relationship in the concentration range of 1-20 µM indicating H_2O_2 sensing at low concentration (Figure 5c, 6c). The detection limit of H_2O_2 was found to be 1.8 µM for both **FCD_b** and **FCD** as determined based on $3\sigma/S$ where σ was the standard deviation and S was the slope of the calibration curve (experiment was repeated thrice). The intrinsic fluorescence of **FCD_b** and **FCD** got quenched in presence of highly reactive oxygen species (hydroxyl ($OH^{\bullet}$) and superoxide ($O_2^{\bullet-}$) radicals) generated during Fenton reactivity of iron (Fe^{2+}) in presence of H_2O_2.[19] These ROS might have oxidized the surface functionalities of carbon dots leading to the quenching of its intrinsic emission.[46]

Paclitaxel-Loaded Biotinylated Fe^{2+}-Doped Carbon Dot…

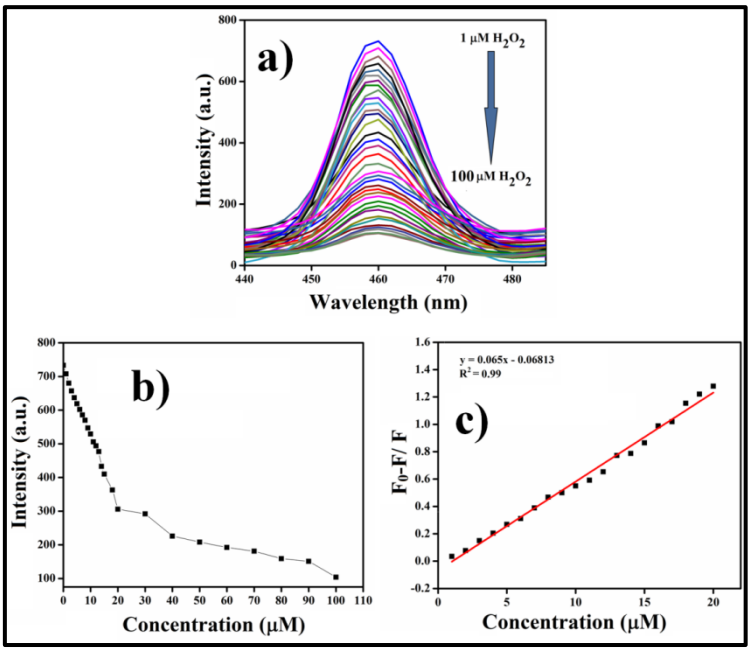

Figure 5. a) Fluorescence spectra of **FCD_b** in presence varying concentration of H_2O_2 (0-100 μM) b) correlation between fluorescence intensity against H_2O_2 over a concentration range of 0-100 μM, and c) linear range of fluorescence response of the **FCD_b** with varying H_2O_2 concentrations. [**FCD_b**] = 25 μg/mL.

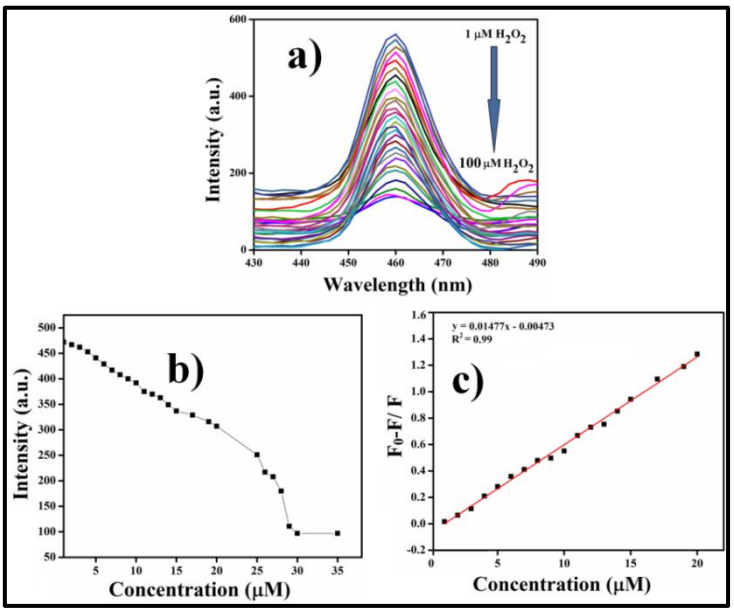

Figure 6. a) Fluorescence spectra of **FCD** with varying concentration of H_2O_2 (0-100 μM)b) correlation between fluorescence intensity against H_2O_2 over a concentration range of 0-100 μM, and c) linear range of fluorescence response of the **FCD** with varying H_2O_2 concentrations. [**FCD**] = 25 μg/mL.

To confirm the production of ROS from H_2O_2 in presence of **FCD_b** and **FCD**, we carried out UV-vis absorption spectroscopic investigation of the same using 1, 3-diphenylisobenzofuran (DPBF) which is a UV- active molecule having high selectivity towards ROS. DPBF, in the presence of reactive oxygen species generated UV inactive 1,2-dibenzoylbenzene through the formation of an endoperoxide (Scheme 3).[47] This reactivity of DPBF towards ROS was used to calculate the alteration in the absorption at λ_{max} (440 nm) in the UV-vis spectra. The intensity of the absorption maxima of DPBF (20 µg/mL) did not change in the presence of only **FCD_b** (25 µg/mL) and **FCD** (25 µg/mL)(Figure 7a, 8a). However, the absorbance of DPBF (20 µg/mL) at λ_{max} (440 nm) was found to be gradually decreased with the increase in H_2O_2 concentration (1-35 µM) in presence of **FCD_b** (25 µg/mL) and **FCD** (25 µg/mL), respectively (Figure 7a, 8a). Hence, ROS generation from both **FCD_b** and **FCD** in presence of H_2O_2 (1-35 µM) led to the decomposition of DPBF (20 µg/mL). Higher is the concentration of ROS, more is the formation of the UV-vis-inactive 1, 2-dibenzoylbenzene that plummeted the absorbance intensity. To further support the **FCD_b** and **FCD** mediated production of reactive oxygen species from H_2O_2, we investigated the same UV-vis experiment of DPBF, H_2O_2 and **FCD_b/FCD** mixture in the presence of thiourea, which is a radical scavenger. Upon the addition of thiourea to the mixture of DPBF (20 µg/mL), H_2O_2 (35 µM)and **FCD_b/FCD** (25 µg/mL), DPBF regained its absorbance intensity steadily at λ_{max} (440 nm) with increasing thiourea concentration from 1 to 5 µM(Figure 7b, 8b). This observation indicates the prevention of degradation of DPBF by ROS. The scavenging property of thiourea towards ROS, generated from H_2O_2 by **FCD_b/FCD** resulting in the minimum decrease of the absorbance of DPBF (Figure 7b, 8b).

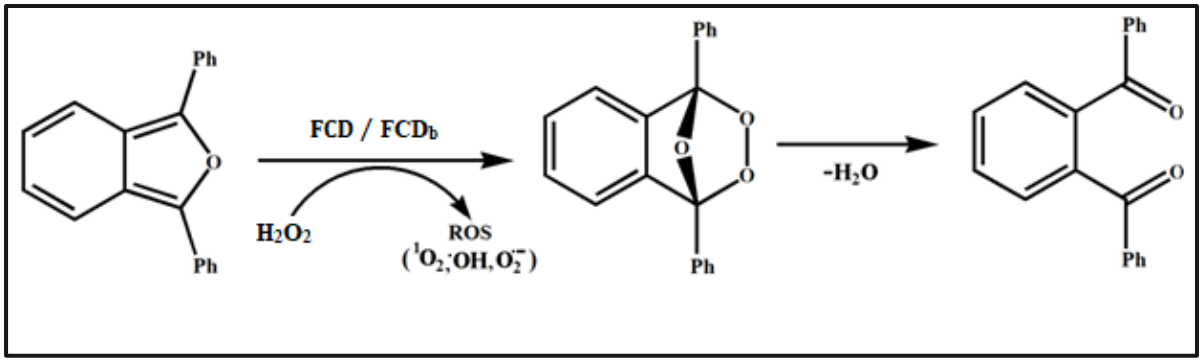

Scheme 3. Scheme of decomposition of DPBF in presence of **FCD/FCD_b** under visible light exposure.

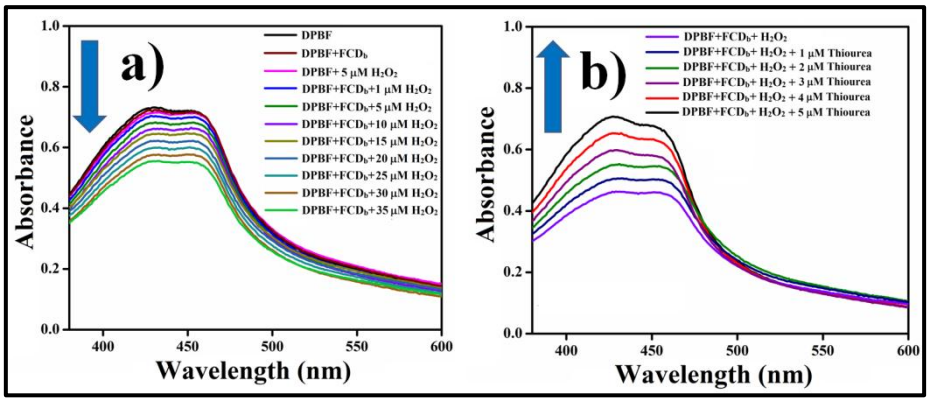

Figure 7. a) Detection of H_2O_2 (1-35 μM) induced ROS generation from **FCD_b** in presence of DPBF (absorption at 440 nm) and b) absorption of DPBF in presence of **FCD_b** where [**FCD_b**] = 25 μg/mL and thiourea (1-5 μM). [DPBF] = 20 μg/mL.

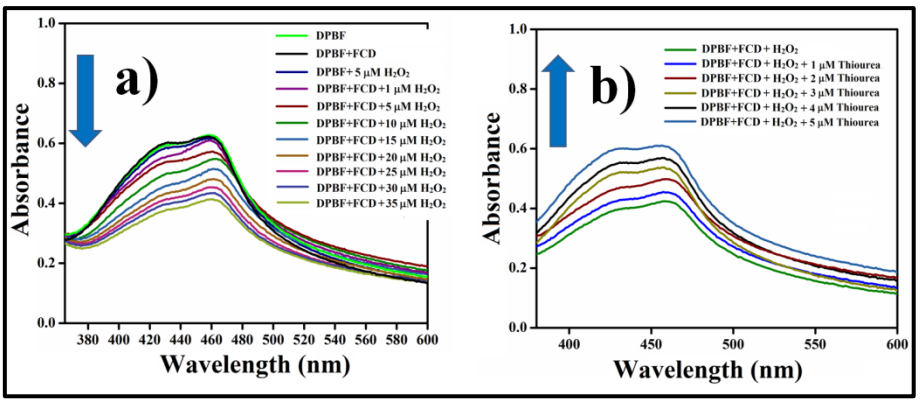

Figure 8. a) Detection of H_2O_2(1-35 μM) induced ROS generation from **FCD** in presence of DPBF (absorption at 440 nm) and b) absorption of DPBF in presence of **FCD** where [**FCD**] = 25 μg/mL and thiourea (1-5 μM). [DPBF] = 20 μg/mL.

2.3 Oxidative DNA Damage upon Pro-Drug Activation.

In view of the one of the primary objectives of the combination therapy (pro-drug-free drug) in the present study, we investigated the ROS (produced by H_2O_2 in presence of **FCD_b/FCD**) mediated oxidative DNA damage. Subsequently, elevated amount of H_2O_2 (pro-drug) in malignant cells can be utilized for anticancer activity by ROS generated in presence of **FCD_b/FCD**. We investigated the oxidative DNA damage by UV-vis and circular dichroism (CD) spectroscopy in presence of H_2O_2 and **FCD_b/FCD**. The absorbance of CT-DNA at absorption maxima (260 nm) remained unaltered in presence of **FCD_b/FCD** (25 μg/mL)and H_2O_2 (5 μM)in

separate experiments (Figure 9a, 10a). However, with gradual addition of H_2O_2 (1-40 µM)in the solution of CT-DNA (25 µg/mL) and **FCD_b/FCD** (25 µg/mL), the spectral pattern steadily got changed and flattened with no specific absorption maxima (Figure 9a, 10a). Similarly, in case of the CD experiment, the spectral nature of CT-DNA remained unchanged in the presence of only **FCD_b/FCD** (25 µg/mL) andonlyH_2O_2 separately with respect of native CT-DNA (Figure 9b, 10b). However, in presence of H_2O_2 (15 µM), a distinct change was also noted in the spectral pattern of CD in the solution of CT-DNA (25 µg/mL), **FCD_b/FCD** (25 µg/mL) (Figure 9b, 10b). The changes observed both in UV-vis and CD spectra signify a loss in the structural pattern of CT-DNA possibly due to interaction between Fe^{2+}, the pro-drug activator, present within **FCD_b/FCD** through ROS mediated oxidative damage. Taking into account the above observations, the over produced intracellular H_2O_2 can be utilized as a pro-drug for cancer cell death in presence of this newly developed **FCD_b/FCD**. This **FCD_b** and **FCD** can both detect and stimulate H_2O_2 resulting in ROS mediated oxidative DNA damage.

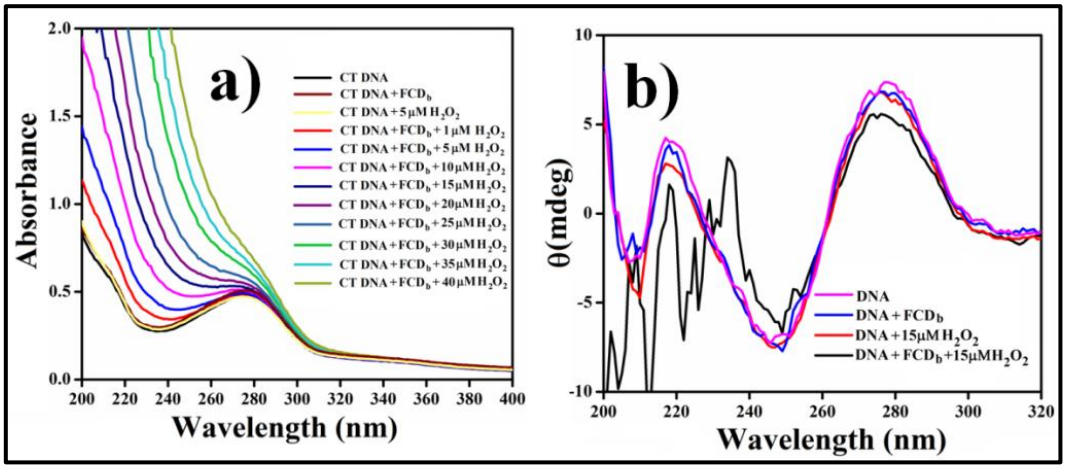

Figure 9. a) UV-vis and b) CD spectra of CT-DNA with increasing concentration of H_2O_2 in the presence of a **FCD_b**. [**FCD_b**] = 25 µg/mL.

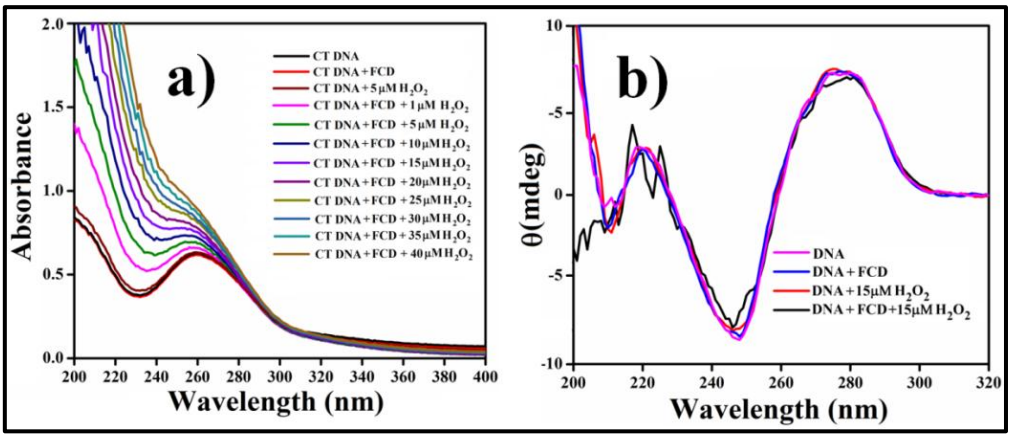

Figure 10. a) UV-vis and b) CD spectra of CT-DNA with increasing concentration of H_2O_2 in the presence of **FCD**. [**FCD**] = 25 μg/mL.

2.4 Media Stability of FCD_b and FCD.

Prior to the utilization of the newly synthesized Fe^{2+} doped carbon dot **FCD** and biotinylated **FCD** (**FCD_b**) as theranostic bioprobe, I investigated their (i) stability in biological media in a time dependent manner and (ii) cytocompatibility toward mammalian cells. In FBS-DMEM media, both 200 μg/mL of **FCD_b** and 200 μg/mL of **FCD** were added separately having FBS of different concentrations (up to 75%) and kept for 48 h (Figure 11a,b). The prolonged stability **FCD_b** and **FCD** were also investigated by keeping the mixtures of **FCD_b** (200 μg/mL)-FBS (10%)-DMEM media and **FCD**(200 μg/mL)-DMEM (10% FBS) media for 10 days (Figure 11c,d). In case of both **FCD_b** and **FCD** and also for 10 days study (FBS (10%)-DMEM), suspension stability index (SSI) in media was 90 ± 2% for different concentrations of FBS (0-75%, Figure 11). The stability of **FCD_b/FCD** in biological media is also concurring with respective visual images (Figure 11a,b). Next, we also investigated the stability of **FCD_b/FCD** under UV light exposure (254 nm and 12 W) where no photobleaching property was observed and even emission property of the fluorescent bioprobes did not change after 200 min of UV irradiation (Figure 12a,b).

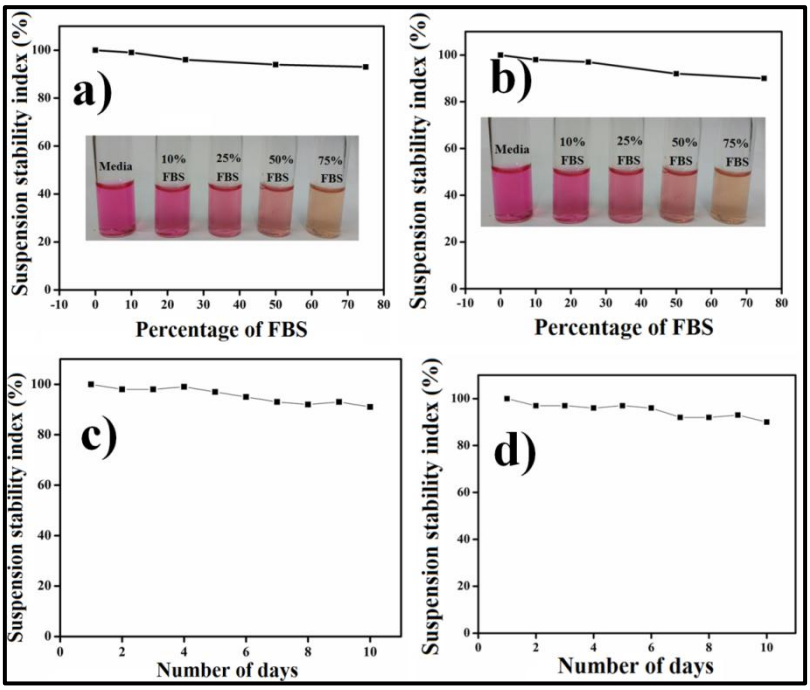

Figure 11. Suspension stability index of **FCD_b** and **FCD** solution where [**FCD_b**] = 200µg/mL and [**FCD**] = 200µg/mL. a)**FCD_b** and b) **FCD** with respect to FBS concentration (0-75%) in DMEM media and c)**FCD_b** and d) **FCD** with respect to number of days in 10% FBS in DMEM media.

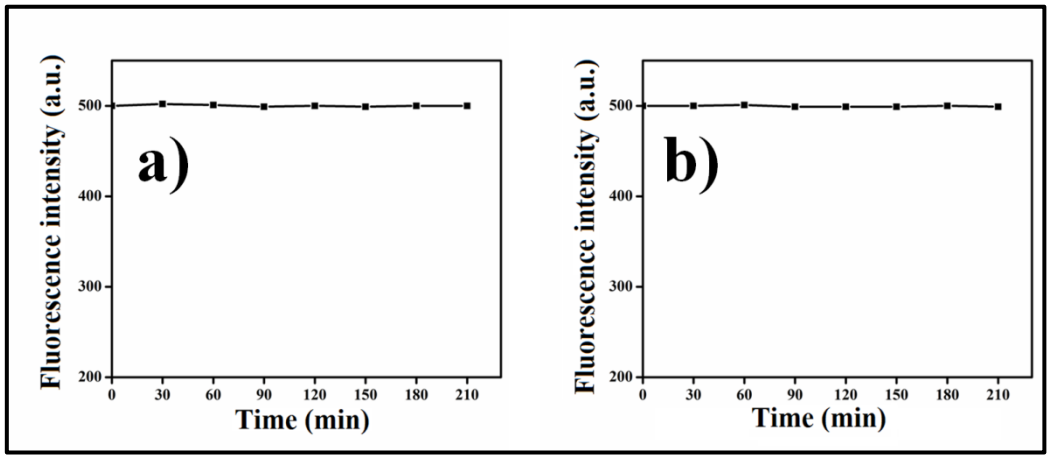

Figure 12. Photostability of a) **FCD_b** and b) **FCD** solution under UV (wavelength 254 nm, power 12 W) lightirradiation up to 200 min.

CHAPTER 2

Paclitaxel-Loaded Biotinylated Fe^{2+}-Doped Carbon Dot…

2.5 Bioimaging and Co-Culture.

Next, we intended to use the intrinsic fluorescence of **FCD_b** and **FCD** in bioimaging of mammalian cells. Also, the ROS (generated from H_2O_2) induced quenching of **FCD_b/FCD** emission encouraged us further to explore these probes in distinguishing between cancer and non-cancer cells. In particular **FCD_b** (biotin surface modified) could selectively diagnose the cancer cells through its facilitated internalization owing to the presence of biotin receptors that remain over expressed in cancer cells. Initially, **FCD** (100 µg/mL) was incubated separately with non-cancer cell NIH3T3 and cancer cell B16F10 for 6 h. After completion of incubation both cells were observed under fluorescence microscope. A bright blue fluorescence was observed in NIH3T3 cells (Figure 13 a,b) in comparison to the quenched fluorescence noted in B16F10 cells under similar experimental conditions (Figure 13 d,e). Fluorescence quenching in both normal cells and cancer cells were also analyzed by flow cytometry. The mean fluorescence intensity was found to be 1543 for NIH3T3 and for 8534 for B16F10, which further established the presence of higher concentration of H_2O_2 in cancer cells than normal cells (Figure 13 c, f). We also co-cultured both the cancer (B16F10) cells and normal cells (NIH3T3) together and incubated the cells with **FCD** (100 µg/mL) for 6 h. With reference to the bright field image, some cells exhibited blue luminescence and few showed quenched blue emission under fluorescence microscopy in the mixed population of both type of cells (Figure 16 c,d). Following cellular internalization, the fluorescence of **FCD** got quenched through the Fenton reaction because of the high H_2O_2 content but it did not take place in marked manner for normal cells (NIH3T3) due to low amount of H_2O_2.

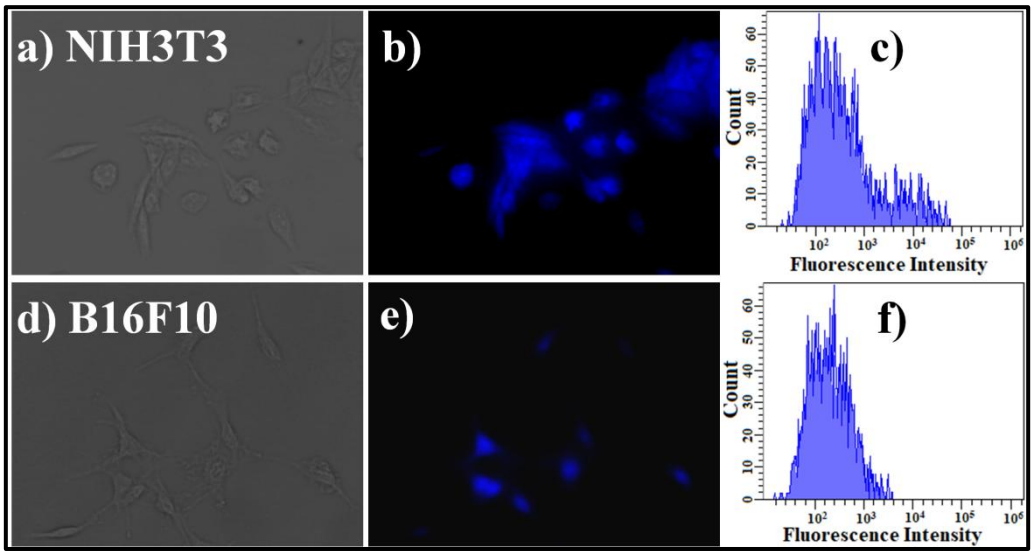

Figure 13. Bright field and fluorescence microscopic images of cells after 6 h incubation with **FCD** where [**FCD**] = 100 µg/mL,(a,b) NIH3T3 (d,e) B16F10 cells. Corresponding flow cytometric plots of c) NIH3T3 cells, f) B16F10 cells. In all the flow cytometric plots, the x-axis denotes the fluorescence intensity. The mean fluorescence values are given in the insets.Scale bars correspond to 20 µm.

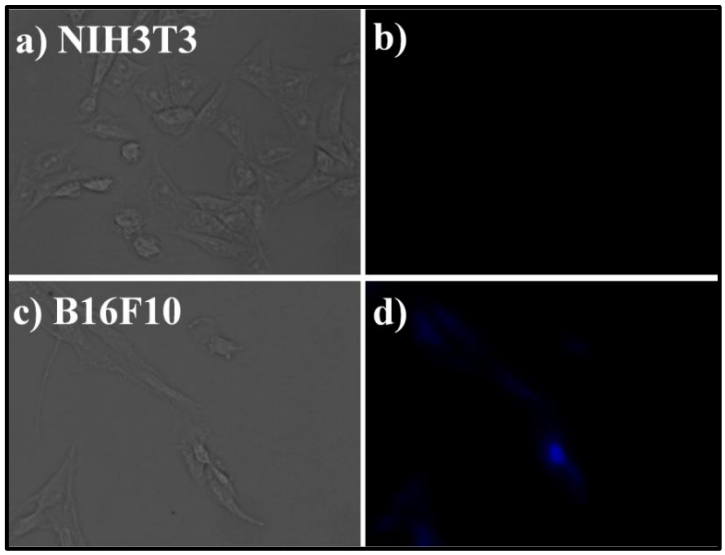

Figure 14. Bright field and fluorescence microscopic images of cells after 6 h incubation with **FCD_b** where [**FCD_b**] = 100 µg/mL,(a,b) NIH3T3 (c,d) B16F10 cells. Scale bars correspond to 20 µm.

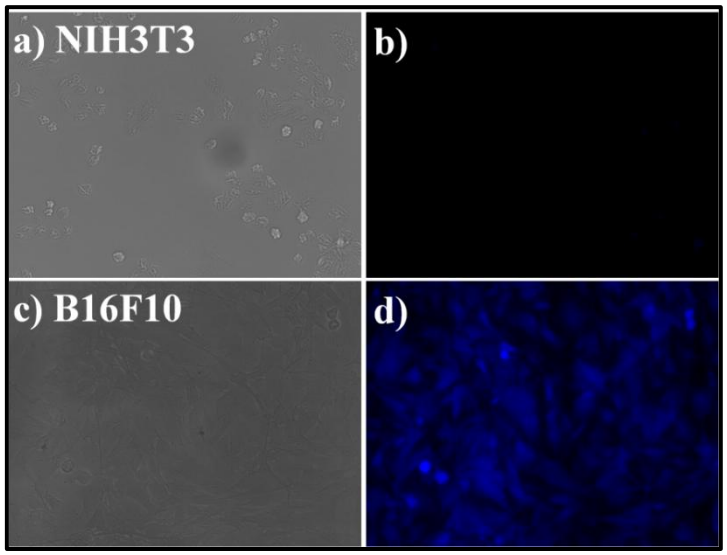

Figure 15. Bright field and fluorescence microscopic images of cells after 6 h incubation with **FCD_b** where [**FCD_b**] = 100 μg/mL,(a,b) NIH3T3 (c,d) B16F10 cells at 20x magnification. Scale bars correspond to 20 μm.

Interestingly, in case of **FCD_b** the selective diagnosis of cancer cells is more distinct and noteworthy. **FCD_b** (100 μg/mL) was also incubated with separately NIH3T3 and B16F10 cells. After incubation (6 h), NIH3T3 cells showed no notable fluorescence (Figure 14 a,b,), whereas B16F10 cells showed significantly quenched fluorescence under microscope (Figure 14 c,d). Images of both type of cells (NIH3T3 and B16F10) were also captured 20x magnification (Figure 15) where the quantity of cells were quite high compared to 40x magnification (Figure 14) and observed similar results upon incubation with **FCD_b**. Here too, we carried away co-culture experiment for **FCD_b** using B16F10 and NIH3T3 cells where lesser number of cells exhibited blue fluorescence compared to the number of cells present in the bright field image (Figure 16 a,b). This observation validates the facilitated internalization of **FCD_b** inside cancer cells, over-expressing biotin receptors and subsequently quenching of its emission in presence of elevated H_2O_2 content in malignant cells. In contrast, internalization of **FCD_b** within normal NIH3T3 cells was very insignificant even notably lower than that of **FCD** mainly due to the absence or low presence of biotin receptor on NIH3T3 cells. Consequently, almost no fluorescence was observed for **FCD_b** within NIH3T3 cells (Figure 14 a,b, 15 a,b). Hence, **FCD** selectively diagnose the cancer cells mainly due to its high amount of H_2O_2 while

presence of biotin receptors along with H_2O_2 made **FCD_b** far more selective in cancer cell diagnosis through synergistic effect.

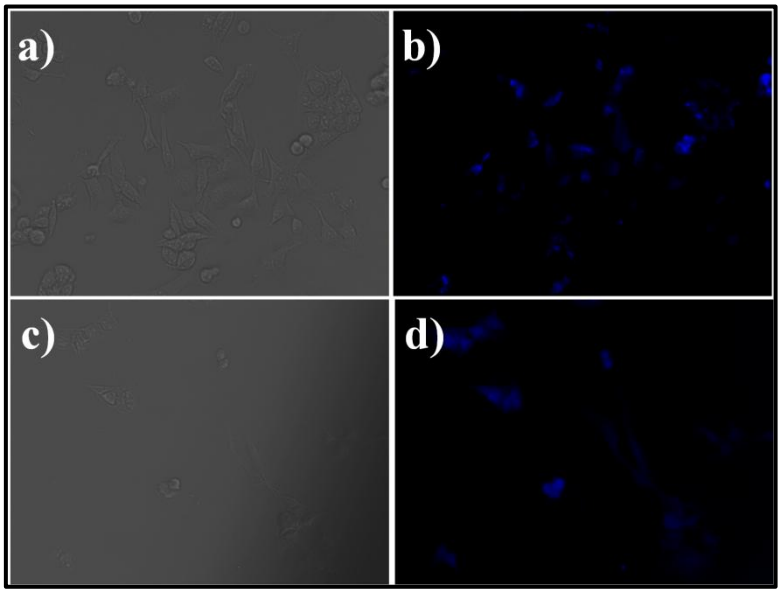

Figure 16. Bright field and fluorescence co-culture images of cells (NIH3T3 and B16F10) after 6 h incubation with (a,b) **FCD_b** where [**FCD_b**] = 100 µg/mL and (c,d) **FCD** where[**FCD**] = 100 µg/mL. Scale bar correspond to 20 µm.

2.6 Paclitaxel Loading on FCD_b and FCD.

With the aim of utilizing this **FCD_b** bioprobe in combination therapy as targeted theranostic agent, the anticancer drug paclitaxel (PTX) was loaded on **FCD_b**. PTX was effective against a wide range of mammalian cancer cell lines such as breast, lung, ovarian, colorectal and melanoma cells.[30] As mentioned earlier, PTX effectively inhibits the growth of malignant cells through reducing the cell migration by perturbing the endothelial cell function and stabilization of the microtubule cytoskeleton.[50] However, poor water solubility of free paclitaxel often led to its early clearance from the body. Moreover, non-selectivity and the poor water solubility are known to cause multiple side effects such as nephrotoxicity, neurotoxicity, and cardiotoxicity etc.[30,48] Therefore, a judiciously developed delivery vehicle for transporting the anti-cancer drugs like paclitaxel (PTX) selectively towards cancer cells would definitely boost its efficacy. Paclitaxel was loaded at 2:1 w/w (**FCD_b**:PTX), where PTX (500 µg) was added to 1 mg of **FCD_b** solution for achieving maximum drug loading of on the surface of **FCD_b**. A red shift of 32 nm (227 to 259

nm) and a blue shift of 21 nm (280 to 259 nm) in the UV-visible spectra of PTX-loaded **FCD_b** (**FCD_b**-PTX) was noted with respect to free PTX (227 nm) and native **FCD_b**(280 nm) (Figure 17a).[27] Possible loading of PTX on the **FCD_b** surface was further investigated by FTIR spectra. The characteristic peaks of PTX were appeared at 3412 cm^{-1} (stretching of -OH), 2925 cm^{-1} (stretching of C-H), 2489 cm^{-1} (stretching of –N-H), 1731 cm^{-1} and 1708 cm^{-1} (stretching of C=O carbonyl ketone), 1637 cm^{-1} (C=O amide stretching), 1437 cm^{-1} (CH_2 scissoring mode of PTX) 1085 cm^{-1} (presence of aromatic moiety), and 614 cm^{-1} (bending of aromatic C-H bond) (Figure 17b(i)).[49,50] For **FCD_b**, the peaks were observed at approximately 3385 cm^{-1} (O-H and N-H stretching), 2937 and 2856 cm^{-1} (C-H stretching), 1655 cm^{-1} (C=O stretching), 1405 cm^{-1} (C=C stretching), 1104 cm^{-1} (C-N stretching), and 630 cm^{-1} (=C-H stretching) (Figure 17b(ii)). Interestingly in case of **FCD_b-PTX**, we observed a broad peak at 3430 cm^{-1} was due to O-H and N-H stretching vibrations and C-H stretching vibration, for both **FCD_b** and PTX. The peak at 2542 cm^{-1} may be the stretching of –NH group of paclitaxel. Peaks at 1646 cm^{-1}, 1430 cm^{-1}, 1395 cm^{-1}, 1117 cm^{-1} and 625 cm^{-1} were due to C=O bond stretching of **FCD_b** and PTX, CH_2 scissoring mode of paclitaxel, C=C stretching, overlapping C-N stretching vibration for **FCD_b** and vibration of aromatic moiety for PTX, and =C-H stretching vibration of **FCD_b** and PTX, respectively, (Figure 17b(iii)). Both UV-vis and FTIR investigations delineated the successful loading of PTX on the surface of **FCD_b**. Non-covalent grafting of the sp^2-carbon network of **FCD_b** with the aromatic moieties of PTX via π-π interactions facilitated drug loading on the surface of carbon dots.[37,51] Surface modified **FCD_b** loaded almost 82% paclitaxel on its surface (413 µg of PTX on 1 mg of **FCD_b**). Similarly, PTX loading on the native **FCD** (**FCD**-PTX) was confirmed by UV-vis and FTIR spectroscopic investigations (Figure 17c,d) and it was found to be 80% (400 µg of PTX on 1 mg of native **FCD**).Microscopic characterization of paclitaxel (PTX) loaded **FCD_b** (**FCD_b**-PTX) was also investigated by TEM and the size was around 5-6 nm (Figure 18a). XRD analysis of paclitaxel (PTX) loaded **FCD_b** (**FCD_b**-PTX) showed similar peak ranges form 20-25° which also established the amorphous nature of **FCD_b**-PTX (Figure 18b). We also observed emission maximum of **FCD_b**-PTX at 468 nm upon excited at 230 nm (Figure 18c).

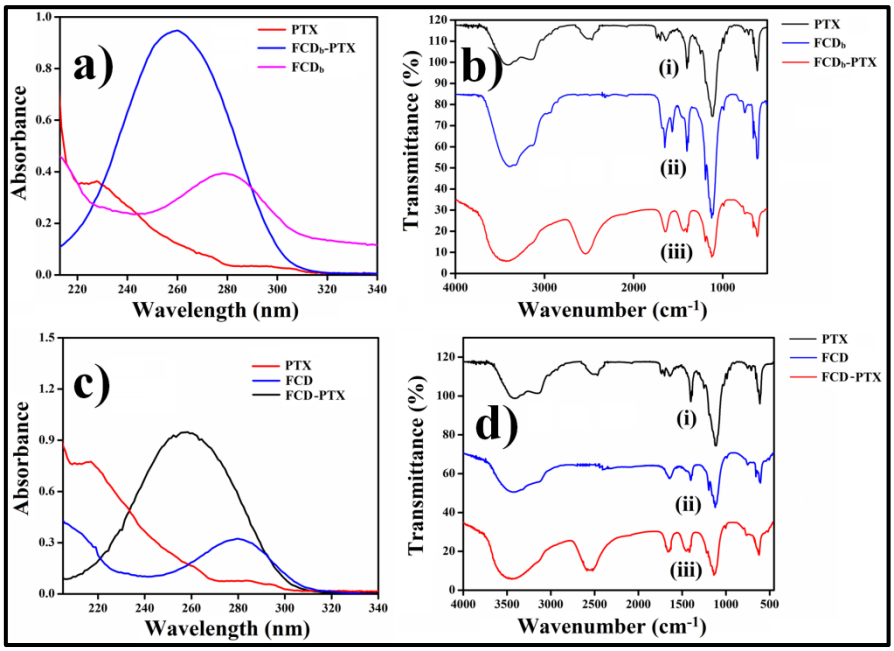

Figure 17. UV-visible spectra of a) free PTX, **FCD$_b$** and PTX loaded **FCD$_b$** where **FCD$_b$** = 50 µg/mL, c) free PTX, **FCD** and PTX loaded **FCD** where **FCD** = 50 µg/mL, and PTX = 25 µg/mL and IR spectra of b) (i) PTX, (ii) **FCD$_b$** and (iii) **FCD$_b$**-PTX, d) (i) PTX, (ii) **FCD** and (iii) **FCD**-PTX.

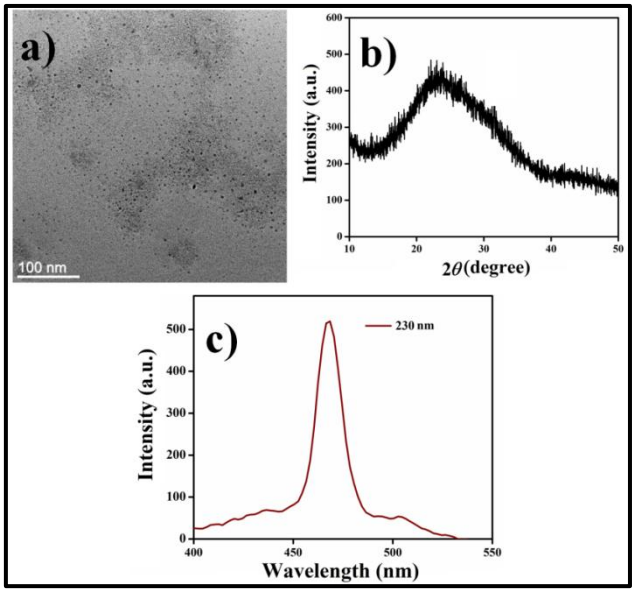

Figure 18. a) TEM image, b) XRD spectrum and c) fluorescence spectrum of **FCD$_b$**-PTX.

CHAPTER 2

Paclitaxel-Loaded Biotinylated Fe^{2+}-Doped Carbon Dot…

2.7 Target Specific Killing of Cancer Cells through Combination Therapy.

These newly developed **FCD_b** and **FCD** have shown the potential to sense and generate ROS through activation of H_2O_2 for oxidative DNA damage as well as selective imaging of the cancer cells. After successful loading of paclitaxel (PTX), herein we investigated the selective cancer cell killing efficiency of the PTX loaded both **FCD_b**-PTX and **FCD**-PTX,by exploiting the synergistic action of both H_2O_2 (as pro-drug) and paclitaxel (anticancer drug) in pro-drug-free drug combination therapy. To this end, free PTX, **FCD**, **FCD_b**, **FCD_b**-PTX and **FCD**-PTX were separately incubated with both normal cells (NIH3T3) and cancer cells (B16F10) for 12 h. Free PTX exhibited comparable killing efficacy against both normal cell, NIH3T3 (10 ± 3% to 41 ± 1%) and cancer cell, B16F10 (12 ± 2% to 43 ± 1%) with varying concentration from 5-100 µg/mL (Figure 19a). Expectedly, PTX could not show selective cancer cell killing ability in absence of target specific cargo transporter. Similarly, in case of **FCD**, with its increasing concentration (10-200 µg/mL), 13 ± 1% to 40 ± 2% killing was observed for NIH3T3 while it was 17 ± 1% to 48 ± 3% for B16F10 (Figure 19b). Absence of any target specific ligand (biotin) on the surface of **FCD** possibly led to the equivalent extent of internalization and subsequent similar killing of both normal and cancer cells via ROS mediated oxidative damage of DNA. Under the similar experimental conditions, **FCD_b** showed difference in the killing efficacy against NIH3T3 (9 ± 2% to 29 ± 1%) and B16F10 (15 ± 1% to 50 ± 1%) cells at different concentrations (10-200 µg/mL)(Figure 19c). The presence of biotin on the surface of **FCD_b**, evidently distinguishes (by ~1.7 fold) between cancer cell B16F10 over normal cell NIH3T3. Thereby, more amount of **FCD_b** got transferred inside cancer cells and exhibited moderately higher killing in contrast to normal cells.

To enhance the therapeutic efficiency, next we used combination of pro-drug and free drug by means of PTX loaded **FCD_b** and **FCD** (**FCD_b/FCD**-PTX) where [**FCD_b/FCD**] = 10-200 µg/mL and [PTX] = 5-100 µg/mL). According to the MTT assay, in case of PTX-loaded native **FCD** (**FCD**-PTX) ([**FCD**] = 10-200 µg/mL and [PTX] = 5-100 µg/mL), 28 ± 2% to 85 ± 3% killing of both non-cancer NIH3T3 and

cancerous B16F10 cells was noted with increasing concentration of **FCD**-PTX (Figure 20). Although the **FCD**-PTX formulation showed synergistic action in killing the cells in comparison to that of only PTX and/or **FCD**; however, the killing was non-selective for **FCD**-PTX. Interestingly, in case of **FCD$_b$**-PTX, B16F10 cancer cell killing steadily increased from 30 ± 2% to 92 ± 1% with increasing concentration of the drug formulation (Figure 19a-c).

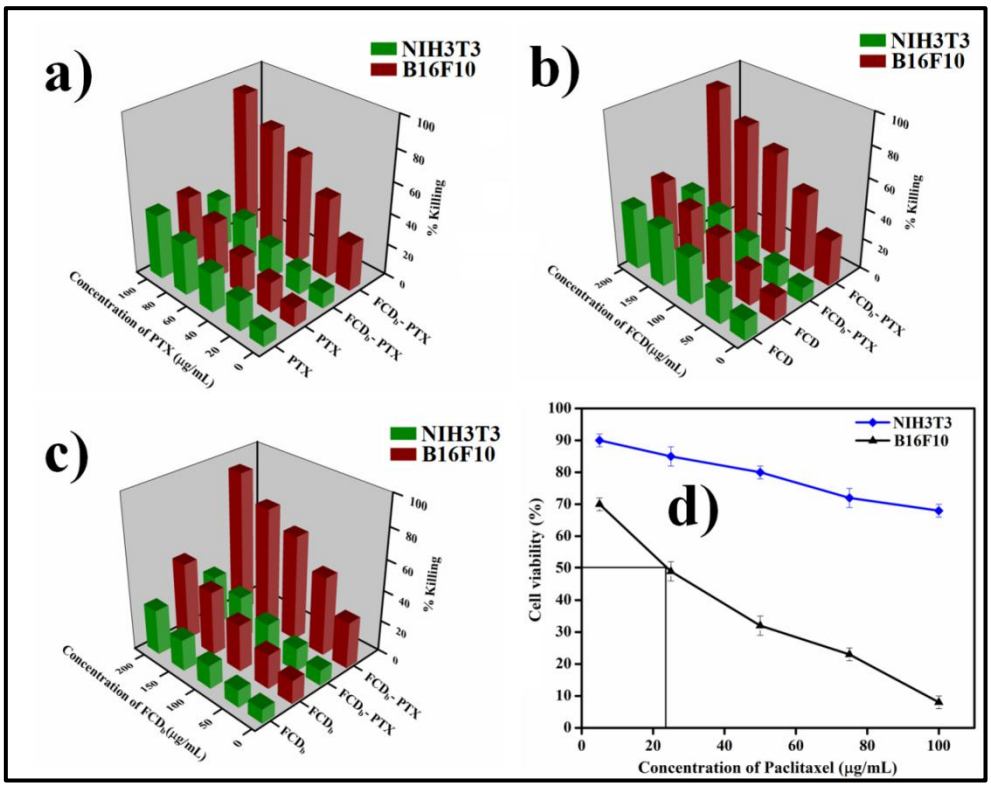

Figure 19. % Killing of cells determined by MTT assay. NIH3T3 and B16F10 cells incubated with varying concentrations of a)PTX (5-100μg/ mL)and **FCD$_b$**- PTX ([**FCD$_b$**] =10-200 μg/mL and [PTX] = 5-100 μg/mL), b) **FCD** (10-200μg/mL and **FCD$_b$**- PTX ([**FCD$_b$**] =10-200 μg/mL and [PTX] = 5-100 μg/mL), c) **FCD$_b$**(10-200μg/mL) and **FCD$_b$**- PTX ([**FCD$_b$**] =10-200 μg/mL and [PTX] = 5-100 μg/mL) for 12 h,d) IC_{50} determination of **FCD$_b$**- PTX ([**FCD$_b$**] =10-200 μg/mL and [PTX] = 5-100 μg/mL) after 12 h incubation of NIH3T3 and B16F10. The standard deviation and experimental errors were in the range of 1-3% and 3-5% respectively in triplicate experiments.

However, for non-cancer cell NIH3T3, that was varied from 10 ± 1% to 32 ± 2% under the similar experimental concentration range. **FCD$_b$**-PTX exhibited ~2.7

to 3.5-fold higher killing of B16F10 malignant cells of over normal cells, NIH3T3 at different concentration of pro-drug-free drug formulation. Here also the **FCD_b**-PTX formulation successfully exhibited synergistic action towards efficient killing compared to that of only PTX and/or **FCD_b** as a result of combination therapy and at the same time it was selective to cancer cells. In comparison to the free PTX, **FCD**, **FCD_b** and **FCD**-PTX, the pro-drug-free drug formulation of **FCD_b**-PTX was found to be most effective and selective in killing cancer cells. Covalent surface modification of Fe^{2+} doped carbon dot by biotin moiety converted the native **FCD** to target-specific **FCD_b** which has been evident from its selective diagnosis of cancer cells to target specific killing of malignant cells by only **FCD_b** as well as by the combined formulation of **FCD_b**-PTX. Once again, the existence of biotin moiety in **FCD_b**-PTX formulation boosted the target-specific internalization within B16F10 cells resulting in specific and effective death of cancer cells. Notably, combination of two modes of cancer therapy (oxidative DNA damage by **FCD_b** induced ROS and anticancer effect by PTX) led to higher killing of cancer cells even with the lower dose of PTX, which is expected to minimize the PTX induced systemic side effects. Hence, **FCD_b**-PTX may emerge as a potential theranostic agent in the field of combination therapy for treating cancer.

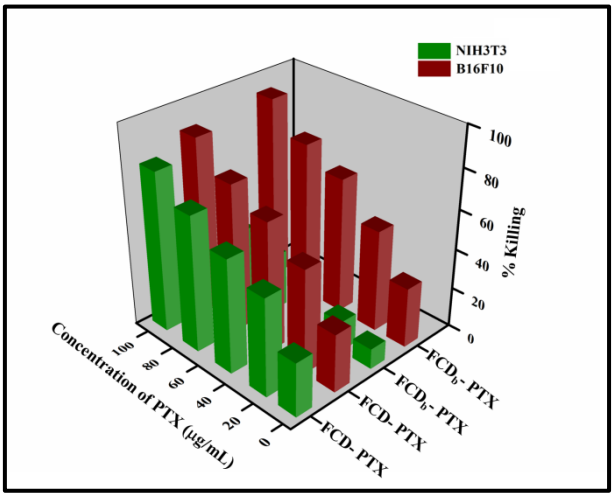

Figure 20. % Killing of cells determined by MTT assay. NIH3T3 and B16F10 cells incubated with varying concentrations of **FCD**-PTX ([**FCD_b**] =10- 200 μg/mL and [PTX] = 5-100 μg/mL) and **FCD_b**-PTX ([**FCD_b**] =10- 200 μg/mL and [PTX] = 5-100 μg/mL for 12 h. The standard deviation and experimental errors were in the range of 1-3% and 3-5%, respectively in triplicate experiments.

The half inhibitory concentration (IC_{50}) calculated for **FCD_b**-PTX for B16F10 cells was 24 µg/mL (Figure 19d). In case of normal cell NIH3T3, we could not measure the IC_{50} value for **FCD_b**-PTX. Furthermore, for free PTX the half inhibitory concentration could not be measured in the case of both NIH3T3 and B16F10 within the investigated experimental concentration. Thus, it can be concluded that combined pro-drug-free drug formulation of **FCD_b**-PTX has high therapeutic efficacy with marked selectivity towards B16F10 cancer cells.

We also performed cancer cell killing experiment where the biotin-mediated specific transportation of **FCD_b** and **FCD_b**-PTX within B16F10 cells was examined by pre-treating the cells with biotin. The biotin receptor positive B16F10 cells were pre-incubated with biotin solution (2 mM) for 1 h and the treated cells were incubated with the **FCD_b**(10- 200 µg/mL) and **FCD_b**-PTX ([**FCD_b**] =10- 200 µg/mL and [PTX] = 5-100 µg/mL for another 12 h, separately. The % killing of B16F10 cells observed from 5% ± 2% to 14% ± 3% and from 10% ± 1% to 24% ± 2% for **FCD_b** (10-200 µg/mL) and **FCD_b**-PTX ([**FCD_b**] =10- 200 µg/mL and [PTX] = 5-100 µg/mL, respectively(Figure 21a,b). These experimental results showed that the extent of killing of biotin receptor positive B16F10 cells were significantly less as compared to that observed for the biotin-untreated B16F10 cells (15 ± 1% to 50 ± 1% for **FCD_b**;30 ± 2% to 92 ± 1% for **FCD_b-PTX**, Figure 19). The pre-treatment with the biotin led to the blocking of the overexpressed biotin receptors in the biotin receptor positive B16F10 cells and subsequently both **FCD_b** and **FCD_b**-PTX could not get internalized in biotin-treated cancerous cells (B16F10) significantly as compared to that of biotin-untreated B16F10 cells. These data further suggest the biotin receptor-mediated target specific internalization of **FCD_b** and **FCD_b**-PTX within in cancer cells.

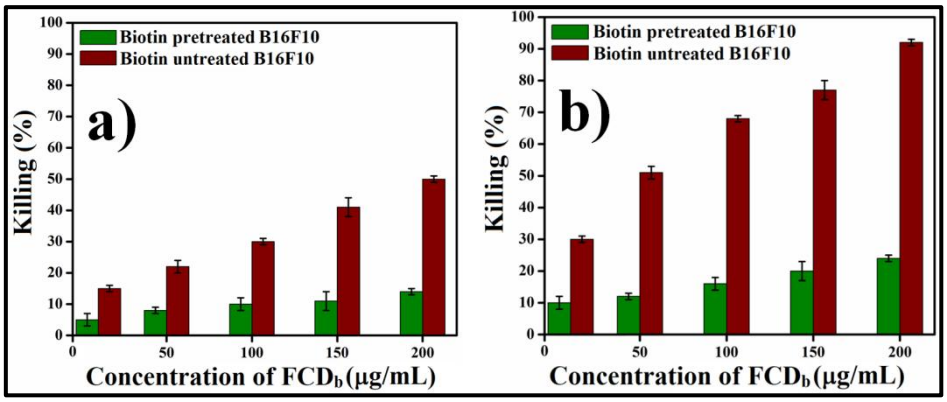

Figure 21. Percentage killing of biotin pre-treated and biotin untreated B16F10 cells with varying concentrations of a) **FCD_b** (10- 200 μg/mL) and b) **FCD_b**-PTX ([**FCD_b**] =10-200 μg/mL and [PTX] = 5-100 μg/mL for 12 h. The standard deviation and experimental errors were in the range of 1-3% and 3-5%, respectively in triplicate experiments.

The selectivity of the combined pro-drug-free drug formulation was further tested by LIVE/DEAD viability kit assay for NIH3T3 and B16F10 cells upon treatment with **FCD_b**-PTX and **FCD**-PTX ([**FCD_b/FCD**] = 100 μg/mL and [PTX] = 50 μg/mL) for 12 h. Fluorescence images were recorded after incubating the treated cells with LIVE/DEAD viability kit for 30 min. In case of **FCD_b**-PTX, primarily presence of green cells was noted for the non-cancer NIH3T3 cell (Figure 22a,b) while for B16F10 cells both green and red cells were observed (Figure 22c,d). Presence of only green cells for NIH3T3 obviously indicates the abundance of alive cells as **FCD_b**-PTX did not get transferred inside the non-cancer cells in absence of biotin receptors. On the other hand, presence of both green and red cells delineates the maximum presence of dead cells for B16F10 owing to the successful internalization of **FCD_b**-PTX within cancer cells having over-expressed biotin receptors on its surface. Interestingly, in case of **FCD**- PTX (devoid of biotin unit), the presence of green and red cells in both NIH3T3 and B16F10 once again points out the non-selective killing of both normal and cancer cells (Figure 23). Hence, LIVE/DEAD assay further concluded the target specific theranostic ability of the biotin comprised pro-drug-free drug formulation of **FCD_b**-PTX in combination cancer therapy.

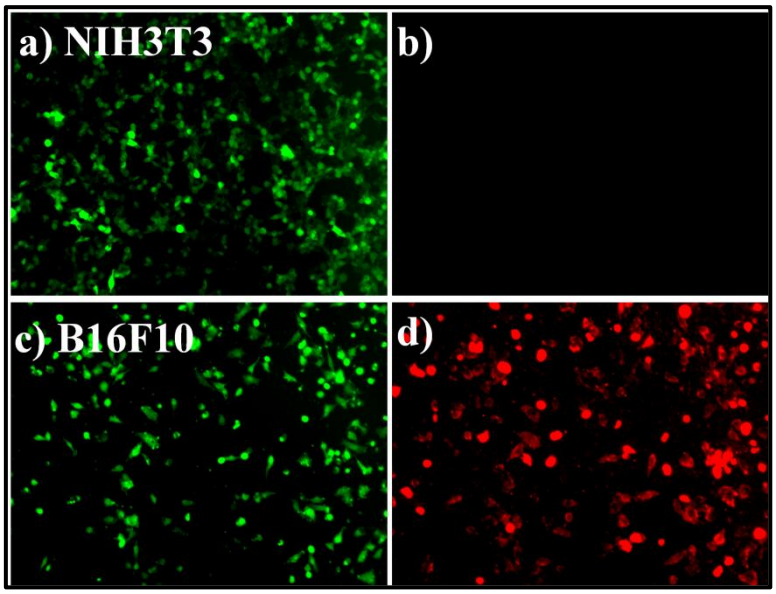

Figure 22. LIVE/DEAD fluorescence microscopic images of the cells incubated for 12 h with **FCD_b**-PTX ([**FCD_b**] = 100µg/mL and [PTX] = 50µg/mL), (a and b) NIH3T3 cells, (c and d) B16F10 cells. Scale bars correspond to 20 µm.

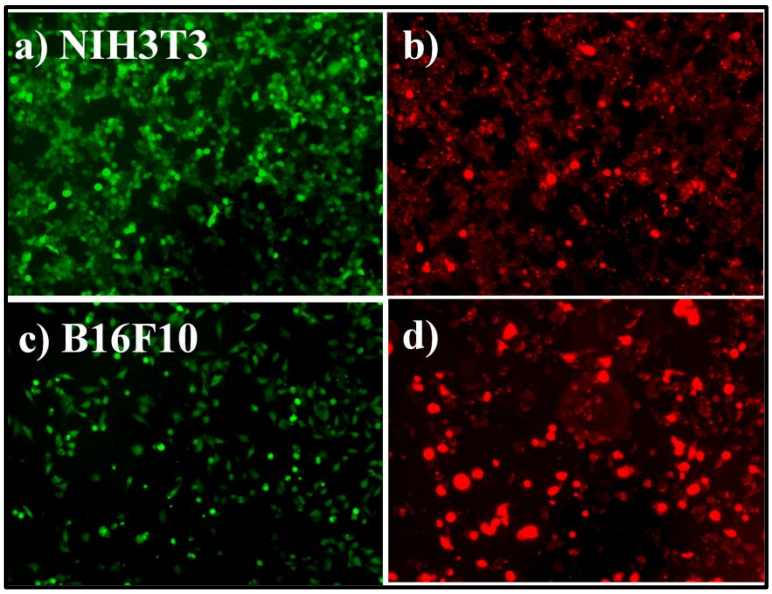

Figure 23. LIVE/DEAD fluorescence microscopic images of the cells incubated for 12 h with **FCD**-PTX ([**FCD**] = 100µg/mL and [PTX] = 50µg/mL), (a and b) NIH3T3 cells, (c and d) B16F10 cells. Scale bars correspond to 20 µm.

2.8 Cell Apoptosis.

Killing pathway of B16F10 cells by free PTX, **FCD**, **FCD_b** and **FCD_b**-PTX were investigated by flow cytometric assay using Annexin V-FITC and PI dye. FITC Annexin V is used to quantitatively determine the percentage of cells within a population that are actively undergoing apoptosis. In apoptotic cells, phosphatidylserine (PS) is translocated from the inner leaflet of the plasma membrane to the outer leaflet, thereby exposing PS to the external environment. Annexin V is a calcium-dependent phospholipid-binding protein that has a high affinity for PS, and is useful for identifying apoptotic cells with exposed PS. Propidium Iodide (PI) is a standard flow cytometric viability probe and is used to distinguish viable from non-viable cells. Membranes of viable cells exclude PI, whereas the membranes of dead and damaged cells are permeable to PI. Cells that stain positive for FITC Annexin V and negative for PI are undergoing apoptosis. Cells that stain positive for both FITC Annexin V and PI are either in the end stage of apoptosis, are undergoing necrosis, or are already dead. Cells that stain negative for both FITC Annexin V and PI are alive and not undergoing measurable apoptosis. There are four different quadrants in the scatter plot on variation of both Annexin V-FITC and PI dye, which indicates the nature of the investigating cells. The population of necrotic cells is observed in Q1 quadrant where Annexin V-FITC negative and PI positive. Q2 shows the population of late apoptotic cells having both Annexin V-FITC and PI positive and Q3 having both Annexin V-FITC and PI negative, exhibits the population of alive cells. In Q4 quadrant population of the early apoptotic cells is noted with Annexin V-FITC positive and PI negative. B16F10 cells were individually treated with free paclitaxel (50 µg/mL), **FCD** (100 µg/mL), **FCD_b** (100 µg/mL), and combined formulation of **FCD_b**-PTX ([**FCD_b**] = 100 µg/mL and [PTX] = 50 µg/mL) for 6 h (Figure 24). These separately treated cells were detached and incubated with both Annexin V-FITC and PI dye and analyzed by flow cytometry. The B16F10 cells without any treatment showed a maximum population at Q3, indicating cells were intact in its native state. Free paclitaxel treated B16F10 cells showed a large population at Q3, some at Q4, and very few population was dispersed between Q1, and Q2 (Figure 24b). This indicates PTX induced killing of

cancer cells primarily took place through early apoptosis and a smaller extent by late apoptosis. In case of **FCD** and **FCD_b**, a significant population at Q4, depicts the early apoptotic pathway of killing of B16F10 cells (Figure 24c,d). Interestingly, cells treated with **FCD_b**-PTX showed maximum population at Q4, and few at Q2. This observation indicates killing of cancer cells primarily took place through early apoptotic pathway and late apoptotic for some number of cells (Figure 24e). Thus, biotin receptor-mediated cellular transportation of **FCD_b**-PTX nanohybrids selectively killed B16F10 cells through early as well as late apoptotic pathway.

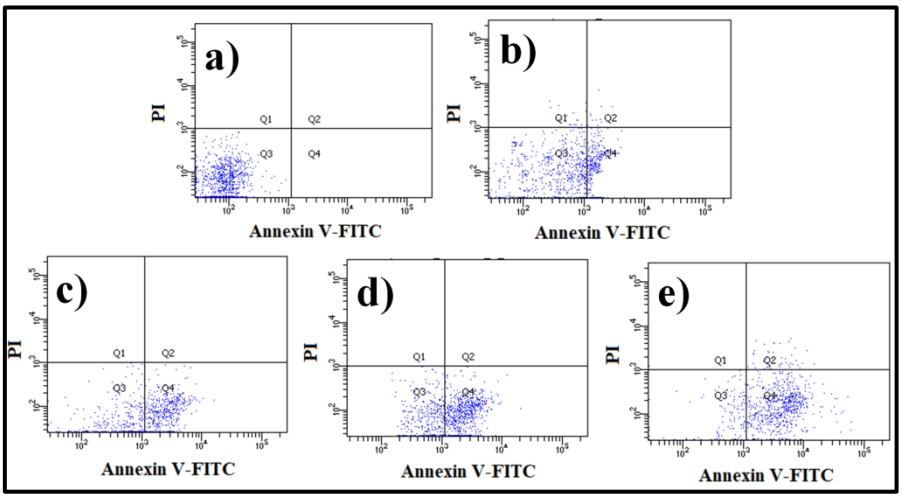

Figure 24. Flow cytometric analysis of apoptosis in a) untreated B16F10 cells. B16F10 cells treated with b) free paclitaxel (50 μg/mL), c) **FCD** (100 μg/mL), d) **FCD_b** (100 μg/mL), e) **FCD_b**- PTX ([**FCD_b**] = 100 μg/mL and [PTX] = 50 μg/mL).

3.CONCLUSION

In summary, I have developed biotin modified surface engineered Fe^{2+} doped carbon dot (**FCD_b**) which can selectively sense and activate H_2O_2 as well as target specifically delivered anticancer drug paclitaxel inside cancer cells. This theranostic agent **FCD_b** showed excellent stability in the biological milieu. H_2O_2 act as a pro-drug in presence of **FCD_b** which has been used in its sensing as well as bioimaging by exploiting the intrinsic fluorescence of **FCD_b**. This sensing and imaging were primarily based on the Fe^{2+} induced production of ROS (hydroxyl/superoxide radicals) from pro-drug H_2O_2 that quenched the intrinsic emission of **FCD_b**. On the basis of this Fe^{2+} doped carbon dot induced ROS production, biotin comprised **FCD_b**

can clearly distinguish between malignant cells B16F10 over non-malignant cells NIH3T3 owing to the fact that both biotin receptors and H_2O_2 was over expressed in malignant cells. **FCD_b** also showed the excellent ability of uploading anticancer drug paclitaxel (**FCD_b**-PTX). This newly developed pro-drug-free drug formulation exhibited ~2.7 to 3.5-fold higher killing of B16F10 cancer cells mostly via early as well as late apoptotic path in comparison to non-cancer NIH3T3 cells in the present combination therapy. Hence, this biotin modified Fe^{2+} doped carbon dot may act as potential candidates as cancer-targeting theranostic agent.

4.EXPERIMENTAL SECTION

4.1 Materials

All chemical reagents, solvents, deuteriated solvents were bought from Thermo Scientific, SRL, Sigma-Aldrich, respectively. Cell culture reagents were purchased from Invitrogen. Normal and cancer cells were received from NCCS, Pune, India. Varian Cary Eclipse luminescence spectrometer, Perkin Elmer Lambda 25 and Spectrum 100 were used to perform fluorescence, UV-vis and FTIR spectra, respectively.

4.2 Synthesis of Native Fe^{2+}-doped Carbon Dot (FCD).

Fe^{2+} doped carbon dot (**FCD**) was synthesized by hydrothermal route. 3.0 g of mono hydrated citric acid (14 mmol), 0.84 g of ethylenediamine (14 mmol) and 3.89 g of hydrated ferrous sulphate ($FeSO_4.7H_2O$) were dissolved in Milli-Q water maintaining 1:1:1 molar ratio. The solution was mixed and sonicated to obtain a transparent solution. The solution was heated at 120 °C for 10 h in a heating platform. The color of the solution gradually turned to brown. The supernatant was obtained after centrifugation at 12000 rpm for 10 min and it was dried using lyophilizer to collect the **FCD** having yield ~68%.

4.3 Synthesis of Surface Modified Fe^{2+}-doped Carbon Dot (FCD_b).

To synthesize biotin tagged surface modified Fe^{2+}-doped carbon dot (**FCD_b**), we took the mixture of above synthesized 1 equiv of **FCD**, 10 equiv of 1-ethyl-3-(3-

(dimethylamino)propyl)-carbodiimide (EDC), 10 equiv of 4-(N,N-dimethylamino) pyridine (DMAP), and 10 equiv of D-biotin in dry DMF and it was stirred for 12 h. After drying the DMF, DCM was added to the crude and the filtrate was evaporated. Next, the dialysis was carried out (MWCO - 3.5K) in PBS buffer (pH = 7.4) and the compound in dialysis tube was lyophilized to obtain biotin modified Fe^{2+} doped carbon dot (**FCD_b**)(Scheme 2).

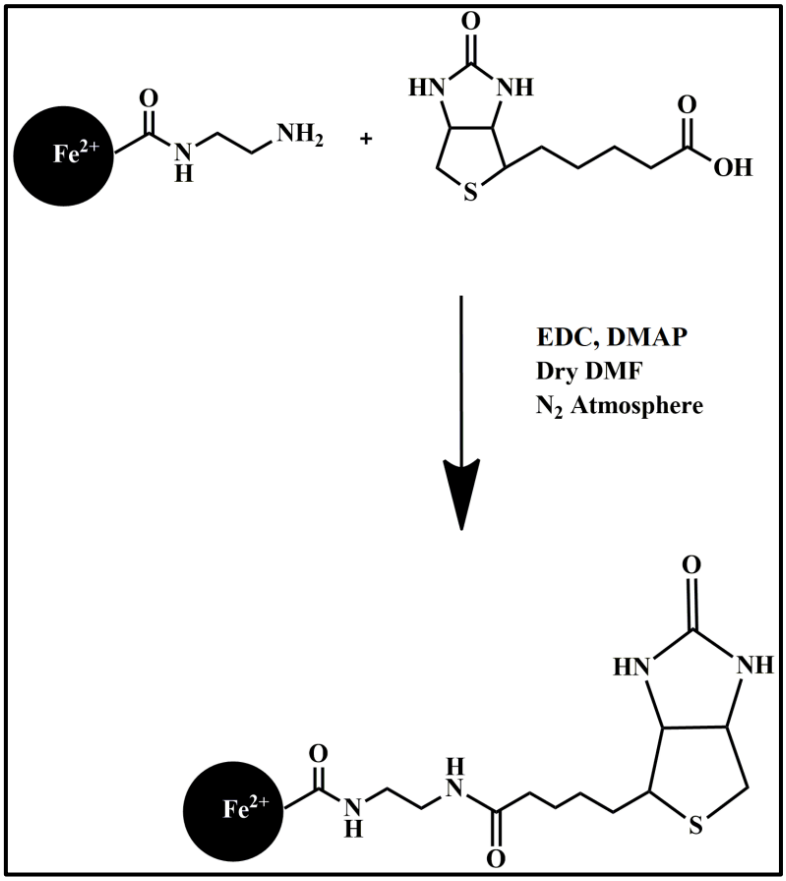

Scheme 2. Synthetic scheme of **FCD_b**.

4.4 Characterization.

Aqueous solution of **FCD_b** was sonicated for 10 min and then Cu-coated grid was used for drop casting of **FCD_b** and dried for imaging in transmission electron microscope (TEM, 2100F UHR microscope JEOL JEM). In case of atomic force microscopic (AFM) imaging (Veeco, model AP0100 microscope), a drop of **FCD_b** solution was air dried on fresh mica surface overnight. For X-ray photoelectron spectroscopy (XPS) (Omicron series 0571) **FCD_b** solution (10 µL) was dried over

night on rectangular Cu plates. Energy-dispersive X-ray (EDX) analysis was investigated using Oxford make EXTREME INCA microscope. X-ray diffraction (XRD) spectra of **FCD_b** were obtained on a diffractometer (Bruker D8 Advance). The zeta (ζ) potential measurements were investigated with aqueous solutions of **FCD_b** at room temperature. All the above-mentioned characterizations were carried out similarly for **FCD**. In case of **FCD_b**-PTX, microscopic characterizations such as TEM and XRD experiments were carried out in similar way.

4.5 Fluorescence Spectroscopy.

Fluorescence spectra of 25 μg/mL of **FCD_b** were recorded with varying λ_{ex} from 220 to 270 nm (excitation and emission slits at 10 nm). In case of 25 μg/mL of **FCD**, the excitation dependent emission spectra were recorded at λ_{ex} = 230 nm (excitation and emission slits at 10 nm). The variation of the fluorescence of 25 μg/mL of **FCD_b** and **FCD** was studied by adding different concentrations of H_2O_2 (1-100 μM). The intensity of fluorescence was measured at 469 nm for **FCD_b** and at 460 nm for **FCD** upon exciting both **FCD_b** and **FCD** at 230 nm. Fluorescence spectra of **FCD_b**-PTX were recorded in similar way. The emission maximum was 468 nm when excited at λ_{ex} = 230 nm (excitation and emission slits at 10 nm).

4.6 UV-vis Spectroscopy.

We wanted to investigate the ROS production from hydrogen peroxide in presence of both **FCD_b** and **FCD**, using 1,3-diphenylisobenzofuran (DPBF) by UV-vis spectroscopy. Peltier thermostat was used to keep the sample temperature fixed at 25 °C. Various sample sets were prepared having (i) only 20 μg/mL of DPBF; (ii) 25 μg/mL of **FCD_b** with 20 μg/mL of DPBF; (iii) 20 μg/mL of DPBF and H_2O_2 (5 μM) and (iv) 25 μg/mL of **FCD_b** with 20 μg/mL of DPBF and different concentration of H_2O_2 (1-35 μM). Similar experiments were also carried out using 25 μg/mL of **FCD_b**, 20 μg/mL of DPBF, H_2O_2 (35 μM) and varying concentration of thiourea from 1 to 4 μM. Next for oxidative DNA damage investigation utilizing **FCD_b** we prepared various conjugated sets having 25 μg/mL of **FCD_b**, and 25 μg/mL of calf thymus (CT) DNA. **FCD_b** and CT-DNA were mixed, shaken for 15 min, and centrifuged (12000 rpm, 30 min). CT-DNA pellets were suspended in PBS buffer solution

having pH = 7.4. Three controlled sets with only 25 µg/mL of CT-DNA, 25 µg/mL of CT-DNA-25 µg/mL of **FCD_b** and 25 µg/mL of CT-DNA - H_2O_2 (5 µM) in PBS buffer were also prepared. All the above-mentioned UV-vis experiments including CT-DNA studies were carried out similarly for **FCD**.

4.7 Circular Dichroism.

The sets containing CT-DNA and **FCD_b**-CT-DNA conjugates at a specific H_2O_2 concentration were investigated in circular dichroism spectra (JASCO Model J-815 spectropolarimeter). 220-320 nm was used which is far-UV region, to record the spectra (scan speed - 50 nm/min). Peltier thermostat was used to fix the sample temperature at 25 °C. The concentration of CT-DNA, **FCD_b** and H_2O_2 was 25 µg/mL, 25 µg/mL and 15 µM, respectively. Similar experimental method was used for **FCD**.

4.8 Fourier Transform Infrared Study.

FTIR (Fourier transform infrared) measurement was investigated for paclitaxel (PTX) in CH_3OD. For paclitaxel loaded Fe^{2+} doped carbon dots(**FCD_b/FCD**-PTX)and **FCD_b/FCD** FTIR was performed in D_2O. Potassium bromide (KBr) was used to mix with all the compounds separately and a hydraulic press was used to granulate them. The range of the spectra was from 400 to 4000 cm^{-1} and all spectra were normalized and scaled. Perkin Elmer Spectrum 100 FTIR spectrometer was used to perform all the experiments using a 1 mm CaF_2 cell.

4.9 Media Stability of FCD_b and FCD.

Stability of aqueous solutions of **FCD/FCD_b** (25 µg/mL) in biological media was investigated using DMEM media where concentration of FBS varied from 0 to 75%. Also, DMEM media (10% FBS) was added to aqueous solutions of **FCD/FCD_b** (25 µg/mL) to study its stability for 10 days. For the above cases the supernatant was collected at varied time points and the absorbance was noted at 295 nm to calculate suspension stability index (SSI).

SSI = $A_t/A_0 \times 100$ where A_t = absorbance of the solution after a specific time span at 295 nm, and A_0 = initial absorbance of the solution at 295 nm.

CHAPTER 2

Paclitaxel-Loaded Biotinylated Fe^{2+}-Doped Carbon Dot…

4.10 Cell Culture.

10% FBS, antibiotic (streptomycin and penicillin) added DMEM media were used to culture NIH3T3 and B16F10 cells in incubator (5% CO_2 and 37 °C). Both type of cells was cultured and trypsinization was performed after every 3 days when the cells were 80% confluent which then used for further studies.

4.11 Bioimaging.

Non-cancerous NIH3T3 and cancer cells B16F10 were cultured ($1x10^4$ cells per well) in a chamber slide. **FCD_b** (100 µg/mL) and **FCD** (100 µg/mL) were separately added to the chamber slide of both type of cells for 6 h incubation. PBS buffer (pH = 7.4) was used for washing of the incubated cells two times. Followed by 4% paraformaldehyde solution was used for fixing purpose (30 min) and 50% glycerol was used for mounting. The cells on slide were covered and kept for 24 h. Olympus IX83 inverted microscope was used for imaging purpose having an excitation filter of BP 330-385 nm and a band absorbance filter below 405 nm at 40x and 20x magnification.

4.12 Co-culture experiment.

NIH3T3 and B16F10 cells were grown in culture flask separately in an incubator (5% CO_2) at 37 °C. Streptomycin and penicillin were used in the cell culture flask. For this experiment we mixed the population of both type of cells (NIH3T3 : B16F10 = 1 : 1) in two wells of the chamber slide by trypsinizing them for 24 h. **FCD_b** (100 µg/mL) and **FCD** (100 µg/mL) separately incubated in those wells for 6 h. After 6 h cells were fixed by performing same cell fixing procedure mentioned above. Images were taken using an IX83 inverted microscope at 20x magnification.

4.13 Loading of Paclitaxel.

To the aqueous **FCD/FCD_b** solutions (1 mg/mL), methanolic solution of paclitaxel (0.5 mg/mL) was added. The mixture was taken in a 10 mL volumetric flask containing 1 mg of **FCD/FCD_b** and 0.5 mg of paclitaxel (PTX) and stirred for 24 h in dark. Thermo Scientific SnakeSkin 3.5K MWCO dialysis tubing was used for dialysis. **FCD/FCD_b**-PTX complex were dialyzed in Milli-Q water for 48 h. The drug

loading efficiency was calculated by recording the UV-vis absorbance (227 nm) and calibration curve (y = 0.06655x + 0.03212).

Drug Loading Efficiency (DLE) =

[(Amount of drug taken − free drug)/Amount of drug taken] × 100

4.14 MTT assay.

Killing of normal and cancer cells were determined by the MTT reduction method.[52] NIH3T3 and B16F10 were grown individually in a 96-well plate for 1 day in DMEM media (10% FBS). The cells were individually incubated (5% CO_2 at 37 °C) in presence of **FCD**-PTX, **FCD$_b$**-PTX, **FCD$_b$**, **FCD** and free paclitaxel (PTX) for 12 h followed by incubation with 5 mg/mL MTT dye for 4 h. The **FCD$_b$**, **FCD** and paclitaxel concentrations separately and also in the combined formulations of **FCD**-PTX, **FCD$_b$**-PTX were varied from 10-200 µg/mL, 10-200 µg/mL and 5-100 µg/mL, respectively, maintaining 2:1, w/w. In this MTT reduction method, alive cells produce water insoluble formazan from the tetrazolium salt using mitochondrial dehydrogenase and that was measured by calculating the absorbance of formazan (570 nm, Biotek Elisa Reader) that is correlated to the number of live cells.

The number of alive cells was expressed as percent viability =

(A_{570}(treated cells) - background)/A_{570}(untreated cells) − background) × 100. (1)

Cell killing experiment was also performed upon pre-treatment of B16F10 cells with excess biotin solution (2 mM). Cells were incubated with **FCD$_b$** and **FCD$_b$**-PTX, respectively for 12 h. The number of survived cells was analyzed following eq 1.

4.15 LIVE/DEAD Viability Assay.

MTT assay for cell killing was further studied by LIVE/DEAD assay kit for both normal (NIH3T3) and cancer (B16F10) cells in the presence of **FCD**-PTX and **FCD$_b$**-PTX.[53] In this assay kit there were two nucleic acid binding stains present. One is Calcein AM (acetomethoxy) (component A) which emit green fluorescence that confirmed the presence of live cells and another is Ethidium homodimer-1 (component B), which emit red fluorescence and confirmed the presence of dead

cells. Just before the experiment, 2 mL of PBS buffer solvent was used for the preparation of the mixture of 4 µL of the EthD-1 and 1 µL of the calcein AM and the solutions were vortexed. The mixed solution was added to the cells which were incubated with **FCD**-PTX and **FCD$_b$**-PTX ([**FCD/FCD$_b$**] = 100 µg/mL and [PTX] = 50 µg/mL),respectively. Next, they were incubated for 30 min with LIVE/DEAD assay kit. Imaging was done using Olympus IX83 microscope at 10x magnification. For calcein intercalation BP460-495 nm excitation filter and wavelength below 505 nm band absorbance filter was used. BP530-550 nm excitation filter and wavelength below 570 nm band absorbance filter was used for intercalation of ethidium homodimer-1.

4.16 Flow Cytometry.

Free paclitaxel (PTX), **FCD**, **FCD$_b$**, and **FCD$_b$**-PTX, were taken in well plate B16F10 cells in DMEM media (10% FBS). The final concentration of paclitaxel was fixed at 50 µg/mL whereas the final concentration of **FCD**, **FCD$_b$**, **FCD$_b$**-PTX was fixed at 100 µg/mL in 500 µL of media. After incubation (6 h), cold PBS was used for washing the cells and trypsin was used to detach the cells from the surface of culture flask. The solution was centrifuged to get cell pellets. Pellets were suspended in 500 µL 10X binding buffer containing Annexin VFITC (0.25 µg) and propidium iodide (PI, 1.0 µg). This mixture was incubated for 15 min at room temperature in the dark. Cells ($1x10^4$ per wells) were analyzed using BD FACS Aria™ III flow cytometer by using excitation wavelength 488 nm and recorded the emission wavelength at a 533 ± 30 (FL-1) bandpass filter for Annexin V-FITC and 585 ± 40 nm (FL-2) bandpass filter for PI.

In a separate well plate, normal cells (NIH3T3) and cancer cells (B16F10) were grown for 24 h for bioimaging experiment, which were incubated with **FCD** (100 µg/mL) for 6 h. Subsequently, both the incubated cells were washed with DMEM media and PBS buffer to remove the excess compounds from the cell medium. We used trypsin to detach the cells from the culture flask and centrifuged it for 5 min. After centrifugation, precipitated cells were suspended in PBS (500 mL) and used for the flow cytometric experiment. BD FACS Ariat III flow cytometer was employed to inspect the cells.

6.REFERENCES

1. Maverakis, E.; Cornelius, L. A.; Bowen, G. M.; Phan, T.; Patel, F. B.; Fitzmaurice, S.; He, Y.; Burrall, B.; Duong, C.; Kloxin, A. M.; Sultani, H.; Wilken, R.; Martinez, S. R.; Patel, F. Metastatic Melanoma - a Review of Current and Future Treatment Options. *Acta Derm Venereol* **2015**, *95*, 516-524.

2. Delaney, G.; Barton, M.; Jacob, S. Estimation of an Optimal Radiotherapy Utilization Rate for Melanoma. *Cancer* **2004**, *100*, 1293-1301.

3. Cumberlin, R.; DeMoss, E.; Lassus, M.; Friedman, M. Isolation Perfusion for Malignant Melanoma of the Extremity: a Review. *J. Clin. Oncol.* **1985**, *3*, 1022-1031.

4. Win-Piazzaa, H.; Schneebergera, V.; Chena, L.; Pernazzac, D.; Lawrencec, H. R.; Sebtib, S. M.; Lawrencec, N. J.; Wu, J. Enhanced Anti-Melanoma Efficacy of Interferon Alfa-2b via Inhibition of Shp2. *Cancer Lett.* **2012**, *320*, 81-85.

5. Bildstein, L.; Dubernet, C.; Couvreur, P. Prodrug-Based Intracellular Delivery of Anticancer Agents. *Adv. Drug Deliv. Rev.* **2011**, *63*, 3-23.

6. He, H.; Wang, Y.; Wen, H.; Jia, X. Dendrimer-Based Multilayer Nanocarrier for Potential Synergistic Paclitaxel-Doxorubicin Combination Drug Delivery. *RSC Adv.* **2014**, *4*, 3643-3652.

7. Desale, S. S.; Soni, K. S.; Romanova, S.; Cohen, S. M.; Bronich, T. K. Targeted Delivery of Platinum-Taxane Combination Therapy in Ovarian Cancer. *J. Control. Release* **2015**, *220*, 651-659.

8. Ge, Y.; Ma, Y.; Li, L. The Application of Prodrug-Based Nano-Drug Delivery Strategy in Cancer Combination Therapy. *Colloids Surf. B* **2016**, *146*, 482-489.

9. Hu, C. M. J.; Zhang, L. Nanoparticle-Based Combination Therapy toward Overcoming Drug Resistance in Cancer. *Biochem. Pharmacol.* **2012**, *83*, 1104-1111.

10. Al-Lazikani, B.; Banerji, U.; Workman, P. Combinatorial Drug Therapy for Cancer in the Post-Genomic Era. *Nat Biotechnol.* **2012**, *30*, 679-92.

11. Mokhtari, R. B.; Homayouni, T. S.; Baluch, N.; Morgatskaya, E.; Kumar, S.; Das, B.; Yeger, H. Combination Therapy in Combating Cancer. *Oncotarget* **2017**, *8*, 38022-38043.

12. Bala, V.; Rao, S.; Boyd, B. J.; Prestidge, C. A. Prodrug and Nanomedicine Approaches for the Delivery of the Camptothecin Analogue SN38. *J. Control. Release* **2013**, *172*, 48-61.

13. Guo, Q.; Wang, H.; Zhao, Y.; Wang, H.; Zeng, F.; Hua, H.; Xu, Q.; Huang, Y. Cell-Penetrating Albumin Conjugates for Enhanced Doxorubicin Delivery. *Polym. Chem.* **2013**, *4*, 4584-4587.

14. Chen, Y.; Zhang, W.; Huang, Y.; Gao, F.; Sha, X.; Fang, X. Pluronic-Based Functional Polymeric Mixed Micelles for Co-delivery of Doxorubicin and Paclitaxel to Multidrug Resistant Tumor. *Int. J. Pharm.* **2015**, *488*, 44-58.

15. Szatrowski, T. P.; Nathan, C. F. Production of Large Amounts of Hydrogen Peroxide by Human Tumor cells. *Cancer Res.* **1991**, *51*, 794-798.

16. Burdon, R. H. Superoxide and Hydrogen Peroxide in Relation to Mammalian Cell Proliferation. *Free Radical Biol. Med.* **1995**, *18*, 775-794.

17. Toyokuni, S.; Okamoto, K.; Yodoi, J.; Hiai, H. Persistent Oxidative Stress in Cancer. *FEBS Lett.* **1995**, *358*, 1-3.

18. Okamoto, K.; Toyokuni, S.; Kim, W.; Ogawa, O.; Kakehi, Y.; Arao, S.; Hiai, H.; Yoshida, O. Over Expression of Human mutT Homologue Gene Messenger RNA in Renal-Cell Carcinoma: Evidence of Persistent Oxidative Stress in Cancer. *Int. J. Cancer* **1996**, *65*, 437-441.

19. Chakraborty, D.; Sarkar, S.; Das, P. K. Blood Dots: Hemoglobin-Derived Carbon Dots as Hydrogen Peroxide Sensors and Pro-Drug Activators, *ACS Sustainable Chem. Eng.* **2018**, *6*, 4661-4670.

20. Dinda, S.; Sarkar S.; Das, P. K. Glucose Oxidase Mediated Targeted Cancer Starving Therapy by Biotinylated Self-assembled Vesicles. *Chem. Commun.* **2018**, *54*, 9929-9932.

21. Wlassoff, W. A.; Albright, C. D.; Sivashinski, M. S.; Ivanova, A.; Appelbaum, J. G.; Salganik, R. I. Hydrogen Peroxide Overproduced in Breast Cancer Cells can Serve as an Anticancer Prodrug Generating Apoptosis-Stimulating Hydroxyl Radicals under the Effect of Tamoxifen Ferrocene Conjugate. *J. Pharm. Pharmacol.* **2007**, *59*, 1549-1553.

22. Sadrzadeh, S. M.; Graf, E.; Panter, S. S.; Hallaway, P. E.; Eaton, J. W. Hemoglobin. A Biological Fenton Reagent. *J. Biol. Chem.* **1984**, *259*, 14354-14356.

23. Ensing, B.; Baerends, E. J. Reaction Path Sampling of the Reaction between Iron(II) and Hydrogen Peroxide in Aqueous Solution. *J. Phys. Chem. A* **2002**, *106*, 7902-7910.

24. Lin, S. S.; Gurol, M. D. Catalytic Decomposition of Hydrogen Peroxide on Iron Oxide: Kinetics, Mechanism, and Implications. *Environ. Sci. Technol.* **1998**, *32*, 1417-1423.

25. Jia, J.; Zhu, F.; Ma, X.; Cao, Z. W.; Li, Y. X.; Chen, Y. Z. Mechanisms of Drug Combinations: Interaction and Network Perspectives, *Nat. Rev. Drug Discov.* **2009**, *8*, 111-128.

26. Denny, W. A. Tumor-Activated Prodrugs-A New Approach to Cancer Therapy. *Cancer Invest.* **2004**, *22*, 604-619.

27. Nam, K.; Nam, H. Y.; Kim, P. H.; Kim, S. W. Paclitaxel-Conjugated PEG and Arginine-Grafted Bioreducible Poly (disulfide amine) Micelles for Co-delivery of Drug and Gene. *Biomaterials* **2012**, *33*, 8122-8130.

28. Feng, T.; Tian, H.; Xu, C.; Lin, L.; Xie, Z.; Lam, M. H. W.; Liang, H.; Chen, X. Synergistic Co-delivery of Doxorubicin and Paclitaxel by Porous PLGA Microspheres for Pulmonary Inhalation Treatment. *Eur. J. Pharm. Biopharm* **2014**, *88*, 1086-1093.

29. Jeon, M.; Lin, G.; Stephen, Z. R.; Kato, F. L.; Zhang, M. Paclitaxel-Loaded Iron Oxide Nanoparticles for Targeted Breast Cancer Therapy. *Adv. Therap*. **2019**, *2*, 1900081 (1-8).

30. Herves, A. S.; Würfel, P.; Wegner, N.; Khandare, J.; Licha, K.; Haag, R.; Welker, P.; Calderón, M. Dendritic Polyglycerol Sulfate as a Novel Platform for Paclitaxel Delivery: Pitfalls of Ester Linkage. *Nanoscale* **2015**, *7*, 3923-3932.

31. Shenoy, V. S.; Gude, R. P.; Nikam, Y.; Murthy, R. S. R. In Vitro Cytotoxic Potential of Paclitaxel-Encapsulated Lipid-Based Drug Delivery Systems. *Austin J Lung Cancer Res*. **2017**, *2*, 1011(1-5).

32. Brahmachari, S.; Ghosh, M.; Dutta, S.; Das, P. K. Biotinylated Amphiphile-Single Walled Carbon Nanotube Conjugate for Target Specific Delivery to Cancer Cells. *J. Mater. Chem. B* **2014**, *2*, 1160-1173.

33. Ahmed, K. K.; Geary, S. M.; Salem, A. K. Surface Engineering Tumor Cells with Adjuvant-Loaded Particles for Use as Cancer Vaccines. *J. Control.Release* **2017**, *248*, 1-9.

34. Yang, W.; Cheng, Y.; Xu, T.; Wang, X.; Wen, L. Targeting Cancer Cells with Biotin-Dendrimer Conjugates. *Eur. J. Med. Chem*. **2009**, *44*, 862-868.

35. Yellepeddi, V. K.; Kumar, A.; Palakurthi, S. Biotinylated Poly(amido)amine (PAMAM) Dendrimers as Carriers for Drug Delivery to Ovarian Cancer Cells in Vitro. *Anticancer Res*. **2009**, *29*, 2933-2944.

36. Baker, S. N.; Baker, G. A. Luminescent Carbon Nanodots: Emergent Nanolights. *Angew. Chem., Int. Ed*. **2010**, *49*, 6726-6744.

37. Sarkar, S.; Das, K.; Das, P. K. Estradiol Hemisuccinate-Modified Surface-Engineered Carbon Dots: Target-Specific Theranostic Agent. *ACS Sustainable Chem. Eng*. **2017**, *5*, 8356-8369.

38. Datta, K. K. R.; Qi, G.; Zboril, R.; Giannelis, E. P. Yellow Emitting Carbon Dots with Superior Colloidal, Thermal, and Photochemical Stabilities. *J. Mater. Chem. C* **2016**, *4*, 9798-9803.

39. Bourlinos, A. B.; Stassinopoulos, A.; Anglos, D.; Zboril, R.; Karakassides, M.; Giannelis, E. P. Surface Functionalized Carbogenic Quantum Dots. *Small* **2008**, *4*, 455-458.

40. Cao, L.; Wang, X.; Meziani, M. J.; Lu, F. S.; Wang, H. F.; Luo, P. G.; Lin, Y.; Harruff, B. A.; Veca, L. M.; Murray, D.; Xie, S. Y.; Sun, Y. P. Carbon Dots for Multiphoton Bioimaging. *J. Am. Chem. Soc.* **2007**, *129*, 11318-11319.

41. Hansen, M. B.; Nielsen, S. E.; Berg, K. Re-examination and Further Development of a Precise and Rapid Dye Method for Measuring Cell Growth/Cell Kill. *J. Immunol. Methods* **1989**, *119*, 203-210.

42. Ghosh, M.; Das, P. K. Doxorubicin Loaded 17β-estradiol based SWNT Dispersions for Target Specific Killing of Cancer Cells. *Colloids Surf. B* **2016**, *142*, 367-376.

43. Yamashita, T.; Hayes, P. Analysis of XPS Spectra of Fe^{2+} and Fe^{3+} Ions in Oxide Materials. *Appl. Surf. Sci.* **2008**, *254*, 2441-2449.

44. Tran, T.; Song, M. Y.; Singh, K. P.; Yang, D.; Yu, J. S. Iron-Polypyrrole Electrocatalyst with Remarkable Activity and Stability for ORR in Both Alkaline and Acidic Conditions: A Comprehensive Assessment of Catalyst Preparation Sequence. *J. Mater. Chem. A* **2016**, *4*, 8645-8657.

45. Chowdhury, M.; Sarkar, S.; Das. P. K. Photosensitizer Tailored Surface Functionalized Carbon Dots for Visible Light Induced Targeted Cancer Therapy *ACS Appl. Bio Mater.* **2019**, *2*, 4953-4965.

46. Oberley, T. D.; Oberley, L. W. Antioxidant Enzyme Levels in Cancer. *Histol. Histopathol.* **1997**, *12*, 525-535.

47. Punnonen, K.; Ahotupa, M.; Asaishi, K.; Hyiity, M.; Kudo, R.; Punnonen, R. Antioxidant Enzyme Activities and Oxidative Stress in Human Breast Cancer. *J. Cancer Res. Clin. Oncol.* **1994**, *120*, 374-377.

48. Li, X.; Zhang, S.; Kulinich, S. A.; Liu, Y.; Zeng, H. Engineering Surface States of Carbon Dots to Achieve Controllable Luminescence for Solid-Luminescent Composites and Sensitive Be^{2+} Detection. *Sci. Rep.* **2015**, *4*, 4967-4974.

Paclitaxel-Loaded Biotinylated Fe^{2+}-Doped Carbon Dot…

49. Wang, Y.; Wang, H.; Liu, D.; Song, S.; Wang, X.; Zhang, H. Graphene Oxide Covalently Grafted Upconversion Nanoparticles for Combined NIR Mediated Imaging and Photothermal/Photodynamic Cancer Therapy. *Biomaterials* **2013**, *34*, 7715-7724.

50. Wu, M.; Xia, Xi. M.; Cui, C.; Yu, P.; Zhang, Y.; Liu, L.; Zhuo, R. X.; Huang, S. W. Highly Efficient Loading of Amorphous Paclitaxel in Mesoporous Hematite Nanorods and Their in Vitro Antitumor Activity. *J. Mater. Chem. B* **2013**, *1*, 1687-1695.

51. Yu, H.; Wang, Y.; Wang, S.; Li, X.; Li, W.; Ding, D.; Gong, X.; Keidar, M.; Zhang, W. Paclitaxel-Loaded Core-Shell Magnetic Nanoparticles and Cold Atmospheric Plasma Inhibit Non-Small Cell Lung Cancer Growth. *ACS Appl. Mater. Interfaces* **2018**, *10*, 43462-43471.

52. Zhang, Z.; Wang, X.; Li, B.; Hou, Y.; Cai, Z.; Yangc, J.; Lid, Y. Paclitaxel-Loaded PLGA Microspheres with a Novel Morphology to Facilitate Drug Delivery and Antitumor Efficiency. *RSC Adv.* **2018**, *8*, 3274-328.

53. Jung, Y. K.; Shin, E.; Kim, B. S. Cell Nucleus-Targeting Zwitterionic Carbon Dots. *Sci. Rep.* **2016**, *5*, 18807-18815.

CHAPTER 3

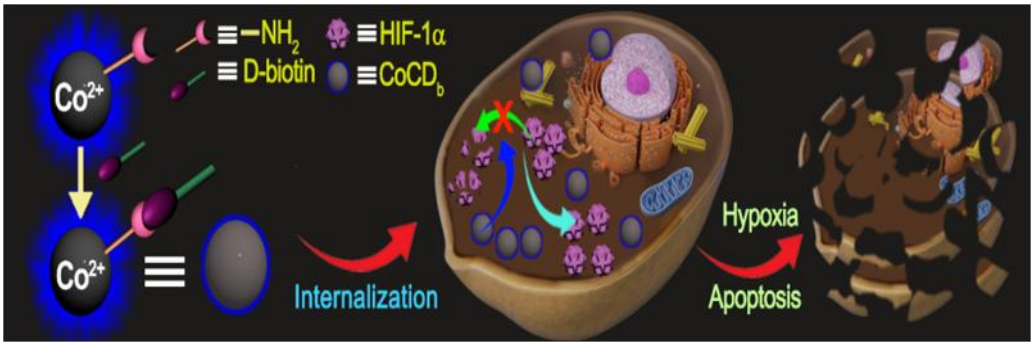

Co^{2+} Doped Biotinylated Carbon Dot: A Theranostic Agent for Target Specific Killing of Cancer Cells via Hypoxia Induced Apoptosis

CHAPTER 3

Co^{2+} Doped Biotinylated Carbon Dot: A Theranostic Agent for …

1.INTRODUCTION

The intricate complexity, diverse gene mutations and potential to invade tissue lineage made the conquest of cancer a great challenge to mankind. For many decades, traditional treatment like surgery, radiotherapy, chemotherapy etc. are the most promising pathways of battling against cancer.[1] As the time went by, notable limitations of these traditional ways of treating cancer made the benefit of the treatments under scrutiny. Surgery is associated with high risk of relapse. Systematic drug therapy (chemotherapy) using anti-cancer drug and radiotherapy are also associated with significant side effects on healthy cells/tissues. On the other hand, immunotherapy is primarily used as an adjuvant therapy.[2-5] Alongside, the non-specificity towards cancer cells and multiple drug resistance demand the development of new alternative paths that can limit the limitations of existing therapies. Hence, the primary focus of strategizing the alternative methods would be to avoid or using minimal help from the traditional systematic therapies. Different characteristics (biochemical, functional and genetical) of cancer cells that distinguish them from normal cells are the important emerging biomarkers for creating alternative therapies.[6-8]

Hypoxia is one of the important features of malignant cells that differ from normal cells. Physiological oxygen concentration in tissues (normoxia) gets reduced during abnormal rate of cell division in cancer progression. This lack of balance in the oxygen level makes the cancer cells hypoxic in nature.[9-11] Evaluation of hypoxia is primarily determined from the expression of endogenous hypoxia-related protein hypoxia-inducible factor (HIF) and the key controller is hypoxia inducible factor 1 (HIF-1). Under hypoxic condition adaptive cellular responses are regulated by the stabilization/degradation ratio of α-subunit of the transcription factor HIF-1. Increase and stabilization of HIF-1α induce several factors that led to cell damage and apoptosis.[12-14] The molecules that are used to stabilize HIF-1α are known as hypoxia-mimetic agents. Some familiar hypoxia-mimetic agents are desferrioxamine (DFO) and cobalt chloride ($CoCl_2$). $CoCl_2$is known to imitate the hypoxia both in vivo and in vitro through inhibition of prolylhydroxylasesdomain-containing protein(PHDs) activity. Co^{2+} substitutes Fe^{2+} in PHDs, the main enzyme that cause

the degradation of HIF-1α under normoxic conditions.[15-18] PHDs catalyses hydroxylation of specific proline residues in HIF-1α.In normoxic condition, 2-oxoglutarate-, O^{2-} and Fe^{2+}-dependent prolyl hydroxylases negatively regulated the expression of HIF-1α. $CoCl_2$ stabilizes HIF-1α from degradation by inhibiting the activity of PHDs, through Fe^{2+} depletion or substitution.So, the hypoxia-mimetic function of cobaltous ions can probably be explained by its inhibition of the the PHDs activity. Co^{2+} acted as pro-drug activator, which can activate HIF-1α and induce apoptotic cell death.[19,20] However, the major limitation of using $CoCl_2$ in cancer treatment is its toxicity to both normal and cancer cells and moreover its non-selectivity towards cancer cells.

Most of the reported drug delivery vehicles also suffers from systematic side effects from the encapsulated anti-cancer drugs. To this end, different types of biocompatible and biomimetic moieties are used in cancer therapy.[21,22] Some are used as diagnostic tools to recognize the change in chemical, biological or physical characteristics of cancer cells. Similarly, therapeutic delivery vehicles can be developed by exploiting the specific biomarker of cancer cells, which will differentiate between cancer and normal cells. However, such examples are really limited.[23,24]To this end, we envisage to develop moieties that can specifically diagnose cancer cells over normal cells and can be used as target specific anti-cancer agent. Subsequently, it should instigate apoptosis by utilizing biochemical environment in cancer cells. Designing of such entities (theranostic agents) having combined properties of diagnostic, therapeutic and target specificity to cancer cells is very challenging.

In this context carbon dot, a zero dimensional carbon nanomaterial, intrinsically fluorescent and biocompatible moiety gained extensive attention in the domain of biomedicine.[25-28] Doping of carbon dot with various materials without affecting itsintrinsic property and using them in therapeutic systems is an interesting research domain, which is growing incessantly over past many years.[29] In this regard, we aim to include Co^{2+} as an integral element of carbon dot (instead of incorporating it as an exogenous agent) that needs to be delivered inside cancer cells.

CHAPTER 3

Co^{2+} Doped Biotinylated Carbon Dot: A Theranostic Agent for …

In the course of developing alternative strategy devoid of chemotherapy in cancer treatment, we report the synthesis and development of biotinylated Co^{2+}-integrated carbon dot ($CoCD_b$) for activating HIF-1α protein, which can specifically and effectively kill cancer cells by hypoxia induced apoptosis. This Co^{2+}-doped carbon dot ($CoCD_b$) was blue-emitting in nature. Co^{2+}- as a doping agent in carbon dot was utilized to activate the pro-drug HIF-1α protein that can induce apoptosis via hypoxia. Alongside, we surface functionalized the carbon dots with biotin moiety that specifically targeted the cancer cells (MDA-MB-231, HeLa) over the normal cells (NIH3T3, HEK-293) as biotin receptors are overexpressed in cancer cells.Various physical characterization and cytocompatibility were conducted before screening the anticancer efficacy of $CoCD_b$ in 2D and 3D cell culture systems. This biotinylated Co^{2+}-doped carbon dot ($CoCD_b$) selectively sensed and killed malignant cells over normal cells via hypoxia induced apoptosis using Co^{2+} as pro-drug activator and HIF-1α as pro-drug. Both 2D and 3D cell studies exhibited ~3-3.1-fold higher killing of cancer cells over normal cells and ~65% killing of tumor spheroid in a span of 72 h.

2.RESULTS AND DISCUSSION

Alternative strategies along with systemic therapies for curbing the deadly cancer had been emerging for past few decades to overcome the limitations of existing systematic therapies. Strategies that include the alteration of specific biological events or biomarkers with high sensitivity towards apoptosis are gaining much attention. Hypoxia is one of the common and important features of cancer cells that predominantly exist across a wide variety of malignancies. Hypoxic stress to cells alters the gene expression regulation that leads to recovery processes or apoptosis depending on the extent of hypoxia generating in the cells. The master regulator of the hypoxia response is hypoxia inducible factor 1 (HIF-1) protein. HIF-1α (one the family members of HIF-1) is important hypoxia inducible factor that is being regulated by the oxygen levels within cells. It was reported that hypoxia-mimetic agent, $CoCl_2$ artificially induces the hypoxia by stabilizing HIF-1α, which subsequently activate hypoxia induced apoptosis. Co^{2+} accumulates HIF-1α protein

through inhibition of activity of PHDs, which is responsible for HIF-1α degradation. So, we aim to use HIF-1α as pro-drug for apoptosis and Co^{2+} as a pro drug activator.[8,30] However, $CoCl_2$ is non-selective towards cancer and normal cells and also toxic in nature. Thus, we fabricated biotin tagged Co^{2+} doped carbon dot as a target specific theranostic agent that can selectively target cancer cells and activateHIF-1α for hypoxia induced apoptosis.

2.1 Synthesis and Characterization of Biotinylated Co^{2+} Doped Carbon Dot ($CoCD_b$) and Native Carbon Dot (CD_b).

Co^{2+} doped carbon dot (**CoCD**) was synthesized via hydrothermal method with equivalent amount of citric acid, ethylenediamine, and $CoCl_2.7H_2O$ (Scheme 1, Experimental section). Citric acid was utilized as source of carbon core, Co^{2+} as doping element and ethylenediamine was utilized for surface functionalization. Synthesized **CoCD** was surface passivated with biotin moiety via covalent amide bond linkage (**$CoCD_b$,** Scheme 1, Experimental section) so as to facilitate targeted delivery by means of recognizing the biotin receptors that are known to over-expressed in malignant cells.[31,32] Biotin (vitamin B7) is an indispensable requisite for the growing cells, especially for the rapidly growing cancer cells where the demand remains highest. Thereby, biotin receptors have become significant target-specific probe. We synthesized another carbon dot (CD) without doping Co^{2+}, using citric acid and ethylenediamine as precursor for control experiment. This CD was also biotinylated to bring in the selectivity towards cancer cells (**CD_b**, Scheme 2, Experimental section). The synthesized **$CoCD_b$** (Figure 1a) and **CD_b** (Figure 2a) were soluble in water and the corresponding zeta potential (ζ) values were found to be -12.73 mV and -16.88 mV, respectively demonstrating its ample stability in aqueous medium. Microscopic analysis of **$CoCD_b$** and **CD_b** was carried out by TEM and AFM. TEM images confirmed the size of **$CoCD_b$** and **CD_b** was between 3-5 nm (Figure 1b, 2b). The data obtained from AFM images also supported the result that was observed in TEM image (Figure 1c, 2c).

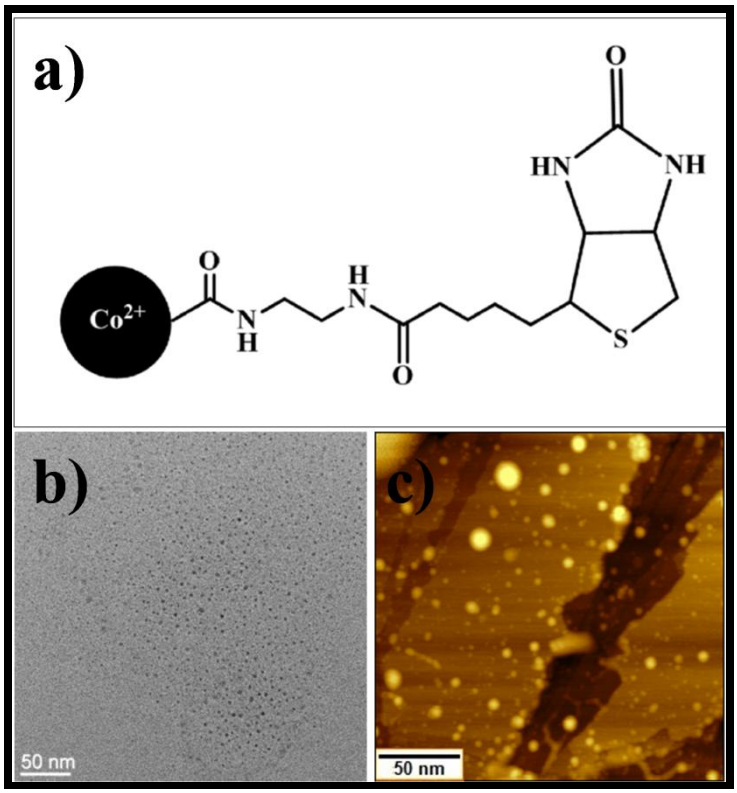

Figure 1. a) Chemical structure of **$CoCD_b$**, b) TEM image, c) AFM image of **$CoCD_b$**.

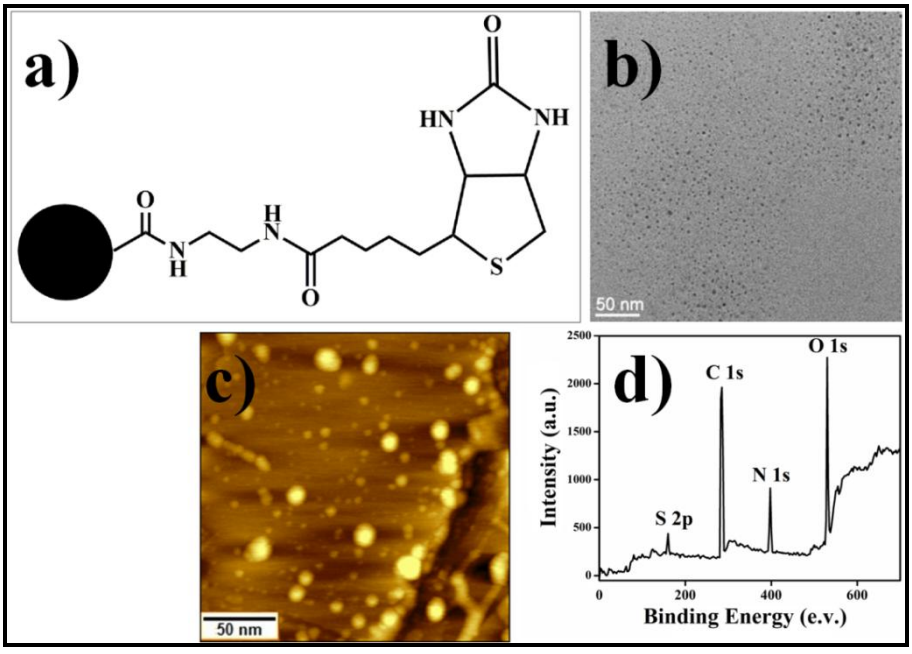

Figure 2. a) Chemical structure of **CD_b**, b) TEM image, c) AFM image and d) XPS spectrum of **CD_b**.

Co^{2+} Doped Biotinylated Carbon Dot: A Theranostic Agent for …

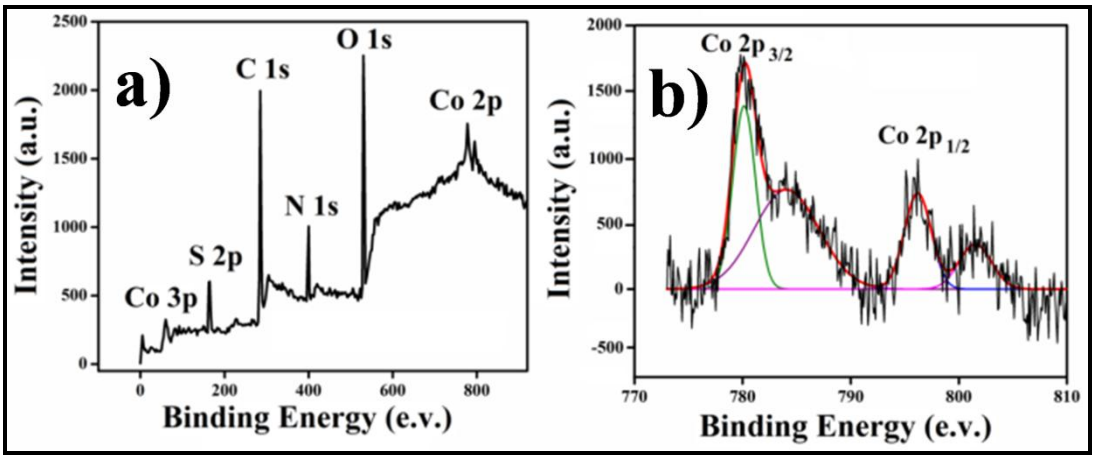

Figure 3. a) XPS spectra of **$CoCD_b$**, b) deconvoluted Co 2p orbital of **$CoCD_b$**.

The basic elemental analysis of **$CoCD_b$** was investigated by X-ray photoelectron spectroscopy (XPS), which exhibited characteristic peaks at 284, 401, 531, and 163 eV corresponding to C 1s, N 1s, O 1s and 2p orbitals of S, (from biotin moiety functionalization) respectively (Figure 3a).[33] Along with these peaks, a peak with doublet character was observed in the region of 780-800 eV, corresponding to the presence of Co in the moiety. The deconvoluted spectra of Co^{2+} showed two typical peaks at 780.14 eV and 796.16 eV with satellite peaks (784.8 eV and 801.4 eV) that were associated with Co $2p_{3/2}$ and Co $2p_{1/2}$ electronic configurations, respectively, indicating the existence of cobalt as Co^{2+} within **$CoCD_b$** (Figure 3b).[28,34]

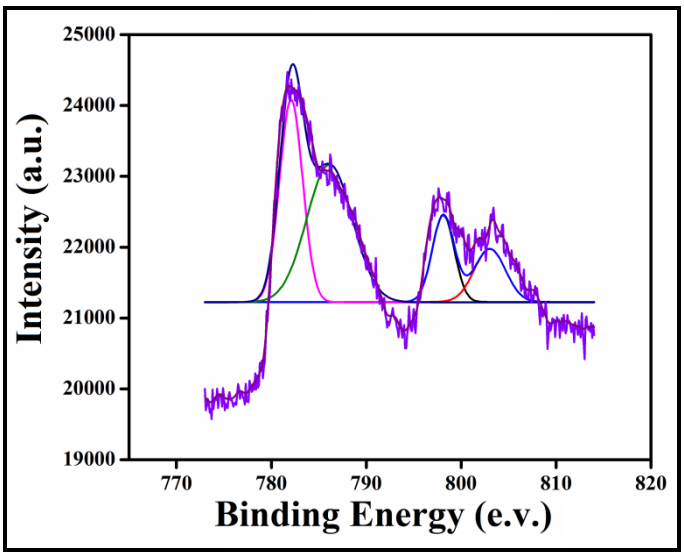

Figure 4. Deconvoluted spectra of Co^{2+} of $CoCl_2$.

Moreover, we investigated the XPS spectra of $CoCl_2$.$Co2P_{3/2}$ at 781.01 eV and $Co2P_{1/2}$ at 798.2 eV were attributed to the spin-orbit splitting of Co^{2+}, and their shake-up resonance peak observed at 785.7 eV and 802.94 eV (Figure 4) that corroborated with the deconvulated spectra of Co^{2+} in **$CoCD_b$**. From the XPS spectra in both the cases of Co^{2+} in **$CoCD_b$** and in $CoCl_2$, it was further confirmed that cobalt did exist as Co^{2+} in **$CoCD_b$**. Next the elemental analysis (XPS) of **CD_b** also confirmed the presence of three main elements C, N, and O C, N, and O in conjunction with S at 284, 397, 530 eV and 160 eV corroborating the successful functionalization of biotin moiety in **CD_b** (Figure 2d). In accordance to the X-ray diffraction (XRD) analysis, a broad peak at 20-25° established the amorphous nature of prepared **$CoCD_b$** and **CD_b** (Figure 5a,c).

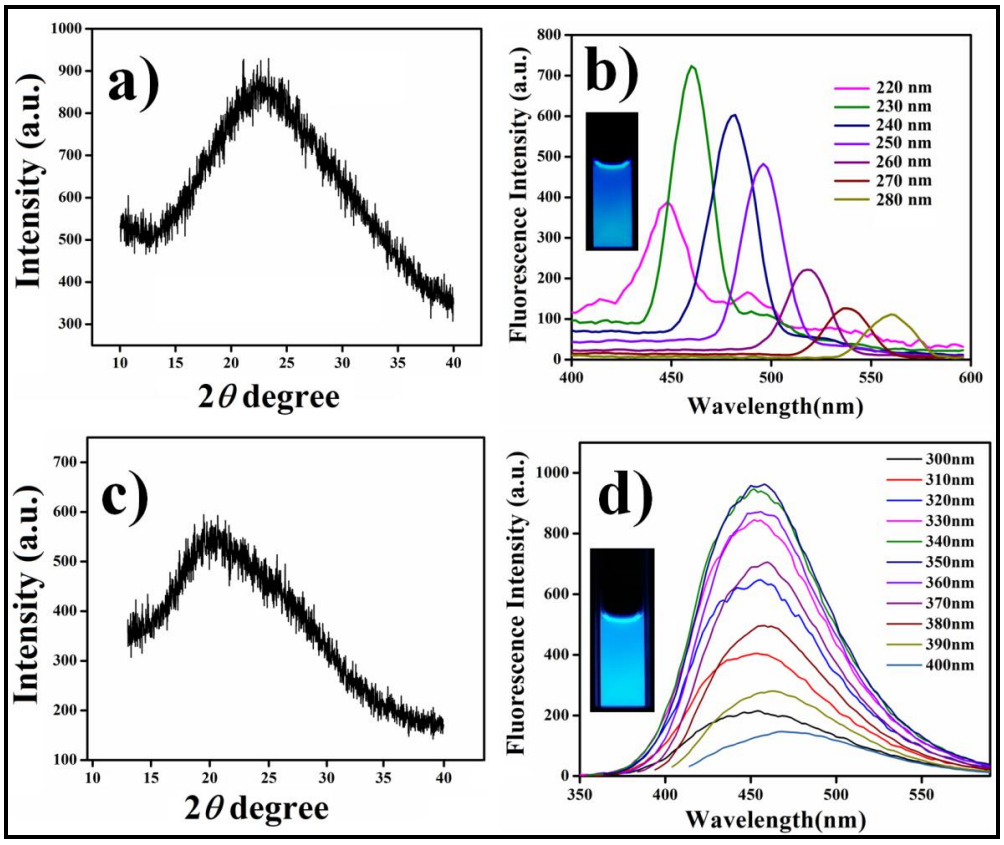

Figure 5. a) XRD spectrum of **$CoCD_b$**, b) excitation-dependent emission spectra of **$CoCD_b$** (inset in panel b) a photograph showing the blue fluorescence of **$CoCD_b$** solution under UV irradiation, 254 nm), c) XRD spectrum of **CD_b** and d) excitation-dependent emission spectra of **CD_b** (inset in panel d) a photograph showing the blue fluorescence of **CD_b** solution under UV irradiation, 254 nm).

2.2 Photoluminescence Study.

Photoluminescence property of both **$CoCD_b$** and **CD_b** were investigated. **$CoCD_b$** showed excitation dependent blue emission with emission maxima at 460 nm upon excitation at 230 nm (Figure 5b). **CD_b** also showed excitation dependent blue emission with emission maxima at 457 when excited at 350 nm (Figure 5d). Both **$CoCD_b$** and **CD_b** exhibited 112 nm and 13 nm red shift, respectively in their excitation dependent emissions. Aqueous solution of both **$CoCD_b$** and **CD_b** showed bright blue fluorescence (inset, Figure 5b,d) under UV light irradiation (254 nm). The quantum yield of **$CoCD_b$** and **CD_b** were found to be 2% and 4%, respectively with respect to quinine sulfate.

2.3 Fourier Transform Infrared Study.

In case of **$CoCD_b$**,the corresponding FTIR spectrum showed O-H stretching at around 3233 cm^{-1}, C=O amide stretching at1655 cm^{-1}, C=C stretching at 1404 cm^{-1}, C-Nstretching at 1100cm^{-1}(Figure 6(ii)). While for **CoCD** (Co^{2+} doped carbon dot devoid of biotin moiety, Scheme 1) O-H stretching around 3314 cm^{-1}, C=O carbonyl stretching at 1646 cm^{-1}, C=C stretching at 1404 cm^{-1}, and C-N stretching at 1126 cm^{-1} were observed (Figure 6(i)). Notably, the nature of C=O carbonyl stretching peak in case of **$CoCD_b$** gotshifted owing to the change of the surface property in comparison to **CoCD** due to presence of biotin moiety through amide bond. Along with these characteristics peaks, both **CoCD** and **$CoCD_b$** exhibited two more peaks at 650 and 596 cm^{-1} and 659 and 596 cm^{-1}, respectively correspond to Co-O stretching.

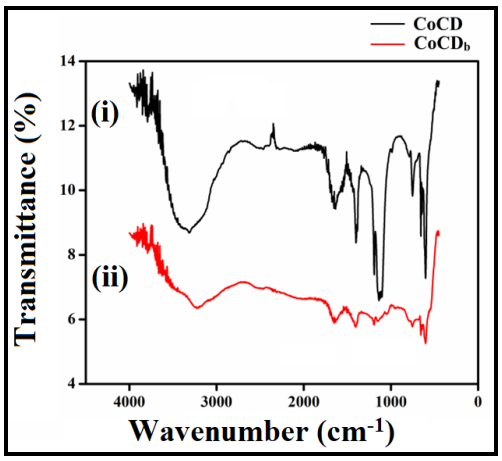

Figure 6. FTIR spectra of i) **CoCD**, and ii) **$CoCD_b$**

2.4 Media Stability of $CoCD_b$ and CD_b.

Prior to the utilization of the newly synthesized **$CoCD_b$** and **CD_b** (devoid of Co^{2+} doping) in cellular studies, we investigated their stability in simulated biological media comprising of FBS-DMEM over a period of time. Stability of **$CoCD_b$** and **CD_b** was examined in DMEM media with varying concentrations of FBS (up to 75%). **$CoCD_b$** (1 mg/mL) and **CD_b** (1 mg/mL) were added in DMEM where amount of FBS has been varied and kept for 48 h (Figure 7a, 8a). The long-time stability of **$CoCD_b$** and **CD_b** was investigated by keeping the mixtures of **$CoCD_b$** (1 mg/mL) and **CD_b** (1 mg/mL) in FBS (10%)-DMEM media for 10 days (Figure 7b, 8b). In both cases of **$CoCD_b$** and **CD_b,** suspension stability index (SSI) in biological media was nearly 90% with varying concentrations of FBS (0-75%) and also for 10 days stability study (Figure 7b, 8b). The observed stability of these synthesized carbon dots was in concurrence with respective visual images (Figure 7a, 8a). Next, we investigated the stability of the aqueous solution of **$CoCD_b$** and **CD_b** under the exposure of UV light (wavelength: 254 nm; and power: 12 W) where no photobleaching of the carbon dots was observed and also the emission property of the bioprobes remained unchanged after 200 min of UV irradiation (Figure 7c, 8c).

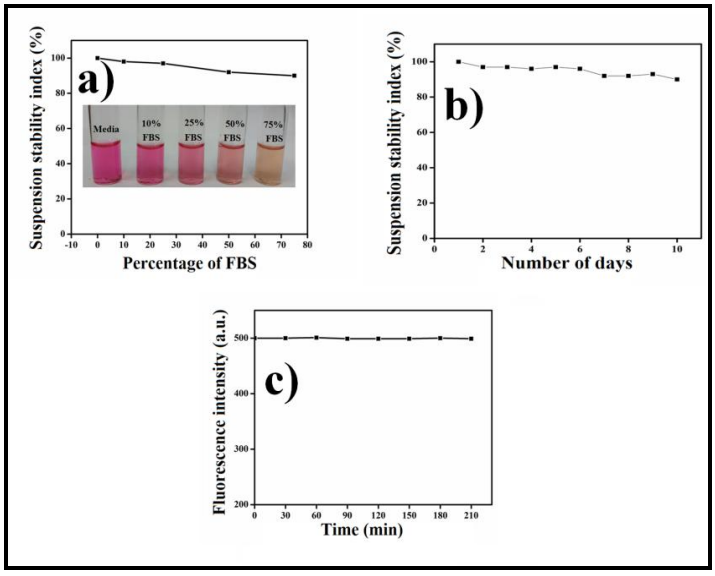

Figure 7. Suspension stability index of **$CoCD_b$** solution where [**$CoCD_b$**] = 1 mg/mL. a) with respect to FBS concentration (0-75%) in DMEM media and b) with respect to number of days in 10% FBS in DMEM media. Photostability of c) **$CoCD_b$** under UV (wavelength 254 nm, power 12 W) light irradiation up to 200 min.

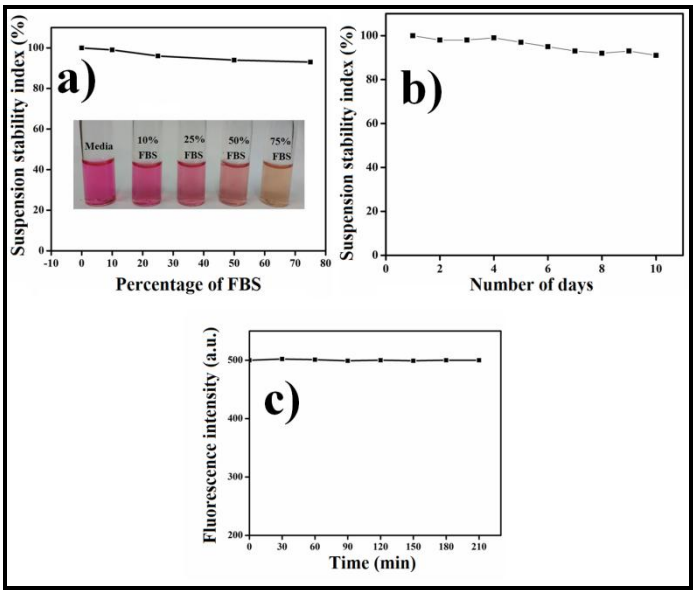

Figure 8. Suspension stability index of **CD_b** solution where [**CD_b**] = 1 mg/mL.a) With respect to FBS concentration (0-75%) in DMEM media and b) with respect to number of days in 10% FBS in DMEM media.Photostability of c) **CD_b** under UV (wavelength 254 nm, power 12 W) light irradiation up to 200 min.

2.5 Bioimaging.

Considering the intrinsic fluorescence of **$CoCD_b$** and **CD_b**, its cytocompatibility in biological milieu and the presence of biotin moiety, we were curious to determine whether these probes can be exploited in distinguishing between cancer and non-cancer cells. The biotin surface modified **$CoCD_b$** and **CD_b** could selectively diagnose the cancer cells through its facilitated internalization owing to the overexpressed biotin receptors in cancer cells. **$CoCD_b$** (500 µg/mL) and **CD_b** (500 µg/mL) were incubated separately with cancer cells MDA-MB-231 and HeLa. After 6 h cells were observed under fluorescence microscope. MDA-MB-231 and HeLa cells showed bright blue emission due to intrinsic fluorescence of **$CoCD_b$** and **CD_b** (Figure 9, 10). Similarly, non-cancer cells NIH3T3 and HEK-293 were incubated with **$CoCD_b$** (500 µg/mL) and **CD_b** (500 µg/mL) for 6 h. However, in both cases of normal cell lines, no notable fluorescence was observed for **$CoCD_b$** as well as for **CD_b** (Figure 9, 10). This ensured the significance of biotin moiety present in both **$CoCD_b$** and **CD_b** that facilitated its internalization specifically inside cancer cells having overexpressed biotin receptors. The internalization of **$CoCD_b$** as observed from the respective as well as overlayed images in Figure 9, confirmed the presence of **$CoCD_b$** throughout

cytosol. Subsequently, the localization experiment of **$CoCD_b$** in specific organelles by different biomarkers was inconclusive owing to the comprehensive distribution of **$CoCD_b$** throughout cytosol. Next, we studied the bioimaging of **CoCD** as a control carbon dot having doped Co^{2+} but devoid of biotin unit (Scheme 1). Under similar experimental conditions, **CoCD** (500 µg/mL) exhibited bright blue fluorescence for both cancer cells (MDA-MB-231 and HeLa) and normal cells (NIH3T3 and HEK-293) (Figure 11). The absence of biotin moiety in **CoCD** made it to be non-specific towards cancer and normal cells resulting in similar internalization in both type of cells. Thus, it is further ascertained that biotin moiety is essential to make the bioprobe to be target specific to cancer cells over the normal cells.

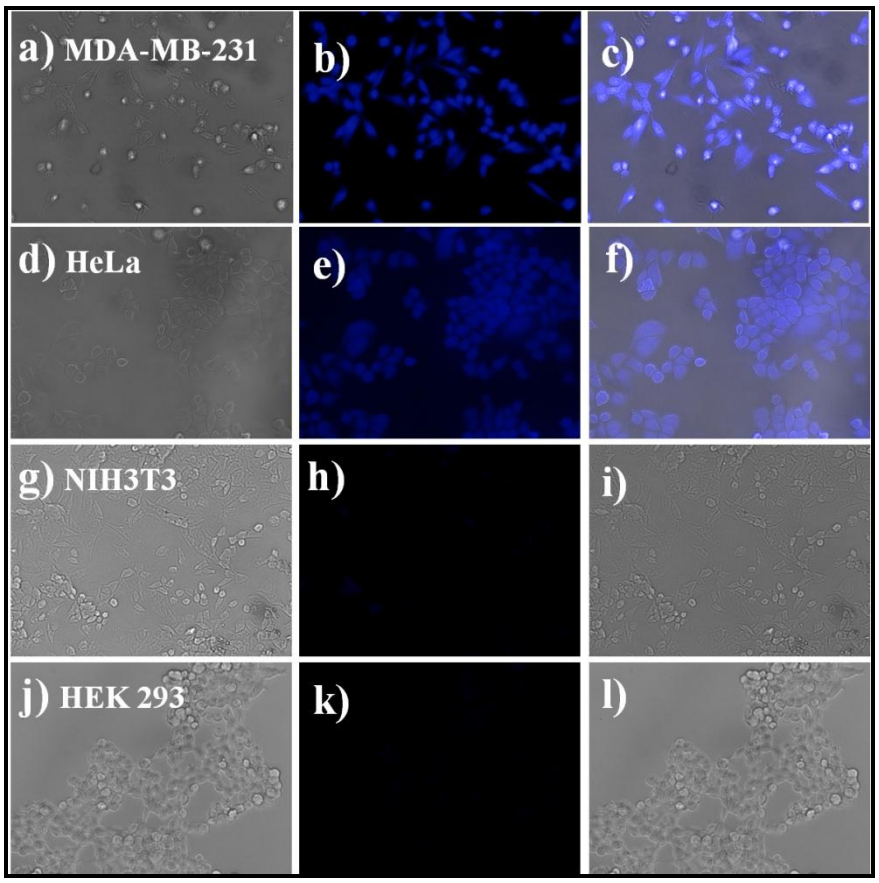

Figure 9. Bright field, fluorescence and merged microscopic images of MDA-MB-231 (a-c), HeLa cancer cells (d-f) and NIH3T3 (g-i), HEK-293 normal cells (j-l) after 6 h incubation with **$CoCD_b$** where [**$CoCD_b$**] = 500 µg/mL, at 20x magnification. Scale bars correspond to 20 µm.

Co^{2+} Doped Biotinylated Carbon Dot: A Theranostic Agent for …

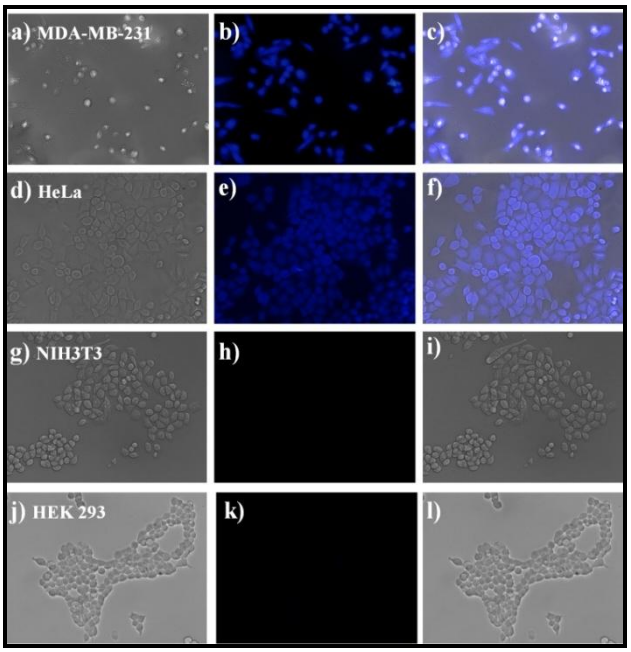

Figure 10. Bright field, fluorescence and merged microscopic images of MDA-MB-231 (a-c), HeLa cancer cells (d-f) and NIH3T3 (g-i), HEK-293 normal cells (j-l) after 6 h incubation with **CD_b** where [**CD_b**] = 500 µg/mL, at 20x magnification. Scale bars correspond to 20 µm.

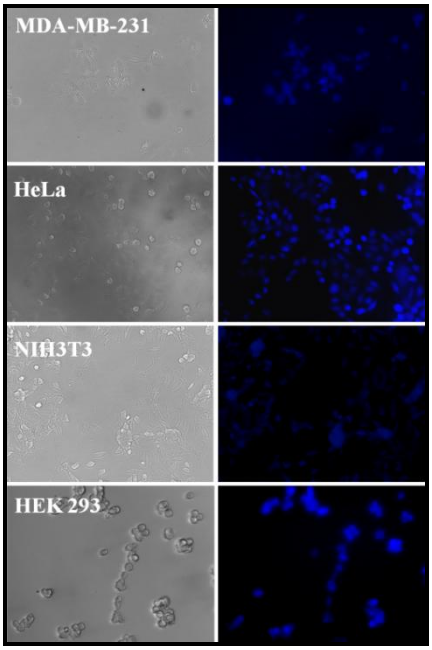

Figure 11. Bright field and fluorescence microscopic images of MDA-MB-231, HeLa cancer cells and NIH3T3, HEK-293 normal cells after 6 h incubation with **CoCD** where [**CoCD**] = 500 µg/mL, at 20x magnification. Scale bars correspond to 20 µm.

2.6 MTT Experiment.

Selective diagnosis of cancer cells by the blue emitting carbon dot (**$CoCD_b$**) prompted us to evaluate its potential as a therapeutic agent. Therapeutic agent generally denotes a drug, protein, peptide, gene, compound or other pharmaceutically active ingredient, which has potential to eliminate the cause in physiological systems through different mechanism. Surgery, radiotherapy, chemotherapy, immunotherapy are the traditional procedures that were used as weapon in the battle against cancer. Each method has its limitation and adverse effects that demand the emergence for alternative pathways to treat this deadly disease. Therapy associated with anticancer drug lacks selectivity as well as induce systemic side effects. In this regard, methods or module that are capable of modifying and/or exploiting the physicochemical environment of cancer cells leading to apoptosis is still at the budding stage. Thus, instead of separately developing different methodologies/systems that minimize the side effects, amalgamation of properties such as diagnostic, therapeutic and selectivity in a singular module will be very effective for optimizing the potential in cancer treatment. However, development of systems that will diagnose as well as treat the cancer cells selectively using its intrinsic biochemical properties remains very challenging. To this end, we intended to make use of the newly developed **$CoCD_b$** for selective killing of cancer cells without using any chemotherapeutic drugs. The selectivity of the agent was taken care of using biotin moiety as surface functionalizing agent as evident from bioimaging study.

$CoCD_b$ was separately incubated with both normal cells (NIH3T3 and HEK-293) and cancer cells (MDA-MB-231 and HeLa) for 24 h. Cell viability was tested by MTT assay as mentioned in the experimental section . **$CoCD_b$** exhibited significant killing efficacy against both cancer cells, MDA-MB-231 (14 ± 1% to 90 ± 1%) and HeLa (12 ± 2% to 88 ± 1%) with varying concentration from 0.5-5 mg/mL (Figure 12a). Under similar experimental conditions, the killing ability of **$CoCD_b$** (0.5-5 mg/mL) was considerably lower against normal cells NIH3T3 (5 ± 2% to 34 ± 1%) and HEK-293 (6 ± 1% to 35 ± 1%) in comparison to that of cancer cells (Figure 12a). Notably **$CoCD_b$** can selectively kill cancer cells (MDA-MB-231 and HeLa) ~ 3-

3.1 times higher efficiency over the normal cells (NIH3T3 and HEK-293). In contrast, biotinylated carbon dot devoid of Co^{2+} (**CD_b**) with its increasing concentration (0.5-5 mg/mL) showed insignificant killing 7 ± 1% to 28 ± 2% of both cancer cells, MDA-MB-231 and HeLa (Figure 12b). Moreover, **CD_b** showed similar killing efficiency (5 ± 1% to 29 ± 1%) against both normal cells NIH3T3 and HEK-293 (Figure 12b). It is well-known that cancer cells are hypoxic in nature than normal cells. Uncontrollable cell propagation, altered metabolism are one of the many causes that resulted in reduced transport of oxygen in cancer cells. Co^{2+}in the core of **$CoCD_b$** might have instigated the extent of hypoxia which caused the irreversible damage to the cancer cells and leading to its death through apoptosis. Although normal cells are mostly normoxic in nature but Co^{2+}also can initiate hypoxia subject to its internalization in normal cells. However, the presence of target specific ligand biotin in **$CoCD_b$** facilitated its internalization selectively only in cancer cells due to the overexpressed biotin receptor in its surface. Insignificant killing of non-cancer cells (NIH3T3 and HEK-293) by **$CoCD_b$** was primarily due to its inefficient internalization inside normal cells having obscure presence of biotin receptors. Consequently, **$CoCD_b$** enabled to differentiate between malignant and non-malignant cells resulting in ~3-3.1 times higher killing of cancercells than normal cells through hypoxia induced apoptosis by accumulation of HIF-1α without the use of traditional chemotherapeutic drugs. Notably the unremarkable killing of both cancer and normal cells by the biotinylated carbon dot devoid of Co^{2+} (**CD_b**) delineates the important role of Co^{2+} integrated within **$CoCD_b$** in efficient killing of cancer cells. Thus, both factors, Co^{2+}in the core and tagging biotin in the surface of carbon dot build a worthier theranostic agent, **$CoCD_b$** which has high diagnostic and therapeutic efficacy with marked selectivity towards cancer cells. The IC_{50} (half inhibitory concentration) calculated for **$CoCD_b$** for MDA-MB-231 and HeLa cells was 2.5 mg/mL and 2.7 mg/mL, respectively (Figure 12c). However, the IC_{50} value for **$CoCD_b$** in case of normal cell NIH3T3 and HEK-293 and for **CD_b** in case of both cancer and normal cells could not be measured within the experimental concentration range.

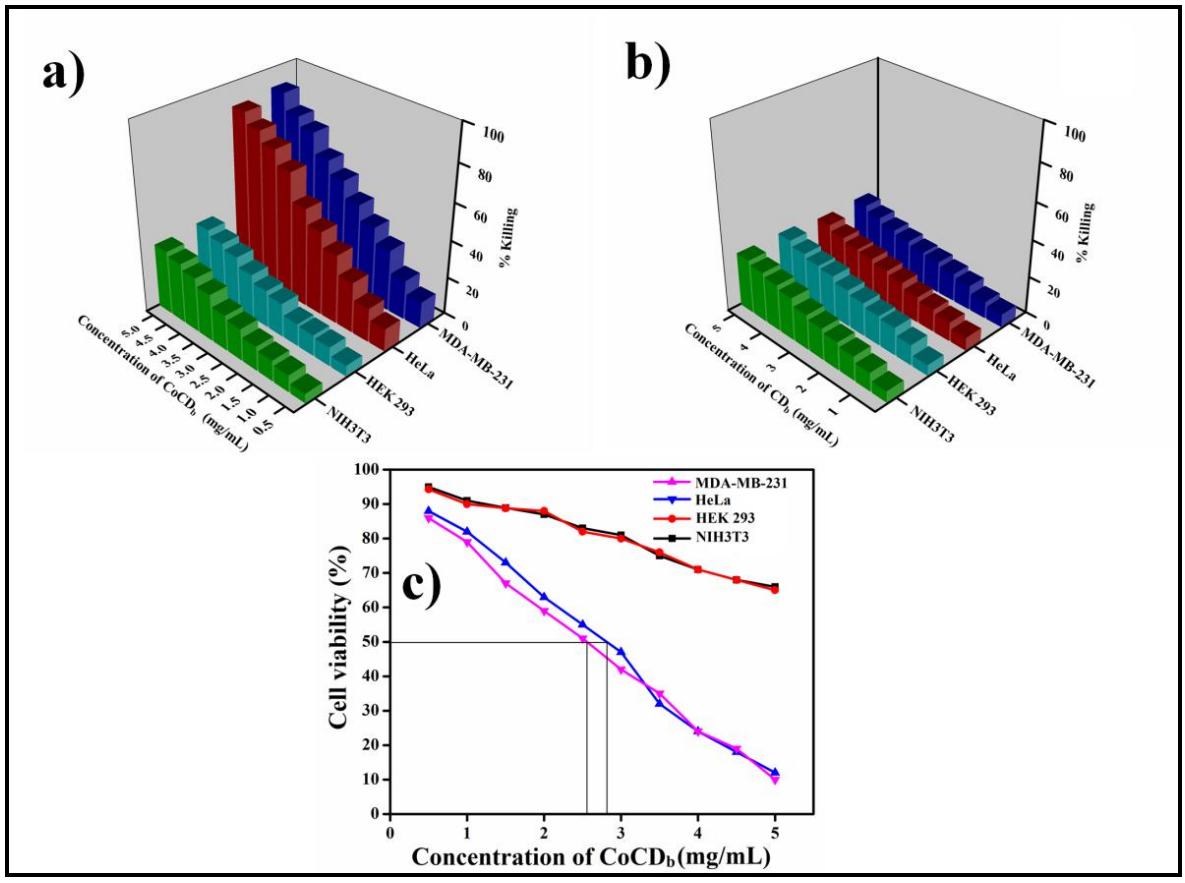

Figure 12. % Killing of MDA-MB-231, HeLa, NIH3T3 and HEK-293 cells incubated with varying concentrations of a) **$CoCD_b$** where [**$CoCD_b$**] = 0.5-5 mg/mL and b) **CD_b** where [**CD_b**] = 0.5-5 mg/mL for 24 h. The experimental errors were in the range of 1−3% in triplicate experiments. c) IC_{50} determination of MDA-MB-231, HeLa, NIH3T3 and HEK-293 for **$CoCD_b$**.

2.7 LIVE/DEAD Assay.

The selectivity and therapeutic competency of the **$CoCD_b$** and **CD_b** was further tested by LIVE/DEAD viability kitassay for normal cells (NIH3T3 and HEK-293) and cancer cells (MDA-MB-231 and HeLa). Both normal and cancer cells were incubated with **$CoCD_b$** (3 mg/mL) and **CD_b** (3 mg/mL) for 12 h. Subsequently, fluorescence images were recorded after incubating the treated cells with LIVE/DEAD viability kit for 30 min. In case of **$CoCD_b$**, primarily the presence of green cells was noted for NIH3T3 and HEK-293 cells while both green and red cells were observed for cancerous MDA-MB-231 and HeLa (Figure 13). The presence of only green cells for non-cancer cells obviously indicates the abundance of alive cells

as **$CoCD_b$** did not get transferred inside the non-cancer cells in absence of biotin receptors. On the other hand, the presence of both green and red cells delineates the maximum presence of dead cells for cancer cells owing to the successful internalization of **$CoCD_b$** within cancer cells having overexpressed biotin receptors. Subsequently, cancer cells got efficiently killed due to hypoxia induced apoptosis in presence of Co^{2+} of **$CoCD_b$**.In case of **CD_b** (devoid of Co^{2+}unit), the presence of maximum green cells and very low number of red cells in both non-cancer and cancer cellsonce again points out the selective sensing of cancer cells (Figure 14). Moreover, in absence of Co^{2+}, **CD_b** became inefficient for killing of cancer cells. Hence, LIVE/DEADassay further confirmed that the target-specific theranostic ability of the biotin comprised **$CoCD_b$** in hypoxia mediated cancer therapy.

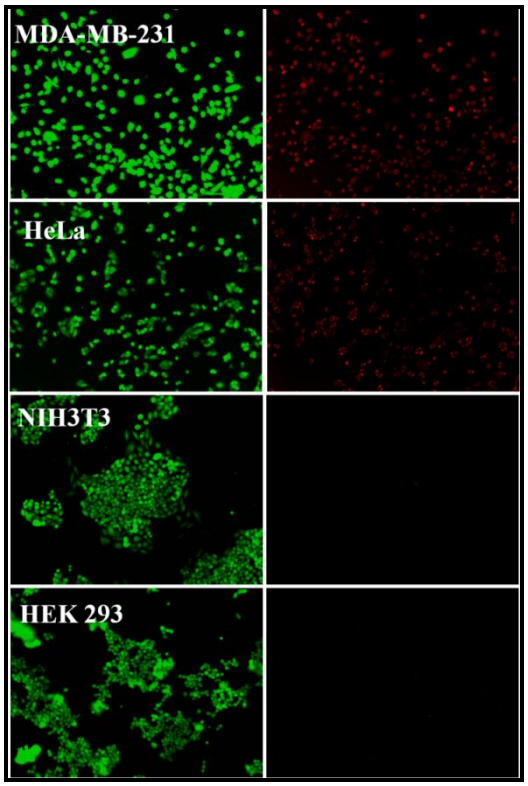

Figure 13. LIVE/DEAD fluorescence microscopic images of MDA-MB-231, HeLa cancer cells and NIH3T3, HEK-293 normal cells after 12 h incubation with **$CoCD_b$** where [**$CoCD_b$**] = 3 mg/mL.

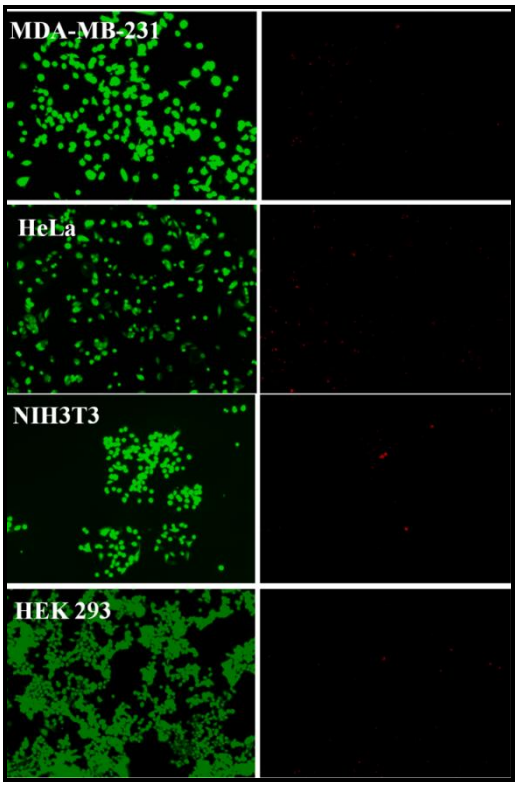

Figure 14. LIVE/DEAD fluorescence microscopic images of MDA-MB-231, HeLa cancer cells and NIH3T3, HEK-293 normal cells after 12 h incubation with **CD_b** where [**CD_b**] = 3 mg/mL.

2.8 Western Blot Analysis.

Studies have shown that hypoxia causes susbstantial responses in cancer cell.The expression of transcription factor, HIF-1 has been studied to determine the regulation of a series of hypoxia stimulated genes that are responsible for critical cellular behaviour in hypoxic environment.[10,12] Therefore, expression of HIF-1α level was examined by immunoblotting in MDA-MB-231 cells incubated for 6 h with **$CoCD_b$** (3 mg/mL) and **CD_b** (3 mg/mL).It was observed that the expression of HIF-1α protein significantly increased following exposure to **$CoCD_b$** (Figure 15).Interestingly, no expression of HIF-1α was found in the control group (**CD_b** (3 mg/mL)), signifying the role of **$CoCD_b$** in the induction of hypoxia stimulated cancer cell death.

HIF-1α is rapidly hydroxylated and degraded by prolyl hydroxylase domain-containing protein (PHDs). In normoxic conditions, PHDs mediate O_2-dependent

hydroxylation of proline residue of HIF-1α, which triggers degradation of HIF-1α. In hypoxic situation Co^{2+} substitutes Fe^{2+}, the cofactor required for PHDs catalytic activities and thus induced the high expression of HIF-1α. To this end, we explored the expression of PHDs protein in the treated cancer cell lysate to investigate the Co^{2+} mediated inhibition of PHDs activity under hypoxic condition within the cancer cells incubated with **$CoCD_b$**. As observed from the immunoblotting data, **$CoCD_b$** treated cancer cells exhibited a downregulated expression of PHDs (Figure 15) in comparison to that of the control groups. This indicates the influence of Co^{2+} on the expression of PHDs under hypoxic condition. To the same end, **$CoCD_b$** treated cancer cells exhibited upregulation expression of HIF-1α in comparison to the control groups indicating the influence of Co^{2+} on the expression of HIF-1α under hypoxic condition (Figure 15). The concurrent downregulation of PHDs and upregulation of HIF-1α complement the hypoxia-mimetic role of **$CoCD_b$**where Co^{2+} of carbon dot stabilize the degradation of HIF-1α via inhibiting the activity of PHDs. This further ascertained the role of **$CoCD_b$** in selective killing of cancer cells via hypoxia induced apoptosis.

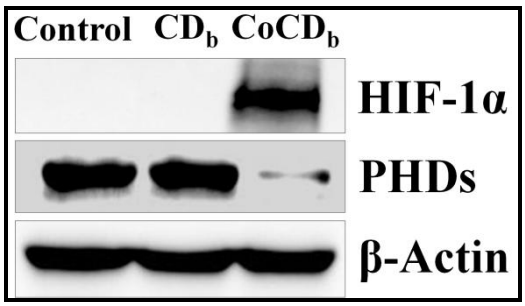

Figure 15. Differential expression pattern of HIF-1α and β-actin in control MDA-MB-231 cells and treated MDA-MB-231 cells with **$CoCD_b$** and **CD_b**; [**$CoCD_b$**] or [**CD_b**] = 3 mg/mL for 6 h.

2.9 Apoptosis in 2D Cell Culture.

Next, we investigated the mode of cancer cell death by **$CoCD_b$** in case of MDA-MB-231 and HeLa in 2D cell culture by flow cytometric assays using Annexin V-FITC and PI dye. Annexin V-FITC is used to determine the percentage of cells within a population that are undergoing different stage of apoptosis. Membranes of viable cells exclude PI, whereas the membranes of dead and damaged cells are permeable to PI. Cells that stain positive for Annexin V-FITC and negative for PI are

undergoing through early apoptosis. Cells that stain positive for both Annexin V-FITC and PI are in the end stage of apoptosis and undergoing through necrosis or already dead. Cells that stain negative for both Annexin V-FITC and PI are alive and not undergoing through measurable apoptosis. Flow cytometry data has four quadrants and the nature of the cells in each quadrant was explained in flow cytometry experimental section. In case of 2D cell culture, both MDA-MB-231 and HeLa were treated with **$CoCD_b$**(5 mg/mL) for 12 h (Figure 16). These separately treated cells were detached and incubated with Annexin V-FITC and PI dye and analyzed by flow cytometry. The untreated MDA-MB-231 and HeLa cells lines showed a maximum population at Q3, indicating that the cells were intact and alive (Figure 16b,d). **$CoCD_b$** treated MDA-MB-231 and HeLa cells showed significant population at Q4 depicting the early apoptotic pathway of cancer cell killing (Figure 16c,e). Hence, the killing of cancer cells by **$CoCD_b$** mainly took place through the early apoptotic pathway.

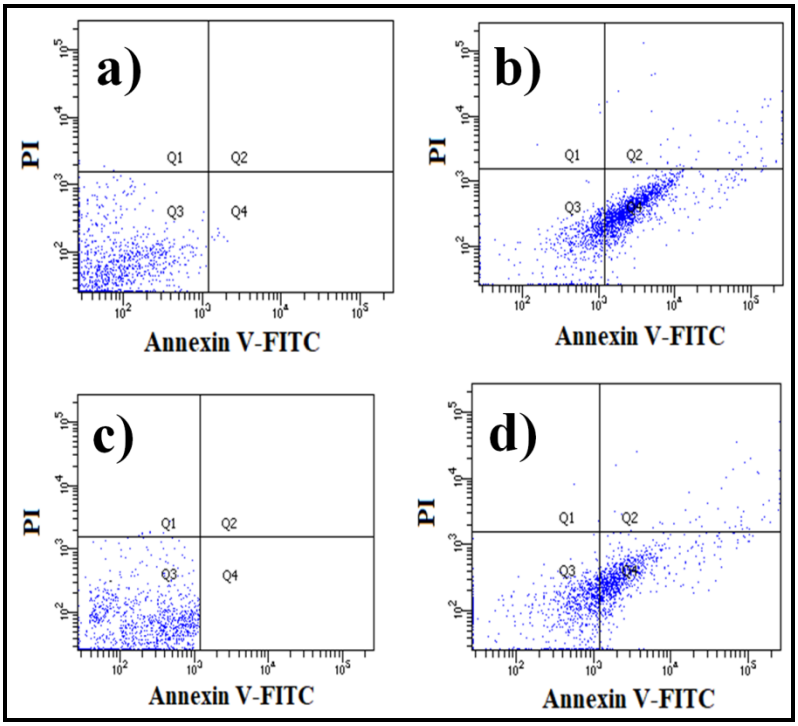

Figure 15. Flow cytometric analysis of apoptosis for 2D cell culture in untreated a) MDA-MB-231cells, c) HeLa cells and treated b) MDA-MB-231cells, d) HeLa cells with **$CoCD_b$** where [**$CoCD_b$**] = 5 mg/mL.

Co^{2+} Doped Biotinylated Carbon Dot: A Theranostic Agent for …

2.10 Nuclear Assessment and localization of $CoCD_b$.

After target selective theranostic accomplishment of **$CoCD_b$** against the cancer cells, we were curious to know the state of nuclear morphology in the process of **$CoCD_b$** mediated hypoxia induced apoptosis. There are many hallmarks of apoptotic cell death. To examine the change innuclear morphology, cancer cells (MDA-MB-231 and HeLa) were incubated with **$CoCD_b$** (3 mg/mL) and **CD_b** (3 mg/mL) for 12 h. Followed by the cells were stained with Hoechst 33342 (Figure 17). The observed fluorescence microscopic images clearly indicated the significant nuclear shrinkage in case of cancer cells treated with **$CoCD_b$**. This could be possible due to chromatin condensation, which is a notable hallmark of apoptosis (Figure 18).[35,36] In case of **CD_b** incubated cancer cells, nucleus morphology remain unaltered.Under similar experimental condition, treatment of the normal cells (NIH3T3 and HEK-293) with **$CoCD_b$** (3 mg/mL) and **CD_b** (3 mg/mL) resulted in negligible changes in nuclear morphology (Figure 19). Therefore, it is significant to mention that biotin **$CoCD_b$**could successfully and selectively alter the morphology of nucleus of cancer cells because of hypoxia generation.

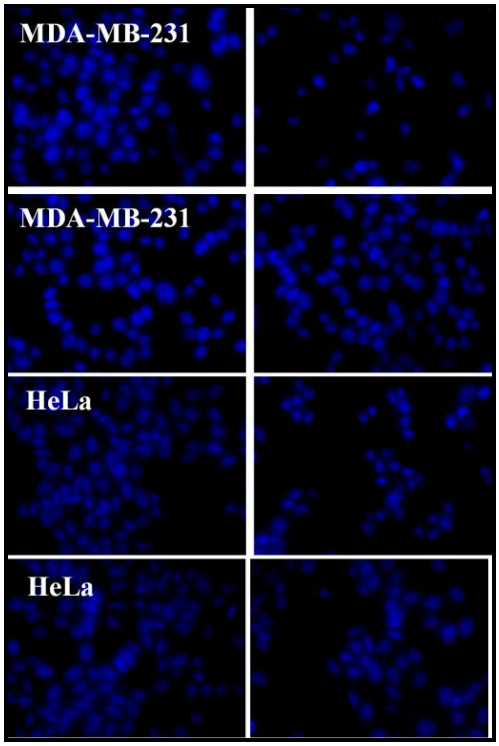

Figure 17. Nuclear staining of MDA-MB-231 and HeLa cancer cells with the Hoechst 33342 dye after the incubation for 12 h with **$CoCD_b$** and **CD_b** where [**$CoCD_b$**] and [**CD_b**] = 3 mg/mL. Scale bars correspond to 20 µm.

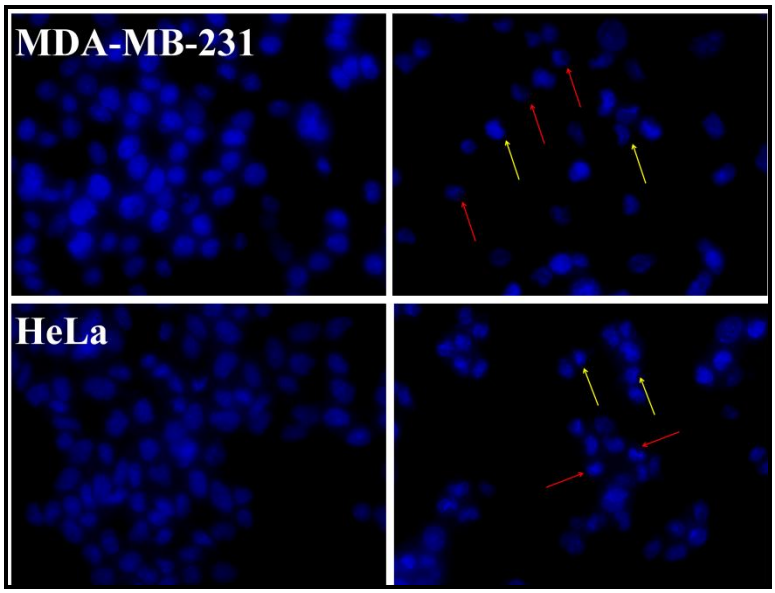

Figure 18. Nuclear staining of MDA-MB-231 and HeLa cancer cells with the Hoechst 33342 dye after the incubation for 12 h with **$CoCD_b$** where [**$CoCD_b$**] = 3 mg/mL. **$CoCD_b$** treated cells showed nuclear condensation (red →) and nuclear fragmentation (yellow →), whereas untreated cells remained uniformly stained with round and intact nuclei.

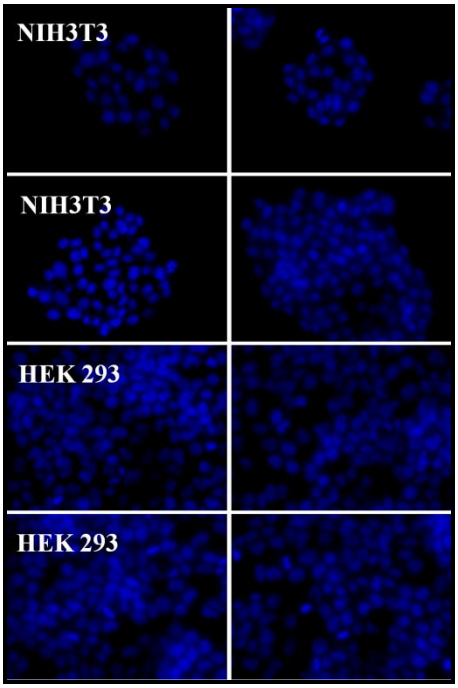

Figure 19. Nuclear staining of NIH3T3 and HEK-293 (normal cells) with the Hoechst 33342 dye after the incubation for 12 h with **$CoCD_b$** and **CD_b** where [**$CoCD_b$**] and [**CD_b**] = 3 mg/mL. Scale bars correspond to 20 µm.

2.11 Effect of $CoCD_b$ on ROS generation.

Co^{2+} also act as fenton catalyst that catalyzes H_2O_2 to generate reactive oxygen species (ROS) and further kill cancer cells. It has been reported that each cell is exposed to ~1.5 × 10^5 oxidative hits per day.[37] If ROS production increases or number of scavenged ROS decreases and then cells experience a condition known as oxidative stress. This may be considered as the threshold value of ROS generation in each cell per day above which further generation of ROS could led to oxidative stress. Intracellular level of ROS such as hydroxyl radical was assessed in the MDA-MB-231 cells upon treatment with **CD_b** (3 mg/mL) and **$CoCD_b$** (3 mg/mL) for varying time period (6 h and 12 h) followed by incubation with dichlorofluorescein diacetate (DCFH-DA) dye in the dark. After cellular uptake, DCFH-DA gets deacetylated by cellular esterases to non-fluorescent compound, which later gets oxidized by ROS into fluorescent, 2'-7'-dichlorofluorescein (DCF).Bright green fluorescence of DCF will be observed inside cells if sufficient ROS generation takes place. In case of untreated cells and **CD_b** (3 mg/mL) incubated cancer cells, no significant fluorescence intensity of DCF was observed in 6 h and 12 h indicating almost negligible intracellular ROS generation (Figure 20 a,b and c,d). Incubation with **$CoCD_b$** (3 mg/mL) also resulted in weak fluorescence enhancement with time indicating meagre intracellular ROS generation in 6 h and low increase of ROS in 12 h (Figure 20 e,f). Corresponding fluorescence microscopy plot displayed <20% and <40% generation of ROS in presence of **$CoCD_b$**, after 6 h and 12 h incubation, respectively (Figure 20g). This is notably low content of ROS in comparison to that of the threshold value for generating oxidative stress. Such low ROS content in presence of **$CoCD_b$** (3 mg/mL) was insufficient to kill cancer cells through oxidative stress. At the same time, **$CoCD_b$** (3 mg/mL) incubated MDA-MB-231 cells exhibited significant generation of HIF-1α only after 6 h (Figure 15). Thus, cancer cells killing primarily took place through hypoxia mediated apoptosis resulted from high expression of HIF-1α induced by Co^{2+} of **$CoCD_b$**.

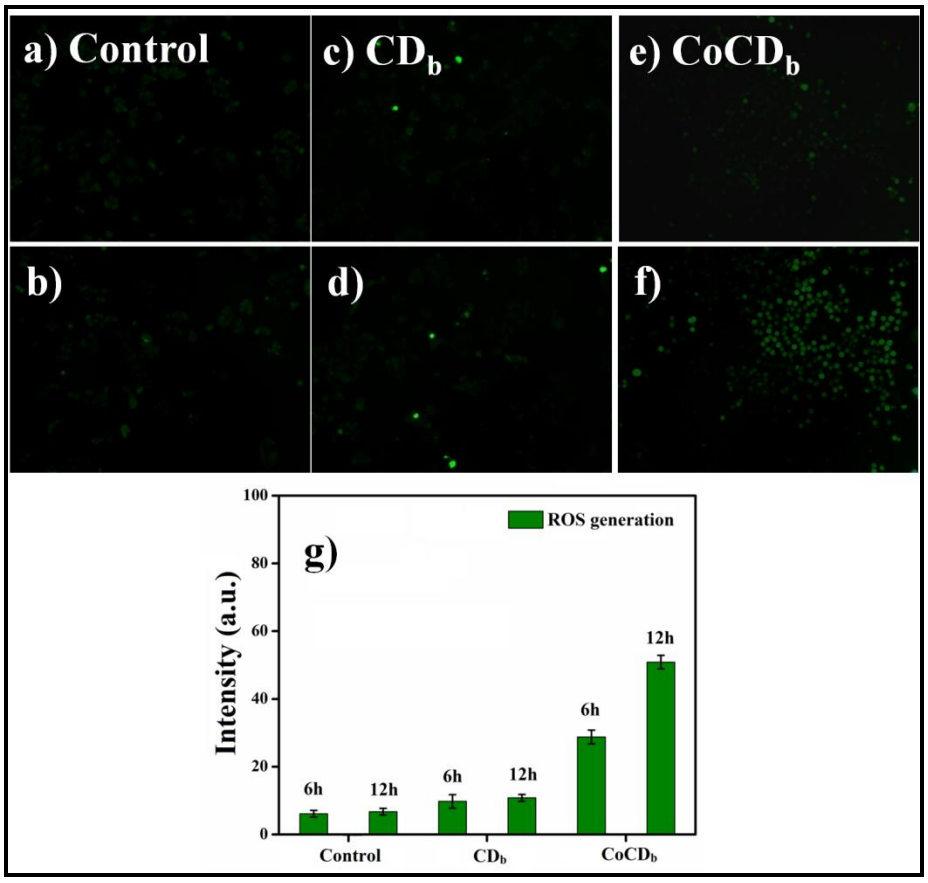

Figure 20. ROS generation in a) 6 h, d) 12 h for control experiment, b) 6 h, (e) 12 h in presence of **CD_b** and c) 6 h, f) 12 h in presence of **$CoCD_b$**. Graphical representation of ROS generation for 6 h and 12 h in case of blank experiment and in presence of **CD_b**, **$CoCD_b$**.

2.12 Tumor Spheroid Formation and Proliferation.

The potential of this hypoxia assisted cancer therapy was further assessed in 3D tumor spheroid model, which mimic the tumor microenvironment (TME) more realistically. 3D tissue culture models have been developed to bridge the gap between in vitro experiments used for drug discovery & screening and in vivo experiments used for safety and effective evaluation before clinical trials. The environmental and metabolic distinct characteristics of the TME play a key role in choosing the non-systematic ways of treating tumors.[38,39] In TME, uncontrolled cell division often exceeds the ability to satisfy the oxygen demand from the pre-existing blood vessels. Hypoxia is a common as well as important feature of solid malignancies and is closely associated with tumor progression, enhanced

metastatic potential and resistance to radio- or chemo-therapy.[40,41] Considering this, we wanted to re-engineer the hypoxic TME in such a way that it led to restrict the growth and proliferation of the tumor cells. So, we aimed to observe the effectiveness of **$CoCD_b$** against treating a tumor spheroid model. In this study, a breast tumor spheroid model was developed by culturing MDA-MB-231 cells in a 3D culture module utilizing the hanging drop method (Figure 21). The initial size of the spheroid was approximately 400 µm and grew to about 2 mm in 96 h (Figure 21b-e), displaying a uniform spherical shape and high cell connection affinity (Figure 21f). The overall developed tumor spheroid structure is highly crucial in the process of evaluating the effectiveness of **$CoCD_b$** in treating the 3D-tumor.

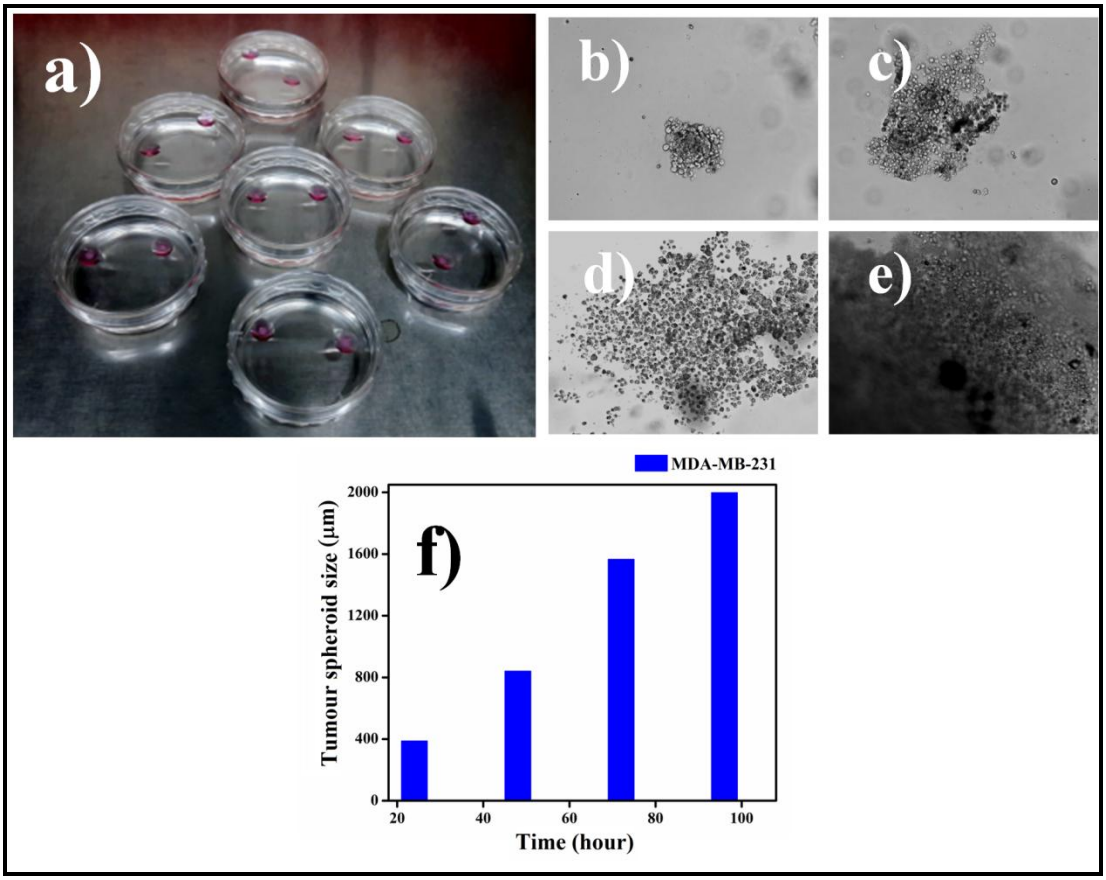

Figure 21. a) Hanging drop method of developing 3D tumor spheroids in 35 mm culture plate; bright-field images of 3D tumor spheroids formed by culturing MDA-MB-231 cells in 3D culture platform for b) 24 h, c) 48 h d) 72 h and e) 96 h; f) time-course monitoring of tumor spheroid diameter.

2.12 Effects of $CoCD_b$ on the 3D Tumor Spheroids.

The anti-tumorigenic efficiency of the **$CoCD_b$** was evaluated on the developed 3D tumor spheroids. We investigated the status of growth and/or shrinkage of the newly developed tumors upon treating with **$CoCD_b$** for varying time period. Dose dependent cancer cell killing efficacy of (0.5-5 mg/mL) was already tested in 2D cell culture by MTT assay for 24 h. Herein, in 3D tumor model, we used 5 mg/mL of **$CoCD_b$** totreat 3D tumor spheroids for 24, 48, and 72 h. With increasing time the structural integrity of the tumor spheroids was found to be gradually compromised (Figure 22a-d). The dimension of spheroids was nearly 2 mm prior to incubation with **$CoCD_b$** (5 mg/mL). After 72 h, the size of the tumor reduced to nearly 0.75 mm primarily due to the cell loss indicating the notable anti-proliferation property of the **$CoCD_b$** (Figure 22e). Subsequently,we conducted the MTT assay to observe the anti-tumorigenic property of **$CoCD_b$**. **$CoCD_b$** was incubated with tumors in dose dependent manner (0.5-5 mg/mL) for 24 - 72 h. After 24, 48, and 72 h, the percentage of cell killing in tumor spheroids was 5 ± 1% to 39 ± 1%, 11 ± 1% to 51 ± 2%, and 19 ± 1% to 66 ± 1.8%, respectively. After 72 h, significant killing of cancer cells (~65%) further ascertained the anti-tumorigenic property of **$CoCD_b$** (Figure 22f). Thus, **$CoCD_b$** exhibited anti-proliferation property through ~2.7 fold tumor size reduction and showed anti-tumorigenic property by killing ~ 65% of tumor cells at highest dose (5 mg/mL). The observed effect of **$CoCD_b$** on MDA -MB-231 tumor spheroid strengthened the potential of **$CoCD_b$** as an alternative cancer treatment method devoid of systematic chemotherapeutic drug.

In addition, we examined the expression of HIF-1α level in 3D tumor by immunoblotting. Expectedly, the expression of HIF-1α protein was significant in **$CoCD_b$** (3 mg/mL) treated MDA-MB-231 cells (Figure 22g). Interestingly, no expression of HIF-1α was found in the control group (**CD_b** (3 mg/mL)), that further affirmed the role of **$CoCD_b$** in hypoxia induced apoptosis as a result of high expression of HIF-1α protein(Figure 22g).Here too, the IC_{50} calculated for **$CoCD_b$** for MDA-MB-231 tumor spheroid was 4.8 mg/mL in case of 48 h and 3.7 mg/mL for 72 h treatment, respectively (Figure 23). However, the IC_{50} value could not be measured for 24 h under the investigated experimental concentration.

Co^{2+} Doped Biotinylated Carbon Dot: A Theranostic Agent for …

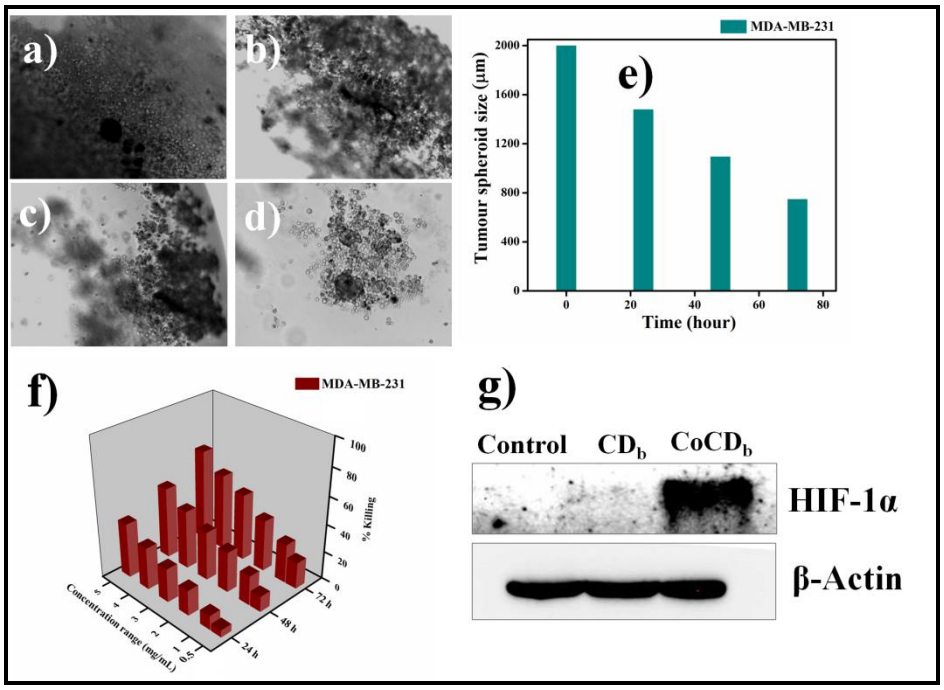

Figure 22. (a-d) Dose-dependent changes in tumor spheroid morphology and diameter following exposure to **$CoCD_b$** for 72 h; (e) time-course monitoring of tumor spheroid diameter; (f) % Killing of MDA-MB-231 cells incubated with **$CoCD_b$**, where [**$CoCD_b$**] = 0.5-5 mg/mL for 72 h; (g) differential expression pattern of HIF-1α and β-actin in control MDA-MB-231 and treated MDA-MB-231 tumor cells with **$CoCD_b$** and **CD_b**; [**$CoCD_b$**] or [**CD_b**] = 3 mg/mL for 48 h. The experimental errors were in the range of 1−3% in triplicate experiments.

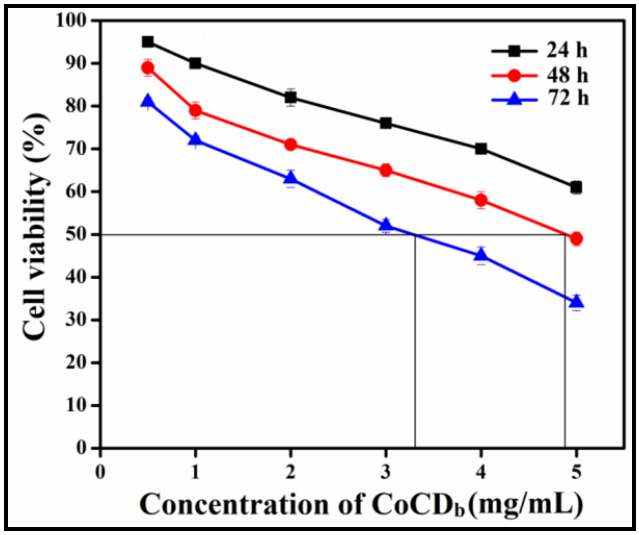

Figure 23. IC_{50} determination of MDA-MB-231 3D-tumor spheroids in (24 h-72 h) after incubated with **$CoCD_b$** where [**$CoCD_b$**] = 5 mg/mL.

2.13 Live/Dead Assay of the 3D Tumor Spheroids.

The effectiveness of **$CoCD_b$** on tumor spheroids was further validated by Live/Dead assay. As it was mentioned that in accordance to the fluorescence images of treated cells, green cells and red cells indicated alive and dead cells respectively. We treated the tumor spheroids with **$CoCD_b$** (5 mg/mL) for 24, 48, and 72 h. With increase in time, the population of red cells got increased over green cells and after 72 h significant amount of red cells were visible (Figure 24a-d). In accordance to the fluorescence intensity of red cells, more than 70% cells were dead in tumor spheroids in comparison to that of from the time of incubation of **$CoCD_b$** (Figure 24e). Therefore, Live/Dead assay data delineated similar killing of cancer cells in presence of **$CoCD_b$** as evident in preceding experiments.

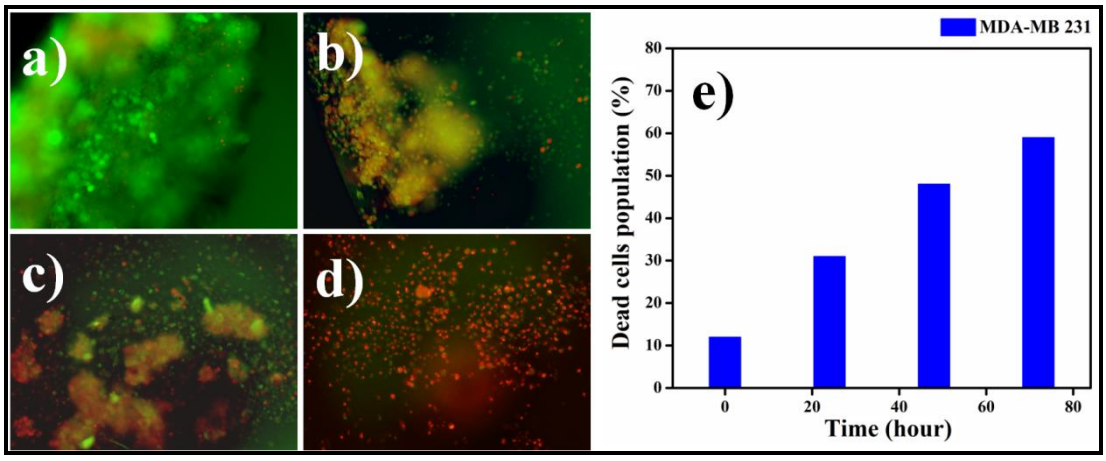

Figure 24. Live/Dead assay of MDA-MB-231 3D-tumor spheroids a) untreated tumor b) 24 h c) 48 h, d) 72 h after incubated with **$CoCD_b$** where [**$CoCD_b$**] = 5 mg/mL. e) Percentage of dead cell population in the tumor spheroids following time dependent treatment with **$CoCD_b$**.

2.14 Hypoxia Genertion in 3D Tumor Spheroids by $CoCD_b$.

Hypoxia within the TME is an intrinsic feature of tumor that can influence tumor-immune interactions. Researchers have availed the much explored route to mimic the hypoxic TME by way of developing tumor spheroids. 3D tumor models bear tenaciously assembled module of tumor cells that recapitulates a tumor-like niche. Herein, to investigate the generation of hypoxia by **$CoCD_b$** in 3D system, we incubated **$CoCD_b$** (3 mg/mL) within as developed 3D tumor spheroids for 24-72 h.

Subsequently, the same was double stained with Image-iT™ Red Hypoxia Reagentalong with Hoechst 33342 and imaged under fluorescence microscope. The plummeted blue emission and enhanced red fluorescence intensity in the treated spheroids was indicative of the time dependent increase in the generation of hypoxia under the influence of **$CoCD_b$** (Figure 25). Encouragingly, the untreated tumor spheroids displayed strong blue fluorescence from Hoechst 33342 demonstrating live nuclei and insignificant red fluorescence that indicates the existence of normoxic condition (Figure 25). Therefore, it may be conclusive from the results that the decrease in cancer cell viability (as displayed by the faint blue fluorescence intensity of Hoechst 33342 dye) following treatment with **$CoCD_b$** is directly proportional to the increase in hypoxic condition in the TME of 3D tumor spheroids.

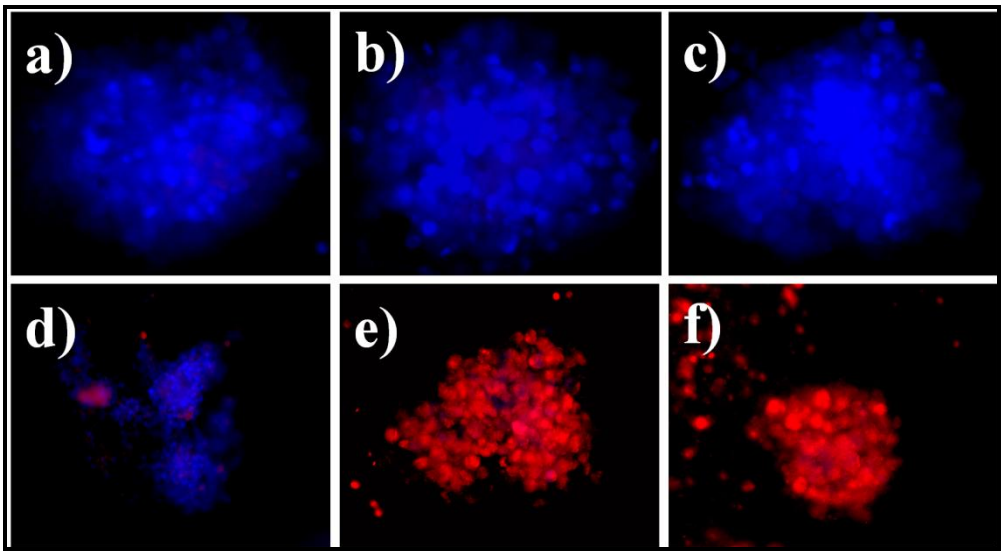

Figure 25. Fluorescence microscopic images of 3D tumor spheroids double stained with Image-iT™ Red Hypoxia Reagent along with Hoechst 33342. Control tumor spheroids (a-c) and tumor spheroids under the influence of **$CoCD_b$** d) 24 h, e) 48 h and f) 72 h.

2.15 Apoptosis in 3D Tumor Spheroid.

Along with the 2D apoptosis, we also investigated the pathway of cancer cell killing in 3D MDA-MB-231 tumor spheroid by flow cytometric assays using Annexin V-FITC and PI dye. The nature and importance of both the dyes were already discussed in the 2D cell culture apoptosis. We investigated the mode of killing of

MDA-MB-231 in 3D tumor spheroid by **$CoCD_b$** (5 mg/mL) for 24, 48, and 72 h. The untreated tumor cells showed a maximum population at Q3, similar to that of 2D cell culture indicating that the cells were alive (Figure 26a). The **$CoCD_b$** treated tumor cell with increase in time showed increased population at Q4 (Figure 26b-d). In case of 3D tumor spheroid, apoptosis by **$CoCD_b$** also indicate the killing of cancer cells through the early apoptotic pathway. Thus, biotin receptor-tagged Co^{2+}integrated carbon dot, **$CoCD_b$** has high therapeutic efficacy that selectively killed cancercells primarily through early apoptotic pathway via hypoxia assisted apoptosis in 2D and 3D assessment of cells.

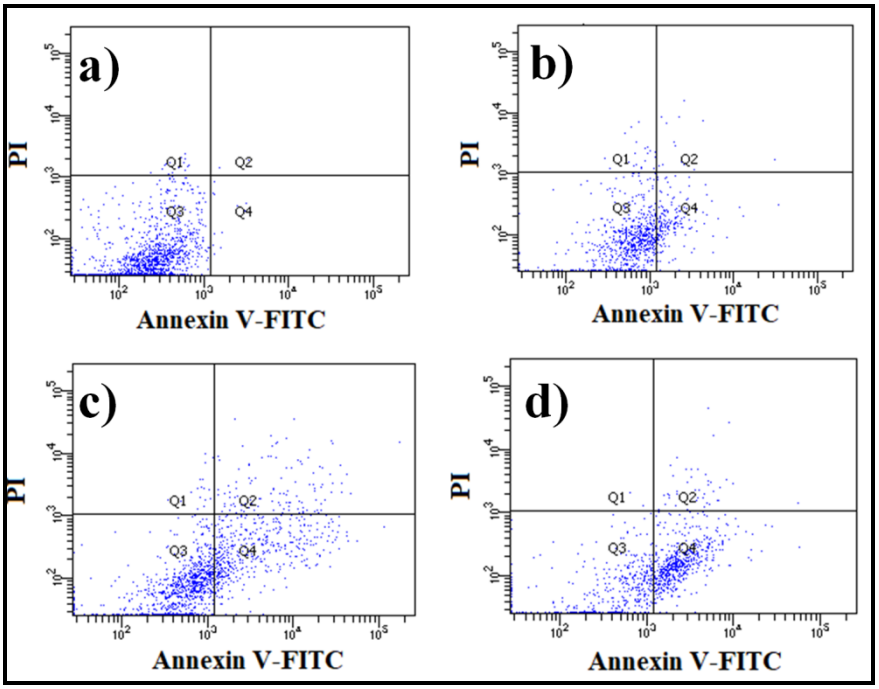

Figure 26. Flow cytometric analysis of apoptosis for 3D MDA-MB-231 tumor spheroid with a) untreated tumor cells and in time span of b) 24 h c) 48 h and d) 72 h with **$CoCD_b$** where [**$CoCD_b$**] = 5 mg/mL.

3.CONCLUSION

The target-specific delivery of Co^{2+} doped biotin-functionalized fluorescent carbon dots (**$CoCD_b$**) have been demonstrated to distinguish cancer cells from non-cancerous one and selective killing of cancer cells through hypoxia induced apoptosis by virtue of stabilized HIF-1α. This **$CoCD_b$** showed promising stability in

the biological medium. HIF-1α protein acts as a pro-drug in the presence of Co^{2+} of **$CoCD_b$**. Pro drug activator Co^{2+} altered the expression of pro drug HIF-1α protein by inhibiting the the activity of PHDs that led to the cancer cell apoptosis. The bioimaging confirmed successful internalization of **$CoCD_b$** primarily in cancer cells due to the presence of biotin moiety in the structure. This newly developed **$CoCD_b$** exhibited ~3-3.1-fold higher killing of cancer cells (MDA-MB-231 and HeLa) over the non-cancer cells (NIH3T3 and HEK-293). Furthermore, immunoblotting confirmed significant upregulation of HIF-1α protein in **$CoCD_b$** treated MDA-MB-231 cells in comparison to that observed in the control groups delineating the significant influence of **$CoCD_b$** in the killing of cancer cells via hypoxia. **$CoCD_b$** showed promising anti-proliferation and anti-tumorogenic property in MDA-MB-231 3D tumor spheroids. Around 65% cell killing was observed for 3D tumor spheroids by **$CoCD_b$**. Both 2D and 3D killing of cancer cell took place via early apoptotic pathway. Thus, biotin tagged Co^{2+} doped carbon dot can selectively diagnose as well as kill the cancer cells without the assistance of any traditional chemotherapeutic drugs. Hence this newly synthesized **$CoCD_b$** can be a promising theranostic agent in the domain of alternative cancer treatment.

4.EXPERIMENTAL SECTION

4.1 Materials

Citric acid, ethylenediamine, cobalt chloride heptahydrate ($CoCl_2$,$7H_2O$), 4-(*N*,*N*-dimethylamino) pyridine (DMAP), 1-ethyl-3-(3-(dimethylamino)propyl)-carbodiimide (EDC), dimethylformamide (DMF) and all other reagents and solvents were bought from SRL, India. D-Biotin, MTT (3-(4,5-dimethylthiazol-2-yl)-2,5-diphenyltetrazolium bromide), Annexin V-FITC apoptosis kit, Bradford Reagent, □-actin and other deuteriated solvents were purchased from Sigma-Aldrich. Dialysis tubing, iT™ Red Hypoxia Reagent, Hoechst 33342,MitoTracker deep red and LysoTracker deep red, RIPA buffer and protease inhibitor were procured from Thermo Scientific SnakeSkin (3.5K MWCO). Live-dead kit for eukaryotic cells was procured from Invitrogen, India. HIF-1α (Cell Signaling Technology), (Sigma Aldrich), secondary antibody (Merck Millipore). Dulbecco's modified Eagle's medium

(DMEM), fetal bovine serum (FBS), and Trypsin–ethylenediaminetetraacetic acid (EDTA) solution 1× (0.25% solution) was bought from Himedia. NIH3T3, HEK 293, MDA-MB-231 and HeLa cells were received from NCCS, Pune, India. All experiments were carried out using Milli-Q water. Agilent Cary Eclipse luminescence spectrometer was used to record fluorescence spectra. Agilent Cary 60 and Perkin Elmer Spectrum 100 were used to record UV-vis and FTIR spectra, respectively. Centrifugation was performed using a Thermo Scientific Espresso centrifuge. Nano-ZS of Malvern Instruments Limited was used to measure zeta potential. A Telsonic bath sonicator was used to perform bath sonication.

4.2 Synthesis of Co^{2+} doped Carbon Dot (CoCD) and Native Carbon Dot (CD).

Co^{2+}doped carbon dot (**CoCD**)was synthesized by hydrothermal route. Citric acid monohydrate (2.93.0 g, 14 mmol), ethylenediamine (0.84 g, 14 mmol) and 3.33 g of hydrated cobalt chloride ($CoCl_2.7H_2O$) were dissolved in 5 mL of Milli-Q water. The solution was mixed and sonicated to obtain a transparent solution. The solution was heated at 180 °C for 4 h in a heating platform. The color of the solution gradually turned to pink. The supernatant was collected by centrifugation (10,000 rpm, 15 min) and mixture was shaken for 15 min followed by dialysis (MWCO - 3.5K) against PBS buffer (pH = 7.4) for 24 h. It was dried by lyophilization to obtain the **CoCD** with yield of ~72%. We also synthesized our control compound **CD** without integrating Co^{2+} using above mentioned hydrothermal method having precursor citric acid monohydrate (2.93.0 g, 14 mmol), and ethylenediamine (0.84 g, 14 mmol) only. The yield obtained was ~75%.

4.3 Synthesis of Surface Modified Carbon Dots ($CoCD_b$ and CD_b) .

To synthesize biotin tagged surface modified Co^{2+} doped carbon dot (**$CoCD_b$**), we took the mixture of above synthesized **CoCD** (1 equiv), EDC (10 equiv), DMAP (10 equiv), and D-biotin (10 equiv) in dry DMF and stirred overnight. The DMF was dried out and the crude was taken in DCM and filtered. The DCM part filtrate was evaporated in rotary evaporator to obtain surface modified carbon dot, **$CoCD_b$**.The mixture was shaken for 15 min followed by dialysis (MWCO - 3.5K) against PBS

buffer (pH = 7.4) for 12 h. The solution remained in the dialysis bag was taken out and lyophilized to get the biotin modified Co^{2+} doped carbon dot (**$CoCD_b$**).Biotin tagged **CD** (**CD_b**) was also prepared in similar way.

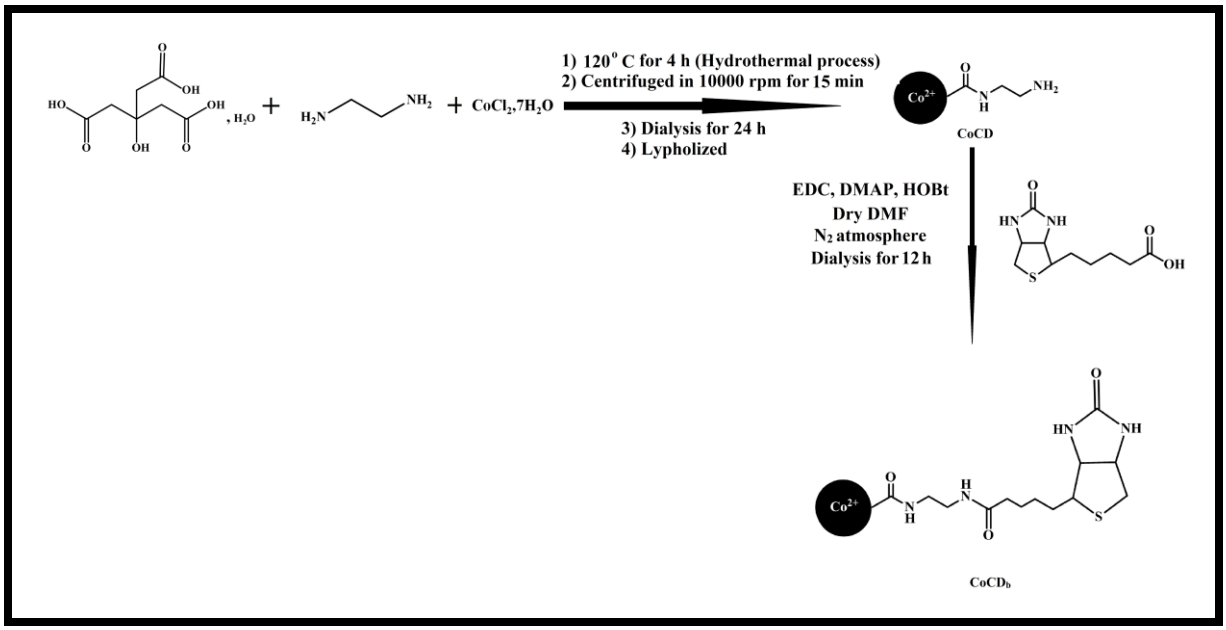

Scheme 1. Synthesis of **$CoCD_b$**.

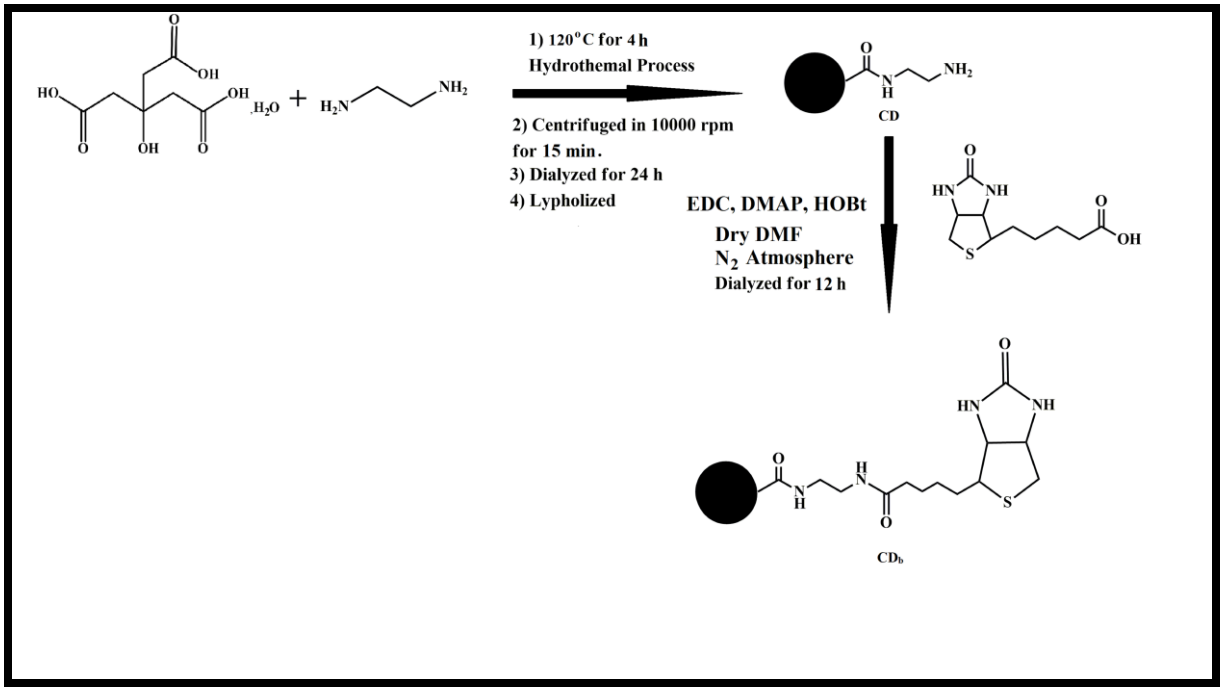

Scheme 2. Synthesis of **CD_b**.

4.4 Characterization.

$CoCD_b$ solution was first sonicated for 15 min and then drop cast on Cu-coated grids (300-mesh) and was dried for 6 h for TEM imaging in 2100F UHR microscope (JEOL JEM). For AFM, after sonication a drop of **$CoCD_b$** solution was put on fresh mica surfaces. It was air-dried overnight before taking images on Asylum Research MFP-3D AFM. In case of X-ray photoelectron spectroscopy (XPS), 3-4 drops of **$CoCD_b$** solution was cast on rectangular Cu plates and dried over night before investigation in Omicron series 0571. Energy-dispersive X-ray (EDX) analysis was carried out using Oxford make EXTREME INCA microscope. X-ray diffraction (XRD) spectra of dried **$CoCD_b$** were obtained on a diffractometer (Bruker D8 Advance) having CuKα radiation (α = 0.15406 nm) as the source (voltage and current was 40 kV and 30 mA, respectively). The zeta (ζ) potential measurements were performed with aqueous solutions of **$CoCD_b$** at room temperature. All the above mentioned characterizations were carried out similarly for **CD_b**. XPS analysis also carried out for $CoCl_2$ as above-mentioned procedure for **$CoCD_b$**.

4.5 Quantum Yield Measurement.

The absorbance value of carbon dot solution was restricted to <0.1, and integrated emission intensities of those solutions were recorded in a luminescence spectrometer. The quantum yield (Q) was obtained using the following equation:

$$\emptyset_u = \left(\frac{A_s F_u n_u^2}{A_u F_s n_s^2}\right)\emptyset_s \qquad (1)$$

where I is the integrated emission intensity measured at the excitation maxima (230 nm), OD denotes the optical density, η represents the refractive index. The subscript "sm" stands for sample and the subscript "st" indicates the standard fluorescence of a known fluorophore. We have used quinine sulfate as a standard dissolved in 0.1 M H_2SO_4. The quantum yield of quinine sulfate is Q = 0.54.

4.6 Fluorescence Spectroscopy.

Excitation dependent emission spectra of **$CoCD_b$** (25 μg/mL) was recorded with varying λ_{ex} from 220 to 290 nm using excitation and emission slits at 10 nm. In

case of **CD_b** (25 µg/mL) the fluorescence spectra were recorded at λ_{ex} = 350 nm using similar slit as **$CoCD_b$**. The fluorescence intensity was measured at 459 nm for **$CoCD_b$** and at 458 nm for **CD_b** upon exciting **$CoCD_b$** at 230 nm and **CD_b** at 350 nm.

4.7 Fourier Transform Infrared Study.

Fourier transform infrared (FTIR) measurement was performed for **$CoCD_b$/CoCD** in D_2O. They were mixed separately with potassium bromide (KBr) and granulated via a hydraulic press. The spectra were obtained in the range of 400-4000 cm^{-1}. All spectra were normalized and scaled. All the experiments were performed in a PerkinElmer Spectrum 100 FTIR spectrometer using a 1 mm CaF_2 cell.

4.8 Media Stability of $CoCD_b$ and CD.

Stability of **$CoCD_b$** in biological media was investigated. The aqueous solutions of **$CoCD_b$** (500 µg/mL) were added to FBS containing DMEM media having a different concentration of FBS (0-75%), and it was kept for 2 days. The long time stability of was investigated by addition of **$CoCD_b$** (500 µg/mL) aqueous solutions to FBS containing DMEM media (10%), and the solutions were kept for 10 days. In each case, the supernatant of the solution was taken at different time spans, and the absorbance of the supernatant was recorded at 295 nm to measure the suspension stability index (SSI).Stability of **CD_b**in biological milieu was also investigated using above mentioned way.

SSI = $A_t/A_0 \times 100$ where A_t = absorbance of the solution after a specific time span at 295 nm, and A_0 = initial absorbance of the solution at 295 nm.

4.9 Cell Culture.

NIH3T3, HEK 293, MDA-MB-231 and HeLa cells were cultured in FBS containing DMEM (10%) medium having antibiotic (100 mg/L streptomycin and 100 IU/mL penicillin). Cells were grown in cell culture flask and kept in a incubator (5% CO_2 and 37 °C). Subculture was performed in every 2 days after 75% confluence of cultured cells. The adherent cells were detached from surface of culture flask by using trypsin. These cells were utilized for further cellular studies.

4.10 Bioimaging.

Cancer cells MDA-MB-231, HeLa and Non-cancerous NIH3T3, HEK 293 cells were grown maintaining 1x104 cells per well in a chamber slide before the experiment. Cells were treated individually with CoCDb (250 µg/mL) and CDb (250 µg/mL) for 5 h. Treated cells were washed with PBS buffer two times and then fixed with paraformaldehyde (4%) for 30 min. Then glycerol solution (50%) was used for mounting. The cells on slide was covered with a coverslip and kept for 1 day. Images were taken in Olympus IX83 inverted microscope using an excitation filter of BP 330-385 nm and a band absorbance filter covering wavelength below 405 nm at 40× magnification. Exposure time was <100 ms, and the microscopic object was 40 X UPIanFLN.

4.11 MTT Assay.

Killing of cancerous and non-cancerous cells were determined by the MTT reduction method. Cancer cells MDA-MB-231, HeLa and Non-cancerous NIH3T3, HEK 293 all were separately grown in a 96-well plate for 24 h with 20,000 cells per well in 10% FBS containing DMEM media. The cells were separately incubated in the presence of **$CoCD_b$**, and **CD_b** under 5% CO_2 at 37 °C for 24 h. The **$CoCD_b$**, and **CD_b** concentrations separately were varied from 0.5-5 mg/mL, respectively. After 24 h, MTT dye was added in the 96 well plates for 4 h. In this MTT reduction method, tetrazolium salt gets converted to a formazan (water insoluble) product by mitochondrial dehydrogenase of alive cells. The quantity of the produced formazan was estimated by measuring the absorbance value of the formazan after dissolving in DMSO. The formazan formation is directly related to the number of live cells. After 4 h the produced formazan in these reactions were dissolved in DMSO and absorbance was measured at 570 nm in Biotek Elisa Reader.

The number of alive cells were expressed as percent viability = (A_{570}(treated cells) - background)/A_{570}(untreated cells) - background) × 100.

4.12 LIVE/DEAD Viability Assay.

Cytocompatibility of MDA-MB-231, HeLa, NIH3T3, and HEK 293 cells in the presence of **$CoCD_b$**, and **CD_b** were examined by LIVE/DEAD assay kit (for

eukaryotic cells). The LIVE/DEAD assay kit is composed of a mixture of two nucleic acid binding stains. One is Calcein AM (acetomethoxy) (component A) and another is ethidium homodimer-1 (component B). The green fluorescence due to Calcein AM indicates live cells while red fluorescence due to ethidium homodimer-1 corresponds to dead cells. Just before the assay, 4 µL of the supplied EthD-1 solution and 1 µL of the supplied calcein AM stock solution were mixed in 2 mL of PBS buffer for each of the above bioprobe, and the solutions were vortexed. The resulting mixtures were then added to MDA-MB-231, HeLa, NIH3T3, and HEK 293 cells which were pretreated with **$CoCD_b$**, and **CD_b** ([**$CoCD_b$**] = 3 mg/mL and [**CD_b**] = 3 mg/mL),respectively for 12 h. Next, they were incubated for 30 min with LIVE/DEAD assay kit. Images of the cells were subsequently taken in Olympus IX83 microscope at 10× magnification. Excitation filter BP460-495 nm and a band absorbance filter covering wavelength below 505 nm were used for calcein intercalation. Excitation filter BP530-550 and a band absorbance filter covering wavelength below 570 nm were used for ethidium homodimer-1 intercalation.

4.13 Western Blot Analysis.

The expression of HIF-1α and PHDs protein was assessed by immunoblotting assay. In case of 2D cell culture, MDA-MB-231 cells were treated with **$CoCD_b$** (3 mg/mL) and **CD_b** (3 mg/mL) for 6 h and were lysed with ice cold RIPA buffer, supplemented with protease inhibitor. Protein concentration of the cell lysates were quantified with Bradford reagent. Protein (30 µg) of the control and the treated groups were separated by SDS-PAGE and transferred into PVDF membrane. The membrane was then blocked with 5% BSA in Tris buffer saline containing Tween-20 (TBST) for 1 h followed by overnight incubation with primary antibodies, HIF-1α (Cell Signaling Technology), PHDs and β–actin (Sigma Aldrich) at 4 °C. Post incubation, the membrane was washed with TBST and probed with secondary antibody for 1hat room temperature. The membrane was thoroughly washed with TBST and detected using Biorad's chemiluminescent reagent (clarity and clarity max ECL WB substrate) under Biorad's CHEMIDOC imaging system. In case of 3D tumor spheroid of MDA-MB-231, cells were treated with **$CoCD_b$** (3 mg/mL) and **CD_b** (3 mg/mL) for 48 h. After 48 h we performed western blot analysis for the expression of HIF-1α, following above mentioned procedure.

4.14 Hoechst 33342 Staining for a cell nucleus Study.

Nuclear staining with Hoechst 33342 (Thermo Fisher Scientific) was conducted to distinguish apoptotic cells from healthy cells. The dye can disseminate through the intact cellular membrane, staining the DNA of the cells and therefore, was used to observe nuclear changes in apoptosis. **$CoCD_b$**, and **CD_b** ([**$CoCD_b$**] = 3 mg/mL and [**CD_b**] = 3 mg/mL) was incubated for 12 h. After the media was removed, MDA-MB-231, HeLa, NIH3T3, and HEK 293 cells were washed with PBS. The cells were then stained with Hoechst 33342 for 10 min in the dark at room temperature and washed thoroughly with PBS, and finally, nuclear morphology was observed under a fluorescence microscope (20× magnification).

4.15 Effect of $CoCD_b$ on Intracellular Reactive Oxygen Species (ROS) Production

Detection of ROS generation in MDA-MB-231 cells following treatment with blank, **CD_b** and **$CoCD_b$** for 6 h and 12 h was carried out by using Dichlorofluorescein diacetate (DCFH-DA, Sigma). After cell uptake, DCFH-DA is deacetylated by cellular esterases to a non-fluorescent compound, which is later oxidized by ROS into 2'-7'dichlorofluorescein (DCF). DCF is a fluorescent compound which can be detected by fluorescence microscope. Briefly, following treatment with **CD_b** and **$CoCD_b$**, the cells were washed thoroughly with PBS and incubated with DCFH-DA for 20 min in the dark. Post incubation, the cells were washed with PBS thrice and monitored under fluorescence microscope (10x magnification)for intracellular ROS production that was proportional to the intensity of green fluorescence of 2′,7′-Dichlorofluorescein (DCF) produced within the living cells.

4.16 Formation of 3D-Tumor Spheroids.

Now in order to examine the antitumorigenic activity of **$CoCD_b$**, we developed 3D tumor spheroid by the hanging drop method using MDA-MB-231 cell lines. At first, confluent MDA-MB-231 cells were trypsinized with 0.05% trypsin−EDTA and centrifuged to collect cell pellets. From the cell pellets, 20 µL of cell suspension were then cultured in DMEM (high glucose) containing 10% FBS and antibiotics (100 mg/ L streptomycin and 100 IU/mL penicillin) in the lid of a 35 mm Petridish

in a humidified condition (5% CO_2 and 37 °C). The cell suspension drops were then monitored every day under a microscope for spheroid colony formation. After 4 days the development of tumour formation was satisfactory for our experimental purpose. We observe the dimension of tumour spheroids for 4 days by the Olympus cellSens Dimension software.

4.17 Effect of $CoCD_b$ on Growth and Proliferation of 3D-Tumor Spheroid.

The antiproliferation and antitumorigenic potential of **$CoCD_b$** was checked on the size of the 3D breast tumor spheroids. Briefly, the cultured tumor spheroids were treated with **$CoCD_b$** at the dose of 5 mg/mL which was the highest dose we use in MTT assay of 2D cell culture in a humidified condition (5% CO_2 and 37 °C) for its antiproliferation efficacy for 3 days. The antitumorigenic effect was also checked using different concentration (0.5-5 mg/mL) for 3 days. Following completion of drug incubation, the tumor spheroids were imaged under a microscope for any morphological alterations. The changes in dimension of the tumor spheroids were studied by the Olympus cellSens Dimension software. The tumor cell viability was checked by MTT assay. The results obtained from these studies further encouraged us to check the antiproliferative and apoptotic potential of **$CoCD_b$** (5 mg/mL) against 3D tumor spheroids by Live/Dead assay and flow cytometric assessment of annexin V-FITC/PI staining. The detailed procedure of Live/Dead assay study and flow cytometry assessment have been already mentioned above.

4.18 Detection of Hypoxia in 3D Tumor Spheroid

Live pre-formed 3D tumor spheroids were treated with **$CoCD_b$** (3 mg/mL) for 24-72h followed by double staining with Image-iT™ Red Hypoxia Reagent (Thermofisher Scientific) along with Hoechst 33342 (Thermofisher Scientific) for 1 h. The stained spheroids were then washed with PBS to remove the dyes and imaged under fluorescence microscope. The expression of HIF-1α was also assessed by immunoblotting of **$CoCD_b$** treated MDA-MB-231 cells.

4.19 Flow Cytometry.

For 2D cell culture **$CoCD_b$** was taken in 24-well plate having confluent MDA-MB-231 and HeLa cells in 10% FBS containing DMEM media. The final concentration of **$CoCD_b$** was fixed at 3 mg/mL in 500 µL of media. After 12 h incubation at 37 °C, cells were washed with cold PBS and trypsinized, followed by centrifugation to obtain the cell pellet. Pellets were suspended in 500 µL of Annexin V FITC (0.25 µg) and propidium iodide (PI, 1.0 µg)-containing 1X binding buffer. The cellular mixture was incubated for 15 min at room temperature in the dark. Cells were immediately analyzed in a BD FACS Aria™ III flow cytometer by exciting the sample at 488 nm and recording the emission at a 533 ± 30 (FL-1) bandpass filter for Annexin V-FITC and 585 ± 40 nm (FL-2) bandpass filter for PI. Experimental data was collected from 15,000 cells. In these data, there are four different quadrants which indicate the nature of the investigating cells. The Q1 quadrant shows the population of necrotic cells where Annexin V-FITC negative and PI-positive. Q2 shows the population of late apoptotic cells having both Annexin V-FITC and PI-positive. Q3 shows the population of alive cells where Annexin V-FITC and PI-negative. In the Q4 quadrant, the population of the early apoptotic cells is noted with Annexin V-FITC positive and PI-negative. In case of 3D tumor we prepared tumour spheroid using MDA-MB-231 cell line. In these sets we incubated **$CoCD_b$** at a dose of 5 mg/mL and analyzed the apoptosis for 24 h, 48 h, and 72 h respectively following same procedure above.

6. REFERENCES

1. Folkman, J.; Shing, Y. Angiogenesis. *J. Biol. Chem.***1992**, *267*, 10931-10934.
2. Maverakis, E.; Cornelius, L. A.; Bowen, G. M.; Phan, T.; Patel, F. B.; Fitzmaurice, S.; He, Y.; Burrall, B.; Duong, C.; Kloxin, A. M.; Sultani, H.; Wilken, R.; Martinez, S. R.; Patel, F. Metastatic Melanoma – A Review of Current and Future Treatment Options. *Acta Derm Venereol* **2015**, *95*, 516-524.
3. Delaney, G.; Barton, M.; Jacob, S. Estimation of an Optimal Radiotherapy Utilization Rate for Melanoma. *Cancer* **2004**, *100*, 1293-1301.
4. Cumberlin, R.; DeMoss, E.; Lassus, M.; Friedman, M. Isolation Perfusion for Malignant Melanoma of the Extremity: A Review. *J. Clin. Oncol.* **1985**, *3*, 1022-1031.
5. Win-Piazzaa, H.; Schneebergera, V.; Chena, L.; Pernazzac, D.; Lawrencec, H. R.; Sebtib, S. M.; Lawrencec, N. J.; Wu, J. Enhanced Anti-Melanoma Efficacy of Interferon Alfa-2b via Inhibition of Shp2. *Cancer Lett.* **2012**, *320*, 81-85.
6. Wlassoff, W. A.; Albright, C. D.; Sivashinski, M. S.; Ivanova, A.; Appelbaum, J.G.; Salganik, R. I. Hydrogen Peroxide Overproduced in Breast Cancer Cells Can Serve as an Anticancer Prodrug Generating Apoptosis-Stimulating Hydroxyl Radicals Under the Effect of Tamoxifen-Ferrocene Conjugate. *J. Pharm. Pharmacol.* **2007**, *59*, 1549-1553.
7. Trachootham, D.; Alexandre, J.; Huang, P. Targeting Cancer Cells by ROS-Mediated Mechanisms: A Radical Therapeutic Approach? *Nat. Rev. Drug Discov.* **2009**, *8*, 579-591.
8. Chakraborty, D.; Sarkar, S.; Das, P. K. Blood Dots: Hemoglobin-Derived Carbon Dots as Hydrogen Peroxide Sensors and Pro-Drug Activators. *ACS Sustain. Chem. Eng.* **2018**, *6*, 4661-4670.
9. Mazure, N. M.; Pouyssegur, J. Hypoxia-Induced Autophagy: Cell Death or Cell Survival? *Curr. Opin. Cell Biol.* **2010**, *22*, 177-180.

10. Challapalli, A.; Carroll, L.; Aboagye, E. O. Molecular Mechanisms of Hypoxia In Cancer. *Clin. Transl. Imaging* **2017**, *5*, 225-253.

11. Vaupel, P.; Mayer, A. Hypoxia in Cancer: Significance and Impact on Clinical Outcome. *Cancer Metastasis Rev.* **2007**, *26*, 225-239.

12. Haugland, H. K.; Vukovic, V.; Pintilie, M.; Fyles, A. W.; Milosevic, M.; Hill, R. P.; Hedley, D. W. Expression of Hypoxia-Inducible Factor-1α in Cervical Carcinomas: Correlation with Tumor Oxygenation. *Int. J. Radiat. Oncol. Biol. Phys.* **2002**, *53*, 854-861.

13. Russell, J.; Carlin, S.; Burke, S. A.; Wen, B.; Yang, K. M.; Ling, C. C. Immuno Histochemical Detection of Changes in Tumor Hypoxia. *Int. J. Radiat. Oncol. Biol. Phys.* **2009**, *73*, 1177-1186.

14. Kim, T.; Kim, H.; Choi,Y.; Kim, Y. meso-ester BODIPYs for the Imaging of Hypoxia in Tumor Cells. *Sens. Actuators B Chem.* **2017**, *249*, 229-234.

15. Caltana, L.; Merelli, A.; Lazarowski, A.; Brusco, A. Neuronal and Glial Alterations due to Focal Cortical Hypoxia Induced by Direct Cobalt Chloride ($CoCl_2$) Brain Injection. *Neurotox. Res.* **2009**, *15*, 348-358.

16. Huang, Y.; Du, K. M.; Xue, Z. H.; Yan, H.; Li, D.; Liu, W.; Chen, Z.; Zhao, Q.; Tong, J-H.; Zhu, Y-S.; Chen, G-Q. Cobalt Chloride and Low Oxygen Tension Trigger Differentiation of Acute Myeloid Leukemic Cells: Possible Mediation of Hypoxia-Inducible Factor-1alpha. *Leukemia* **2003**, *17*, 2065-2073.

17. Yuan, Y.; Hilliard,G.; Ferguson, T.; Millhorn, D. E. Cobalt Inhibits the Interaction Between Hypoxia-Inducible Factor-Alpha and Von Hippel-Lindau Protein by Direct Binding to Hypoxia-Inducible Factor-Alpha. *J. Biol. Chem.* **2003**, *278*, 15911-15916.

18. Matsuura, H.; Ichiki,T.;Ikeda, J.; Takeda, K.; Miyazaki, R.; Hashimot, T.; Nar abayashi, E.; Kitamoto, S.; Tokunou, T.; Sunagawa, K. Inhibition of Prolyl Hydroxylase Domain-Containing Protein Downregulates Vascular Angiotensin II Type 1 Receptor. *Hypertension.* **2011**, *58*, 386-393.

19. Rana, N. K.; Singh, P.; Koch, B. Polydatin Protects H9c2 Cells from Hypoxia-Induced Injury via Up-Regulating Long Non-Coding RNA DGCR5. *Biol. Res.* **2019**, *52,* 12.

20. Orozco-Ibarra, M.; Muñoz-Sánchez, J.; Zavala-Medina, M. E.; Pineda, B.; Magaña-Maldonado, R.; Vázquez-Contreras, E.; Maldonado, P. D.; Pedraza-Chaverri, J.; Chánez-Cárdenas, M. E. Aged Garlic Extract and S-Allylcysteine Prevent Apoptotic Cell Death in a Chemical Hypoxia Model. *Biol. Res.* **2016**, *49*, 7.

21. Sarkar, D.; Chowdhury, M.; Das, P. K. Naphthalimide Based Fluorescent Organic Nanoparticles in Selective Sensing of Fe^{3+} and as a Diagnostic Probe For Fe^{2+}/Fe^{3+} Transition. *J. Mater. Chem. B* **2021,** *9*, 494-507.

22. Liu, L.; Zhou, Q.; He, Q.; Duan, W.; Huang, Y.A pH-Responsive Supramolecular Drug Delivery System Constructed by Cationic Pillar[5]arene for Enhancing Antitumor Activity. *Front. Chem.* **2021**, *9*, 661143.

23. Roling, O.; Wendeln, C.; Kauscher, U.; Seelheim, P.; Galla, H. J.; Ravoo, B. J. Layer-by-Layer Deposition of Vesicles Mediated by Supramolecular Interactions. *Langmuir* **2013**, *29*, 10174-10182.

24. Dinda, S.; Sarkar, S.; Das, P. K. Glucose Oxidase Mediated Targeted Cancer-Starving Therapy by Biotinylated Self-Assembled Vesicles. *Chem. Commun.* **2018**, *54*, 9929-9932

25. Baker, S. N.; Baker, G. A. Luminescent Carbon Nanodots: Emergent Nanolights. *Angew. Chem., Int. Ed.* **2010**, *49*, 6726-6744.

26. Mansuriya, B. D.; Altintas, Z. Carbon Dots: Classification, Properties, Synthesis, Characterization, and Applications in Health Care-An Updated Review (2018–2021) *Nanomaterials* **2021**, *11*, 2525.

27. da Silva, J. C. G. E.; Goncalves, H. M. R. Analytical and bioanalytical Applications of Carbon Dots. *Trends Anal. Chem.* **2011**, *30*, 1327-1336.

28. Wareing, T. C.; Gentile, P.; Phan, A. N. Biomass-Based Carbon Dots: Current Development and Future Perspectives. *ACS Nano* **2021**,*15*, 15471-15501.

29. Zhang, H.; Wang, Y.; Xiao, S.; Wang, H.; Wang, J.; Feng, L. Rapid Detection of Cr(VI) Ions Based on Cobalt(II)-Doped Carbon Dots. *Biosens. Bioelectron.* **2017**, *87*, 46-52.

30. Ge, Y.; Ma, Y.; Li, L. The Application of Prodrug-Based Nano-Drug Delivery Strategy in Cancer Combination Therapy. *Colloids Surf.B* **2016**, *146*, 482-489.

31. Brahmachari, S.; Ghosh, M.; Dutta, S.; Das, P. K. Biotinylated Amphiphile-Single Walled Carbon Nanotube Conjugate for Target-Specific Delivery to Cancer Cells. *J. Mater. Chem. B.* **2014**, *2*, 1160- 1173.

32. Yang, W.; Cheng, Y.; Xu, T.; Wang, X.; Wen, L. Targeting Cancer Cells with Biotin-Dendrimer Conjugates. *Eur. J. Med. Chem.* **2009**, *44*, 862-868.

33. Chowdhury, M.; Das, P. K. Paclitaxel-Loaded Biotinylated Fe^{2+}-Doped Carbon Dot: Combination Therapy in Cancer Treatment. *ACS Appl. Bio Mater.* **2021**, *4*, 5132-5144.

34. Yang, M.; Feng, T.; Chen, Y.; Zhao, X.; Dr. Yang, B. Ionic-State Cobalt and Iron Co-doped Carbon Dots with Superior Electrocatalytic Activity for the Oxygen Evolution Reaction. *Chem. Electro. Chem.* **2019**, *6*, 2088-2094.

35. He, B.; Lu, N.; Zhou, Z. Cellular and Nuclear Degradation During Apoptosis. *Curr. Opin. Cell Biol.* **2009**, *21*, 900-912.

36. Ghosh, A.; Ghosh, A. K.; Chowdhury, M.; Das, P. K. Folic Acid-Functionalized Carbon Dot-Enabled Starvation Therapy in Synergism with Paclitaxel against Breast Cancer. *ACS Appl. Bio Mater.* **2022**, *5*, 2389-2402.

37. Perillo, B.; Donato, M. D.; Pezone, A.; Zazzo, E.D.; Giovannelli, P.; Galasso, G.; Castoria, G.; Migliaccio, A. ROS in Cancer Therapy: The Bright Side of the Moon. *Exp. Mol. Med.* **2020,** *52,*192-203.

38. Mittler, F.; Obeïd, P.; Rulina, A. V.; Haguet, V.; Gidrol, X.; Balakirev, M. Y. High-Content Monitoring of Drug Effects in a 3D Spheroid Model. *Front. Oncol.* **2017**, *7*, 293.

39. Kessel, S.; Cribbes, S.; Déry, O.; Kuksin, D.; Sincoff, E.; Qiu, J.; Chan, L. L. Y. High-Throughput 3D Tumor Spheroid Screening Method for Cancer Drug Discovery Using Celigo Image Cytometry. *SLAS Technol.* **2017**, *22*, 454-465.

40. Roy, S.; Kumaravel, S.; Sharma, A.; Duran, C. L.; Bayless, K. J.; Chakraborty, S. Hypoxic Tumor Microenvironment: Implications for Cancer Therapy. *Exp. Biol. Med.* **2020**, *245*, 1073-1086.

41. Nejad, A. E.; Najafgholian, S.; Rostami, A.; Sistani, A.; Shojaeifar, S.; Esparvarinha, M.; Nedaeinia, R.; Javanmard, S. H.; Taherian, M.; Ahmadlou, M.; Salehi, R.; Sadeghi, B.; Manian, M. The Role of Hypoxia in the Tumor Microenvironment and Development of Cancer Stem Cell: A Novel Approach to Developing Treatment. *Cancer Cell Int.* **2021**, *21*, 62.

CHAPTER 4

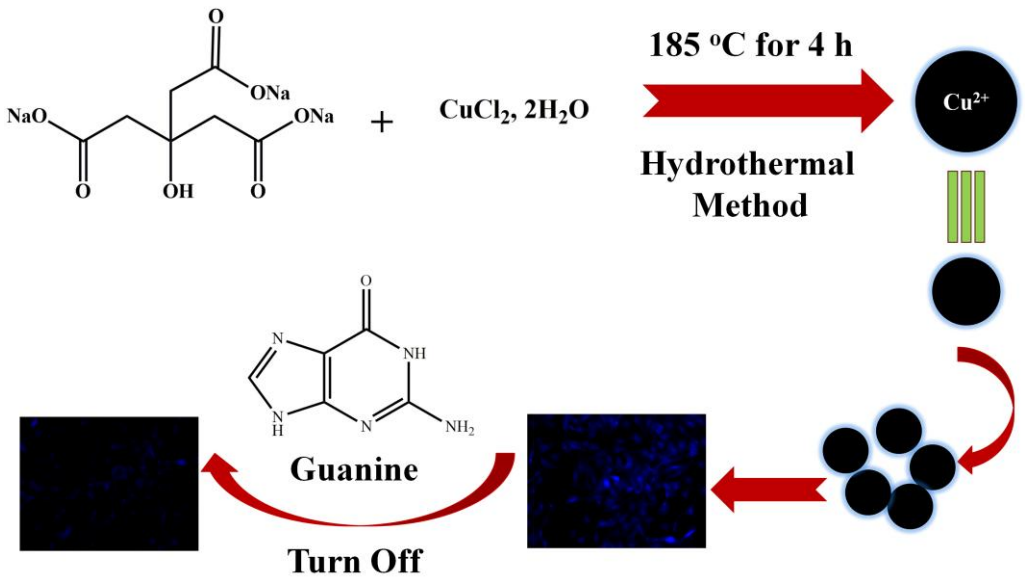

Cu^{2+} Integrated Carbon Dot as Efficient Bioprobe for Guanine Nucleobase

CHAPTER 4

Cu^{2+} Integrated Carbon Dot as Efficient Bioprobe...

1.INTRODUCTION

The human chromosome is a fascinating biopolymer that contains intricate design of deoxyribonucleic acid (DNA). DNA is a genetic molecule, which is made up of bases and nucleotides that plays significant role in biological heritage storage, lifecycle process and biosynthesis of protein in all living cells.[1-4]DNA associated with the development of every biological functions by replication and transcription of genetic information through distinctive amalgamation of guanine (G), adenine (A),thymine (T), and cytosine (C) nucleobases.[5-7]Guanine, one of the important purine bases existing in DNA, involved in processes such as energy transduction, metabolic cofactors, and cell signaling is of great importance to human and other creatures.[8-10]Among all the nucleotide bases, guanine is the most vulnerable to oxidize. The principal oxidation product of guanine is 8-oxo-Gua, was considered as a useful biomarker of DNA damage by oxidative stress which may be involved with the change of its content in organism. In other words, the alteration of variation in guanine concentration can cause deficiency and mutation in the immunity systems and it leads to some diseases including liver disease, AIDS, renal calculi and cancer.[8,11-16]Thus, to find an appropriate way to diagnose and determine the guanine is very significant for bioanalytical chemistry.

For this purpose, numerous methods have been employed such as laser inducedfluorimetry(LF),[17]chromatography,[18]capillaryelectrophoresis,[19]chemilumines cence,[20]high-performance liquid chromatography (HPLC),[21] mass spectrometry (MS) and others.[22] Despite these methods are sensitive, complicated instruments and time-consuming sample pretreatment restrict their wide applications. For instance, chromatography based techniques need the complex sample preparation steps, high overpotential. Poor reproducibility usually limits the use of the electrochemical methods. Also, capillary electrophoresis has the weakness of low stability and poor reproducibility etc.[4,23,24]Despite having these techniques well explored in the detection of guanine, it still remains a problem for developing more convenient, sensitive and stable methods for guanine sensing.

Fluorescence sensing has always been regarded as most promising method for biosensing due to simple operation, low cost and high sensitivity.[25,26]In this

regard, emission properties of nanomaterials could enhance biosensing and bioreceptors ability that would expand their applicability significantly. As such, various nanomaterials such as metal nanoparticles,[27] semiconductor-based quantum dots,[28] dye-doped materials[29]haveall been exploited in this arena. However, these nanomaterials-based biosensors have limitations, such as using of toxic heavy metals (i.e., cadmium, lead), potential hazards to environment, low photostability etc.[30,31]Therefore developing of a simple, sensitive and selective fluorescent probe is still in high demand irrespective of sensing applications in vitro or in vivo.

In this context, carbon dots (CDs) have received enormous attention in biosensing. CDs are a new family member of zero dimensional carbon-based nanomaterials with diameters less than 10 nm, known for their unique inherent fluorescence properties, cytocompatability, easy synthesis, high photostability, high water solubility, and chemical inertness.[32-36]Considering the above facts, herein we aim to develop copper (Cu^{2+}) doped carbon dot (**CuCD**)via hydrothermal method. We explored this blue emitting fluorescence (λ_{max}= 428 nm) **CuCD** as fluorescent probes through fluorescent turn-off method to realize a simple, sensitive and selective analysis of guanine. The fluorescence intensity of **CuCD** got quenched significantly in presence of guanine due to the formation of a stable interaction between Cu^{2+}ions and guanine. Accordingly, the **CuCD** are used as fluorescence probes for application inthe detecting guanine having the limit of detection(LOD)= 1.57 μM. Importantly, the guanine sensing by **CuCD** was found to be selective in solution against all the other nucleobases like adenine, thymine, cytosine as well as with respect to different biomolecules and metal ions that are abundant in cellular environment. All these investigated molecules have no interference for the detection of guanine. Moreover, in cellular studies, this **CuCD** can efficiently quenched guanine treated cell line (B16F0 and NIH3T3) with respect to the control untreated ones and having cell viability upto ~90%.Thus, a highly sensitive and selective ratiometric fluorescence probe **CuCD** for selective guanine detection was synthesized which also can sense guanine enriched cells through fluorescence turn off mechanism.

2.RESULTS AND DISCUSSION

In comparison to traditional nanomaterials, carbon dots (CDs) have various advantages in biosensing due to their unique physicochemical properties. In company with their nontoxicity, photoluminescence (PL) stability, chemical inertness is very advantageous in biosensing. As it is well-known, optical biosensors function by converting intangible information about target analytes into detectable optical signals (i.e., fluorescence intensity/wavelength, color change).[37]Interestingly, the PL property of CDs can be tuned by carefully selecting carbon precursors,[38]synthesis conditions,[39] and heteroatom doping.[40]Doping could provide a means for emerging chemical reactivities and potential applications of CDs. More interestingly, metal atom doping can improve novel functionalities of the CDs because of its different band structures and makes it a potent candidate for desired molecule sensing nanoprobe.[41,42] Copper (Cu^{2+}) complexes are being investigated extensively along with other transition metals (Fe^{2+}, Co^{2+}, Ni^{2+}) due to its biocompatible properties and oxidative nature.[43]It has gained importance rapidly in biological applications and industrial processes. Literature survey speaks about a number of Cu^{2+}complexes with mixed ligand donor type or with Schiff Base donors.[44] Cu^{2+}can bind with DNA and that led to DNA denaturation which is similar to acid denaturation.Importantly,Cu^{2+}can form a stronger binding in presence of guanine.[45,46]Guanine is crucial part of DNA and any alteration in the concentration of this nucleobase can cause mutations, tumorigenesis and cell death. So, precise detection of this component in bio-sample is essential to know the early signals of various diseases and monitoring cellular environment.[47]The above facts led us to create a selective, sensitive and easy to synthesize nanoprobe for guanine sensing. We synthesized Cu^{2+}doped carbon dot (**CuCD**) having blue emission under UV light irradiation. Cu^{2+}acted as an integral component of the synthesized carbon dot and thus used as a selective sensor for guanine (Scheme 1).

CHAPTER 4

Cu^{2+} Integrated Carbon Dot as Efficient Bioprobe...

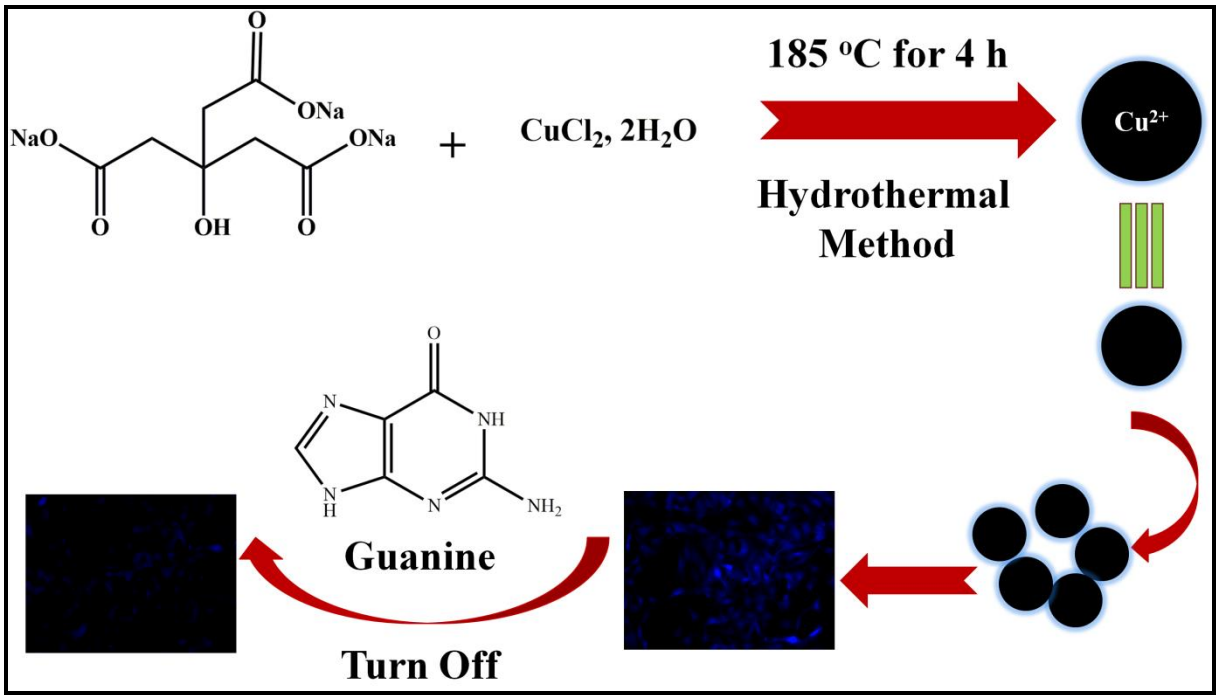

Scheme 1. Schematic representation of guanine sensing via Cu^{2+} doped carbon dot (**CuCD**).

2.1 Synthesis of Cu^{2+}-Doped CarbonDot (CuCD).

Cu^{2+} doped carbon dot (**CuCD**) was prepared via hydrothermal method using equivalent amount of tri sodium citrate, and $CuCl_2$, $2H_2O$. Tri sodium citrate was used as source of carbon core, Cu^{2+} as doping element (Figure 1a). Synthesized **CuCD** (Scheme 2, Experimental Section) was surface functionalized by carboxylic acid of citrate group. The synthesized **CuCD** was soluble in water and the corresponding zeta potential (ζ) value was -13.1 mV, indicating its stability in aqueous medium. Microscopic characterization of Cu^{2+} doped carbon dot **CuCD** was investigated by TEM and AFM. The data from TEM images confirmed the size of **CuCD** was ~ 5 nm (Figure 1b). AFM images also indicated the size of **CuCD** was between 2-5 nm which supported the result obtained from TEM image (Figure 1c).The XRD analysis was carried out for the characterization of **CuCD**. The peak ranges from 20-25°established the amorphous nature of prepared **CuCD** (Figure 1d).In accordance to the XPS analysis of **CuCD**, peaks at 284, 406, and 529 eV confirmed the presence of C (1s), N (1s), and O (1s) orbitals, respectively (Figure 2a).Along with these peaks, a peak with doublet character was observed in the

region of 935-962 eV, corresponding to the presence of Cu in the moiety. The deconvoluted spectra of Cu^{2+} showed two typical peaks at 935.18 eV and 956.05 eV with satellite peaks (942 eV and 962 eV) that were associated with Cu $2p_{3/2}$ and Cu $2p_{1/2}$ electronic configurations, respectively, indicating the existence of copper as Cu^{2+} within **CuCD**(Figure 2b).

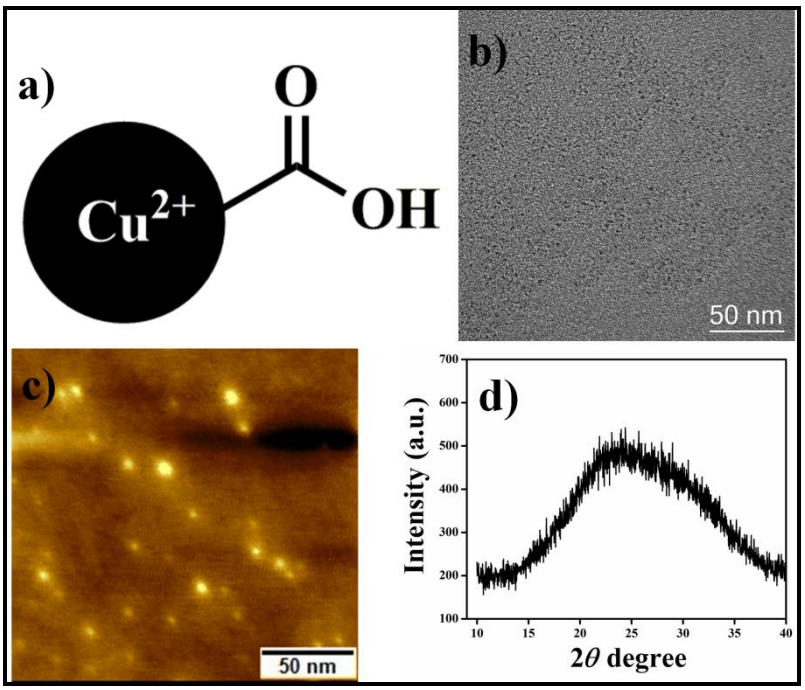

Figure 1. a) Chemical structure of **CuCD**, b) TEM image, c) AFM image and d) XRD of **CuCD**.

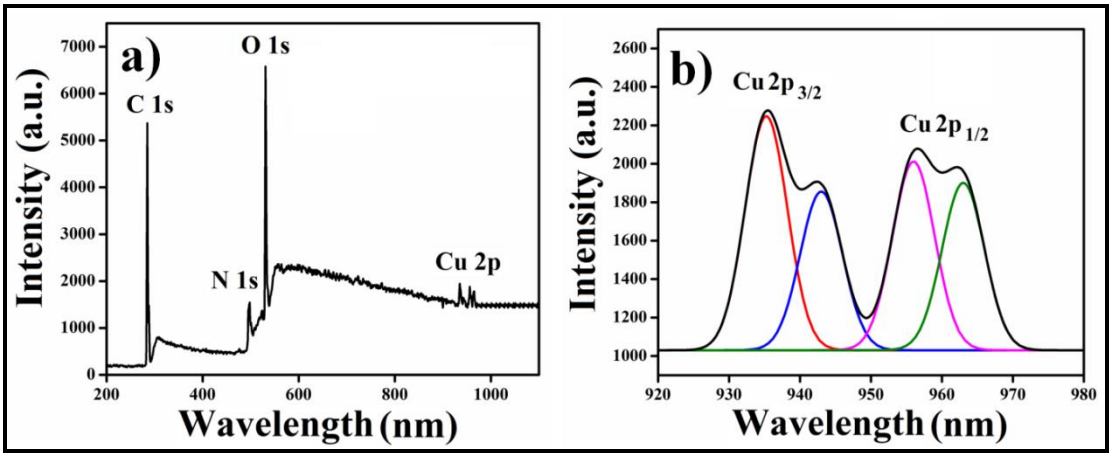

Figure 2. a) XPS spectra of **CuCD**, b) deconvoluted Cu 2p orbital of **CuCD**.

CHAPTER 4

Cu^{2+} Integrated Carbon Dot as Efficient Bioprobe…

2.2 Spectroscopic Study ofCuCD.

Next the spectroscopic property of **CuCD** was investigated. The UV-visible spectra of aqueous solution of **CuCD** showed one prominent feature centered at 333 nm (Figure 3a). After UV-visible study, we wanted to investigate the surface property of **CuCD** by IR spectra. In case of IR spectrum of **CuCD**, the corresponding FTIR spectrum showed O-H stretching of –COOH group at around 3370 cm^{-1} merged with 3200 cm^{-1} for O-H stretching of alcohol group, C=C bending of alkyne at 1644 cm^{-1}, O-H bending of –COOH group at 1408 cm^{-1} and C=C bending at 999 cm^{-1} (Figure 3b). The above frequency peaks in IR spectrum of **CuCD** concludes the presence of carboxylic acid in the surface of newly synthesized carbon dot. Next, we investigated the fluorescence spectra of **CuCD**. The **CuCD** showed excitation dependent blue emission with emission maxima at 428 nm (λ_{max}) upon excitation at 340 nm (Figure 3c). Aqueous solution of **CuCD** showed bright blue fluorescence (inset, Figure 3c) under UV light irradiation (365 nm). The quantum yield of **CuCD** was observed around 4% with respect to quinine sulfate. Thus, the spectroscopic studies informed us about the surface functionality and intrinsic fluorescence property of **CuCD** which then we can explore for sensing purpose.

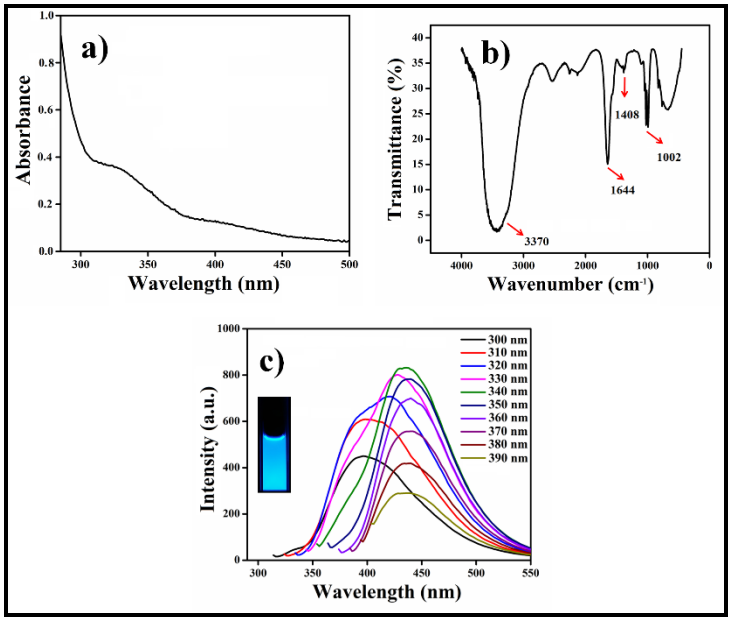

Figure 3. a) UV-visible spectrum, b) IR spectrum and c) Excitation-dependent emission spectra of **CuCD** (inset in panel are photographs showing the blue fluorescence of **CuCD** solution under UV irradiation, 365 nm)

2.3 Guanine Sensing by CuCD.

After we successfully prepared Cu doped carbon dot (**CuCD**) and investigated its microscopic and spectroscopic properties, we intend to explore its fluorescence property in sensing of one of the nucleobases, Guanine. Guanine is one of the two essential purine bases of DNA, which play a major role in coronary blood flow regulation, energy transduction, cell proliferation etc and the modulation of its concentration leads to mutation and multiple diseases.[10]Therefore, we aim to explore the inherent fluorescence property of **CuCD** in selective sensing of guanine. In this regard, the intensity of the fluorescence spectra of **CuCD** (250 μg/mL) at 428 nm was recorded in the presence of varying concentrations of guanine (1-100 μM). Interestingly, with the gradual increasing concentration of guanine the emission intensity of **CuCD** got gradually quenched (Figure 4a). The quenching effect by guanine steadily increased up to 100 μM and thereafter no significant change in the quenching effect was noted up to 250 μM of guanine. The quenching of **CuCD** by guanine was analyzed quantitatively by using the Stern–Volmer equation,

$$F/F_0 = 1 + K_{SV}[Q] \qquad (1)$$

In this equation, F and F_0 are the fluorescence intensities of **CuCD** in the presence and absence of guanine respectively; K_{SV} is the Stern–Volmer constant; and [Q] is the quencher concentration. The change in F/F_0 of **CuCD** with guanine up to 10μMwas observed and the Stern–Volmer plot showed linearity in fluorescence quenching of **CuCD** by guanine with a K_{SV} of $0.017\mu M^{-1}$(Figure 4b).

As the **CuCD** displayed a sensitive quenching response to guanine, therefore we measured the detection limits of guanine. The emission intensity of **CuCD** (250 μg/mL) at 428 nm decreased proportionately with the concentration of guanine ranging from (1-100 μM)(Figure 4a).The sensitivity was measured based on the relationships between the ratios of emission intensities of **CuCD** with varying concentration of guanine. A good linear behavior was observed in the fluorescence response curve which was plotted (defined as $(F_0 - F)/F_0$, where F_0 is the emission intensity of the native **CuCD** and F is the emission intensity of **CuCD** in presence of

guanine) against the concentration of guanine that demonstrated a linear relationship in the concentration range of 1-10 μM indicating efficient guanine sensing at low concentration (Figure 4c).The detection limit of guanine was found to be 1.57 μM for **CuCD** as determined based on 3σ/S where σ was the standard deviation and S was the slope of the calibration curve. The linear regression equation was $(F_0 - F)/F_0$= -0.01+ 0.017x concentration of guanine (μM); correlation coefficient (R^2) of 0.99.

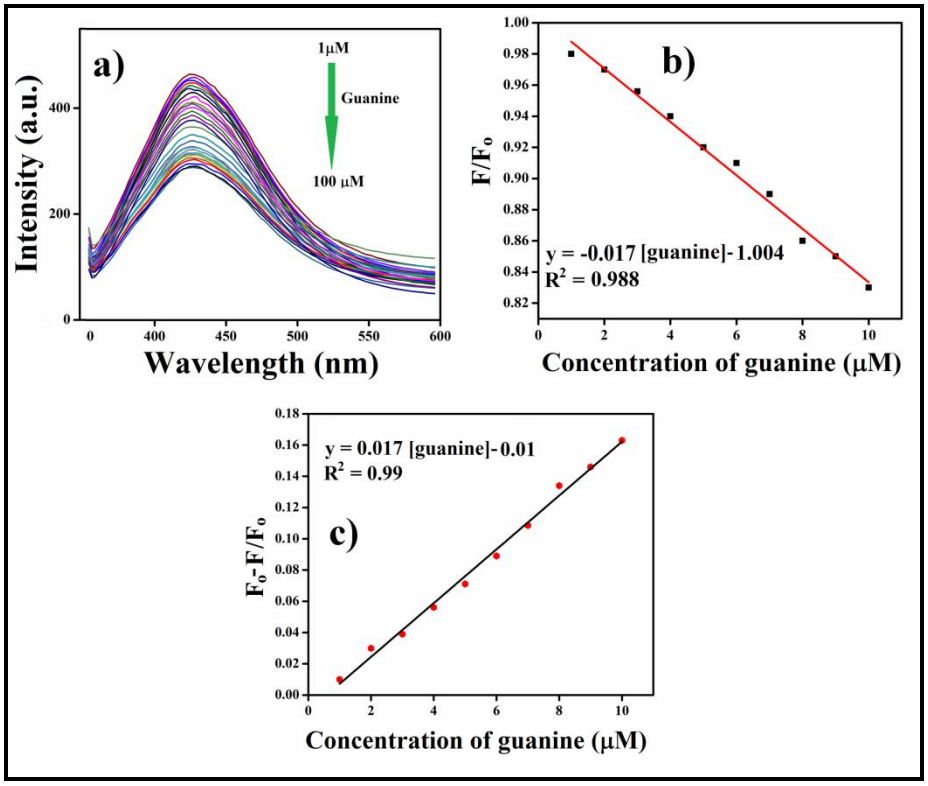

Figure 4. a) Quenching of **CuCD** (250 μg/mL) emission intensity in presence of guanine (1-100 μM) (b) Stern–Volmer plot of guanine in aqueous solution of **CuCD** (250 μg/mL), (c) fluorescence response of **CuCD** (250 μg/mL) towards guanine sensing with varying concentration of guanine (1-10 μM).

The next obvious intriguing issue arises that how will be the influences of other nucleobases on the emission property of **CuCD**. Other than guanine (G), DNA have another three nucleobases i.e. adenine (A), cytosine (C) and thymine (T). We investigated the sensitivity as well as selectivity of **CuCD** towards other nucleobase bases (A,T, and C). Selectivity is essential as well as crucial for the credibility of any

new sensor. To this end, in different set of experiments A, T, C (250 μM) were separately added to 1mL of **CuCD** (250 μg/mL) solution. Interestingly, in comparison to the native emission intensity of **CuCD**, very less significant changes in the fluorescence intensity of **CuCD** was noted in presence of adenine, cytosine and thymine (Figure 5a). Moreover, the emission quenching in presence of guanine (100 μM) overwhelmingly significant compared to that in presence of A, T and C (Figure 5a). A lesser amount of guanine is capable of enough to quench the emission of **CuCD** far more significantly. This observation undoubtedly increases the reliability of our newly developed Cu doped carbon dot (**CuCD**) as a selective and sensitive guanine base sensor among other nucleobases (Figure 5a,b).

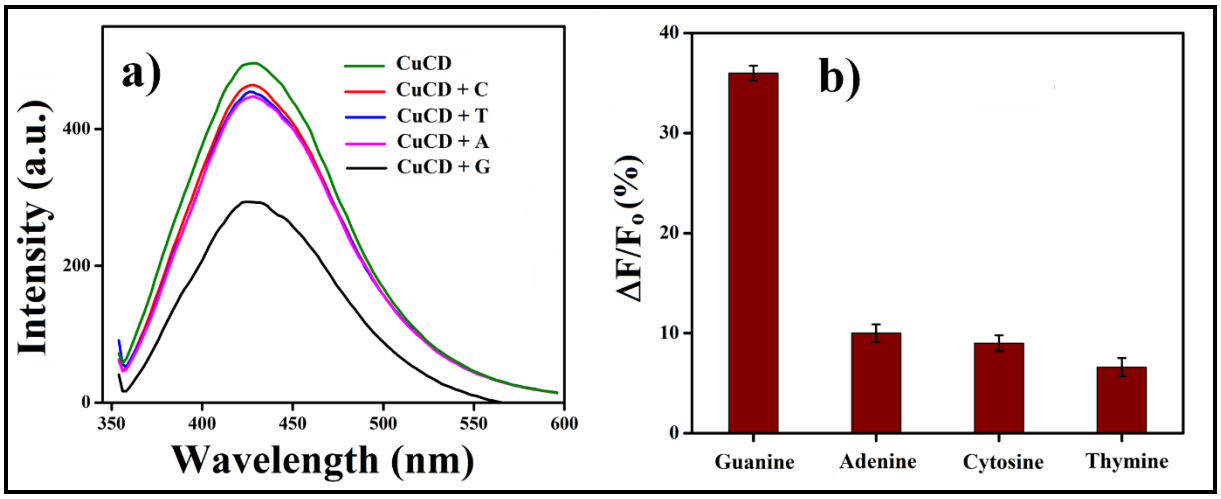

Figure 5. Selectivity of **CuCD** (250 μg/mL) to guanine (100μM) over other nucleobases (250μM). (a) Fluorescence intensity plot (b) relative intensity of **CuCD** in presence of different nucleobases. The error bars represent the standard deviations.

Molecular sensing always depends how it interacts with the particular sensor. At the same time, selectivity of that sensor towards that particular molecule gets influenced by the specific interaction. It is a well-established fact that $Cu^{2+}$is capable of making strong interaction with Schiff bases, oxygen, nitrogen, sulphur containing units specially mix ligand donor type moieties.[44] All the nucleobases of DNA have one of these structural properties within them(Figure 6). A, G, C have Schiff bases whereas T have oxygen as a donor ligand in it's structure. Among all the nucleobases only A and G have both Schiff bases, oxygen and nitrogen as

donor ligands so that they can from better interaction with the **CuCD** in comparison to that by C and T. It is interesting that despite having similar structural properties of adenine and guanine, **CuCD** was more selective towards guanine. According to literature survey, guanine oxygen at C6 and N7 have the perfect arrangement for making suitable interaction with Cu^{2+} of **CuCD**.[46,48,49]Additionally,primary amine at C2 of guanine can possibly engaged in the resonance and as a result of that the lone pair of oxygen at C6 could be readily available for creating impactful interactions with $Cu^{2+}$of **CuCD**. Thereby it has led to the significant quenching of the fluorescence of **CuCD**. In the light of this, it may be assumed that adenine with primary amine at C6 and N7 have the optimal arrangement for making suitable interaction with $Cu^{2+}$of **CuCD**. However, the lone pair of primary amine at C6 was not available for making interactions with Cu^{2+}as it was possibly engaged in extended resonance within the six membered ring of adenine. Consequently, $Cu^{2+}$of **CuCD** could not form an effective interaction with adenine in comparison to that by guanine. Therefore, adenine could not quench the inherent emission intensity of **CuCD**.

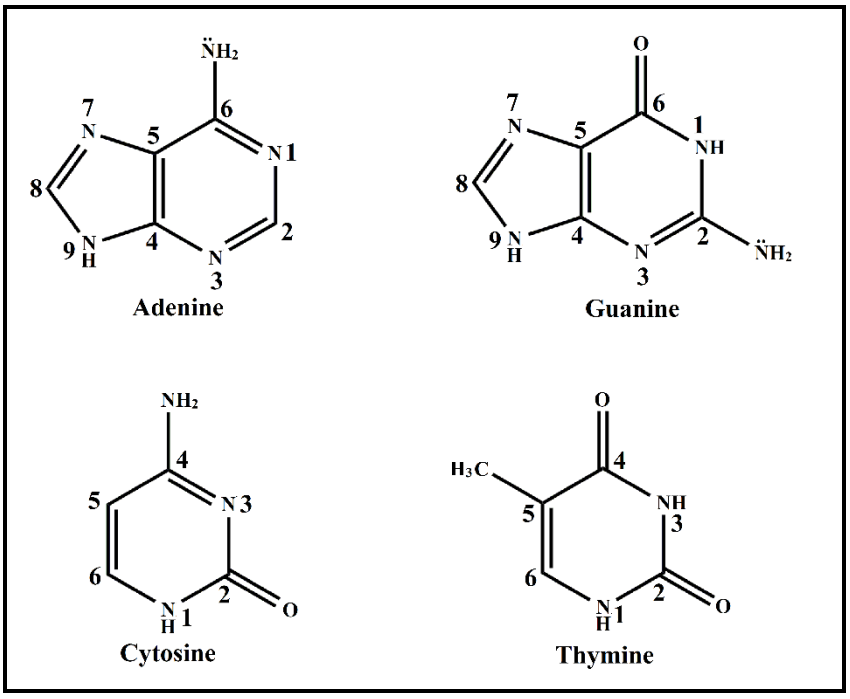

Figure 6. Structures of Adenine, Guanine, Cytosine and thymine nucleobases.

An interference study was further performed to investigate the selective sensing of guanine even in presence of other nucleobases. The fluorescence intensity response of **CuCD** (250 μg/mL) solution in presence of all the other nucleobases (A, T, and C) were separately recorded in absence of guanine. As expected, there were not prominent changes in emission intensity with respect to the native **CuCD**. Follow ed by guanine was added in each sample of **CuCD** and nucleobase mixture. In each case, fluorescence intensity got markedly quenched upon addition of guanine in that mixture (Figure 7 a,b,c).These observations conclude that **CuCD** can selectively sense guanine even in the presence of other nucleobases (A,C, and T).

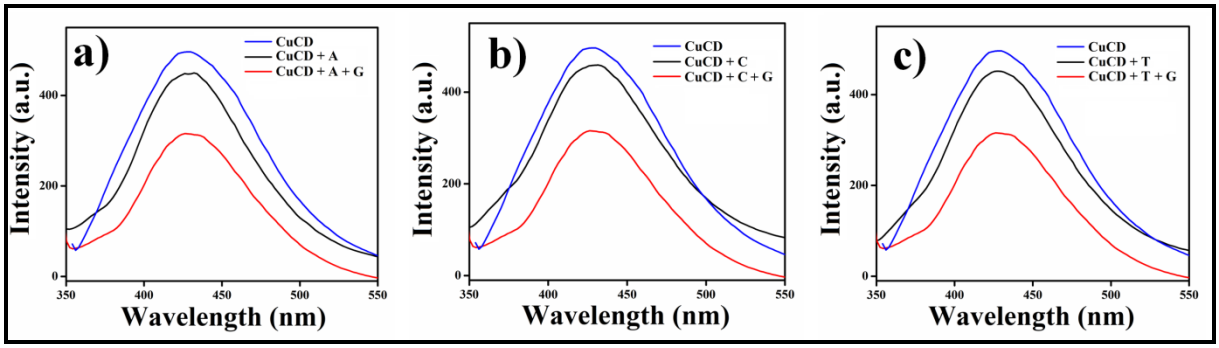

Figure 7. Interference studies between guanine (100 μM) and a) sample of **CuCD** (250 μg/mL) and Adenine mixture, b) sample of **CuCD** (250 μg/mL) and Cytosine mixture and c) sample of **CuCD** (250 μg/mL) and Thymine mixture.

As previously stated, guanine is a major part of DNA. Apart from that it is also an essential biomolecule for cell itself. Thus, the selective of sensing guanine with respect to different monovalent ions, divalent ions, amino acids and biomolecules which are abundant in cell environmentis also very important. To this end, 1mLfluorescence intensity of **CuCD** (250 μg/mL) solution was recorded in presence of monovalent ion (Na^{+}, K+), divalent ion (Ca^{2+}, Fe^{2+}, Zn^{2+}), amino acids (L-Cys, L-Trp, L-Tyr, L-Arg, L-Asp acid) and biomolecule (GSH). In each instance, 100 μM concentration of every component was used in this experiment. In case of monovalent and divalent ions there were no alterations in the fluorescence intensity of **CuCD** with respect to its native emission (Figure 8). In case of amino acids and GSH there were very meager quenching in the fluorescence intensity of **CuCD**in comparison to the significant quenching observed in presence of guanine

(100 μM)(Figure 8a,b).These results further established the strong interaction of **CuCD** with guanine compared to all other investigated molecules. After analyzing the above observations, we can certainly assume that our newly synthesized **CuCD** detect guanine with high selectivity and sensitivity against all other DNA nucleobases, different ions, amino acids and biomolecule.

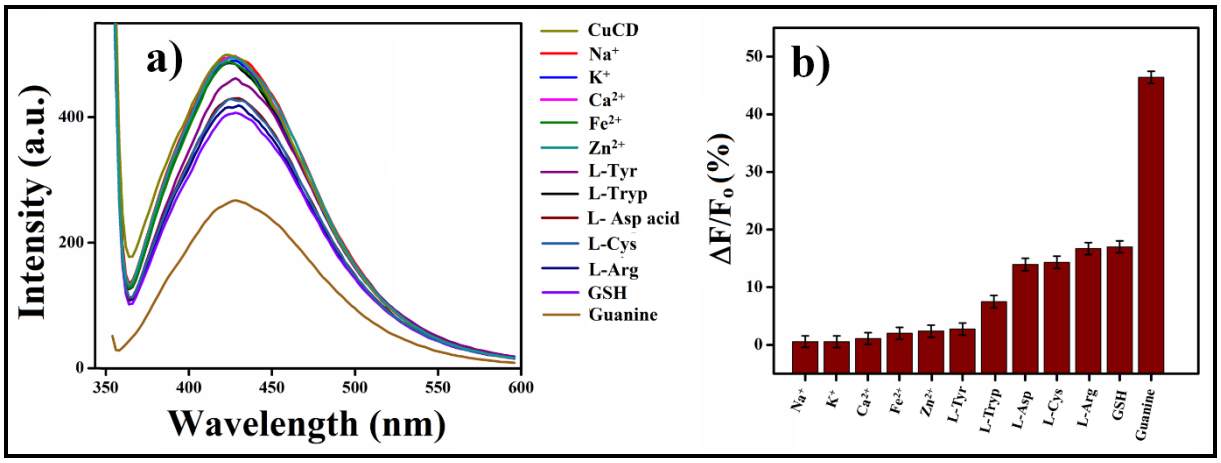

Figure 8. Selectivity of **CuCD** (250 μg/mL)to guanine over other metal ions and biomolecules (100 μM). (a) Fluorescence intensity plot (b) relative intensity of **CuCD** in presence of different metal ions and biomolecules. The error bars represent the standard deviations.

2.4 Media Stability of CuCD.

Prior to the utilization of the newly synthesized Cu^{2+} doped carbon dot **CuCD** as a potential bioprobe for guanine sensing in cellular environment, we investigated its (i) stability in biological media in a time dependent manner and (ii) cytocompatibility toward mammalian cells. In FBS-DMEM media, 500 μg/mL of **CuCD** was added having FBS of different concentrations (up to 75%) and kept for 48 h (Figure 9a). The prolonged stability of **CuCD** was also investigated by keeping the mixtures of **CuCD** (500 μg/mL)-FBS (10%)-DMEM media for 10 days (Figure 9b). In both the cases suspension stability index (SSI) of **CuCD** in media was found 90 ± 2% for varying concentrations of FBS (0-75%, (Figure 9a,b). The stability of **CuCD** in biological media is also in concurrence with respective its visual images (Figure 9a). Next, we also investigated the stability of **CuCD** under UV light exposure (365 nm and 12 W) where no photobleaching property was observed and

even emission property of the fluorescent bioprobes did not change after 200 min of UV irradiation (Figure 9c).

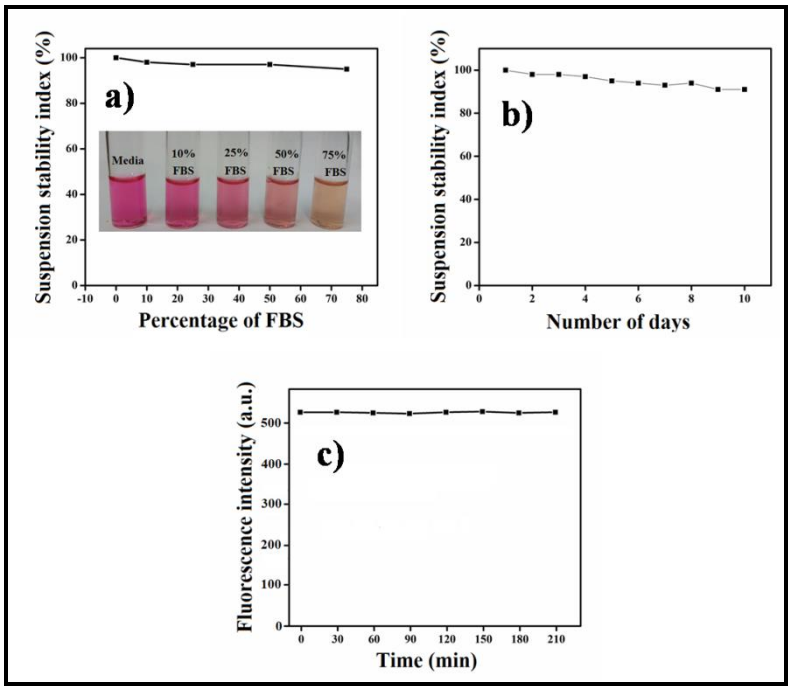

Figure 9. Suspension stability index of **CuCD** solution where [**CuCD**] = 500µg/mL a)**CuCD** with respect to FBS concentration (0-75%) in DMEM media, b) **CuCD** with respect to number of days in 10% FBS in DMEM media and c) Photostability of **CuCD** solution under UV (wavelength 365 nm, power 12 W) light irradiation up to 200 min.

2.5 Cytocompatibility of CuCD.

After confirming the stability of **CuCD** in biological milieu for a course of time, we also investigated the cytocompatibility of **CuCD** against mammalian cells as we wanted to utilize this bioprobe for cellular imaging. We investigated the cytocompatibility of **CuCD** against B16F10, and NIH3T3 cells by MTT assay. Different concentrations of **CuCD** = 50-500µg/mL were incubated with B16F10 melanoma cells, and noncancerous NIH3T3 cells. Interestingly, it was found that the cell viability of **CuCD** were 90-95% toward B16F10 melanoma cells as well as noncancerous NIH3T3 cells after 12 h incubation(Figure 10). Hence the newly synthesized **CuCD** did not exert any toxicity to the mammalian cells and safe to be used for biomedicinal applications including bioimaging.

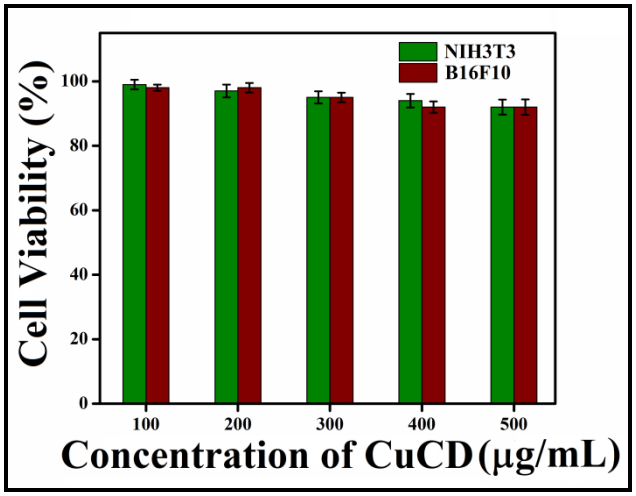

Figure 10. Cell viability experiment of **CuCD** where [**CuCD**] = 50-500 μg/mL in both NIH3T3 and B16F10 cell lines after 12 h of incubation. The standard deviation was in the range of 1-3% in triplicate experiments.

2.6 Bioimaging.

Guanine plays major role in mutation, tumorogenesis, cancer, AIDS etc. Thus,its sensing in cellular environmentis necessary for early diagnosis of numerous biological functions and diseases.[10]The guanine induced quenching of **CuCD** emission encouraged us further to explore this probe in distinguishing between guanine incubated cells and their respective control cell lines. So, we intended to exploit the intrinsic fluorescence of **CuCD** in the sensing of guanine treated non cancer and cancer cell lines. We choose cancerous B16F10 cell lines and NIH3T3 normal cell lines for this purpose. Initially, we incubated guanine (100 μM) with both B16F10 and NIH3T3 cell lines for 24 h. After 24 h, guanine treated and untreated cell lines were washed with PBS three times. Followed by guanine treated cell lines were incubated with **CuCD** (500 μg/mL) for 8 h. Along with them we also took guanine non treated native B16F10 and NIH3T3 cell lines and incubated with **CuCD** (500 μg/mL) for 8 h also. After completion of incubation, both guanine treated and non-treated cells were observed under fluorescence microscope. We observed a bright blue fluorescence of internalized **CuCD** in guanine non-treated NIH3T3 cells (Figure 11 b,d) in comparison to the quenched fluorescence noted in guanine treated NIH3T3 cells under similar experimental conditions. In case of B16F10 cells, similar phenomenon was observed having bright blue fluorescence of internalized **CuCD** for guanine non-treated cells and quenched fluorescence of

CuCD within guanine treated cells. (Figure 12b,d). The observed cellular internalization of **CuCD** and the quenching of its fluorescence in guanine treated cell lines could certainly made it a potential biomarker for guanine nucleobase both in vitro as well as within mammalian cells.

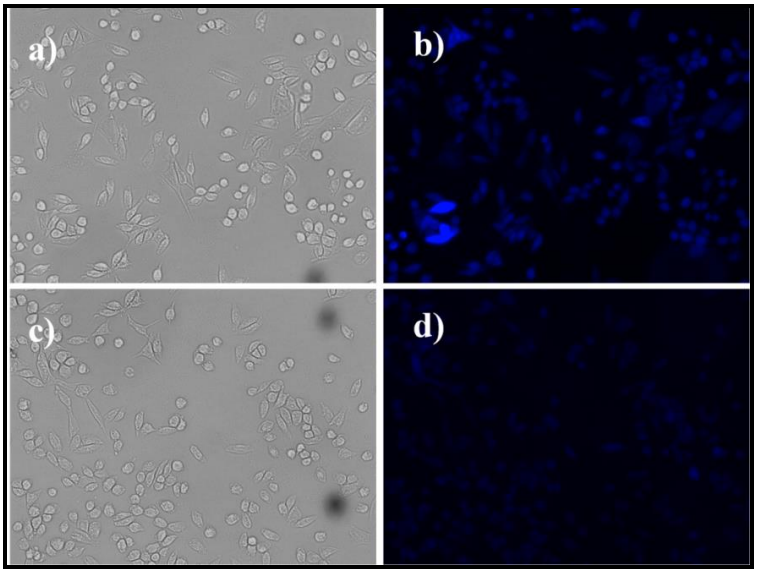

Figure 11. Bright field and fluorescence microscopic images of cells after 8 h incubation with **CuCD** where [**CuCD**] = 500 μg/mL, (a,b) untreated NIH3T3 (c,d) treated NIH3T3 cells with guanine (100 μM).

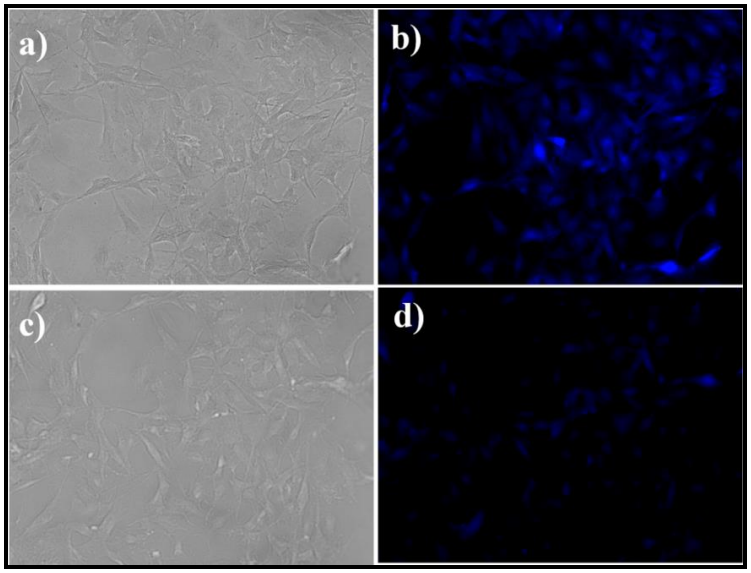

Figure 12. Bright field and fluorescence microscopic images of cells after 8 h incubation with **CuCD** where [**CuCD**] = 500 μg/mL, (a,b) untreated B16F10 (c,d) treated B16F10 cells with guanine (100 μM).

CHAPTER 4

Cu^{2+} Integrated Carbon Dot as Efficient Bioprobe…

3.CONCLUSION

In this present work, we have synthesized a Cu^{+2} doped carbon dot (**CuCD**) via hydrothermal method which exhibited concentration dependent blue fluorescence at 428 nm when excited at 340 nm. All microscopic and spectroscopic characterization was carried out for this newly synthesized Cu^{2+}doped carbon dot.TEM, AFM concluded its size ~5 nm and XPS confirmed the presence of Cu^{2+}in **CuCD. CuCD** can effectively sense guanine nucleobase with a limit of dectection of 1.57 μM. This Cu^{+2}doped carbon dot can also selectively detect guanine with high sensitivity against other nucleobases of DNA (A, T and C) and with respect to monovalent, divalent ions, amino acids and biomolecule. Concurrently, **CuCD** was successfully employed for bioimaging guanine enriched B16F10 and guanine NIH3T3 cell lines via fluorescence quenching within living cells with respect to control B16F10 and NIH3T3 cells. Hence, **CuCD** can be used as a selective and sensitive diagnostic probe for guanine sensing.

4.EXPERIMENTAL SECTION

4.1 Materials

Sodium citrate, ethylenediamine, copper chloride dihydrate ($CuCl_2$,$2H_2O$), Adenine, Guanine, Cytosine, Thymineand all other reagents and solvents were bought from SRL, India. MTT (3-(4,5-dimethylthiazol-2-yl)-2,5-diphenyltetrazolium bromide), and other deuterated solvents were purchased from Sigma-Aldrich. Dialysis tubing was procured from Thermo Scientific SnakeSkin (3.5K MWCO). Dulbecco's modified Eagle's medium (DMEM), fetal bovine serum (FBS), and Trypsin−ethylenediaminetetraacetic acid (EDTA) solution 1× (0.25% solution) was bought from Himedia. NIH3T3 andB16F10 cells were received from NCCS, Pune, India. All experiments were carried out using Milli-Q water. Agilent Cary Eclipse luminescence spectrometer was used to record fluorescence spectra. Perkin Elmer Spectrum 100 was used to record FTIR spectra. Centrifugation was performed using a Thermo Scientific Espresso centrifuge. Nano-ZS of Malvern Instruments Limited was used to measure zeta potential. A Telsonic bath sonicator was used to perform bath sonication.

4.2 Synthesis of Cu^{2+}-doped Carbon Dot (CuCD).

Cu^{2+} doped carbon dot (**CuCD**) was synthesized by hydrothermal route. 147 mg of tri sodium citrate (0.1M) and17 mg of copper chloride (0.025 M) were dissolved in 5 ml Milli-Q water. The solution was mixed and sonicated to obtain a transparent solution. The solution was heated at 185 °C for 6 h in a heating platform. After 6 h the color of the solution gradually turned to yellow. The solution was filtered by 0.22 μm syringe filter and it was dried using lyophilize to collect the **CuCD** having yield ~60% (Scheme 2).

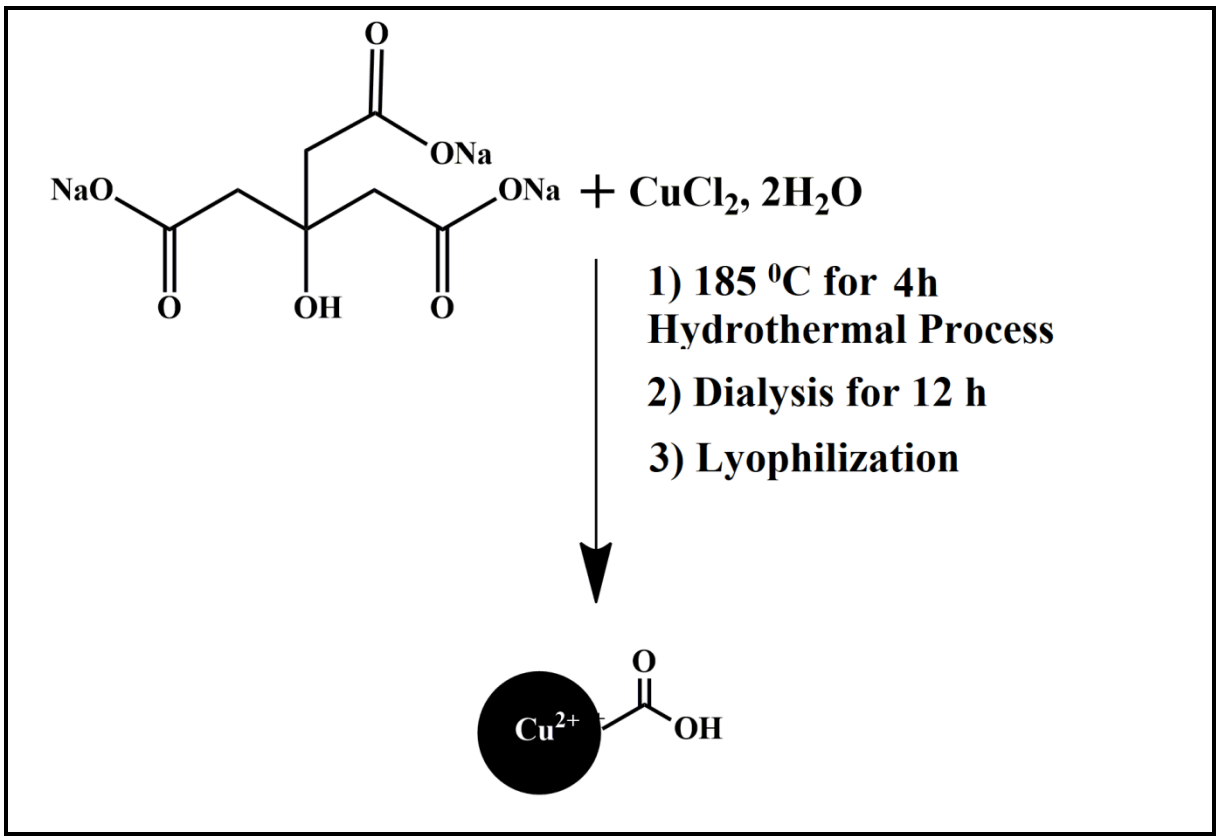

Scheme 2. Synthetic scheme of **CuCD**.

4.3 Characterization.

Aqueous solution of **CuCD** was sonicated for few min and then Cu-coated grid was used for drop casting of **CuCD** and dried for imaging in transmission electron microscope (TEM, 2100F UHR microscope JEOL JEM). In case of atomic force microscopic (AFM) imaging (Veeco, model AP0100 microscope), a drop of **CuCD**

solution was air dried on fresh mica surface overnight. For X-ray photoelectron spectroscopy (XPS) (Omicron series 0571) **CuCD** solution (8 µL) was dried overnight on rectangular glass plates. X-ray diffraction (XRD) spectra of **CuCD** were obtained on a diffractometer (Bruker D8 Advance). The zeta (ζ) potential measurement was investigated with aqueous solutions of **CuCD** at room temperature.

4.4 Quantum Yield Measurement.

The absorbance value of carbon dot solution was restricted to <0.1, and integrated emission intensities of those solutions were recorded in a luminescence spectrometer. The quantum yield (Q) was obtained using the following equation:

$$\emptyset_u = \left(\frac{A_s F_u n_u^2}{A_u F_s n_s^2}\right)\emptyset_s \qquad (1)$$

where I is the integrated emission intensity measured at the excitation maxima (350 nm), OD denotes the optical density, η represents the refractive index. The subscript "sm" stands for sample and the subscript "st" indicates the standard fluorescence of a known fluorophore. We have used quinine sulfate as a standard dissolved in 0.1 M H_2SO_4. The quantum yield of quinine sulfate is Q = 0.54.

4.5 Fluorescence Spectroscopy.

Fluorescence spectra of 500 µg/mL of **CuCD** were recorded with varying λ_{ex} from 300 to 390 nm. The variation of the fluorescence of 250 µg/mL of **CuCD** was studied by adding different concentrations of Guanine (1-100 µM).We carried out all the sensing studies in Milli Q water. The Stern–Volmer constant(K_{SV}) of the kinetics of fluorescence quenching of **CuCD** with respect to guanine concentration was obtained using the equation $F/F_0 = 1+K_{SV}[Q]$, where F and F_0 are the fluorescence intensities of **CuCD** in the presence/absence of guanine and[Q] denotes concentration guanine. The guanine detection limit was evaluated from the linear curve obtainedfrom $(F_0-F)/F_0$ vs. the guanine concentration. The intensity of fluorescence was measured at 428 nm for **CuCD** and upon exciting 340 nm. In selectivity study the fluorescence of **CuCD** was also investigated by A, T, C (250 µM) and Na^+, K+, Ca^{2+}, Fe^{2+}, Zn^{2+},L-cys, L-trp, L-tyr, L-Arg, L-asp acid, GSH having concentration 100 µM.

4.6 Fourier Transform Infrared Study.

FTIR (Fourier transform infrared) measurement was investigated for **CuCD** in D_2O. Potassium bromide (KBr) was used to mix with **CuCD** and a hydraulic press was used to granulate it. The range of the spectra was from 400 to 4000 cm^{-1} and the spectrum was normalized and scaled. Perkin Elmer Spectrum 100 FTIR spectrometer was used to perform all the experiments using a 1 mm CaF_2 cell.

4.7 Media Stability of CuCD.

Stability of aqueous solutions of **CuCD** (500 µg/mL) in biological media was investigated using DMEM media where concentration of FBS varied from 0 to 75%. Also, DMEM media (10% FBS) was added to aqueous solutions of **CuCD** (250 µg/mL) to study its stability for 10 days. For the above cases the supernatant was collected at varied time points and the absorbance was noted at 365 nm to calculate suspension stability index (SSI).

$SSI = A_t/A_0 \times 100$ where A_t = absorbance of the solution after a specific time span at 365 nm, and A_0 = initial absorbance of the solution at 365 nm.

4.8 Cell Culture.

10% FBS, antibiotic (streptomycin and penicillin) added DMEM media were used to culture NIH3T3 and B16F10 cells in incubator (5% CO_2 and 37 °C). Both type of cells was cultured and trypsinization was performed after every 3 days when the cells were 80% confluent which then used for further studies.

4.9 Cell Viability.

Cell viability of **CuCD** in normal and cancer cells were determined by the MTT reduction method. NIH3T3 and B16F10 were grown individually in a 96-well plate for 1 day in DMEM media (10% FBS). The cells were individually incubated (5% CO_2 at 37 °C) in presence of **CuCD** (50-500 µg) for 12 h. Then the MTT dye was incubated for 4 h. In this MTT reduction method, alive cells produce water insoluble formazan from the tetrazolium salt using mitochondrial dehydrogenase and that was measured by calculating the absorbance of formazan (570 nm, Biotek Elisa Reader) that is correlated to the number of live cells.

The number of alive cells was expressed as percent viability =

$(A_{570}(\text{treated cells}) - \text{background})/A_{570}(\text{untreated cells}) - \text{background}) \times 100.$ (1)

4.10 Bioimaging.

Non-cancerous NIH3T3 and cancer cells B16F10 were cultured ($1x10^4$ cells per well) in a chamber slide. At first guanine (100 µM) was separately added to the chamber slide of both type of cells for 24 h incubation. After 24 h, guanine treated and untreated cell lines were washed with PBS three times. Then **CuCD** (500 µg/mL) was added to the chamber slide of both type of cell lines for control as well as guanine incubated cell wells. After 8 h incubation, PBS buffer (pH = 7.4) was used for washing of the incubated cells two times. Followed by 4% paraformaldehyde solution was used for fixing purpose (30 min) and 50% glycerol was used for mounting. The cells on slide were covered and kept for 24 h. Olympus IX83 inverted microscope was used for imaging purpose having an excitation filter of BP 330-385 nm and a band absorbance filter below 405 nm at 40x and 20x magnification.

6.REFERENCES

1. Kamel, A.H.; Moreira, F.T.C.; Delerue-Matos, C.; Sales, M.G.F. Electrochemical Determination of Antioxidant Capacities in Flavored Waters by Guanine and Adenine Biosensors. *Biosens. Bioelectron.* **2008**, *24*, 591-599.

2. Wang, D.; Huang, B.; Liu, J.; Guo, X.; Abudukeyoumu, G.; Zhang, Y.; Ye, B.; Li, Y. A Novel Electrochemical Sensor Based on Cu@Ni/Mwcnts Nanocomposite for Simultaneous Determination of Guanine and Adenine. *Biosens. Bioelectron.* **2018**, *102*, 389-395.

3. Palecek, E. Electrochemical Behaviour of Biological Macromolecules. *Bioelectrochem. Bioenerg.***1986**, *15*, 275–295.

4. Vishnu, N.; Badhulika, S. Single Step Grown Mos_2 on Pencil Graphite as an Electrochemical Sensor for Guanine and Adenine: A Novel and Low Cost Electrode for DNA Studies. *Biosens. Bioelectron.* **2019**, *124-125*, 122-128.

5. Ng, K.L.; Khor, S.M. Graphite-Based Nanocomposite Electrochemical Sensor for Multiplex Detection of Adenine, Guanine, Thymine, and Cytosine: A Biomedical Prospect for Studying DNA Damage. *Anal. Chem.* **2017**, *89*, 10004-10012.

6. Hirao, I.; Kimoto, M.; Yamashige, R. Natural Versus Artificial Creation of Base Pairs in DNA: Origin of Nucleobases from the Perspectives of Unnatural Base Pair Studies. *Acc. Chem. Res.* **2012**, *45*, 2055-2065.

7. Wetmur, J.G. DNA Probes: Applications of the Principles of Nucleic Acid Hybridization. *Crit. Rev. Biochem. Mol. Biol.* **1991**, *26*, 227-259.

8. Jeevagan, A. J.; John, S. A. Electrochemical Sensor for Guanine Using A Self-Assembled Monolayer of 1,8,15,22-Tetraaminophthalocyanatonickel(II) on Glassy Carbon Electrode. *Anal. Biochem.* **2012**, *424*, 21-26.

9. Saenger, W.; Cantor, C.R. Principles of Nucleic Acid Structure, Springer, NewYork, 1984.

10. Chetankumar, K.; Kumara Swamy, B.E.; Bhojya Naik, H.S. MgO and MWCNTs amplified electrochemical sensor for guanine, adenine and epinephrine. *Mater. Chem. Phys.* **2021**, *267*, 124610.

11. Wallace, S.S. Biological Consequences of Free Radical-Damaged DNA Bases. *Free Radical Biol. Med.* **2002**, *33*, 1-14.

12. Wang, X.; Zhang, J.; Wei, Y.; Xing, T.; Cao, T.; Wu, S.; Zhu, F. Copper-Based Metal-Organic Framework/Graphene Nanocomposite for Sensitive and Stable Electrochemical Detection of DNA Bases. *Analyst*, **2020**,*145*, 1933-1942.

13. Ferancova, A.; Rengaraj, S.; Kim, Y.; Labuda, J.; Sillanpaa, M. Electrochemical Determination of Guanine and Adenine by Cds Microspheres Modified Electrode and Evaluation of Damage to DNA Purine Bases by UV Radiation. *Biosens. Bioelectron.* **2010**, *26*, 314-320.

14. Arvand, M.; Ghodsi, N.; Zanjanchi, M.A. A New Microplatform Based on Titanium Dioxide Nanofibers/Graphene Oxide Nanosheets Nanocomposite Modified Screen Printed Carbon Electrode for Electrochemical Determination of Adenine in the Presence Of Guanine. *Biosens. Bioelectron.* **2016**, *77*, 837-844.

15. Jesny, S.; Menon, S.; Kumar, K.G. Simultaneous Determination of Guanine and Adenine in the Presence of Uric Acid by A Poly(Para Toluene Sulfonic Acid) Mediated Electrochemical Sensor in Alkaline Medium. *RSC Adv.* **2016**, *6*, 75741-75748.

16. Marvel, C.C.; Delrowe, J.; Bremer, E.G.; Moskal, J.R. Altered RNA Turnover in Carcinogenesis the Diagnostic Potential of Modified Base Excretion. *Mol. Chem. Neuropathol.* **1994**, *21*, 353-368.

17. Li, C.; Wang, H. Selective Enzymatic Cleavage and Labeling for Sensitive Capillary Electrophoresis Laser-Induced Fluorescence Analysis of Oxidized DNA Bases. *J. Chromatogr. A*, **2015**, *1406*, 324-330.

18. Graven, P.; Tambalo, M.; Scapozza, L.; Perozzo, R. Purine Metabolite and Energy Charge Analysis of Trypanosoma Brucei Cells in Different Growth Phases

Using an Optimized Ion-Pair RP-HPLC/UV for the Quantification of Adenine and Guanine Pools. *Exp. Parasitol.* **2014**, *141*, 28-38.

19. Chen, G.; Chu, Q.C.; Zhang, L.Y.; Ye, J.N. Separation of Six Purine Bases by Capillary Electrophoresis with Electrochemical Detection. *Anal. Chim. Acta* **2002**, *457*, 225-233.

20. Gill, B.D.; Indyk, H.E. Development and Application of a Liquid Chromatographic Method for Analysis of Nucleotides and Nucleosides in Milk and Infant Formulas. *Int. Dairy J.* **2007**, *17*, 596-605.

21. Yang, F.; Guan, J.; Li, S.P. Fast Simultaneous Determination of 14 Nucleosides and Nucleobases in Cultured Cordyceps Using Ultra-Performance Liquid Chromatography. *Talanta*, **2007**, *73*, 269-273.

22. Huang, Y.; Chang, H. Analysis of Adenosine Triphosphate and Glutathione through Gold Nanoparticles Assisted Laser Desorption/Ionization Mass Spectrometry. *Anal. Chem.* **2007**, *79*, 4852-4859.

23. Xua, X.; Hea, L.; Longa, Y.; Pana, S.; Liub, H.; Yangc, J.; Hu, X. S-Doped Carbon Dots Capped ZnCdTe Quantum Dots for Ratiometric Fluorescence Sensing of Guanine. *Sens. Actuators B Chem.* **2019**, *279*, 44-52.

24. Zou, L.; Li, Y.; Ye, B. Voltammetric Sensing of Guanine and Adenine Using a Glassy Carbon Electrode Modified with a Tetraoxocalix[2]Arene[2] Triazine Langmuir-Blodgett Film. *Microchim Acta* **2011**, *173*, 285-291.

25. Li, X.; Gao, X.; Shi, W.; Ma, H. Design Strategies for Water-Soluble Small Molecular Chromogenic and Fluorogenic Probes. *Chem. Rev.* **2014**, *114*, 590–659.

26. Xu, Y.; Shi, W.; He, X.; Wu, X.; Li, X.; Ma, H. Facile and Sensitive Method for Protein Kinase a Activity Assay Based on Fluorescent off-On Polyu-Peptide Assembly. *Anal. Chem.* **2017**, *89*, 10980-10984.

27. Li, G. Nano-Inspired Biosensors for Protein Assay With Clinical Applications. Elsevier: 2018.

28. Wang, Z.; Xiao, X.; Zou, T.; Yang, Y.; Xing, X.; Zhao, R.; Wang, Z.; Wang, Y. Citric Acid Capped Cds Quantum Dots for Fluorescence Detection of Copper Ions (II) in Aqueous Solution. *Nanomaterials*, **2019**, *9*, 32.

29. Gubala, V.; Giovannini, G.; Kunc, F.; Monopoli, M. P.; Moore, C. J. Dye-Doped Silica Nanoparticles: Synthesis, Surface Chemistry and Bioapplications. *Cancer Nanotechnol.* **2020**, *11*, 1-43.

30. Lee, B. H.; Suresh, S.; Ekpenyong, A. Fluorescence Intensity Modulation of Cdse/Zns Quantum Dots Assesses Reactive Oxygen Species During Chemotherapy and Radiotherapy for Cancer Cells. *J. Biophotonics,* **2018**, *12*, e201800172.

31. Yang, G.; Phua, S. Z. F.; Bindra, A. K.; Zhao, Y. Degradability and Clearance Of Inorganic Nanoparticles for Biomedical Applications. *Adv. Mater.* **2019**, *31*, 1805730.

32. Baker, S. N.; Baker, G. A. Luminescent Carbon Nanodots: Emergent Nanolights. *Angew. Chem., Int. Ed.* **2010**, *49*, 6726-6744.

33. Sarkar, S.; Das, K.; Das, P. K. Estradiol Hemisuccinate-Modified Surface-Engineered Carbon Dots: Target-Specific Theranostic Agent. *ACS Sustainable Chem. Eng.* **2017**, *5*, 8356-8369.

34. Datta, K. K. R.; Qi, G.; Zboril, R.; Giannelis, E. P. Yellow Emitting Carbon Dots with Superior Colloidal, Thermal, and Photochemical Stabilities. *J. Mater. Chem. C* **2016**, *4*, 9798-9803.

35. Bourlinos, A. B.; Stassinopoulos, A.; Anglos, D.; Zboril, R.; Karakassides, M.; Giannelis, E. P. Surface Functionalized Carbogenic Quantum Dots. *Small,* **2008**, *4*, 455-458.

36. Cao, L.; Wang, X.; Meziani, M. J.; Lu, F. S.; Wang, H. F.; Luo, P. G.; Lin, Y.; Harruff, B. A.; Veca, L. M.; Murray, D.; Xie, S. Y.; Sun, Y. P. Carbon Dots for Multiphoton Bioimaging. *J. Am. Chem. Soc.* **2007**, *129*, 11318-11319.

37. Ji, C.; Zhou, Y.; Leblanc, R. M.; Peng, Z. Recent Developments of Carbon Dots in Biosensing: A Review. *ACS Sens.* **2020**, *5*, 2724-2741.

38. Ge, J.; Jia, Q.; Liu, W.; Guo, L.; Liu, Q.; Lan, M.; Zhang, H.; Meng, X.; Wang, P. Red-Emissive Carbon Dots for Fluorescent, Photoacoustic, and Thermal Theranostics in Living Mice. *Adv. Mater.* **2015**, *27*, 4169-4177.

39. Loi, E.; Ng, R. W. C.; Chang, M. M. F.; Fong, J. F. Y.; Ng, Y.H.; Ng, S. M. One-Pot Synthesis of Carbon Dots Using Two Different Acids and their Respective Unique Photoluminescence Property. *Luminescence*, **2017**, *32*, 114-118.

40. Jiang, L.; Ding, H. Z.; Lu, S. Y.; Geng, T.; Xiao, G. J.; Zou, B.; Bi, H. Photoactivated Fluorescence Enhancement in F,N-Doped Carbon Dots with Piezochromic Behavior. *Angew. Chem., Int. Ed.* **2020**, *59*, 9986-9991.

41. Va´zquez-Gonza´lez, M.; Liao, W.C.; Cazelles, R.; Wang, S.; Yu, X.; Gutkin, V.; Willner, I. Mimicking Horseradish Peroxidase Functions Using Cu^{2+}-Modified Carbon Nitride Nanoparticles or Cu^{2+}-Modified Carbon Dots as Heterogeneous Catalysts. ACS *Nano,* **2017**, *11*, 3247-3253.

42. Du, J.; Zhao, Y.; Chen, J.; Zhang, P.; Gao, L.; Wang, M.; Cao, C.; Wen, W.; Zhu, C. Difunctional Cu-Doped Carbon Dots: Catalytic Activity and Fluorescence Indication for the Reduction Reaction of p- Nitrophenol. *RSC Adv.* **2017**, *7*, 33929-33936.

43. Han, T.Y.; Guan, T.S.; Iqbal, M.A.; Haque, R.A.; Rajeswari, K.S.; Ahamed, M.B.K.; Majid, A.M.S.A. Synthesis of Water Soluble Copper (II) Complexes: Crystal Structures, DNA Binding, Oxidative DNA Cleavage, and in Vitro Anticancer Studies. *Med. Chem. Res.* **2014**, *23*, 2347-2359.

44. Jaina, S.; Khana, T. A.; Patilb, Y. P.; Pagariyac, D.; Kishorec, N.; Tapryald, S.; Naike, A. D.; Naik. S. G.; Bio-Affinity of Copper(II) Complexes with Nitrogen And Oxygen Donor Ligands: Synthesis, Structural Studies and in Vitro DNA and HSA Interaction of Copper(II) Complexes. *J. Photochem. Photobiol. B, Biol.* **2017**, *174*, 35-43.

45. Sissoeff, I.; Grisvard, J.; Prog, G. E. Studies on Metal Ions-DNA Interactions: Specific Behaviour of Reiterative DNA Sequences. *Biophys Mol Biol*, **1976**, *31*, 165-199.

46. Andrushchenko, V.; Van De Sande, J. H.; Wieser, H. Vibrational Circular Dichroism and IR Absorption of DNA Complexes with Cu^{2+} Ions. Biopolymers (Biospectroscopy), **2003**, *72*, 374-390.

47. Pradhan, S.; Biswas, S.; Das, D.K.; Bhar, R.; Bandyopadhyay, R.; Pramanik, P. An Efficient Electrode for Simultaneous Determination of Guanine and Adenine Using Nano Sized Lead Telluride with Graphene. *New J. Chem.* **2018**, *42*, 564-573.

48. Xing, D.X.; Tan, X.J.; Jiang, X.B.; Wang, B. Deprotonation Studies of Cu^{+}–Guanine and Cu^{2+}–Guanine Complexes by Theoretical Investigation. *Comput. Theor. Chem.* **2011**, *963*, 490-496.

49. Panga, S.; Zhangb, Y.; Wua, C.; Feng. S. Fluorescent Carbon Dots Sensor for Highly Sensitive Detection of Guanine. *Sens. Actuators B Chem.* **2016**, *222*, 857-863.

POSTLUDE

In today's modern world scientists are trying to follow nature's footsteps in the area of nano-dimension. Nature carefully wove cellular structures from interconnected nanometer scale materials called nanomaterials and nanotechnology is the engineering of functional systems of these nanomaterials.

It offers the most promising opportunity to get a grip on the desired purpose of utilizing functional nanomaterials in different domain from surface science, organic chemistry, semiconductor to molecular biology, biocatalysis, nano-medicine, drug delivery etc.

Among many kinds of nanomaterials, carbon dot, also known as the carbon nanodot, carbon quantum dot, represents an interesting class of carbonaceous nanomaterials which is more suitable for biological domain than other nanomaterials (metal nanoparticles, 2D, 1D carbon nanomaterial). In case of metal nanoparticles, 2D, 1D carbon nanomaterial several parameters such as toxicity in biological systems, potential environmental hazardness and difficulty of synthesis associated with many of these materials may represent serious limitations. On other hand carbon dots have intrinsic fluorescence property, cytocompatibility, easy to synthesize, tunable emission property etc which created enormous opportunity for exploiting it in the arena of sensing, bioimaging and theranostic.

The prime research objective of our group at IACS is to design various types of carbon dots for developing different strategies to fight cancer as well as in sensing applications. These carbon dots played vital role in multiple domains ranging from biochemical to bio-medicinal applications. The present thesis describes the role of carbon dot from sensor to drug delivery vehicle to a vehicle as well as a theranostic agent itself and last but not the least as only theranostic agent. The scientific work documented in this thesis is the outcome of our constant endeavour towards developing functional carbon dots contributing to the scientific advancement and ends with a hope that it could be interpretable to the interested individuals.

PUBLICATIONS

1. **Chowdhury**, **M**.; Pal, S.; Ghosh, A.; Das*, P. K.Co^{2+} Doped Biotinylated Carbon Dot: A Theranostic Agent for Target Specific Killing of Cancer Cells via Hypoxia Induced Apoptosis. *Chem. Eur. J.* **2023**, *29*, e202300928.

2. **Chowdhury**, **M**.; Das*, P. K**.** Paclitaxel-Loaded Biotinylated Fe^{2+}-Doped Carbon Dot: Combination Therapy in Cancer Treatment. *ACS Appl. Bio Mater*. **2021**, *4*, 5132-5144.

3. **Chowdhury**, **M**.; Sarkar, S.; Das*, P. K. Photosensitizer Tailored Surface Functionalized Carbon Dots for Visible Light Induced Targeted Cancer Therapy. *ACS Appl. Bio Mater*. **2019**, *2*, 4953-4965.

4. **Chowdhury**, **M**.; Basu, D.; Khan, A. H.; Das*, P. K. Cu^{2+} Integrated Carbon Dot as Efficient Bioprobe for Guanine Nucleobase. *(Manuscript under preparation)*

5. Pal, S.; Jana, M.; **Chowdhury**, **M**.; Das*, P. K**.** Selective Sensing of Epinephrine by Phenylboronic Acid Tethered Carbon Dot. *Chem. Asian J.* **2023**, *18*, 10.1002/asia.202300415.

6. Pal, S.; Khan, A. H.; **Chowdhury**, **M**.; Das*, P. K. Peptide Amphiphilic Supramolecular Nanogel: Competent Host for Notably Efficient Lipase Catalyzed Hydrolysis of Water Insoluble Substrates. *ChemBioChem* 10.1002/cbic.202300253.

7. Sarkar, D.; **Chowdhury**, **M**.; Das*, P. K. Naphthalimide-Based Azo-Functionalized Supramolecular Vesicle in Hypoxia-Responsive Drug Delivery. *Langmuir* **2022**, *38*, 3480-3492.

8. Ghosh, A. K.; **Chowdhury**, **M**.; Das*, P. K. Nipecotic Acid Tethered Naphthalene Diimide based Orange Emitting Organic Nanoparticles as Targeted Theranostic Probe for $GABA_A$ Receptor Enriched Cancer Cells. *ACS Appl. Bio Mater.* **2021**, *4*, 7563-7577.

9. Sarkar, D.; **Chowdhury**, **M**.; Das*, P. K. Naphthalimide Based Fluorescent Organic Nanoparticle in Selective Sensing of Fe^{3+} and as Diagnostic Probe for Fe^{2+}/Fe^{3+} Transition. *J. Mater. Chem. B* **2021**, *9*, 494-507.

10. Ghosh, A.; Ghosh, A. K.; **Chowdhury**, **M**.; Das*, P. K. Folic Acid-Functionalized Carbon Dot-Enabled Starvation Therapy in Synergism with Paclitaxel against Breast Cancer. *ACS Appl. Bio Mater.* **2022**, *5*, 2389-2402.

11. Chakraborty, D.; Dinda, S.; **Chowdhury**, **M**.; Das*, P. K. Morphological Transformation of Self-Assemblies by Tuning Hydrophobic Segment of Small Amphiphiles. *J. Colloid Interface Sci.* **2019**, *539*, 414-424.